INVESTIGATION OF MOTOR PROTEINS IN HOMOLOGOUS RECOMBINATION

A Dissertation

Presented to the Faculty of the Graduate School

of Cornell University

In Partial Fulfillment of the Requirements for the Degree of

Doctor of Philosophy

by

Jingyi Hu

December 2025

INVESTIGATION OF MOTOR PROTEINS IN HOMOLOGOUS RECOMBINATION

Jingyi Hu, Ph. D.
Cornell University 2025

Homologous recombination (HR) is a high-fidelity pathway for repairing DNA double-strand breaks (DSBs) that is choreographed by the HR machinery, the DNA-damage checkpoint, and cell-cycle regulators. A central challenge in HR is locating a homologous DNA template while maintaining genome integrity. The transient intermediates that arise during homology search are dynamically regulated by multiple factors, ultimately shaping repair outcomes. Two key DNA motors in this process are Rad54 and Rdh54, Snf2-family ATP-dependent DNA translocases that remodel the Rad51-mediated presynaptic complex to promote template location and strand invasion. However, how these motors are regulated and how they function mechanically during homology search remain open questions.

Here, I show that phosphorylation of Rdh54 by the effector kinase Rad53 decouples ATP hydrolysis from DNA translocation, thereby increasing HR fidelity. Structural modeling suggests that the phosphorylation site lies at an intermolecular interface, consistent with regulation through protein-protein interactions.

I also identify a separation-of-function mutant of Rad54 that exhibits reduced motor activity due to an increased DNA dissociation rate. Within the presynaptic complex, the mutant regains approximately 60% of wildtype translocation activity but remains less

capable of resisting external forces. *In vivo*, the mutant suppresses the Rad51-overexpression phenotype and is synthetically lethal with *srs2*Δ, indicating that a later pathway rather than presynaptic filament assembly is primarily affected. The mutant displays reduced efficiency in D-loop capture and DNA repair in ectopic recombination, but its repair deficiency in allelic recombination can be compensated by longer-track gene conversion events. This suggests that the HR intermediates formed by the mutant are less stable but can be functionally rescued by extended homology. The instability of these intermediates also leads to increased frequencies of non-crossover (NCO) and reinvasion-induced break-induced replication (BIR) events.

Taken together, I propose a DNA compaction model, in which Rad54 locally compacts large fragments of DNA through multiple Rad54-DNA contacts, enabling a 1-dimensional search within the constrained DNA. A stable anchor motor is critical for maintaining this structure and ensuring efficient search. The separation-of-function Rad54 mutant loses the ability to clamp and constrain DNA, rendering search intermediates more vulnerable to mechanical disruption and thereby reducing homology search efficiency.

BIOGRAPHICAL SKETCH

Jingyi Hu was born and raised in Taizhou, a city on the southeast coast in China. She received her bachelor's degree in Biological Science from the School of Life Sciences at Fudan University in 2020, where she studied nucleolar protein phase separation in cultured human cells. She then joined the Department of Molecular Biology and Genetics at Cornell University to pursue her Ph.D. under the mentorship of Dr. John Brooks Crickard. Her doctoral research focused on the molecular mechanisms of DNA motor proteins in homologous recombination.

To my parents, my friend Rongrong, and my advisor Brooks

for their generous support.

ACKNOWLEDGMENTS

First of all, I would like to express my deepest gratitude to my advisor, Dr. J. Brooks Crickard, for his invaluable mentorship, support, and encouragement throughout my Ph.D. studies. When I first moved to the United States, I struggled with English and knew little about life or study here. He was always patient in answering my questions, guiding me through experiments, encouraging me to try new techniques, and showing me that I was capable of succeeding as a Ph.D. student and as a researcher. He also cared deeply about my career development and provided me with opportunities to present my work and connect with the scientific community.

I am grateful to my first friend at Cornell, Jennifer Dau, who was a technician in the Crickard lab when I joined. She helped me adjust to life in Ithaca and supported me in the lab. She also contributed to building the lab's plasmid repository and carried out the primary mutation screen in my first project on Rdh54. I also wish to thank former postdoctoral researchers in the lab, Dr. Bryan Ferlez and Dr. Renna Costa. They are meticulous, rigorous, responsible, and generous scientists who shared with me their invaluable experience. Bryan's knowledge of molecular biology and phylogeny, and Renna's expertise in mammalian systems, broadened my scientific perspective. They also supported me beyond lab work: Renna often shared her baking with us and once drove me to a colleague's wedding, and Bryan kindly drove me to Penn State University for a conference and showed me its beautiful campus.

I thank my committee members, Prof. Eric Alani and Prof. Marcus Smolka, who invested time in following my research progress and provided valuable advice during my A exam, student seminar, annual committee meetings, and the R3 group meetings (Cornell DNA Replication, Repair, and Recombination group). I am also grateful to the entire Cornell R3 community, where I have learned a great deal about the field of chromosome integrity.

I would also like to thank my labmates: Mitch Woodhouse, David Moraga, Peter Huang, Sejal Bakhati, and Ilayda Korkmaz. There is an old Chinese saying: “There are differences in the time of learning the truth and in the areas of expertise (闻道有先后，术业有专攻).” Since we come from different backgrounds and follow different research paths, we have been able to learn from and support one another from diverse perspectives. I also thank the dedicated undergraduate students who contributed to projects I have been involved in: Amanda Xu, Margaret Keymakh, Lauren Peysakhova, Krishay Sridalla, Jessica Scheer, and Katelyn Acrie (REU student from Penn State University). In particular, working with Amanda, Lauren, and Katelyn showed me that teaching is also a form of learning.

I would like to thank my collaborators: Dr. Bokun Xie (alumnus), Mateusz Wagner, and Shrijan Bhattarai from the Smolka Lab, and our friends and colleagues from the Alani Lab: Dr. Beata Mackenroth (alumna), Premila Edamala, Isaac Chizhik, Madeleine Brown, and Ricky Shan. Their expertise, collaboration, and friendship have greatly enriched my research and my time at Cornell.

I would like to thank Prof. Chris Fromme, Prof. Carolyn Sevier, and Prof. Fenghua Hu, who served as Directors of Graduate Studies in the department during my Ph.D. In particular, I am grateful to Chris, who made it possible for me to defer my enrollment and take online courses during the COVID-19 pandemic. I also thank the departmental staff who helped me with administrative matters: Casey Moore (retired), Vic Shaff, Elizabeth Seldin, Jennifer Robinson, Nicole Pierpont and Steve Sparling.

I am grateful to the Genomics, Proteomics, and Imaging Facilities of the Cornell Institute of Biotechnology, whose expertise and services supported my research.

Beyond academics, I want to thank my friends in Ithaca. Xiangqi Meng and Weijie Hao, my first two roommates, shared with me a long and cold winter, but with their companionship the season became much easier to endure. I also thank Dr. Shufen Chen, a postdoctoral researcher in the Breeding Insight at Cornell University, who was my roommate for two years. During that time, we became close friends, sharing both happiness and challenges. I am also grateful to Ping Li, who briefly joined Shufen and me in our apartment and left us with lovely memories. I thank my friends from badminton and beyond: Dr. Lin Zeng, Dr. Yi Wu, Dr. Helffor Tang, Dr. Min Jin, Haipei Zou, Xuemei Xiao, and Zixia Huang, with whom I spent much of my time outside the lab.

I also want to acknowledge my long-term friends from college: Jianghui Zhu, Fangfei Ye, Shengyi Lu, and Hengchi Chen. Although we do not meet often, our friendship continues to make me feel cared for and supported.

I am also grateful to Ithaca, a beautiful and tranquil place. I also thank the Cornell campus, whose beauty I have cherished throughout my time here. I would like to thank TCAT system. Although it sometimes breaks down, it has provided me with great convenience in daily life.

I wish to express my gratitude to Shen Zhou (周深), my favorite singer, whose music helped me through many difficult times. I also thank the Bilibili video uploader "Liaodianshenmeba (聊点什么叭)," whose videos became my background music for years.

I want to thank knitting, crocheting and sudoku, which brought me many peaceful and fruitful moments. I also thank coffee and tea. I am grateful to vitamins B, C, and D, which helped support my health along the way.

Most importantly, I thank my parents and other family members, whose understanding, support, and trust made this long journey across the ocean possible, safe, and meaningful. Their pride in me gives me strength and hope.

I am also deeply grateful to my friend Rongrong Du, who has always believed that doing research is a calling. Her pure faith and firm confidence in science are powerful and inspiring to everyone around her.

Last but not least, I want to thank myself for overcoming the many challenges, and for allowing each experience to reshape me along the way.

TABLE OF CONTENTS

LIST OF FIGURES

LIST OF TABLES

LIST OF ABBREVIATIONS

Alt-NHEJ	Alternative nonhomologous end joining
BIR	Break-induced replication
CDK	Cyclin-dependent kinase
CO	Crossover
Co-IP	Co-immunoprecipitation
CPT	Camptothecin
CTD	C-terminal domain
dHJ	Double Holliday junction
DLC	D-loop capture
DLE	D-loop extension
DNA	Deoxyribonucleic acid
DNA-PK	DNA-dependent protein kinase
DNA-PKcs	DNA-dependent protein kinase catalytic subunit
DSB	Double-strand break
DSBR	Double-strand break repair
dsDNA	Double-strand DNA
D-loop	Displacement loop
UV	Ultraviolet
HJ	Holliday junction
HR	Homologous recombination
HU	Hydroxyurea
IP	Immunoprecipitation
IR	Ionizing radiation
LOH	Loss-of-heterozygosity
LTGC	Long tract gene conversion

MMEJ	Microhomology-mediated end joining
MMS	Methyl methanesulfonate
MRX/MRN	Mre11-Rad50-Xrs2/MRE11-RAD50-NBS1
NCO	Non-crossover
NHEJ	Non-homologous end joining
PIKK	Phosphoinositide 3-kinase-related kinase
PSC	Presynaptic complex
ROS	Reactive oxygen species
RPA	Replication protein A
SDSA	Synthesis-dependent strand annealing
SSA	single-strand annealing
ssDNA	Single-strand DNA
STGC	Short tract gene conversion
STR/BTRR	Sgs1-Top3-Rmi1/BLM-TOPO3α-RMI1-RMI2
WCE	Whole cell extract
WT	Wildtype
4-NQO	4-Nitroquinoline 1-Oxide

CHAPTER 1

Introduction to DNA double-strand break repair and homologous recombination

Deoxyribonucleic acid (DNA) is a major genetic material that carries hereditary genetic information passed from parents to offspring. To preserve its integrity, it must be appropriately compacted to chromosomes in eukaryotes and prokaryotes while remain dynamically accessible to allow for its replication and expression. Throughout these processes, DNA damage can occur, and failure to respond to and repair the damage leads to chromosome instability, including mutations, chromosome re-arrangements, aneuploidy and ultimately diseases or death. Among DNA lesions, DNA double-strand break (DSB) is considered the most deleterious since the continuity of both DNA strands is disrupted. Unlike mismatches or single-strand breaks, where the intact complementary strand can guide repair, the loss of both strands makes recovery of genetic information especially difficult. Therefore, DSB needs to be closely monitored and properly repaired or protected during cell cycle. To understand the underlying mechanisms is essential for advancing our knowledge of genome integrity maintenance and its relationship to disease development.

1.1 Sources of DSBs

Both external and endogenous sources can generate similar types of DNA lesions. Natural radiation, including ultraviolet (UV) light from sunlight and ionizing radiation (IR) from cosmic rays or radioactive decay, can generate reactive oxygen species (ROS) that penetrate cells and induce DNA strand breaks. Two closely spaced single-strand DNA (ssDNA) breaks on opposite strands of DNA can ultimately form a DSB (Figure

1.1A(a)) (1). During normal oxidative respiration, mitochondria also generate ROS including superoxide, hydrogen peroxide and hydroxyl radicals, which induce oxidative DNA lesions and threaten genome integrity (2). In addition, UV radiation can induce adjacent pyrimidines to crosslink and form pyrimidine dimers, which may cause mutations, block DNA replication and transcription, and lead to DSBs (3–5).

Enzyme activity can cause chromatid breaks, both inadvertently and as programmable events. For instance, failures of type II topoisomerases, which transiently break both strands, can cause DSBs (2). Conversely, Spo11, a topoisomerase II-like enzyme, deliberately creates DSBs during meiosis to initiate homologous recombination (HR), thereby promoting homologous chromosome alignment, which is essential for meiosis I division (6). Similarly, engineered and inducible site-specific DNA endonucleases are frequently used to generate DSBs in cells for studying DNA repair mechanisms (Figure 1.1A(b)) (7).

During DNA replication, replication fork stalling and collapse can also result in DSBs. Fragile sites on chromosomes may spontaneously induce fork stalling or do so under mild replication stress. Unresolved lesion can persist into next cell cycle, where they are sequestered by nuclear bodies (8). Additional obstacles, UV-induced DNA crosslinks, mismatches, protein-DNA adducts or nucleotides depletion, can also block replication (Figure 1.1A(c,d,e,f)). Although translesion synthesis and template switching are the primary repair pathways to deal with replication stress, HR, one of the major DSB repair pathways, can also assist, especially when there are no converging forks to complete replication or when the stalled replication forks are processed to DSBs (9).

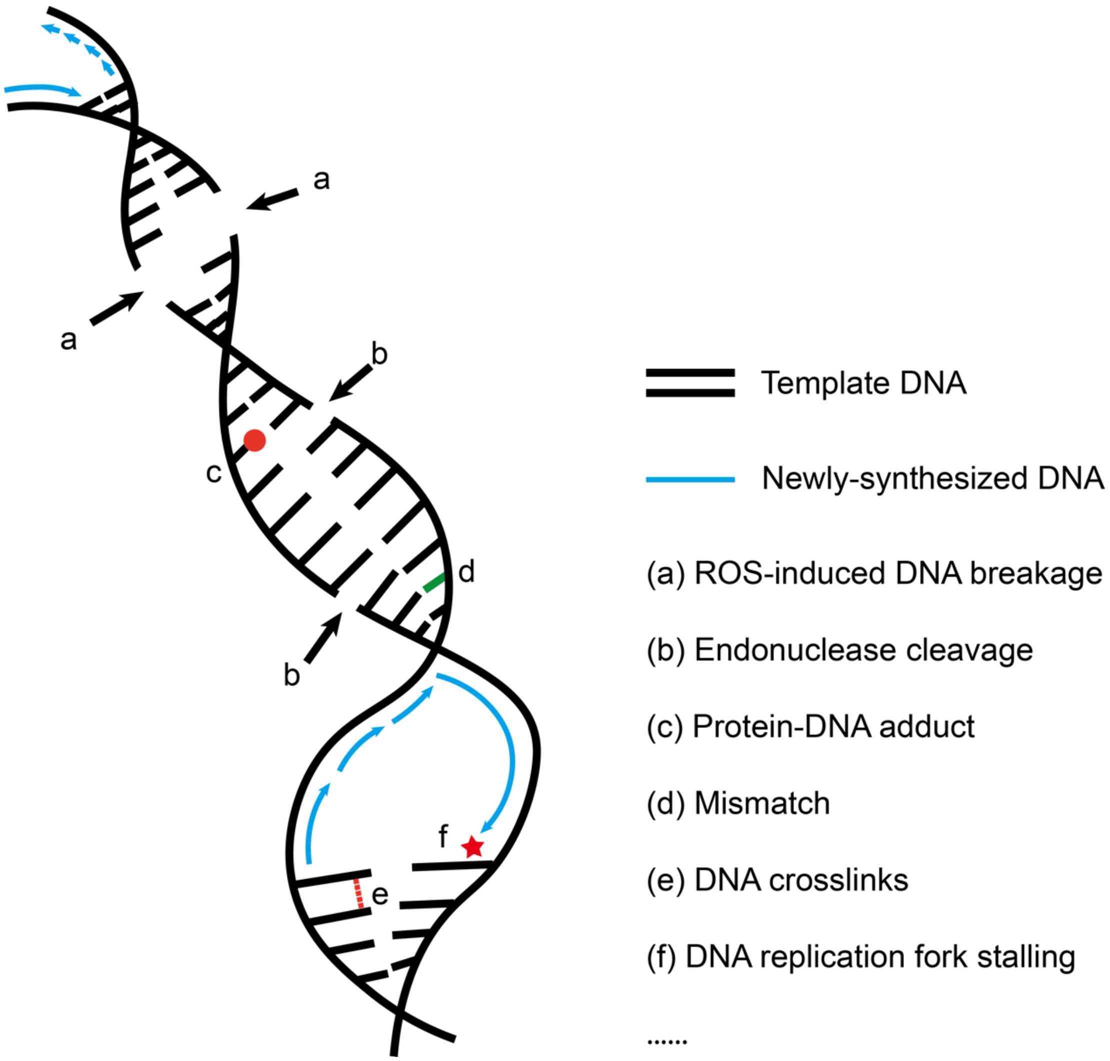

Figure 1.1: The schematic of DSB sources.

The diverse causes of DSBs give rise to DNA ends with variable chemical structures. While nuclease-induced DNA ends are typically "clean" with ligatable 3' hydroxyls and 5' phosphates, most DSB ends are more complicated. They often contain non-ligatable nucleotides such as glycosidic fragments generated by IR, protein adducts, or secondary structures that must first be removed (10). The two ends are usually not blunt but instead have overhangs, and spontaneous end-joining is not always energetically favorable because the pairing between strands can be imprecise (11). Repair mechanisms must therefore be both flexible and sufficiently faithful to handle such variability.

To study DSB repair mechanism, researchers often induce DSBs deliberately. UV light and gamma rays have been used to stress cells and identify DSB repair-deficient mutants (12). Chemicals are also used to generate DNA damages. For example, DNA alkylation reagent methyl methanesulfonate (MMS) induces mispairings and replication stress. While MMS-induced DNA damage is primarily repaired through the excision repair pathway, disruption of HR also leads to increased sensitivity of *Saccharomyces cerevisiae* to MMS (13). Phleomycin is a glycopeptide antibiotic from *Streptomyces verticillus* that can mimic IR by causing oxidative stress and DNA strand breaks (14). 4-Nitroquinoline 1-Oxide (4-NQO) is a UV-like carcinogen that induces base adducts and blocks replication (15, 16). 4-NQO also exerts oxidative stress on cells (17). And as mentioned above, engineered DNA nucleases remain a powerful tool to generate time- and site-controllable DSBs *in vivo*.

1.2 DSB repair

1.2.1 Non-homologous end joining

To repair DSB, there are two major pathways. The first one is the non-homologous end joining (NHEJ). As the name suggests, this pathway repairs the damage by directly rejoining the two broken ends through a range of enzymes. In *S. cerevisiae*, the Ku complex, a heterodimer consisting of yKu70 and yKu80, is rapidly recruited to the broken ends, providing a platform to load other factors, including polymerases, nucleases and ligases, to process the ends. The Mre11-Rad50-Xrs2 (MRX) complex carries out limited DNA end resection, while DNA polymerase IV (Pol4) in polymerase X family fills nucleotide gaps. DNA ligase IV (Dnl4) ligates two ends together, stabilized by its binding partners Lif1 and Nej1. Rad27 also contributes to NHEJ by cleaving 5' flaps (11).

The pathway is conserved across prokaryotes and eukaryotes, following similar mechanisms but involving different factors. In *Homo sapiens*, the Ku complex is a subunit of DNA-dependent protein kinase (DNA-PK). The catalytic subunit of DNA-PK (DNA-PKcs) is a serine/threonine kinase that phosphorylates itself and other factors after being recruited the DNA damage sites by the Ku complex. Artemis acts as the nuclease in human NHEJ, activated through its association with DNA-PKcs, and the XRCC4-DNA ligase IV complex is the ligase (18, 19). The XRCC4-like factor (XLF) interacts with XRCC4 both *in vivo* and *in vitro*, and disruption of XLF leads to higher radiosensitivity (20). Members of DNA polymerase X family including Pol μ and Pol λ are also involved in gap filling during NHEJ (21–23).

NHEJ is a relatively error-prone pathway. One identical break can be repaired with various outcomes by NHEJ due to several factors. First, the enzymes serving in the pathway are functionally flexible. Nucleases such as Artemis in human exhibit multiple activities, including 5' to 3' endonuclease, 3' to 5' endonuclease, hairpin-opening and 5' to 3' exonuclease activities (18). Polymerases like Pol4 in budding yeast and Pol μ and Pol λ in human are more error-prone and less dependent on templates than replicative polymerases. Ligases can act asymmetrically, sealing one DNA strand while the complementary strand remains incompatible for ligation (23). Second, the two DNA ends can be processed independently, and their processing is often iterative with multiple possible reaction sequences leading to a final joining event, making end processing highly unpredictable. For example, one strand can be ligated first if at least a 2-bp microhomology is present, leaving the other end to be resected or filled before ligation. Alternatively, both ends may be processed separately until both ends are ligated (Figure 1.1B) (18, 23). This mechanistic flexibility increases joining variability in V(D)J recombination, which is essential for B lymphocytes to produce a wide repertoire of antibodies for adaptive immunity.

1.2.2 Homologous recombination

The second repair pathway is homologous recombination (HR), which is a template-based repair pathway. The broken DNA (recipient DNA) needs to search the genome for a homologous sequence to serve as a template (donor DNA) to guide DNA synthesis, aided by a series of proteins. HR is active in S, G2 and M phases of the cell cycle, when a sister chromatid is available to serve as the donor DNA. In meiosis, homologous chromosomes are preferentially used to ensure accurate chromosome alignment and segregation. This also promotes genetic exchange between homologous chromosomes, thereby increasing genetic diversity from parents to offspring. When a donor template is not available in G0 and G1 phases, NHEJ is more active than HR. The balance between HR and NHEJ also varies among species. Unlike in yeast, where HR predominates, NHEJ is more prevalent in human cells despite its lower repair fidelity.

HR is conserved across prokaryotes and eukaryotes. In budding yeast, HR is initiated by 5’ to 3’ end resection, which generates 3’ ssDNA overhangs. The 3’ ssDNA overhangs are first covered by the replication protein A (RPA) complex, which recruits the signaling kinase Mec1 to initiate cell cycle arrest through the Mec1-Rad9-Rad53 signaling axis. Subsequently, RPA is replaced by the Rad51 recombinase, forming Rad51-ssDNA filaments, which can be referred as presynaptic complex (PSC) (Figure 1.2A). The PSC searches the genome for a donor sequence, and once found, promotes strand invasion event to form a displacement loop (D-loop), in which one strand of the donor DNA will be displaced by the invading ssDNA (Figure 1.2BC). DNA synthesis then proceeds from the 3' end of the invading strand using the complementary DNA as a template. D-loops are dynamically regulated and can be resolved through multiple pathways, as discussed below in Section 1.3.2.

1.2.3 Other repair mechanisms

There are other mechanisms that repair DSBs, including single-strand annealing (SSA) and alternative non-homologous end joining (alt-NHEJ).

SSA also requires end resection to yield 3' ssDNA overhangs. The ssDNA can anneal with a flanking homologous sequence aided by Rad52, and the non-homologous tails are removed by Rad1-Rad10 in *S. cerevisiae* and by XPF-ERCC10 in *H. sapiens* (24–26). Intra-chromosomal SSA can lead to chromosome deletion, whereas inter-chromosomal SSA can result in chromosome translocations.

Unlike classical NHEJ, alt-NHEJ doesn't dependent on the Ku complex (27). Many alt-NHEJ events are classified as microhomology-mediated end joining (MMEJ). End resection is required for MMEJ, during which a 5-25 bp microhomology at the end can anneal and guide joining. MMEJ also leads to sequence deletions. Compared with SSA, resection during MMEJ is more limited, and the complementary region required are correspondingly smaller (28). MMEJ is not strictly dependent on Rad52, and the involvement of Rad52 may relate to the extent of sequence deletion (29).

1.3 Mechanisms of HR

1.3.1 End resection

HR begins with 5' to 3' DNA end resection to generate 3' ssDNA overhangs, which serves as substrates for homology search and subsequent DNA synthesis. DNA end resection proceeds in two steps. The first step is short-range resection performed by the MRX complex with its cofactor Sae2 in *S. cerevisiae* and by the MRE11-RAD50-NBS1 (MRN) complex with CtIP in *H. sapiens*. The second step is long-range resection catalyzed by Exo1 or Dna2 in *S. cerevisiae* and by their homologs EXO1 or DNA2 in human. Short-range resection occurs near the DSB, proceeds more slowly and processes diverse DNA ends including protein adducts and secondary structures. Long-range resection is faster but less effective on non-canonical DNA ends. Together, the two steps provide both efficiency and flexibility for DSB end resection (10).

1.3.1.1 Short-range resection

Biochemical studies showed Mre11 has a manganese-dependent 3' to 5' exonuclease activity and a hairpin-opening activity. Rad50 forms a 1:1 complex with Mre11 and enhances these activities to different extents across organisms, and this stimulation is dependent on Rad50's ATP hydrolysis activity (30, 31). Structural analysis of the *Pyrococcus furiosus* Mre11-Rad50 complex showed a heterotetramer containing two Mre11 and two Rad50 molecules (M_2R_2). The Mre11 nuclease and Rad50 ATPase domains form a globular head with long Rad50 coiled-coil tails (32). Human NBS1, mutated in Nijmegen breakage syndrome, associates with human MRE11 and RAD50 (33). Xrs2 is the budding yeast counterpart of NBS1. Xrs2/NBS1 mediates Mre11-Rad50/MRE11-RAD50 nuclease activities, recruits Sae2/CtIP to breaks, and coordinates DNA damage repair with checkpoint activation (34–37).

Studies of Mre11 3' to 5' exonuclease activity initially appeared inconsistent with *in vivo* observation of 5' to 3' DSB end resection. To address this paradox, further research demonstrated that the cofactor Sae2/CtIP stimulates the endonuclease activity of the MRX/MRN complex, acting preferentially on 5'-terminated DNA, and this activity is further enhanced by the presence of protein adducts at the DNA termini (38, 39). These findings support a bidirectional resection model: the MRX/MRN complex with Sae2/CtIP incises the 5'-terminated DNA at some distance from the DSB end. This internal cleavage site is an initial point for MRX/MRN to perform 3' to 5' resection back to the break, releasing protein adducts and secondary DNA structure, and for Exo1/EXO and Dna2/DNA2 to carry out 5' to 3' long-range resection (10, 40, 41). This model accounts for the versatility of the complex in bypassing protein obstacles and noncanonical structures at DSB ends.

1.3.1.2 Long-range resection

Exo1/EXO1 and Dna2/DNA2 have partially overlapping functions, but their relative contributions vary by organism. In budding yeast meiosis, Exo1 is the primary nuclease, while in mouse, loss of EXO1 leaves most long-range resection intact (42, 43). Exo1 is Rad2 family nuclease with 5' to 3' exonuclease activity (44). It can enter through a DNA nick to initiate resection (45). Dna2 nuclease activity requires a free 5' end (46). Long-range resection by Dna2 requires a helicase, which is Sgs1 in *S. cerevisiae* and BLM or WRN in human (47–49).

Short-range resection promotes long-range resection, likely because the long-range resection machinery is sensitive to DNA end adducts (50, 51). In *S. cerevisiae*, depletion of long-range nucleases only causes a moderate decrease in IR-induced recombination (52). *In vivo*, resection can be extremely extensive in donor-less cells, reaching up to 30 kb, in SSA systems where track length scales with the distance to the donor DNA. In meiosis cells, resection tracts are typically shorter, from hundreds to a few thousand nucleotides (41, 53, 54). Additionally, multiple rounds of MRX/MRN and Sae2/CtIP directed nicking and resection may compensate when long-range nucleases are removed. These observations indicate that long-range resection is relatively dispensable for sister chromatid and meiotic recombination but more important when recombination occurs within repeated sequences, where longer tracts help favor the correct donor over ectopic donors. Beyond its role in HR, long-range resection also contributes to cell cycle checkpoint activation (55).

1.3.1.3 Overlap with NHEJ

At mismatched breaks, MRX-mediated end process can expose micro-homologies that lead to end joining, showing a role for MRX/MRN in NHEJ (30, 56). Inhibiting the endonuclease activity of Mre11 reduces HR and shifts repair toward NHEJ, whereas inhibiting the exonuclease activity broadly impairs repair (57). Multiple roles of MRX/MRN complex give a glimpse that different repair pathways are intrinsically competitive yet coordinated in the cellular environment. The Ku complex binding to

DNA end can aid MRX loading and limit 3’ to 5’ resection, which favors NHEJ when microhomologies are available. On the other hand, the addition of Sae2 can turn MRX exonuclease into an endonuclease and launch end resection to favor HR. The Ku complex can also act as a protein obstacle that increases this endonuclease activity, thereby promoting HR. Other factors including cell cycle kinases and homologous sequence availability are also involved to further shape pathway choice.

1.3.2 Homology search

Note: This section has been previously published as:

Hu, J. and Crickard, J. B. (2023) “All who wander are not lost: the search for homology during homologous recombination.” Biochemical Society Transactions. © The Biochemical Society. Reproduced here with permission.

After end resection, the ssDNA can then be used as a guide by recombinase filaments to find a matching sequence elsewhere in the genome (10, 58, 59) (Figure 1.2). The key recombinases are RecA in eubacteria, RadA in archaea, and Rad51/Dmc1 in eukaryotes. Dmc1 is meiosis specific.

The homology search step controls template selection by pairing the damaged recipient DNA to a matching donor DNA (60). The identity of this donor then governs the fidelity of the reaction. In most HR reactions, the sister chromatid is used to repair the DNA (61). This is considered the highest fidelity repair pathway. Changes to the genome can occur when an ectopic sequence or a homologous chromosome is selected, leading to potential gene conversion and crossover (CO) outcomes (62–64). In the case of meiotic HR, gene conversion and COs are used to promote genetic diversity within populations. Therefore, mechanisms of template selection are deeply entrenched in genome maintenance, both on a short-term and a long-term timeline. This review will focus on the homology search and template selection during mitotic growth. While conceptually similar, mechanisms that govern meiotic homology search involve a different set of genes (6, 65).

1.3.2.1 RecA/Rad51 family recombinases, the engine that drives the homology search

Recombinase proteins are conserved across the kingdoms of life (66). The general role of the RecA/Rad51 family of recombinases is to pair donor and recipient DNA. RecA/Rad51, a family of DNA recombinases, catalyzes the homology search during HR by assembling as a filament on ssDNA called the presynaptic complex (PSC). The PSC can interrogate the genome for a matching sequence element in the donor dsDNA. Once the specific homology has been identified, the filament transitions into a strand invasion reaction. In this reaction, the ssDNA anneals with the complementary strand and displaces the non-complementary strand to form a displacement loop (D-loop).

The filamentous structure of recombinases is one of the defining features of this group of enzymes. They form a right-handed helical filament with a ~95-Å pitch and a turn of ~6 RecA monomers on DNA. This structure stretches the DNA 1.5 times, lengthening the DNA (67–69). Although the DNA is stretched by RecA filaments globally, it is locally organized into B-DNA-like triplets, allowing them to recover energy through base stacking (68). Physical modeling suggests that the binding and opening of a dsDNA involves the secondary DNA binding site and the C-terminal domain (CTD) of the RecA filament (70, 71). Cryo-electron microscopy demonstrated that upon binding to the CTD,

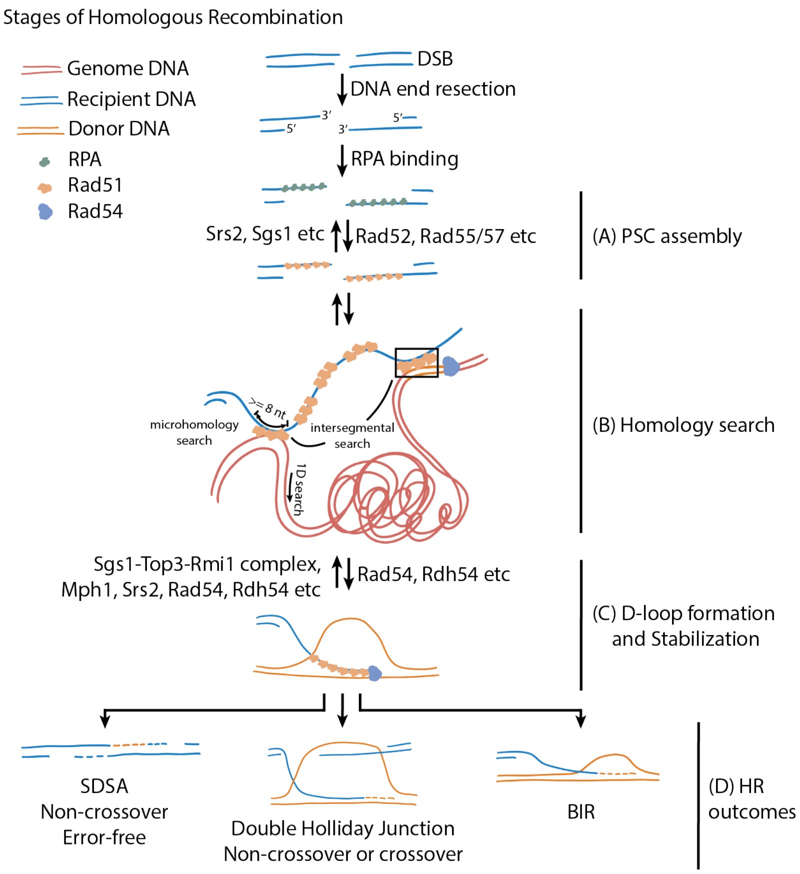

Figure 1.2: Illustrating the HR process in *Saccharomyces cerevisiae*.

Homologous recombination (HR) initiates with DNA end resection of a DSB, creating 3' overhangs of ssDNA. The ssDNA is initially bound by replication protein A (RPA) and (A) followed by recombinase binding which is regulated by a series of mediators and anti-recombinases, culminating in the formation of an active presynaptic complex (PSC). The PSC gains the capability to perform (B) the homology search among the genome by microhomology kinetic search, intersegmental search and local 1D sliding search. Once the homologous sequence is identified, the ssDNA invades into the dsDNA to form a D-loop. (C) Zoom in the black box in (B). The D-loop is reversible and regulated by several helicases and a topoisomerase, which eventually leads to different (D) HR outcomes.

dsDNA is directed and opened by RecA L2 loop. This facilitates the subsequent sequestering of the non-complementary strand to the secondary DNA binding site. This promotes the pairing between the recipient and donor DNA (69, 72). The opening of dsDNA can be terminated at each protomer step, with the homologous DNA sequence suppressing the termination. This mechanism enhances the fidelity of homology search (69, 73, 74).

The direct visualization of reconstituted systems has defined assembly of both RecA and Rad51 on ssDNA. Filament assembly occurs by a two-step kinetic mechanism where RecA nucleates on transiently exposed ssDNA followed by extension and filament growth (75). Similar observations have been made for Rad51 (76). Fluorescence microscopy has also revealed a direct mechanism by which the RecA/Rad51 family of proteins reduces the complexity of the homology search by adopting a length-based microhomology recognition. Recombinase filaments kinetically reject dsDNA that lack 8-nt microhomology motifs (77–79). The PSC can also probe different dsDNA regions simultaneously by “intersegmental contact sampling” in a three-dimensional manner to increase the probability of encountering the target and decreasing reaction time (69, 80). The biophysical properties of RecA/Rad51 filaments have generated a wealth of knowledge that can be used to interpret recent advances in *in vivo* imaging used to track recombinase activity, as discussed below.

1.3.2.2 Versatile factors help with the homology search

Without an active recombinase filament, the homology search will not go to completion. Therefore, we consider filament assembly and dynamics a key regulator of the homology search (Figure 1.2A). This section will discuss some of the many eukaryotic mediator proteins that ensure proper assembly and regulation of Rad51 filaments during the homology search.

The formation of fully active Rad51 filaments in eukaryotes is dependent on mediator proteins, including Rad52 (81, 82) in *Saccharomyces cerevisiae*, and BRCA2 (Breast cancer type 2 susceptibility protein) (83–86) in humans. Several Rad51 paralogs including Rad55/57 (87) and Csm2-Psy3-Shu1-Shu2 (known as Shu complex) (88) in yeast and RAD51B, RAD51C, RAD51D, XRCC2, XRCC3 (89–91) in higher eukaryotes also regulate RAD51 filaments. The necessity of these mediators occurs due to differences between RecA and Rad51. RecA inherently differentiates between binding to ssDNA and dsDNA, while Rad51 requires additional factors to promote productive binding to ssDNA over dsDNA (92). Rad51 also competes with replication protein A (RPA), which binds to resected ssDNA following DSBs, preventing the formation of secondary structures (92). The Rad51 mediators relieve these competitive inhibitors for ssDNA binding. Examples of these mechanisms include: BRCA2 nucleating Rad51 binding events along the DNA (93, 94), a role carried out by Rad52 in *S. cerevisiae* (95), Rad51 paralogs Rad55/57 serving as mediators to regulate the assembly and reassembly of Rad51 filaments (96, 97), and RAD51B-RAD51C-RAD51D-XRCC2 complex (BCDX2) stimulating the nucleation and extension of RAD51 filaments (93, 98).

Rad51 also recruits the DNA motor proteins Rad54 and Rdh54, known as RAD54L and RAD54B in higher eukaryotes during the homology search and strand invasion steps. These two motor proteins promote D-loop formation (99–110) and translocate along dsDNA to support a chromosome-remodeling activity, which aids recombination in the context of chromatin *in vivo* (103, 111, 112). Importantly, they prevent toxic accumulation of Rad51 on dsDNA, which is important for the maintenance of Rad51 pools necessary for promoting productive recombination (113–115). Additional helicases contribute to balancing Rad51 pools by controlling Rad51 filaments bound to ssDNA. These include Srs2, Sgs1 and Mph1 in *S. cerevisiae*. Srs2 functions by stimulating the ATP hydrolysis activity of Rad51, causing dissociation from ssDNA (116–119). The anti-recombinase activity of Srs2 can be restricted by a cooperative interaction between motor proteins Rad54 and Rdh54 (120). The activity of the Rad55/57 complex also antagonizes Srs2 by forming a more complete Rad51 filament (96, 121). Factors that load Rad51 on ssDNA and modulate the activity of the filament collaborate to balance recombinase pools required to maintain healthy recombinase filaments through both direct and indirect means.

1.3.2.3 The reversibility of mitotic recombination intermediates

The initial sequence selection of homologous DNA is kinetic (Figure 1.2B). However, correct sequence identification requires the maturation and stabilization of D-loop structures. This makes D-loop stability an inherent regulator of the homology search. This section will focus on how D-loop regulation factors into the homology search pathway (Figure 1.2C) and exit from the homology search step in HR.

Several helicases can disrupt the nascent D-loop. For example, Sgs1-Top3-Rmi1 (known as STR complex) in yeast, and their human homologs BLM (Bloom syndrome protein) -TOPO3α-RMI1-RMI2 complex, Mph1 in yeast known as FANCM in mammals, and Srs2 in yeast. The homolog of Srs2 in mammals is still unclear but is thought to be FBH1, a UvrD helicase (118, 122). Each of these motors promotes mechanistically distinct modes of D-loop regulation. Biochemical studies have shown that Sgs1 alone can dissociate protein-free D-loops but cannot dissociate D-loops formed with Rad51, Rad54 and RPA proteins. In this situation adding Top3-Rmi1 dissolves D-loops in a topoisomerase dependent manner (123). Human BLM is less efficient in disrupting D-loops unless complexed with TOPO3α-RMI1-RMI2 complex (124). Mph1 can disrupt both protein free D-loops and those containing Rad51, Rad54, and RPA (118). Finally, Srs2 is only able to disrupt D-loops composed of Rad51 only and is kinetically blocked by the cooperative efforts of Rad54 and Rdh54 (120). These differences imply that each helicase may function at unique stages of nascent D-loop metabolism.

Recent work in *S. cerevisiae* has identified two types of nascent D-loops regulated by specific helicases. Srs2 controls one type, and the STR complex, along with Mph1, modulates the other. Rdh54 helps delineate these two pathways and shifts the process towards the STR-Mph1 axis (107). These pathways may also be delineated by the enzymatic activities of their regulating proteins. For example, Top3 is a type 1A topoisomerase that can introduce positive supercoils into DNA, which could contribute to destabilizing D-loop structures (123, 125). In contrast, Srs2 strips Rad51 filaments from DNA and disrupts short D-loops that may form in the presence of Rad51 alone (116, 122). A fundamental question about D-loop reversal post-synapsis is the stability of Rad51 filaments. Two primary models exist. One model predicts continuous disruption of Rad51 filaments at D-loops, requiring cycles of filament disruption and re-formation to identify the homologous sequence. Alternatively, Rad51 filaments may remain stable during the homology search, and reversal mechanisms may rely on strategies that manipulate the donor DNA and do not cause disruption of Rad51 filaments. Versions of both models likely contribute to regulation of nascent D-loops. Further work will need to be done to understand the difference between these types of D-loops and a definite reversal mechanism.

The stability of mature D-loops also relies on the length of homologous pairing. Longer tracts of invading homology will become stable intermediates (112) whose stability depends on the sum of the stability of all the bases in the product (126, 127). Regulation of stable intermediates is then some combination of helicase activity and the efficiency of base pairing within the DNA joint molecule. For example, if many mismatches are present, reversal is more likely with weaker helicase activity. In contrast, if the sequence is highly complementary, strong helicase activity will be required for disruption. This activity is also regulated by mismatch repair proteins, which can be reviewed here (128). D-loop disruption is also a critical component of the synthesis-dependent strand annealing pathway (SDSA). This occurs after D-loop extension (Figure 1.2D). In this pathway, the newly synthesized DNA strand anneals with the second broken end. This promotes DNA replication of the second end using the newly synthesized strand as a template (129–131). If the D-loop is not disrupted, the extended D-loop gains the ability to form a double Holliday junction (dHJ) structure. Regulation of dHJ necessitates structure-selective endonucleases that recognize and cleave DNA junctions. Resolution of recombination intermediates will finally go to either crossover (CO) or non-crossover (NCO) outcomes (132, 133). If no second end is found, long-range DNA replication can occur as part of the break-induced replication (BIR) pathway (134, 135). Both CO and BIR pathways can lead to loss of heterozygosity if the template is an ectopic sequence or the homologous chromosome (136).

Mechanisms underlying the dynamic regulation of PSCs and D-loops are fundamental to defining how gene conversion and CO events can occur. Deletion of any one of the helicases mentioned above causes an increase in CO (118, 137–139), suggesting a more stable intermediate may be more prone to CO events during mitotic HR. Future work will need to better define the process of template selection and HR outcomes.

1.3.2.4 Physiological mechanisms of homology search

We have discussed the molecular underpinnings of DNA selection during the homology search. However, for selection to occur, DNA from different sites in the genome must physically meet each other. This requires the large-scale movement of chromosomes to achieve increased contact probability between recipient and donor sites. While there are shared features between eubacteria and eukaryotes, there are also some major differences. This section will discuss models for the *in vivo* homology search.

In eukaryotes, chromatin has a significant role during the homology search. Activities associated with chromatin include managing the DNA damage response signaling pathway (140, 141), chromosome movement (142), topological domain organization (140, 143), and proper stabilization of strand pairing (144). These roles are too substantial to productively review here, and instead, we direct the reader to some of the excellent papers listed above.

The net result of chromatin remodeling in response to a DSB is increased diffusive movement of chromosomes within the nucleus, which leads to productive collisions between donor and recipient DNA molecules (142, 145). In diploid yeast, this movement can promote recombination events between homologous chromosomes (145).

More recent evidence suggests that a global reduction in nucleosomes may also improve the homology search by decompaction of localized domains, creating more efficient searches (146, 147). A second component of chromosome movement during the homology search is the recruitment of the Arp2/3 complex to sites of DNA DSBs (140, 148–151). The polymerization of nuclear actin is a requirement for chromosome movement, promoting improved collisions between distal sites within the genome (145). Together, this response improves collisions between DNA sites within the genome.

The structural maintenance of chromosome (SMC) family of proteins is important during the homology search in both prokaryotes and eukaryotes, although these activities need further definition. This group of proteins include the Condensin, Cohesion, SMC5/6 proteins, and RecN in prokaryotes (152). Recently, it has been shown that Cohesion acts as a topological barrier to promote local homology search and inhibit long range homology searches that can lead to genomic rearrangements (143, 153). While the structural contribution of these proteins has been identified, more work will be needed to understand how their role in topological insulation of specific domains may contribute to the rates of homologous DNA selection.

Together, chromatin structure in the form of nucleosomes, SMC proteins, and the nuclear cytoskeleton collaborate to improve chromosome movement during the homology search. This leads to an increased donor DNA identification. Future work will need to understand how movement is connected to the DNA template selection process.

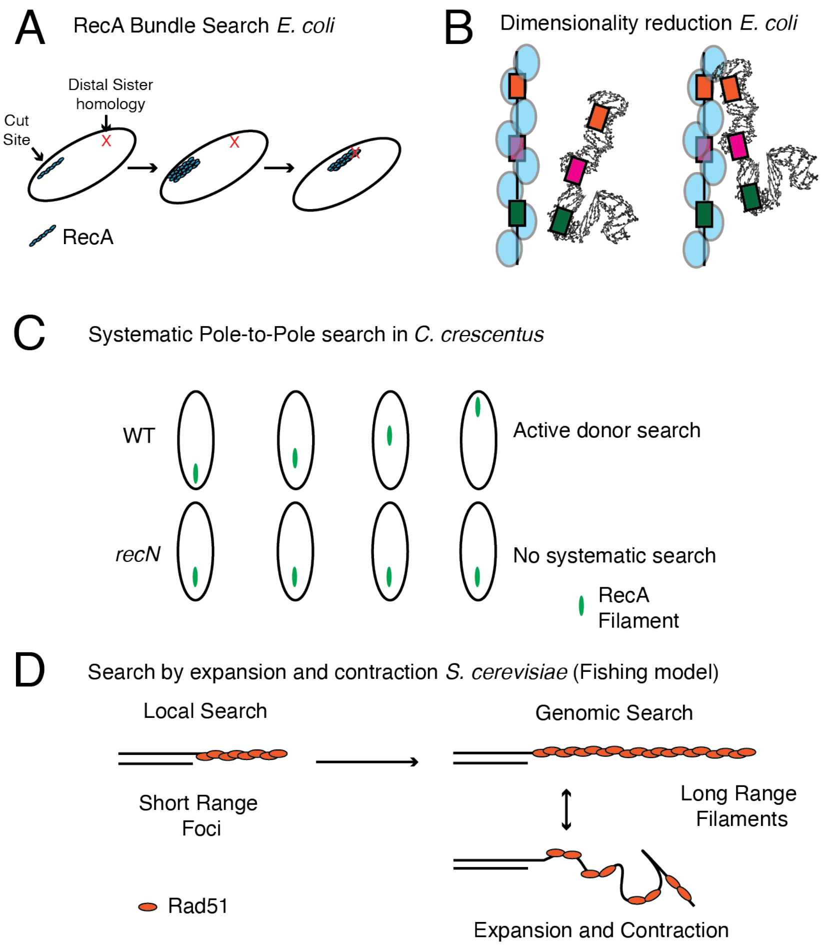

Figure 1.3: Cytological models of the homology search.

(A) The RecA bundle model proposes that RecA nucleates at sites of double strand breaks and then forms a bundle of filaments to promote the homology search. This allows identification of distant sister sites. (B) The dimensionality reduction model proposes that the growth of the RecA filament allows a matching sequence of the donor strand to dimensionally match at least a small portion of the RecA filament, which can then recognize a matching sequence in 2D space. (C) The direct pole-to-pole movement of RecA filaments observed in *C. crescentus*. Movement is dependent on the SMC motor protein RecN. (D) An expansion and contraction model were developed from *in vivo* imaging of Rad51. This model proposes that rounds of expansion and contraction help to promote pairing during the homology search.

1.3.2.5 Current cytological models for the homology search

Direct labelling of RecA generally results in inactivation of the enzyme, which makes tracking the protein *in vivo* challenging. However, several strategies have been employed to solve this problem. These experiments have developed cytological models and provided a general understanding of the RecA/Rad51-mediated homology search in cells. In this section we will discuss these models (Figure 1.3).

A standard strategy used to visualize RecA in cells is to express a fluorescently labeled RecA in a WT background. This strategy showed that RecA in *Escherichia coli* initially nucleated at the DSB locus and then extend to dynamic bundle or filament structures (Figure 1.3A) (154, 155). In these experiments, RecA filaments formed before the rapid movement and pairing of two sisters, indicating that homology search happened along the RecA structures. Further work revealed that RecA filaments functioned by a reduced-dimensionality mechanism (Figure 1.3B) (155). An extensive homology search is not required when DSBs occurred at stalled DNA replication forks. In this case, RecA formed transient foci instead of bundles or filaments (156). These observations suggest a diversity of RecA dynamics corresponding to different types of DSBs, describing a context-dependent homology search process.

The second activity of RecA filaments is recruiting factors to promote the homology search and strand invasion reactions. RecN is an SMC type protein that has been shown to aid the homology search. The RecN protein from *Deinococcus radiodurans* and *E. coli* promote RecA-mediated D-loop formation *in vitro* (157, 158). Furthermore, RecA filaments in the bacterium *Caulobacter crescentus* show directional movement during the homology search and undergo several pole-to-pole traversals *in vivo*. Without RecN, RecA filaments remain at the damage sites, cannot move across the cell, and fail to repair DNA (159). This pole-to-pole movement illustrates a systematic scan of genomic DNA is a part of the homology search in bacteria (Figure 1.3C).

In eukaryotes, the direct labelling of Rad51 was achieved in live cells by introducing a fluorescent tag in the least conserved region of *S. cerevisiae* Rad51 N-terminus. This advance allowed for direct visualization of the homology search and described a Rad51 filament that was able to undergo repeated rounds of expansion and contraction while searching for a homologous sequence (Figure 1.3D) (160). This contrasted the bacterial search model and allowed for the search of a spherical nucleus. Without the repeated rounds of expansion and contraction, the rigid Rad51 filament would remain stuck in the same place. This would prevent an exhaustive search of the genome. These observations were a major advance in understanding eukaryotic homology search.

This study highlighted that the long-range DNA resection machinery of Exo1 and Sgs1 contributed to the homology search, suggesting long-range search may require longer tracts of ssDNA. Likewise, Srs2 and Rad54 contributed to controlling the occupancy of Rad51 within a filament. Like in bacteria, short-range searches are likely carried out by Rad51 foci, suggesting a common mechanism for RecA/Rad51 mediated homology search.

In summary, physiological mechanisms that govern the homology search appear to occur through expansion and contraction of RecA/Rad51 filaments or mediated genome scanning. The ability of RecA/Rad51 to transition from local structures to expanded filaments signifies an ability to conduct both local searches and long-range searches.

Future work will need to be directed at understanding how the accessory factors that aid Rad51 contribute to these expansion and contraction-based search mechanisms.

1.3.2.6 Conclusion

The observations so far paint an elegant but incomplete picture of the mechanisms governing the homology search. It remains a difficult problem to solve because most strategies designed to probe the question rely on end-point measurements that genetically perturb the structure of Rad51 filaments or D-loops. Further exploration of this subject will be required to complete the picture. Functionally connecting physical observation to the genetic observations will require the direct observation of homolog pairing *in vivo* combined with functional mutations in regulating enzymes. Given that most enzymes are now known to show diverse functions and perform in more than one stage of HR, these experiments need to involve specific functional mutants instead of deletions. This will preserve the overall structural integrity of the Rad51 filament while isolating known functions of accessory factors.

Perspectives

◊ The dynamic nature of the homology search is critical for understanding the outcomes of homologous recombination.

◊ The current thinking on this topic is that homology search is a dynamic process that RecA/Rad51 regulates through both enzymatic function and recruitment of accessory factors that stimulate the formation and reversal of homology search intermediates.

◊ Future directions in this area will be to understand how accessory homology search factors contribute to the rate of both long-range and short-range homology searches coordinated by Rad51.

◊ Chromatin remodeling upon DNA damage regulates chromosome movement and homology search efficiency.

1.3.3 Double Holliday junction

After homology search and donor recognition, the nascent D-loop can mature through 3’ end extension, and the displaced strand may capture the second broken end. The displaced strand can also serve as a template for the second broken to fill in lost nucleotides. The resulting four-way DNA intermediate is a Holliday junction (HJ). Additional DNA synthesis and nick ligation generate a double Holliday junction (dHJ). The dHJ structures can form between sister chromatids or between homologous chromosomes. In mitosis, junctions form less frequently than in meiosis, and sister chromatids are preferred (136).

In vivo, dHJs can be removed by the Sgs1-Top3-Rmi1 (STR) complex in *S. cerevisiae* or by the BLM-TOPO3α-RMI1-RMI2 (BTRR) complex in *H. sapiens*. These complexes combine branch migration and strand decatenation activities to convert dHJs into NCO products through a process termed dissolution. Alternatively, dHJs can be processed by resolution, in which structure-selective endonucleases cleave the junctions. After ligation, resolution can yield either NCO or CO products. Resolution can be divided into canonical resolution, catalyzed by RuvC in *Escherichia coli*, Yen1 in *S. cerevisiae* and GEN1 in *H. sapiens*, which introduce symmetric nicks across dHJs; and non-canonical resolution mediated by *S. cerevisiae* Mus81-Mms4 and *H. sapiens* MUS81-EME1 or SLX1-SLX4, which generate asymmetric cleavages on dHJs. These structure-selective endonucleases are collectively referred as HJ resolvases (132, 161).

1.3.3.1 Holliday junction dissolution

Budding yeast Sgs1 and human BLM are RecQ family helicases that unwind a broad range of DNA substrates in a 3’ to 5’, ATP-dependent manner (161). Loss of *SGS1* suppresses the slow growth phenotype of *top3* mutant in *S. cerevisiae*, and the gene was therefore named slow growth suppressor 1 (162). Human BLM was identified as the gene mutated in Bloom’s syndrome (163). *In vivo*, Sgs1 and BLM are essential for chromosome integrity. Disrupting Sgs1 causes hyper-recombination, increased CO outcomes, accumulation of HJ intermediates in mitosis and elevated inter-chromosomal contacts in meiosis (118, 137, 164–168). *In vitro*, BLM together with TOPO3α can dissolve dHJs through strand passage, resulting in products without strand exchange (169).

The relationship between RecQ helicase and type 1A topoisomerase is conserved across prokaryotes and eukaryotes. Type 1A topoisomerases introduce a transient nick in partially denatured DNA and catalyze strand passage event to relax negative supercoils or decatenate two DNA molecules (170). In budding yeast, depletion of *TOP3* causes hype-recombination and slow growth (162, 171). *S. cerevisiae* Rmi1 and human RMI1, RMI2, although lacking obvious catalytic activity, associate with Sgs1-Top3/BLM-TOPO3α and are indispensable for proper complex function and localization (172–176).

The STR complex and BTRR complex also act at stalled replication fork (161, 176–178).

A widely accepted model posits that STR/BTRR complex dissolves dHJs in two steps. First, the RecQ helicase promotes branch migration to fuse the two junctions, possibly by locally unwinding and reanneal the DNA, thus forming a hemi-catenated structure without changing the overall linking number. Then, type 1A topoisomerase generates a transient nick and performs strand passage through this gap to untangle the inter-twined strands (179). The dHJ is thereby dissolved, and no strand exchange occurs during the process.

1.3.3.2 Holliday junction resolution

Early study of recombination intermediate resolution focused on bacteriophage endonucleases. Endonuclease VII in T4 bacteriophage resolves intermediates of RecA-mediated strand exchange reaction, and Endonucleases I in T7 bacteriophage resolves synthetic HJ and related branched structures (180, 181). *E. coli* RuvC was subsequently shown to resolve RecA-mediated strand exchange intermediates and synthetic HJs by introducing symmetrically opposite nicks across the junction. RuvC functions as a homodimer, binds selectively to junction structures independent on metal ions and DNA sequences, and cleaves in the presence of divalent cations with a preferred tetranucleotide consensus (182–186). After cleavage, strands with the same orientation may or may not be exchanged before re-ligation, yielding CO or NCO outcomes.

Eukaryotic canonical HJ resolvases include Yen1 in *S. cerevisiae*, GEN1 in *H. sapiens* and their orthologs in other species, and the mitochondrial nuclease Cce1 in *S. cerevisiae*

(132). Yen1 and GEN1 represent a subclass of Rad2/XPG family endonuclease and resolve HJs through introducing symmetric nicks across the junction, a mechanism analogous to that of RuvC. GEN1 exists as a monomer in solution and dimerizes upon binding to HJs (132, 187, 188).

Ectopic expression of GEN1 N-terminal fragment is shown to rescue meiotic defect in *Schizosaccharomyces pombe mus81* mutant and reduce MMS-induced DNA junction accumulation in *S. cerevisiae sgs1* mutant, which supports *in vivo* roles for canonical nuclear resolvases (167, 189). However, loss of Yen1 or GEN1 alone causes little or no sensitivity to DNA damage reagent in yeast or human cells. In contrast, disrupting combinations of resolvase produces more severe phenotypes than single mutant. For example, *S. cerevisiae mus81* mutant is more sensitive to DNA damage upon Yen1 deletion (190, 191). And similar genetic relationships are observed in human cells between GEN1 and MUS81 or SLX4, in *Drosophila* between Gen (Yen1/GEN1 ortholog) and Mus81, and in *Caenorhabditis elegans* between GEN1 and SLX1 (192–197). These findings indicate that multiple structure-selective enzymes act in parallel or partially overlapping pathways to remove recombination intermediates *in vivo*. Moreover, resolvases are essential in the absence of Sgs1/BLM, underscoring that both dissolution and resolution contribute to clearing HJs and dHJs (195, 197–199).

Mus81/MUS81 is ERCC4/XPF family endonuclease. Many 3'-flap endonucleases, including Rad1-Rad10 in SSA pathway, belong to this family. Purified *S. pombe* Mus81-Eme1, *S. cerevisiae* Mus81-Mms4 and human MMS-EME1 introduce asymmetric nicks on HJs, classifying them as non-canonical HJ resolvases. *In vitro*, the Mus81-Mms4/MMS-EME1 heterodimer preferentially cleaves nicked HJ structures (200–204).

Yeast Slx1-Slx4 also cleaves synthetic HJs asymmetrically and flapped DNA substrates (194, 205, 206). In higher eukaryotes, MMS-EME1 and SLX1-SLX4 are more closely related functionally than their yeast counterparts (132). The relatively low efficiency of non-canonical resolvases on intact HJs likely reflects a need for upstream HJ processing or nuclease activation by other factors. Products of non-canonical cleavage are often poorly ligatable and require additional processing, further implicating accessory proteins. Future work is needed to define these steps and fill the knowledge gap.

1.4 Cell cycle checkpoint and DNA damage response

Cell cycle checkpoint is activated in response to DNA damage to delay mitotic procession and ensure DNA is properly repaired and replicated before cell division. Checkpoint is essential for maintaining integrity in eukaryotic cells. It operates in three stages of the cell cycle, each serving slightly different functions. At G1 phase, DNA damages activate the G1 checkpoint, delaying entry into S phase to allow DNA repair before the onset of DNA replication. During S phase, replication stress or damage triggers the S checkpoint and slows down replication to coordinate DNA synthesis and repair. If DNA lesions remain after replication, the G2/M checkpoint is activated to temporarily stall cell division until the damage is resolved. Once repair is complete, the cell cycle resumes in a process known as checkpoint recovery. If the damage persists and cannot be repaired within a defined period, the cell eventually proceeds through the cell cycle by checkpoint adaptation.

In budding yeast, G2/M checkpoint is related to spindle-assembly checkpoint (SAC). Cell division arrest at G2/M is maintained by inhibiting the APC-Cdc20 complex and preventing degradation of the molecular chaperone protein Pds1 (securin). Pds1 binds to the cohesin protease Esp1 (separase) and de-activates it before cell division. During metaphase to anaphase transition in undamaged cells, Pds1 releases Esp1 upon being ubiquitinated by APC-Cdc20, allowing cohesin cleavage and sister chromatid segregation. When G2/M checkpoint is activated, Pds1 is phosphorylated, which protects it from being ubiquitinated by APC-Cdc20. The interaction between Cdc20 and Pds1 is also blocked. The SAC arrests cell cycle through the same mechanism, indicating that the two checkpoints have shared components and signaling pathway (7, 207). Disruption of SAC genes shortens DNA damage-induced cell cycle delay and suppresses the permanent arrest phenotype observed in adaptation-defective mutants, consistent with the notion that two checkpoint pathways partially overlap (208).

1.4.1 PIKK kinases: primary initiators for checkpoint

Checkpoint initiates with members of the phosphoinositide 3-kinase-related kinase (PIKK) family including Tel1 and Mec1 in *S. cerevisiae*, and their respective homologs ATM and ATR in mammals. A third member, DNA-PKcs, functions in mammals but is absent in budding yeast. These PIKKs are very large proteins with similar overall architecture: an N-terminal region containing extensive HEAT (Huntingtin, elongation factor EF3, PR65/A subunit of protein phosphatase 2A and the yeast kinase TOR1) repeats, followed by a FAT (focal adhesion targeting) domain, a kinase domain and a FATC (FAT-associated C terminal) domain at the C terminus. The catalytic kinase domain represents only a small part of the whole protein, with the remainder contributing to structural stability and regulatory interactions (209). Tel1/ATM and

Mec1/ATR recognize and phosphorylate serine and threonine in SQ/TQ motifs in substrates and launch a cascade of signals to establish the checkpoint and cell cycle arrest.

1.4.1.1 PIKK recruitment and activation

After a DSB is generated, the short-range resection complex MRX/MRN recruits Tel1/ATM to the break end, though the precise mechanism remains unclarified yet. In budding yeast, this recruitment dependents on the C terminus of Xrs2, whereas in cultured mouse cells, a fragment of Nbs1 compromising the Mre11 interface is sufficient to activate ATM (210, 211). In ATM, the autophosphorylation of the conserved serine 1981 correlates with its activation (212).

Following end resection, Mec1/ATR is recruited to RPA-coated ssDNA via Ddc2/ATRIP (ATR-interacting protein in mammals). Structural studies reveal that Mec1-Ddc2 forms a dimer of heterodimer (213). Mec1-Ddc2 is activated through several partially redundant factors, including Dpb11, the Ddc1-Mec3-Rad17 complex (human Rad9-Hus1-Rad1, the 9-1-1 complex) at ssDNA/dsDNA junctions, and Dna2 specifically during S phase (214–217). In vertebrates, ATR activation is mediated by TOPBP1 (Dpb11 ortholog) and ETAA1, which contains dual RPA-interaction motifs (218–221).

1.4.1.2 Checkpoint activation and DNA repair

Tel1/ATM is recruited to blunt and unresected DSB ends, whereas Mec1/ATR recruitment requires RPA bound to ssDNA, indicating that DSB end resection, which is tightly regulated during cell cycle, is essential for Mec1/ATR-mediated checkpoint.

Short-range resection factors Sae2/CtIP are phosphorylated and activated by cyclin-dependent kinase (CDK, Cdc28 in *S. cerevisiae*) (38, 222, 223). CDK-dependent phosphorylation also stimulates Dna2 recruitment to DSBs (224). Thus, in G1 phase when CDK is inactive, DSB end resection is suppressed, HR is not favored, and Mec1/ATR is generally not activated. Under these differences, Tel1/ATM, together with DNA-PKcs, plays central roles in NHEJ-mediated DNA repair during G1 stage, while Mec1/ATR contributes to HR-mediated repair during S and G2/M phases.

However, exceptions have also been reported. In G1-arrested cells treated with 4-NQO, which causes nucleotide-adducts, and in S-arrest cells exposed to Hydroxyurea (HU), a ribonucleotide reductase inhibitor causing replication fork stall, Mec1 substrate Rad53, is phosphorylated even when CDK is depleted. This suggests that Mec1-mediated checkpoint activation can occur through CDK-independent pathways, presumably in response to ssDNA intermediates formed during repair. In HU treated S-phase cells, Srs2 phosphorylation is not complete in the absence of CDK activity, indicating that while HR is suppressed, Mec1-mediated checkpoint retains broader functions in coordinating DNA repair (225, 226).

A more extreme example is in undamaged cells, fusing Ddc1 (9-1-1 complex clamp member) and Ddc2 to LacI protein and tethering them to LacO arrays can promote phosphorylation of Rad53 and another Mec1 substrate Rad9, indicating Mec1 activation can be mediated by co-localization of sensors without DNA damage occurring (227).

1.4.2 Signaling cascade

After being activated, Tel1/ATM and Mec1/ATR provoke a series of downstream reactions by phosphorylating broad substrates on SQ/TQ sites to spread and amplify signaling transmission like a cascade.

1.4.2.1 Phosphorylation of H2A

The first layer of the cascade is the phosphorylation of histone H2A, which happens rapidly and widely after DNA damage. In mammals, the histone variant H2AX is phosphorylated at C-terminal S139 and referred as γ-H2AX. Human core histone H2A1 does not have the equivalent serine. The appearance of γ-H2AX starts within minutes and soon covers thousands of kilobase pairs around the break in human cells after IR exposure (228, 229). Budding yeast doesn't have the variant, and the phosphorylation is catalyzed on the core histone H2A at the equivalent C-terminal S129 (230). The phosphorylated H2A in budding yeast is also referred as γ-H2AX.

In mammals, all three checkpoint PIKKs are shown to phosphorylate H2AX (7). The details are not discussed here. In budding yeast, Mec1 and Tel1 cooperate to establish γ-H2AX spreading, which can extend to distal chromatin regions tens of kilobase pairs away from the DSB site within one hour. In contrast, proximal regions within 1-2 kb of the break show remarkedly lower γ-H2AX signals, where Mre11, Rad51, and other HR proteins are enriched (231). The distribution of γ-H2AX along chromatin is not uniform, and negatively correlated with transcriptional activity. Highly transcribed regions exhibit reduced γ-H2AX, which can be rapidly restored when transcription is turned off, a process primarily dependent on Mec1. Upon transcription reactivation, γ-H2AX is lost again (232). Mec1 appears to be more efficient than Tel1 in phosphorylating H2A at distal regions, and mathematical modelling suggests that Tel1 moves directionally along chromatin during phosphorylation, whereas Mec1 acts a three-dimensional diffusive mechanism.

In cells, γ-H2AX serves as a landing pad for key checkpoint and DNA repair factors, several of which have been shown to interact with γ-H2AX even though their recruitment does not strictly depend on it. This modification is thought to locally increase the concentration of DNA and DNA damage response proteins, thereby facilitating the repair efficiency. Alternatively, γ-H2AX may aid DNA damage repair through promoting chromatin remodeling around the lesion, although the mechanism remains to be elucidated (233, 234). In both basic research and clinical analysis, γ-H2AX is a sensitive molecular maker for monitoring the initiation and resolution of DNA damages (235).

1.4.2.2 Adaptors and checkpoint kinases

In *S. cerevisiae*, Tel1 activates Chk1 while Mec1 activates both Rad53 and Chk1, and the activation requires adaptor protein Rad9. Another adaptor protein Mrc1 is also involved in Rad53 activation especially in response to replication stress (236). The relationship is different in mammals, where ATM activates CHK2 (Rad53 homolog), and ATR contributes to CHK1 activation. Adaptor proteins in mammals include 53BP1 and MDC1. Rad53/CHK2 and Chk1/CHK1 are checkpoint kinases that also have broad substrates and play central roles in DNA damage signal transduction.

The adaptor protein Rad9 is required for robust G2/M checkpoint activation. Rad9 is recruited to DNA lesions through Dpb11, Ddc1 and γ-H2AX. Upon recruitment to a DSB, Rad9 is phosphorylated by Mec1 and Tel1 on multiple SQ/TQ sites (237–239). The phosphorylated Rad9 then interacts with the C-terminal FHA2 (fork-head homology-associated) domain of Rad53, promoting the activation of Rad53 through Mec1-primed phosphorylation and Rad53 autophosphorylation (237, 239–242). Rad9 oligomerization, mediated by its tandem BRCT domain and SQ/TQ cluster domain, is also promoted by Mec1- and Tel1-dependent phosphorylation and is essential for maintaining the checkpoint (243). It is worth noting that forced dimerization of Rad53 *in vivo* can induce its autophosphorylation and activation even in the absence of Mec1, providing a model in which Mec1 and adaptor Rad9 primarily function to locally enrich Rad53 rather than directly catalyze the activation (244). Rad9 is also important for Chk1 activation. In contrast to Rad53, Chk1 activation requires the N-terminal Chk1 activation domain (CAD) of Rad9, whereas the SQ/TQ cluster is dispensable (237, 245). A negative feedback loop exists between Rad53 and Rad9. Activated Rad53 limits further Rad9 accumulation, releases Rad53 from Rad9 and dissembles Rad53 oligomers in a kinase activity-dependent manner (243, 244).

Rad53 is the principal effector kinase in the DNA damage checkpoint. Upon activation, it orchestrates a cascade of transcriptional responses and activates downstream kinase Dun1 to restrain mitotic progress (7, 246). In addition, several HR factors, including Rad55 and Rdh54, are phosphorylated and regulated through Mec1-Rad9-Rad53 axis following DNA damage (247, 248). The relationship between Mec1-Rad9-Rad53 checkpoint axis and HR machinery needs further investigation. Chk1 contributes minorly in UV- or endonuclease-induced G2/M checkpoint. Instead, its activation is more important in telomere-unprotected cells (246).

To inhibit the entry of anaphase, Rad53 and Chk1 play independent roles. Chk1 targets and phosphorylates Pds1 to inhibit the ubiquitination of Pds1 by the APC-Cdc20 complex. Rad53 blocks the interaction between Pds1 and Cdc20. It also antagonizes with Cdc5, the polo-like kinase in yeast functioning in mitotic exit, to slow down mitosis progression (249, 250).

In mammals, ATM-CHK2 axis responses early after DSB occurrence, whereas after end resection, ATR-CHK1 is activated. The details about how the signals are transduced in these two axes are not discussed here.

Importantly, the mammalian tumor suppressor and transcription factor p53, which is absent in yeast, is phosphorylated by all major checkpoint kinases and governs the cellular decisions among proliferation, apoptosis and senescence. Dysregulation or loss of p53 functions leads to uncontrolled cell proliferation and tumorigenesis. This highlights a key difference in cell cycle regulation between unicellular and multicellular organisms.

1.4.3 Checkpoint deactivation

Deactivation is catalyzed by phosphatases and checkpoint competitors. Phosphatases include but are not limited to PP2C (Ptc2 and Ptc3) and PP4 phosphatases in *S. cerevisiae*, and PP2A phosphatases in higher eukaryotes (7). These enzymes primarily remove phosphorylation markers from downstream kinases and H2A to terminate signal transduction.

In parallel, the scaffold proteins Slx4 and Rtt107 counteract checkpoint through physical interactions with Dpb11 and γ-H2AX, respectively, thereby competing with adaptor Rad9. Loss of Slx4 results in Rad9 accumulation, hyperactivation of Rad53 and an exaggerated checkpoint response under conditions of MMS-induced damage, a persistent DSB, or unprotected telomeres (251, 252). Moreover, phosphorylation of histone H4 at threonine 80 (H4T80) promotes checkpoint recovery by recruiting Rtt107 to DNA lesions, illustrating how chromatin remodeling contributes to maintaining genome integrity in a chromatin-protein interacting context (253).

Checkpoint adaptation occurs when a DSB persists for approximately 8-10 hours, after which the damage no longer reactivates the checkpoint in the following cell cycle. Although the molecular basis of triggering adaptation is unclear yet, it is thought to involve monitoring the rate of DNA end resection. In *yku70Δ* cells, adaptation is abolished when an irreparable DSB is induced, but this phenotype can be rescued by *rad50* or *mre11* deletions. Similarly, a mutation in RPA can also rescued the permanent arrest, suggesting that RPA-ssDNA is one of the key intermediates or sensors during adaptation (254).

The yeast polo-like kinase Cdc5, and Ckb2, a nonessential subunit of casein kinase II, regulate checkpoint adaptation, with Cdc5 playing the dominant role (255). Exit of IR-induced checkpoint in human cells is also regulated by the polo-like kinase 1 (PLK1) (256). Overexpression of Cdc5 in yeast reveals that early checkpoint factors remain active while Rad53 hyper-phosphorylation is suppressed, indicating that Cdc5 mediates adaptation by attenuating Rad53 activity in a kinase-dependent manner (257). Furthermore, Mec1 autophosphorylation at serine 1964 and Ddc2 degradation are key events in adaptation (258). Cells lacking motor protein Rdh54 are unable to adapt, and the overexpression of its paralog Rad54 fails to rescue this phenotype, implying a distinct role for Rdh54 in the adaptation process. Interestingly, RPA mutants that can rescue the permanent arrest in *yku70Δ* cells can also suppress the *rdh54Δ* adaptation defect, reinforcing the model that ssDNA intermediates are involved in adaptation (259). In summary, the repair of DSBs need to be tightly coordinated through the interplays among chromatin dynamics, DNA repair proteins, cell cycle regulation and checkpoint responses. Depicting this complex network remains challenging yet profoundly meaningful endeavor, as it advances both human knowledge of genome maintenance and the development of medical interventions.

References

1. R. Greinert, B. Volkmer, S. Henning, E. W. Breitbart, K. O. Greulich, M. C. Cardoso, A. Rapp, UVA-induced DNA double-strand breaks result from the repair of clustered oxidative DNA damages. *Nucleic Acids Res* **40**, 10263–10273 (2012).

2. M. R. Lieber, The mechanism of double-strand DNA break repair by the nonhomologous DNA end-joining pathway. *Annu Rev Biochem* **79**, 181–211 (2010).

3. L. F. Z. Batista, B. Kaina, R. Meneghini, C. F. M. Menck, How DNA lesions are turned into powerful killing structures: Insights from UV-induced apoptosis. *Mutation Research/Reviews in Mutation Research* **681**, 197–208 (2009).

4. C. L. Limoli, E. Giedzinski, W. M. Bonner, J. E. Cleaver, UV-induced replication arrest in the xeroderma pigmentosum variant leads to DNA double-strand breaks, γ-H2AX formation, and Mre11 relocalization. *Proc Natl Acad Sci U S A* **1**, 233–238 (2001).

5. G. A. Garinis, J. R. Mitchell, M. J. Moorhouse, K. Hanada, H. De Waard, D. Vandeputte, J. Jans, K. Brand, M. Smid, P. J. Van Der Spek, J. H. J. Hoeijmakers, R. Kanaar, G. T. J. Van Der Horst, Transcriptome analysis reveals cyclobutane pyrimidine dimers as a major source of UV-induced DNA breaks. *EMBO J* **24**, 3952–3962 (2005).

6. M. S. Brown, D. K. Bishop, DNA strand exchange and RecA homologs in meiosis. *Cold Spring Harb Perspect Biol* **7**, a016659 (2015).

7. D. P. Waterman, J. E. Haber, M. B. Smolka, Checkpoint responses to DNA double-strand breaks. *Annu Rev Biochem* **89**, 103–133 (2020).

8. C. Lukas, V. Savic, S. Bekker-Jensen, C. Doil, B. Neumann, R. S. Pedersen, M. Grøhfte, K. L. Chan, I. D. Hickson, J. Bartek, J. Lukas, 53BP1 nuclear bodies form around DNA lesions generated by mitotic transmission of chromosomes under replication stress. *Nat Cell Biol* **13**, 243–253 (2011).

9. D. Branzei, M. Foiani, The DNA damage response during DNA replication. *Curr Opin Cell Biol* **17**, 568–575 (2005).

10. P. Cejka, L. S. Symington, DNA end resection: mechanism and control. *Annu Rev Genet* **55**, 285–307 (2021).

11. J. M. Daley, P. L. Palmbos, D. Wu, T. E. Wilson, Nonhomologous end joining in yeast. *Annu Rev Genet* **39**, 431–451 (2005).

12. R. Chanet, M. Heude, A. Adjiri, L. Maloisel, F. Fabre, Semidominant mutations in the yeast Rad51 protein and their relationships with the Srs2 helicase. *Mol Cell Biol* **16**, 4782–4789 (1996).

13. C. Lundin, M. North, K. Erixon, K. Walters, D. Jenssen, A. S. H. Goldman, T. Helleday, Methyl methanesulfonate (MMS) produces heat-labile DNA damage but no detectable *in vivo* DNA double-strand breaks. *Nucleic Acids Res* **33**, 3799–3811 (2005).

14. M. J. Sleigh, The mechanism of DNA breakage by phleomycin *in vitro*. *Nucleic Acids Res* **3**, 891–901 (1976).

15. M. Nagao, T. Sugirnura, M. Tokyo Japan, Molecular biology of the carcinogen 4-nitroquinoline 1-oxide. *Adv Cancer Res* **23**, 131–169 (1976).

16. M. Ikenaga, H. Ichikawa-Ryo, S. Kondo, The major cause of inactivation and mutation by 4-Nitroquinoline 1-Oxide in *Escherichia coli*: excisable 4NQO-purine adducts. *J Mol Biol* **92**, 341–356 (1975).

17. T. Nunoshiba, B. Demple, Potent intracellular oxidative stress exerted by the carcinogen 4-Nitroquinoline-N-oxide. *Cancer Res* **53**, 3250–3252 (1993).

18. M. R. Lieber, The mechanism of double-strand DNA break repair by the nonhomologous DNA end-joining pathway. *Annu Rev Biochem* **79**, 181–211 (2010).

19. S. Burma, B. P. C. Chen, D. J. Chen, Role of non-homologous end joining (NHEJ) in maintaining genomic integrity. *DNA Repair (Amst)* **5**, 1042–1048 (2006).

20. P. Ahnesorg, P. Smith, S. P. Jackson, XLF interacts with the XRCC4-DNA Ligase IV complex to promote DNA nonhomologous end-joining. *Cell* **124**, 301–313 (2006).

21. K. N. Mahajan, S. A. Nick McElhinny, B. S. Mitchell, D. A. Ramsden, Association of DNA polymerase μ (pol μ) with Ku and ligase IV: role for pol μ in end-joining double-strand break repair. *Mol Cell Biol* **22**, 5194–5202 (2002).

22. J. W. Lee, L. Blanco, T. Zhou, M. Garcia-Diaz, K. Bebenek, T. A. Kunkel, Z. Wang, L. F. Povirk, Implication of DNA polymerase λ in alignment-based gap filling for nonhomologous DNA end joining in human nuclear extracts. *J Biol Chem* **279**, 805–811 (2004).

23. Y. Ma, H. Lu, B. Tippin, M. F. Goodman, N. Shimazaki, O. Koiwai, C. L. Hsieh, K. Schwarz, M. R. Lieber, A biochemically defined system for mammalian nonhomologous DNA end joining. *Mol Cell* **16**, 701–713 (2004).

24. R. Bhargava, D. O. Onyango, J. M. Stark, Regulation of single-strand annealing and its role in genome maintenance. *Trends Genet* **32**, 566–575 (2016).

25. J. Fishman-Lobell, J. E. Haber, Removal of nonhomologous DNA ends in double-strand break recombination-the role of the yeast ultraviolet repair gene RAD1. *Science* **258**, 480–484 (1992).

26. T. A. Motycka, T. Bessho, S. M. Post, P. Sung, A. E. Tomkinson, Physical and functional interaction between the XPF/ERCC1 endonuclease and hRad52. *J Biol Chem* **279**, 13634–13639 (2004).

27. A. Nussenzweig, M. C. Nussenzweig, A backup DNA repair pathway moves to the forefront. *Cell* **131**, 223–225 (2007).

28. M. McVey, S. E. Lee, MMEJ repair of double-strand breaks (director's cut): deleted sequences and alternative endings. *Trends Genet* **24**, 529–538 (2008).

29. J.-L. Ma, E. M. Kim, J. E. Haber, S. E. Lee, Yeast Mre11 and Rad1 proteins define a Ku-independent mechanism to repair double-strand breaks lacking overlapping end sequences. *Mol Cell Biol* **23**, 8820–8828 (2003).

30. T. T. Paull, M. Gellert, The 3' to 5' exonuclease activity of Mre11 facilitates repair of DNA double-strand breaks. *Mol Cell* **1**, 969–979 (1998).

31. K. M. Trujillo, P. Sung, DNA structure-specific nuclease activities in the *Saccharomyces cerevisiae* Rad50-Mre11 complex. *J Biol Chem* **276**, 35458–35464 (2001).

32. K.-P. Hopfner, A. Karcher, L. Craig, T. T. Woo, J. P. Carney, J. A. Tainer, Structural biochemistry and interaction architecture of the DNA double-strand break repair Mre11 nuclease and Rad50-ATPase. *Cell* **105**, 473–485 (2001).

33. J. P. Carney, R. S. Maser, H. Olivares, E. M. Davis, M. Le Beau, J. R. Yates III, L. Hays, W. F. Morgan, J. H. J. Petrini, The hMre11/hRad50 protein complex and Nijmegen breakage syndrome: linkage of double-strand break repair to the cellular DNA damage response. *Cell* **93**, 477–486 (1998).

34. Z. You, C. Chahwan, J. Bailis, T. Hunter, P. Russell, ATM activation and its recruitment to damaged DNA require binding to the C terminus of Nbs1. *Mol Cell Biol* **25**, 5363–5379 (2005).

35. R. S. Williams, G. E. Dodson, O. Limbo, Y. Yamada, J. S. Williams, G. Guenther, S. Classen, J. N. M. Glover, H. Iwasaki, P. Russell, J. A. Tainer, Nbs1 flexibly tethers Ctp1 and Mre11-Rad50 to coordinate DNA double-strand break processing and repair. *Cell* **139**, 87–99 (2009).

36. T. T. Paull, M. Gellert, Nbs1 potentiates ATP-driven DNA unwinding and endonuclease cleavage by the Mre11/Rad50 complex. *Genes Dev* **13**, 1276–88 (1999).

37. J. Oh, A. Al-Zain, E. Cannavo, P. Cejka, L. S. Symington, Xrs2 dependent and independent functions of the Mre11-Rad50 complex. *Mol Cell* **64**, 405–415 (2016).

38. R. Anand, L. Ranjha, E. Cannavo, P. Cejka, Phosphorylated CtIP functions as a co-factor of the MRE11-RAD50-NBS1 endonuclease in DNA end resection. *Mol Cell* **64**, 940–950 (2016).

39. E. Cannavo, P. Cejka, Sae2 promotes dsDNA endonuclease activity within Mre11-Rad50-Xrs2 to resect DNA breaks. *Nature* **514**, 122–125 (2014).

40. V. Garcia, S. E. L. Phelps, S. Gray, M. J. Neale, Bidirectional resection of DNA double-strand breaks by Mre11 and Exo1. *Nature* **479**, 241–244 (2011).

41. E. P. Mimitou, L. S. Symington, Sae2, Exo1 and Sgs1 collaborate in DNA double-strand break processing. *Nature* **455**, 770–774 (2008).

42. K. Zakharyevich, Y. Ma, S. Tang, P. Y.-H. Hwang, S. Boiteux, N. Hunter, Temporally and biochemically distinct activities of Exo1 during meiosis: double-strand break resection and resolution of double Holliday junctions. *Mol Cell* **40**, 1001–1015 (2010).

43. J. Paiano, W. Wu, S. Yamada, N. Sciascia, E. Callen, A. Paola Cotrim, R. A. Deshpande, Y. Maman, A. Day, T. T. Paull, A. Nussenzweig, ATM and PRDM9 regulate SPO11-bound recombination intermediates during meiosis. *Nat Commun* **11**, 857 (2020).

44. P. T. Tran, N. Erdeniz, S. Dudley, R. M. Liskay, Characterization of nuclease-dependent functions of Exo1p in *Saccharomyces cerevisiae*. *DNA Repair (Amst)* **1**, 895–912 (2002).

45. W. Wang, J. M. Daley, Y. Kwon, X. Xue, D. S. Krasner, A. S. Miller, K. A. Nguyen, E. A. Williamson, E. Y. Shim, S. E. Lee, R. Hromas, P. Sung, A DNA nick at Ku-blocked double-strand break ends serves as an entry site for exonuclease 1 (Exo1) or Sgs1–Dna2 in long-range DNA end resection. *J Biol Chem* **293**, 17061–17069 (2018).

46. H.-I. Kao, J. L. Campbell, R. A. Bambara, Dna2p helicase/nuclease is a tracking protein, like FEN1, for flap cleavage during okazaki fragment maturation. *J Biol Chem* **279**, 50840–50849 (2004).

47. A. Sturzenegger, K. Burdova, R. Kanagaraj, M. Levikova, C. Pinto, P. Cejka, P. Janscak, DNA2 cooperates with the WRN and BLM RecQ helicases to mediate long-range DNA end resection in human cells. *J Biol Chem* **289**, 27314–27326 (2014).

48. P. Cejka, E. Cannavo, P. Polaczek, T. Masuda-Sasa, S. Pokharel, J. L. Campbell, S. C. Kowalczykowski, DNA end resection by Dna2-Sgs1-RPA and its stimulation by Top3-Rmi1 and Mre11-Rad50-Xrs2. *Nature* **467**, 112–116 (2010).

49. S. Gravel, J. R. Chapman, C. Magill, S. P. Jackson, DNA helicases Sgs1 and BLM promote DNA double-strand break resection. *Genes Dev* **22**, 2767–2772 (2008).

50. E. P. Mimitou, L. S. Symington, Ku prevents Exo1 and Sgs1-dependent resection of DNA ends in the absence of a functional MRX complex or Sae2. *EMBO J* **29**, 3358–3369 (2010).

51. E. Y. Shim, W.-H. Chung, M. L. Nicolette, Y. Zhang, M. Davis, Z. Zhu, T. T. Paull, G. Ira, S. E. Lee, *Saccharomyces cerevisiae* Mre11/Rad50/Xrs2 and Ku proteins regulate association of Exo1 and Dna2 with DNA breaks. *EMBO J* **29**, 3370–3380 (2010).

52. J. W. Westmoreland, M. A. Resnick, Recombinational repair of radiation-induced double-strand breaks occurs in the absence of extensive resection. *Nucleic Acids Res* **44**, 695–704 (2016).

53. Z. Zhu, W.-H. Chung, E. Y. Shim, S. E. Lee, G. Ira, Sgs1 helicase and two nucleases Dna2 and Exo1 resect DNA double-strand break ends. *Cell* **134**, 981–994 (2008).

54. E. P. Mimitou, S. Yamada, S. Keeney, A global view of meiotic double-strand break end resection. *Science* **355**, 40–45 (2017).

55. M. T. Kimble, M. J. Johnson, M. R. Nester, L. S. Symington, Long-range DNA end resection supports homologous recombination by checkpoint activation rather than extensive homology generation. *Elife* **12** e84322 (2023).

56. T. T. Paull, M. Gellert, A mechanistic basis for Mre11-directed DNA joining at microhomologies. *Proc Natl Acad Sci U S A* **97**, 6409–6414 (2000).

57. A. Shibata, D. Moiani, A. S. Arvai, J. Perry, S. M. Harding, M.-M. Genois, R. Maity, S. van Rossum-Fikkert, A. Kertokalio, F. Romoli, A. Ismail, E. Ismalaj, E. Petricci, M. J. Neale, R. G. Bristow, J.-Y. Masson, C. Wyman, P. A. Jeggo, J. A. Tainer, DNA double-

strand break repair pathway choice is directed by distinct MRE11 nuclease activities. *Mol Cell* **53**, 7–18 (2014).

58. L. S. Symington, End resection at double-strand breaks: mechanism and regulation. *Cold Spring Harb Perspect Biol* **6**, a016436 (2014).

59. L. S. Symington, R. Rothstein, M. Lisby, Mechanisms and regulation of mitotic recombination in *Saccharomyces cerevisiae*. *Genetics* **198**, 795–835 (2014).

60. J. E. Haber, DNA repair: the search for homology. *BioEssays* **40**, e1700229 (2018).

61. L. C. Kadyk, L. H. Hartwell, Sister chromatids are preferred over homologs as substrates for recombinational repair in *Saccharomyces cerevisiae*. *Genetics* **132**, 387–402 (1992).

62. E. A. H. Neuwirth, M. Honma, A. J. Grosovsky, Interchromosomal crossover in human cells is associated with long gene conversion tracts. *Mol Cell Biol* **27**, 5261–5274 (2007).

63. A. Hügel, N. Wernert, Loss of heterozygosity (LOH), malignancy grade and clonality in microdissected prostate cancer. *Br J Cancer* **79**, 551–557 (1999).

64. M. E. Moynahan, M. Jasin, Loss of heterozygosity induced by a chromosomal double-strand break. *Biochemistry* **94**, 8988–8993 (1997).

65. J. B. Crickard, E. C. Greene, The biochemistry of early meiotic recombination intermediates. *Cell Cycle* **17**, 2520–2530 (2018).

66. Z. Lin, H. Kong, M. Nei, H. Ma, Origins and evolution of the recA/RAD51 gene family: evidence for ancient gene duplication and endosymbiotic gene transfer. *Proc Natl Acad Sci U S A* **103**, 10328–10333 (2006).

67. A. Stasiak, E. Di Capua, The helicity of DNA in complexes with recA protein. *Nature* **299**, 185–186 (1982).

68. Z. Chen, H. Yang, N. P. Pavletich, Mechanism of homologous recombination from the RecA-ssDNA/dsDNA structures. *Nature* **453**, 489–494 (2008).

69. H. Yang, C. Zhou, A. Dhar, N. P. Pavletich, Mechanism of strand exchange from RecA-DNA synaptic and D-loop structures. *Nature* **586**, 801–806 (2020).

70. D. Yang, B. Boyer, C. Prévost, C. Danilowicz, M. Prentiss, Integrating multi-scale data on homologous recombination into a new recognition mechanism based on simulations of the RecA-ssDNA/dsDNA structure. *Nucleic Acids Res* **43**, 10251–10263 (2015).

71. M. Prentiss, C. Prévost, C. Danilowicz, Structure/function relationships in RecA protein-mediated homology recognition and strand exchange. *Crit Rev Biochem Mol Biol* **50**, 453–476 (2015).

72. H. Yang, N. P. Pavletich, Insights into homology search from cryo-EM structures of RecA-DNA recombination intermediates. *Curr Opin Genet Dev* **71**, 188–194 (2021).

73. J. M. Short, Y. Liu, S. Chen, N. Soni, M. S. Madhusudhan, M. K. K. Shivji, A. R. Venkitaraman, High-resolution structure of the presynaptic RAD51 filament on single-stranded DNA by electron cryo-microscopy. *Nucleic Acids Res* **44**, 9017–9030 (2016).

74. J. Xu, L. Zhao, Y. Xu, W. Zhao, P. Sung, H. W. Wang, Cryo-EM structures of human RAD51 recombinase filaments during catalysis of DNA-strand exchange. *Nat Struct Mol Biol* **24**, 40–46 (2017).

75. J. C. Bell, J. L. Plank, C. C. Dombrowski, S. C. Kowalczykowski, Direct imaging of RecA nucleation and growth on single molecules of SSB-coated ssDNA. *Nature* **491**, 274–278 (2012).

76. J. Hilario, I. Amitani, R. J. Baskin, S. C. Kowalczykowski, Direct imaging of human Rad51 nucleoprotein dynamics on individual DNA molecules. *Proc Natl Acad Sci U S A* **106**, 361–368 (2009).

77. Z. Qi, S. Redding, J. Y. Lee, B. Gibb, Y. Kwon, H. Niu, W. A. Gaines, P. Sung, E. C. Greene, DNA sequence alignment by microhomology sampling during homologous recombination. *Cell* **160**, 856–869 (2015).

78. C. Danilowicz, D. Yang, C. Kelley, C. Prévost, M. Prentiss, The poor homology stringency in the heteroduplex allows strand exchange to incorporate desirable mismatches without sacrificing recognition *in vivo*. *Nucleic Acids Res* **43**, 6473–6485 (2015).

79. J. Y. Lee, T. Terakawa, Z. Qi, J. B. Steinfeld, S. Redding, Y. Kwon, W. A. Gaines, W. Zhao, P. Sung, E. C. Greene, Base triplet stepping by the Rad51/RecA family of recombinases. *Science* **349**, 977–981 (2015).

80. A. L. Forget, S. C. Kowalczykowski, Single-molecule imaging of DNA pairing by RecA reveals a three-dimensional homology search. *Nature* **482**, 423–427 (2012).

81. P. Sung, Function of yeast Rad52 protein as a mediator between replication protein A and the Rad51 recombinase. *J Biol Chem* **272**, 28194–28197 (1997).

82. J. H. New, T. Sugiyama, E. Zaitseva, S. C. Kowalczykowski, Rad52 protein stimulates DNA strand exchange by Rad51 and replication protein A. *Nature* **391**, 407–410 (1998).

83. T. Thorslund, M. J. McIlwraith, S. A. Compton, S. Lekomtsev, M. Petronczki, J. D. Griffith, S. C. West, The breast cancer tumor suppressor BRCA2 promotes the specific targeting of RAD51 to single-stranded DNA. *Nat Struct Mol Biol* **17**, 1263–1265 (2010).

84. R. B. Jensen, A. Carreira, S. C. Kowalczykowski, Purified human BRCA2 stimulates RAD51-mediated recombination. *Nature* **467**, 678–683 (2010).

85. J. Liu, T. Doty, B. Gibson, W.-D. Heyer, Human BRCA2 protein promotes RAD51 filament formation on RPA-covered single-stranded DNA. *Nat Struct Mol Biol* **17**, 1260–1262 (2010).

86. W. Zhao, S. Vaithiyalingam, J. San Filippo, D. G. Maranon, J. Jimenez-Sainz, G. V. Fontenay, Y. Kwon, S. G. Leung, L. Lu, R. B. Jensen, W. J. Chazin, C. Wiese, P. Sung,

Promotion of BRCA2-dependent homologous recombination by DSS1 via RPA targeting and DNA mimicry. *Mol Cell* **59**, 176–187 (2015).

87. P. Sung, Yeast Rad55 and Rad57 proteins form a heterodimer that functions with replication protein A to promote DNA strand exchange by Rad51 recombinase. *Genes Dev* **11**, 1111–1121 (1997).

88. W. A. Gaines, S. K. Godin, F. F. Kabbinavar, T. Rao, A. P. VanDemark, P. Sung, K. A. Bernstein, Promotion of presynaptic filament assembly by the ensemble of *S. cerevisiae* Rad51 paralogues with Rad52. *Nat Commun* **6**, 7834 (2015).

89. S. Sigurdsson, S. Van Komen, W. Bussen, D. Schild, J. S. Albala, P. Sung, Mediator function of the human Rad51B-Rad51C complex in Rad51/RPA-catalyzed DNA strand exchange. *Genes Dev* **15**, 3308–3318 (2001).

90. N. Liu, J. E. Lamerdin, R. S. Tebbs, D. Schild, J. D. Tucker, M. R. Shen, K. W. Brookman, M. J. Siciliano, C. A. Walter, W. Fan, L. S. Narayana, Z.-Q. Zhou, A. W. Adamson, K. J. Sorensen, D. J. Chen, N. J. Jones, L. H. Thompson, XRCC2 and XRCC3, new human Rad51-family members, promote chromosome stability and protect against DNA cross-links and other damages. *Mol Cell* **1**, 783–793 (1998).

91. J. Y. Masson, M. C. Tarsounas, A. Z. Stasiak, A. Stasiak, R. Shah, M. J. McIlwraith, F. E. Benson, S. C. West, Identification and purification of two distinct complexes containing the five RAD51 paralogs. *Genes Dev* **15**, 3296–3307 (2001).

92. R. Kanaar, J. H. J. Hoeijmakers, From competition to collaboration. *Nature* **391**, 335–337 (1998).

93. O. Belan, L. Greenhough, L. Kuhlen, R. Anand, A. Kaczmarczyk, D. T. Gruszka, H. Yardimci, X. Zhang, D. S. Rueda, S. C. West, S. J. Boulton, Visualization of direct and diffusion-assisted RAD51 nucleation by full-length human BRCA2 protein. *Mol Cell* **83**, 2925-2940.e8 (2023).

94. T. Shahid, J. Soroka, E. H. Kong, L. Malivert, M. J. McIlwraith, T. Pape, S. C. West, X. Zhang, Structure and mechanism of action of the BRCA2 breast cancer tumor suppressor. *Nat Struct Mol Biol* **21**, 962–968 (2014).

95. J. Deveryshetty, R. Chadda, J. Mattice, S. Karunakaran, M. J. Rau, K. Basore, N. Pokhrel, N. Englander, J. A. Fitzpatrick, B. Bothner, E. Antony, Homodecameric Rad52 promotes single-position Rad51 nucleation in homologous recombination. *bioRxiv*, doi: 10.1101/2023.02.05.527205 (2023).

96. U. Roy, Y. Kwon, L. Marie, L. Symington, P. Sung, M. Lisby, E. C. Greene, The Rad51 paralog complex Rad55-Rad57 acts as a molecular chaperone during homologous recombination. *Mol Cell* **81**, 1043-1057.e8 (2021).

97. P. S. Malik, L. S. Symington, Rad51 gain-of-function mutants that exhibit high affinity DNA binding cause DNA damage sensitivity in the absence of Srs2. *Nucleic Acids Res* **36**, 6504–6510 (2008).

98. Y. Rawal, L. Jia, A. Meir, S. Zhou, H. Kaur, E. A. Ruben, Y. Kwon, K. A. Bernstein, M. Jasin, A. B. Taylor, S. Burma, R. Hromas, A. V. Mazin, W. Zhao, D. Zhou, E. V.

Wasmuth, E. C. Greene, P. Sung, S. K. Olsen, Structural insights into BCDX2 complex function in homologous recombination. *Nature* **619**, 640–649 (2023).

99. P. Chi, Y. Kwon, C. Seong, A. Epshtein, I. Lam, P. Sung, H. L. Klein, Yeast recombination factor Rdh54 functionally interacts with the Rad51 recombinase and catalyzes Rad51 removal from DNA. *J Biol Chem* **281**, 26268–26279 (2006).

100. J. B. Crickard, K. Kaniecki, Y. Kwon, P. Sung, M. Lisby, E. C. Greene, Regulation of Hed1 and Rad54 binding during maturation of the meiosis-specific presynaptic complex. *EMBO J* **37**, e98728 (2018).

101. J. B. Crickard, Y. Kwon, P. Sung, E. C. Greene, Rad54 and Rdh54 occupy spatially and functionally distinct sites within the Rad51-ssDNA presynaptic complex. *EMBO J* **39**, e105705 (2020).

102. J. B. Crickard, C. J. Moevus, Y. Kwon, P. Sung, E. C. Greene, Rad54 drives ATP hydrolysis-dependent DNA sequence alignment during homologous recombination. *Cell* **181**, 1380-1394.e18 (2020).

103. M. Jaskelioff, S. Van Komen, J. E. Krebs, P. Sung, C. L. Peterson, Rad54p is a chromatin remodeling enzyme required for heteroduplex DNA joint formation with chromatin. *J Biol Chem* **278**, 9212–9218 (2003).

104. G. Petukhova, P. Sung, H. Klein, Promotion of Rad51-dependent D-loop formation by yeast recombination factor Rdh54/Tid1. *Genes Dev* **14**, 2206–2215 (2000).

105. N. Sugawara, X. Wang, J. E. Haber, *In vivo* roles of Rad52, Rad54, and Rad55 proteins in Rad51-mediated recombination. *Mol Cell* **12**, 209–219 (2003).

106. A. Piazza, W.-D. Heyer, Moving forward one step back at a time: reversibility during homologous recombination. *Curr Genet* **65**, 1333–1340 (2019).

107. A. Piazza, S. S. Shah, W. D. Wright, S. K. Gore, R. Koszul, W.-D. Heyer, Dynamic processing of displacement loops during recombinational DNA repair. *Mol Cell* **73**, 1255-1266.e4 (2019).

108. S. S. Shah, S. Hartono, A. Piazza, V. Som, W. Wright, F. Chédin, W.-D. Heyer, Rdh54/Tid1 inhibits rad51-rad54-mediated d-loop formation and limits d-loop length. *Elife* **9**, e59112 (2020).

109. E. M. Tavares, W. D. Wright, W.-D. Heyer, E. Le Cam, P. Dupaigne, *In vitro* role of Rad54 in Rad51-ssDNA filament-dependent homology search and synaptic complexes formation. *Nat Commun* **10**, 4058 (2019).

110. W. D. Wright, W.-D. Heyer, Rad54 functions as a heteroduplex DNA pump modulated by its DNA substrates and Rad51 during D loop formation. *Mol Cell* **53**, 420–432 (2014).

111. I. Amitani, R. J. Baskin, S. C. Kowalczykowski, Visualization of Rad54, a chromatin remodeling protein, translocating on single DNA molecules. *Mol Cell* **23**, 143–148 (2006).

112. T. K. Prasad, R. B. Robertson, M. L. Visnapuu, P. Chi, P. Sung, E. C. Greene, A DNA-translocating Snf2 molecular motor: *Saccharomyces cerevisiae* Rdh54 displays processive translocation and extrudes DNA loops. *J Mol Biol* **369**, 940–953 (2007).

113. J. M. Mason, K. Dusad, W. D. Wright, J. Grubb, B. Budke, W.-D. Heyer, P. P. Connell, R. R. Weichselbaum, D. K. Bishop, RAD54 family translocases counter genotoxic effects of RAD51 in human tumor cells. *Nucleic Acids Res* **43**, 3180–3196 (2015).

114. P. P. Shah, X. Zheng, A. Epshtein, J. N. Carey, D. K. Bishop, H. L. Klein, Swi2/Snf2-related translocases prevent accumulation of toxic Rad51 complexes during mitotic growth. *Mol Cell* **39**, 862–872 (2010).

115. K. Yamaya, B. Wang, N. Memar, A. S. Odiba, A. Woglar, A. Gartner, A. M. Villeneuve, Disparate roles for *C. elegans* DNA translocase paralogs RAD-54.L and RAD-54.B in meiotic prophase germ cells. *Nucleic Acids Res* **51**, 9183–9202 (2023).

116. E. Antony, E. J. Tomko, Q. Xiao, L. Krejci, T. M. Lohman, T. Ellenberger, Srs2 disassembles Rad51 filaments by a protein-protein interaction triggering ATP turnover and dissociation of Rad51 from DNA. *Mol Cell* **35**, 105–115 (2009).

117. Y. Qiu, E. Antony, S. Doganay, H. Ran Koh, T. M. Lohman, S. Myong, Srs2 prevents Rad51 filament formation by repetitive motion on DNA. *Nat Commun* **4**, 2281 (2013).

118. R. Prakash, D. Satory, E. Dray, A. Papusha, J. Scheller, W. Kramer, L. Krejci, H. Klein, J. E. Haber, P. Sung, G. Ira, Yeast Mph1 helicase dissociates Rad51-made D-loops: implications for crossover control in mitotic recombination. *Genes Dev* **23**, 67–79 (2009).

119. J. B. Crickard, C. Xue, W. Wang, Y. Kwon, P. Sung, E. C. Greene, The RecQ helicase Sgs1 drives ATP-dependent disruption of Rad51 filaments. *Nucleic Acids Res* **47**, 4694–4706 (2019).

120. A. Meir, J. B. Crickard, Y. Kwon, P. Sung, E. C. Greene, Rad54 and Rdh54 prevent Srs2-mediated disruption of Rad51 presynaptic filaments. *Proc Natl Acad Sci U S A* **119**, e2113871119 (2022).

121. J. Liu, L. Renault, X. Veaute, F. Fabre, H. Stahlberg, W.-D. Heyer, Rad51 paralogues Rad55-Rad57 balance the antirecombinase Srs2 in Rad51 filament formation. *Nature* **479**, 245–248 (2011).

122. K. Kaniecki, L. De Tullio, B. Gibb, Y. Kwon, P. Sung, E. C. Greene, Dissociation of Rad51 presynaptic complexes and heteroduplex DNA joints by tandem assemblies of Srs2. *Cell Rep* **21**, 3166–3177 (2017).

123. C. L. Fasching, P. Cejka, S. C. Kowalczykowski, W.-D. Heyer, Top3-Rmi1 dissolve Rad51-mediated D loops by a topoisomerase-based mechanism. *Mol Cell* **57**, 595–606 (2015).

124. G. M. Harami, J. Pálinkás, Y. Seol, Z. J. Kovács, M. Gyimesi, H. Harami-Papp, K. C. Neuman, M. Kovács, The toposiomerase IIIalpha-RMI1-RMI2 complex orients

human Bloom's syndrome helicase for efficient disruption of D-loops. *Nat Commun* **13** (2022).

125. C.-F. Chen, S. J. Brill, Binding and activation of DNA topoisomerase III by the Rmi1 subunit. *J Biol Chem* **282**, 28971–28979 (2007).

126. P. Yakovchuk, E. Protozanova, M. D. Frank-Kamenetskii, Base-stacking and base-pairing contributions into thermal stability of the DNA double helix. *Nucleic Acids Res* **34**, 564–574 (2006).

127. J. Choi, M. Kong, D. N. Gallagher, K. Li, G. Bronk, Y. Cao, E. C. Greene, J. E. Haber, Repair of mismatched templates during Rad51-dependent Break-Induced Replication. *PLoS Genet* **18**, e1010056 (2022).

128. U. Chakraborty, E. Alani, Understanding how mismatch repair proteins participate in the repair/anti-recombination decision. *FEMS Yeast Res* **16**, fow071 (2016).

129. M. J. McIlwraith, S. C. West, DNA repair synthesis facilitates RAD52-mediated second-end capture during DSB repair. *Mol Cell* **29**, 510–516 (2008).

130. N. Mazloum, W. K. Holloman, Second-end capture in DNA double-strand break repair promoted by Brh2 protein of *Ustilago maydis*. *Mol Cell* **33**, 160–170 (2009).

131. J. Liu, C. Ede, W. D. Wright, S. K. Gore, S. S. Jenkins, B. D. Freudenthal, M. Todd Washington, X. Veaute, W.-D. Heyer, Srs2 promotes synthesis-dependent strand annealing by disrupting DNA polymerase δ-extending D-loops. *Elife* **6**, e22195 (2017).

132. H. D. M. Wyatt, S. C. West, Holliday junction resolvases. *Cold Spring Harb Perspect Biol* **6**, a023192 (2014).

133. J. W. Szostak, T. L. Orr-Weaver, R. J. Rothstein, F. W. Stahl, The double-strand-break repair model for recombination. *Cell* **33**, 25–35 (1983).

134. X. Wu, A. Malkova, Break-induced replication mechanisms in yeast and mammals. *Curr Opin Genet Dev* **71**, 163–170 (2021).

135. N. Pham, Z. Yan, Y. Yu, M. Faria Afreen, A. Malkova, J. E. Haber, G. Ira, Mechanisms restraining break-induced replication at two-ended DNA double-strand breaks. *EMBO J* **40**, e104847 (2021).

136. M. Bzymek, N. H. Thayer, S. D. Oh, N. Kleckner, N. Hunter, Double Holliday junctions are intermediates of DNA break repair. *Nature* **464**, 937–941 (2010).

137. G. Ira, A. Malkova, G. Liberi, M. Foiani, J. E. Haber, Srs2 and Sgs1-Top3 suppress crossovers during double-strand break repair in yeast. *Cell* **115**, 401–411 (2003).

138. K. Mitchel, K. Lehner, S. Jinks-Robertson, Heteroduplex DNA position defines the roles of the Sgs1, Srs2, and Mph1 helicases in promoting distinct recombination outcomes. *PLoS Genet* **9**, e1003340 (2013).

139. G. Mazón, L. S. Symington, Mph1 and Mus81-Mms4 prevent aberrant processing of mitotic recombination intermediates. *Mol Cell* **52**, 63–74 (2013).

140. C. Arnould, V. Rocher, F. Saur, A. S. Bader, F. Muzzopappa, S. Collins, E. Lesage, B. Le Bozec, N. Puget, T. Clouaire, T. Mangeat, R. Mourad, N. Ahituv, D. Noordermeer, F. Erdel, M. Bushell, A. Marnef, G. Legube, Chromatin compartmentalization regulates the response to DNA damage. *Nature* **623**, 183–192 (2023).

141. M. Tsabar, J. E. Haber, Chromatin modifications and chromatin remodeling during DNA repair in budding yeast. *Curr Opin Genet Dev* **23**, 166–173 (2013).

142. V. Dion, V. Kalck, C. Horigome, B. D. Towbin, S. M. Gasser, Increased mobility of double-strand breaks requires Mec1, Rad9 and the homologous recombination machinery. *Nat Cell Biol* **14**, 502–509 (2012).

143. A. Piazza, H. Bordelet, A. Dumont, A. Thierry, J. Savocco, F. Girard, R. Koszul, Cohesin regulates homology search during recombinational DNA repair. *Nat Cell Biol* **23**, 1176–1186 (2021).

144. U. Chakraborty, B. Mackenroth, D. Shalloway, E. Alani, Chromatin modifiers alter recombination between divergent DNA sequences. *Genetics* **212**, 1147–1162 (2019).

145. J. Miné-Hattab, R. Rothstein, Increased chromosome mobility facilitates homology search during recombination. *Nat Cell Biol* **14**, 510–517 (2012).

146. A. Cheblal, K. Challa, A. Seeber, K. Shimada, H. Yoshida, H. C. Ferreira, A. Amitai, S. M. Gasser, DNA damage-induced nucleosome depletion enhances homology search independently of local break movement. *Mol Cell* **80**, 311-326.e4 (2020).

147. H. Bordelet, K. Dubrana, Keep moving and stay in a good shape to find your homologous recombination partner. *Curr Genet* **65**, 29–39 (2019).

148. B. R. Schrank, T. Aparicio, Y. Li, W. Chang, B. T. Chait, G. G. Gundersen, M. E. Gottesman, J. Gautier, Nuclear ARP2/3 drives DNA break clustering for homology-directed repair. *Nature* **559**, 61–66 (2018).

149. J. Zagelbaum, J. Gautier, Double-strand break repair and mis-repair in 3D. *DNA Repair (Amst)* **121**, 103430 (2023).

150. J. Zagelbaum, A. Schooley, J. Zhao, B. R. Schrank, E. Callen, S. Zha, M. E. Gottesman, A. Nussenzweig, R. Rabadan, J. Dekker, J. Gautier, Multiscale reorganization of the genome following DNA damage facilitates chromosome translocations via nuclear actin polymerization. *Nat Struct Mol Biol* **30**, 99–106 (2023).

151. F. Aymard, M. Aguirrebengoa, E. Guillou, B. M. Javierre, B. Bugler, C. Arnould, V. Rocher, J. S. Iacovoni, A. Biernacka, M. Skrzypczak, K. Ginalski, M. Rowicka, P. Fraser, G. Legube, Genome-wide mapping of long-range contacts unveils clustering of DNA double-strand breaks at damaged active genes. *Nat Struct Mol Biol* **24**, 353–361 (2017).

152. N. Wu, H. Yu, The Smc complexes in DNA damage response. *Cell Biosci* **2**, 5 (2012).

153. A. Dumont, N. Mendiboure, J. Savocco, L. Anani, P. Moreau, A. Thierry, L. Modolo, D. Jost, A. Piazza, Mechanism of homology search expansion during recombinational DNA break repair. *Mol Cell* **84**, 3237-3253.e6 (2024).

154. C. Lesterlin, G. Ball, L. Schermelleh, D. J. Sherratt, RecA bundles mediate homology pairing between distant sisters during DNA break repair. *Nature* **506**, 249–253 (2014).

155. J. Wiktor, A. H. Gynnå, P. Leroy, J. Larsson, G. Coceano, I. Testa, J. Elf, RecA finds homologous DNA by reduced dimensionality search. *Nature* **597**, 426–429 (2021).

156. V. Amarh, M. A. White, D. R. F. Leach, Dynamics of RecA-mediated repair of replication-dependent DNA breaks. *J Cell Biol* **217**, 2299–2307 (2018).

157. L. A. Uranga, E. D. Reyes, P. L. Patidar, L. N. Redman, S. L. Lusetti, The cohesin-like RecN protein stimulates RecA-mediated recombinational repair of DNA double-strand breaks. *Nat Commun* **8**, 15282 (2017).

158. K. Keyamura, T. Hishida, Topological DNA-binding of structural maintenance of chromosomes-like RecN promotes DNA double-strand break repair in *Escherichia coli*. *Commun Biol* **2**, 413 (2019).

159. A. Chimthanawala, J. J. Parmar, S. Kumar, K. S. Iyer, M. Rao, A. Badrinarayanan, SMC protein RecN drives RecA filament translocation for *in vivo* homology search. *Proc Natl Acad Sci U S A* **119**, e2209304119 (2022).

160. S. Liu, J. Miné-Hattab, M. Villemeur, R. Guerois, H. D. Pinholt, L. A. Mirny, A. Taddei, *In vivo* tracking of functionally tagged Rad51 unveils a robust strategy of homology search. *Nat Struct Mol Biol* **30**, 1582–1591 (2023).

161. J. K. Karow, L. Wu, I. D. Hickson, RecQ family helicases: roles in cancer and aging. *Curr Opin Genet Dev* **10**, 32–38 (2000).

162. S. Gangloff, J. P. Mcdonald, C. Bendixen, L. Arthur, R. Rothstein, The yeast Type I topoisomerase Top3 interacts with Sgsl, a DNA helicase homolog: a potential eukaryotic reverse gyrase. *Mol Cell Biol* **14**, 8391–8398 (1994).

163. J. German, Bloom syndrome-a mendelian prototype of somatic mutational disease. *Medicine* **72**, 393–406 (1993).

164. Y.-C. Lo, K. S. Paffett, O. Amit, J. A. Clikeman, R. Sterk, M. A. Brenneman, J. A. Nickoloff, Sgs1 regulates gene conversion tract lengths and crossovers independently of its helicase activity. *Mol Cell Biol* **26**, 4086–4094 (2006).

165. A. Kerrest, R. P. Anand, R. Sundararajan, R. Bermejo, G. Liberi, B. Dujon, C. H. Freudenreich, G.-F. Richard, SRS2 and SGS1 prevent chromosomal breaks and stabilize triplet repeats by restraining recombination. *Nat Struct Mol Biol* **16**, 159–167 (2009).

166. B. Rockmill, J. C. Fung, S. S. Branda, G. S. Roeder, The Sgs1 helicase regulates chromosome synapsis and meiotic crossing over. *Curr Biol* **13**, 1954–1962 (2003).

167. H. W. Mankouri, T. M. Ashton, I. D. Hickson, Holliday junction-containing DNA structures persist in cells lacking Sgs1 or Top3 following exposure to DNA damage. *Proc Natl Acad Sci U S A* **108**, 4944–4949 (2011).

168. P. M. Watt, I. D. Hickson, R. H. Bortst, E. J. Louist, SGS1, a Homologue of the Bloom's and Werner's Syndrome Genes, Is Required for Maintenance of Genome Stability in *Saccharomyces cerevisiae*. *Genetics* **144**, 935–945 (1996).

169. L. Wu, I. D. Hickson, The Bloom's syndrome helicase suppresses crossing over during homologous recombination. *Nature* **426**, 870–874 (2003).

170. Z. Li, A. Mondragó, R. J. Digate, The mechanism of Type IA topoisomerase-mediated DNA topological transformations. *Mol Cell* **7**, 301–307 (2001).

171. J. W. Wallis, G. Chrebet, G. Brodsky, M. Rolfe, R. Rothstein', A hyper-recombination mutation in *S. cerevisiae* identifies a novel eukaryotic topoisomerase. *Cell* **58**, 409–419 (1989).

172. J. R. Mullen, F. S. Nallaseth, Y. Q. Lan, C. E. Slagle, S. J. Brill, Yeast Rmi1/Nce4 controls genome stability as a subunit of the Sgs1-Top3 complex. *Mol Cell Biol* **25**, 4476–4487 (2005).

173. M. Chang, M. Bellaoui, C. Zhang, R. Desai, P. Morozov, L. Delgado-Cruzata, R. Rothstein, G. A. Freyer, C. Boone, G. W. Brown, RMI1/NCE4, a suppressor of genome instability, encodes a member of the RecQ helicase/Topo III complex. *EMBO J* **24**, 2024–2033 (2005).

174. P. Cejka, J. L. Plank, C. Z. Bachrati, I. D. Hickson, S. C. Kowalczykowski, Rmi1 stimulates decatenation of double Holliday junctions during dissolution by Sgs1-Top3. *Nat Struct Mol Biol* **17**, 1377–1382 (2010).

175. T. R. Singh, A. M. Ali, V. Busygina, S. Raynard, Q. Fan, C. Du, P. R. Andreassen, P. Sung, A. R. Meetei, BLAP18/RMI2, a novel OB-fold-containing protein, is an essential component of the Bloom helicase-double Holliday junction dissolvasome. *Genes Dev* **22**, 2856–2868 (2008).

176. H. W. Mankouri, I. D. Hickson, The RecQ helicase-topoisomerase III-Rmi1 complex: a DNA structure-specific "dissolvasome"? *Trends Biochem Sci* **32**, 538–546 (2007).

177. K. A. Bernstein, E. Shor, I. Sunjevaric, M. Fumasoni, R. C. Burgess, M. Foiani, D. Branzei, R. Rothstein, Sgs1 function in the repair of DNA replication intermediates is separable from its role in homologous recombinational repair. *EMBO J* **28**, 915–925 (2009).

178. K. A. Manthei, J. L. Keck, The BLM dissolvasome in DNA replication and repair. *Cell Mol Life Sci* **70**, 4067–4084 (2013).

179. A. H. Bizard, I. D. Hickson, The dissolution of double Holliday junctions. *Cold Spring Harb Perspect Biol* **6**, a016477 (2014).

180. B. Miller, C. Jones, B. Kemper, S. C. West', Enzymatic formation and resolution of Holliday junctions *in vitro*. *Cell* **60**, 329–336 (1990).

181. P. Dickie, G. McFadden, A. R. Morgan, The site-specific cleavage of synthetic Holliday junction analogs and related branched DNA structures by bacteriophage T7 endonuclease I. *J Biol Chem* **262**, 14826–14836 (1987).

182. B. Connolly, S. C. West, Genetic recombination in *Escherichia coli*: Holliday junctions made by RecA protein are resolved by fractionated cell-free extracts. *Proc Natl Acad Sci U S A* **87**, 8476–8480 (1990).

183. B. Connolly, C. A. Parsons, F. E. Benson, H. J. Dunderdale, G. J. Sharples, R. G. Lloyd, S. C. West, Resolution of Holliday junctions *in vitro* requires the *Escherichia coli* ruvC gene product. *Proc Natl Acad Sci U S A* **88**, 6063–6067 (1991).

184. H. J. Dunderdale, F. E. Benson, C. A. Parsons, G. J. Sharples, R. G. Lloyd, S. C. Wese, Formation and resolution of recombination intermediates by *E. coli* RecA and RuvC proteins. *Nature* **354**, 506–510 (1991).

185. R. J. Bennett, S. C. Westt, Resolution of Holliday junctions in genetic recombination: RuvC protein nicks DNA at the point of strand exchange. *Proc Natl Acad Sci U S A* **93**, 12217–12222 (1996).

186. M. Ariyoshi, D. G. Vassylyev, H. Iwasaki, H. Nakamura, H. Shinagawa, K. Morikawa, Atomic structure of the RuvC resolvase: a Holliday junction-specific endonuclease from *E. coli*. *Cell* **78**, 1063–1072 (1994).

187. S. C. Y. Ip, U. Rass, M. G. Blanco, H. R. Flynn, J. M. Skehel, S. C. West, Identification of Holliday junction resolvases from humans and yeast. *Nature* **456**, 357–361 (2008).

188. U. Rass, S. A. Compton, J. Matos, M. R. Singleton, S. C. Y. Ip, M. G. Blanco, J. D. Griffith, S. C. West, Mechanism of Holliday junction resolution by the human GEN1 protein. *Genes Dev* **24**, 1559–1569 (2010).

189. A. Lorenz, S. C. West, M. C. Whitby, The human Holliday junction resolvase GEN1 rescues the meiotic phenotype of a *Schizosaccharomyces pombe* mus81 mutant. *Nucleic Acids Res* **38**, 1866–1873 (2009).

190. C. K. Ho, G. Mazón, A. F. Lam, L. S. Symington, Mus81 and Yen1 promote reciprocal exchange during mitotic recombination to maintain genome integrity in budding yeast. *Mol Cell* **40**, 988–1000 (2010).

191. M. G. Blanco, J. Matos, U. Rass, S. C. Y. Ip, S. C. West, Functional overlap between the structure-specific nucleases Yen1 and Mus81-Mms4 for DNA-damage repair in *S. cerevisiae*. *DNA Repair (Amst)* **9**, 394–402 (2010).

192. J. Matos, M. G. Blanco, S. Maslen, J. M. Skehel, S. C. West, Regulatory control of the resolution of DNA recombination intermediates during meiosis and mitosis. *Cell* **147**, 158–172 (2011).

193. T. Wechsler, S. Newman, S. C. West, Aberrant chromosome morphology in human cells defective for Holliday junction resolution. *Nature* **471**, 642–646 (2011).

194. H. D. M. Wyatt, S. Sarbajna, J. Matos, S. C. West, Coordinated actions of SLX1-SLX4 and MUS81-EME1 for holliday junction resolution in human cells. *Mol Cell* **52**, 234–247 (2013).

195. E. Garner, Y. Kim, F. P. Lach, M. C. Kottemann, A. Smogorzewska, Human GEN1 and the SLX4-associated nucleases MUS81 and SLX1 are essential for the resolution of replication-induced Holliday junctions. *Cell Rep* **5**, 207–215 (2013).

196. S. L. Andersen, H. K. Kuo, D. Savukoski, M. H. Brodsky, J. Sekelsky, Three structure-selective endonucleases are essential in the absence of BLM helicase in *Drosophila*. *PLoS Genet* **7**, e1002315 (2011).

197. T. T. Saito, D. Y. Lui, H. M. Kim, K. Meyer, M. P. Colaiácovo, Interplay between structure-specific endonucleases for crossover control during *Caenorhabditis elegans* meiosis. *PLoS Genet* **9**, e1003586 (2013).

198. L. Jessop, M. Lichten, Mus81/Mms4 endonuclease and Sgs1 helicase collaborate to ensure proper recombination intermediate metabolism during meiosis. *Mol Cell* **31**, 313–323 (2008).

199. J. R. Mullen, V. Kaliraman, S. S. Ibrahim, S. J. Brill, Requirement for three novel protein complexes in the absence of the Sgs1 DNA helicase in *Saccharomyces cerevisiae*. *Genetics* **157**, 103–118 (2001).

200. M. N. Boddy, P.-H. L. Gaillard, W. H. McDonald, P. Shanahan, J. R. Yates 3rd, P. Russell, Mus81-Eme1 are essential components of a Holliday junction resolvase. *Cell* **107**, 537–548 (2001).

201. X.-B. Chen, R. Melchionna, C.-M. Denis, P.-H. L. Gaillard, A. Blasina, I. Van De Weyer, M. N. Boddy, P. Russell, J. Vialard, C. H. Mcgowan, Human Mus81-associated endonuclease cleaves Holliday junctions *in vitro*. *Mol Cell* **8**, 1117–1127 (2001).

202. A. Ciccia, A. Constantinou, S. C. West, Identification and characterization of the human mus81-eme1 endonuclease. *J Biol Chem* **278**, 25172–25178 (2003).

203. W. M. Fricke, S. A. Bastin-Shanower, S. J. Brill, Substrate specificity of the *Saccharomyces cerevisiae* Mus81-Mms4 endonuclease. *DNA Repair (Amst)* **4**, 243–251 (2005).

204. P.-H. L. Gaillard, E. Noguchi, P. Shanahan, P. Russell, The endogenous Mus81-Eme1 complex resolves Holliday Junctions by a nick and counternick mechanism. *Mol Cell* **12**, 747–759 (2003).

205. S. Coulon, P.-H. L. Gaillard, C. Chahwan, W. H. Mcdonald, J. R. Yates Iii, P. Russell, Slx1-Slx4 are subunits of a structure-specific endonuclease that maintains ribosomal DNA in fission yeast. *Mol Biol Cell* **15**, 71–80 (2004).

206. W. M. Fricke, S. J. Brill, Slx1-Slx4 is a second structure-specific endonuclease functionally redundant with Sgs1-Top3. *Genes Dev* **17**, 1768–1778 (2003).

207. A. D. McAinsh, G. J. P. L. Kops, Principles and dynamics of spindle assembly checkpoint signalling. *Nat Rev Mol Cell Biol* **24**, 543–559 (2023).

208. F. Dotiwala, J. C. Harrison, S. Jain, N. Sugawara, J. E. Haber, Mad2 prolongs DNA damage checkpoint arrest caused by a double-strand break via a centromere-dependent mechanism. *Curr Biol* **20**, 328–332 (2010).

209. X. Wang, H. Chu, M. Lv, Z. Zhang, S. Qiu, H. Liu, X. Shen, W. Wang, G. Cai, Structure of the intact ATM/Tel1 kinase. *Nat Commun* **7**, 11655 (2016).

210. D. Nakada, K. Matsumoto, K. Sugimoto, ATM-related Tel1 associates with double-strand breaks through an Xrs2-dependent mechanism. *Genes Dev* **17**, 1957–1962 (2003).

211. J. H. Kim, M. Grosbart, R. Anand, C. Wyman, P. Cejka, J. H. J. Petrini, The Mre11-Nbs1 interface is essential for viability and tumor suppression. *Cell Rep* **18**, 496–507 (2017).

212. C. J. Bakkenist, M. B. Kastan, DNA damage activates ATM through intermolecular autophosphorylation and dimer dissociation. *Nature* **421**, 499–506 (2003).

213. X. Wang, T. Ran, X. Zhang, J. Xin, Z. Zhang, T. Wu, W. Wang, G. Cai, 3.9 Å structure of the yeast Mec1-Ddc2 complex, a homolog of human ATR-ATRIP. *Science* **358**, 1206–1209 (2017).

214. D. A. Mordes, E. A. Nam, D. Cortez, Dpb11 activates the Mec1-Ddc2 complex. *Proc Natl Acad Sci U S A* **105**, 18730–18734 (2008).

215. J. Majka, A. Niedziela-Majka, P. M. M. J. Burgers, The checkpoint clamp activates Mec1 kinase during initiation of the DNA damage checkpoint. *Mol Cell* **24**, 891–901 (2006).

216. V. M. Navadgi-Patil, P. M. Burgers, Yeast DNA replication protein Dpb11 activates the Mec1/ATR checkpoint kinase. *J Biol Chem* **283**, 35853–35859 (2008).

217. S. Kumar, P. M. Burgers, Lagging strand maturation factor Dna2 is a component of the replication checkpoint initiation machinery. *Genes Dev* **27**, 313–321 (2013).

218. P. Haahr, S. Hoffmann, M. A. X. Tollenaere, T. Ho, L. I. Toledo, M. Mann, S. Bekker-Jensen, M. Räschle, N. Mailand, Activation of the ATR kinase by the RPA-binding protein ETAA1. *Nat Cell Biol* **18**, 1196–1207 (2016).

219. T. E. Bass, J. W. Luzwick, G. Kavanaugh, C. Carroll, H. Dungrawala, G. G. Glick, M. D. Feldkamp, R. Putney, W. J. Chazin, D. Cortez, ETAA1 acts at stalled replication forks to maintain genome integrity. *Nat Cell Biol* **18**, 1185–1195 (2016).

220. Y.-C. Lee, Q. Zhou, J. Chen, J. Yuan, RPA-binding protein ETAA1 is an ATR activator involved in DNA replication stress response. *Curr Biol* **26**, 3257–3268 (2016).

221. A. Kumagai, J. Lee, H. Y. Yoo, W. G. Dunphy, TopBP1 activates the ATR-ATRIP complex. *Cell* **124**, 943–955 (2006).

222. P. Huertas, F. Cortés-Ledesma, A. A. Sartori, A. Aguilera, S. P. Jackson, CDK targets Sae2 to control DNA-end resection and homologous recombination. *Nature* **455**, 689–692 (2008).

223. P. Huertas, S. P. Jackason, Human CtIP mediates cell cycle control of DNA end resection and double strand break repair. *J Biol Chem* **284**, 9558–9565 (2009).

224. X. Chen, H. Niu, W. H. Chung, Z. Zhu, A. Papusha, E. Y. Shim, S. E. Lee, P. Sung, G. Ira, Cell cycle regulation of DNA double-strand break end resection by Cdk1-dependent Dna2 phosphorylation. *Nat Struct Mol Biol* **18**, 1015–1019 (2011).

225. G. Ira, A. Pellicioli, A. Balijja, X. Wang, S. Fiorani, W. Carotenuto, G. Liberi, D. Bressan, L. Wan, N. M. Hollingsworth, J. E. Haber, M. Foiani, DNA end resection, homologous recombination and DNA damage checkpoint activation require CDK1. *Nature* **431**, 1011–1017 (2004).

226. G. Liberi, I. Chiolo, A. Pellicioli, M. Lopes, P. Plevani, M. Muzi-Falconi, M. Foiani, Srs2 DNA helicase is involved in checkpoint response and its regulation requires a functional Mec1-dependent pathway and Cdk1 activity. *EMBO J* **19**, 5027–5038 (2000).

227. C. Y. Bonilla, J. A. Melo, D. P. Toczyski, Colocalization of sensors is sufficient to activate the DNA damage checkpoint in the absence of damage. *Mol Cell* **30**, 267–276 (2008).

228. E. P. Rogakou, C. Boon, C. Redon, W. M. Bonner, Megabase chromatin domains involved in DNA double-strand breaks *in vivo*. *J Cell Biol* **146**, 905–916 (1999).

229. E. P. Rogakou, D. R. Pilch, A. H. Orr, V. S. Ivanova, W. M. Bonner, DNA double-stranded breaks induce histone H2AX phosphorylation on serine 139*. *J Biol Chem* **273**, 5858–5868 (1998).

230. J. A. Downs, N. F. Lowndes, S. P. Jackson, A role for *Saccharomyces cerevisiae* histone H2A in DNA repair. *Nature* **408**, 1001–1004 (2000).

231. R. Shroff, A. Arbel-Eden, D. Pilch, G. Ira, W. M. Bonner, J. H. Petrini, J. E. Haber, M. Lichten, Distribution and dynamics of chromatin modification induced by a defined DNA double-strand break. *Curr Biol* **14**, 1703–1711 (2004).

232. C.-S. Lee, K. Lee, G. Legube, J. E. Haber, Dynamics of yeast histone H2A and H2B phosphorylation in response to a double-strand break. *Nat Struct Mol Biol* **21**, 103–109 (2014).

233. A. Kinner, W. Wu, C. Staudt, G. Iliakis, γ-H2AX in recognition and signaling of DNA double-strand breaks in the context of chromatin. *Nucleic Acids Res* **36**, 5678–5694 (2008).

234. C. H. Bassing, F. W. Alt, H2AX may function as an anchor to hold broken chromosomal DNA ends in close proximity. *Cell Cycle* **3**, 147–153 (2004).

235. L.-J. Mah, A. El-Osta, T. Karagiannis, γH2AX: A sensitive molecular marker of DNA damage and repair. *Leukemia* **24**, 679–686 (2010).

236. A. A. Alcasabas, A. J. Osborn, J. Bachant, F. Hu, P. J. H. Werler, K. Bousset, K. Furuya, J. F. X. Diffley, A. M. Carr, S. J. Elledge, Mrc1 transduces signals of DNA replication stress to activate Rad53. *Nat Cell Biol* **3**, 958–965 (2001).

237. M. F. Schwartz, J. K. Duong, Z. Sun, J. S. Morrow, D. Pradhan, D. F. Stern, Rad9 phosphorylation sites couple Rad53 to the *Saccharomyces cerevisiae* DNA damage checkpoint. *Mol Cell* **9**, 1055–1065 (2002).

238. A. Emili, MEC1-dependent phosphorylation of Rad9p in response to DNA damage. *Mol Cell* **2**, 183–189 (1998).

239. J. E. Vialard, C. S. Gilbert, C. M. Green, N. F. Lowndes, The budding yeast Rad9 checkpoint protein is subjected to Mec1/Tel1-dependent hyperphosphorylation and interacts with Rad53 after DNA damage. *EMBO J* **17**, 5679–5688 (1998).

240. Z. Sun, J. Hsiao, D. S. Fay, D. F. Stern, Rad53 FHA domain associated with phosphorylated Rad9 in the DNA damage checkpoint. *Science* **281**, 272–274 (1998).

241. C. S. Gilbert, C. M. Green, N. F. Lowndes, Budding yeast Rad9 is an ATP-dependent Rad53 activating machine. *Mol Cell* **8**, 129–136 (2001).

242. E. S. W. Chen, N. C. Hoch, S. C. Wang, A. Pellicioli, J. Heierhorst, M. D. Tsai, Use of quantitative mass spectrometric analysis to elucidate the mechanisms of phospho-priming and auto-activation of the checkpoint kinase rad53 *in vivo*. *Mol Cell Proteomics* **13**, 551–565 (2014).

243. T. Usui, S. S. Foster, J. H. J. Petrini, Maintenance of the DNA-damage checkpoint requires DNA-damage-induced mediator protein oligomerization. *Mol Cell* **33**, 147–159 (2009).

244. N. Jia-Lin Ma, D. F. Stern, Regulation of the Rad53 protein kinase in signal amplification by oligomer assembly and disassembly. *Cell Cycle* **7**, 808–817 (2008).

245. R. T. Blankley, D. Lydall, A domain of Rad9 specifically required for activation of Chk1 in budding yeast. *J Cell Sci* **117**, 601–608 (2004).

246. Z. Zhou, S. J. Elledge, DUN1 encodes a protein kinase that controls the DNA damage response in yeast. *Cell* **75**, 1119–127 (1993).

247. V. I. Bashkirov, J. S. King, E. V. Bashkirova, J. Schmuckli-Maurer, W.-D. Heyer, DNA repair protein Rad55 ss a terminal substrate of the DNA damage checkpoints. *Mol Cell Biol* **20**, 4393–4404 (2000).

248. J. Hu, B. Ferlez, J. Dau, J. B. Crickard, Rad53 regulates the lifetime of Rdh54 at homologous recombination intermediates. *Nucleic Acids Res* **51**, 11688–11705 (2023).

249. Y. Sanchez, J. Bachant, H. Wang, F. Hu, D. Liu, M. Tetzlaff, S. J. Elledge, Control of the DNA damage checkpoint by Chk1 and Rad53 protein kinases through distinct mechanisms. *Science* **286**, 1166–1171 (1999).

250. R. Agarwal, Z. Tang, H. Yu, O. Cohen-Fix, Two distinct pathways for inhibiting Pds1 ubiquitination in response to DNA damage. *J Biol Chem* **278**, 45027–45033 (2003).

251. P. Y. Ohouo, F. M. Bastos De Oliveira, Y. Liu, C. J. Ma, M. B. Smolka, DNA-repair scaffolds dampen checkpoint signalling by counteracting the adaptor Rad9. *Nature* **493**, 120–124 (2013).

252. D. Dibitetto, M. Ferrari, C. C. Rawal, A. Balint, T. Kim, Z. Zhang, M. B. Smolka, G. W. Brown, F. Marini, A. Pellicioli, Slx4 and Rtt107 control checkpoint signalling and DNA resection at double-strand breaks. *Nucleic Acids Res* **44**, 669–682 (2015).

253. G. Millan-Zambrano, H. Santos-Rosa, F. Puddu, S. C. Robson, S. P. Jackson, T. Kouzarides, Phosphorylation of histone H4T80 triggers DNA damage checkpoint recovery. *Mol Cell* **72**, 625-635.e4 (2018).

254. S. E. Lee, J. K. Moore, A. Holmes, K. Umezu, R. D. Kolodner, J. E. Haber, *Saccharomyces* Ku70, Mre11/Rad50, and RPA proteins regulate adaptation to G2/M arrest after DNA damage. *Cell* **94**, 399–409 (1998).

255. D. P. Toczyski, D. J. Galgoczy, L. H. Hartwell, CDC5 and CKII control adaptation to the yeast DNA damage checkpoint. *Cell* **90**, 1097–1106 (1997).

256. R. G. Syljuåsen, S. Jensen, J. Bartek, J. Lukas, Adaptation to the ionizing radiation-induced G2 checkpoint occurs in human cells and depends on checkpoint kinase 1 and Polo-like kinase 1 kinases. *Cancer Res* **66**, 10253–10257 (2006).

257. G. M. Vidanes, F. D. Sweeney, S. Galicia, S. Cheung, J. P. Doyle, D. Durocher, D. P. Toczyski, CDC5 inhibits the hyperphosphorylation of the checkpoint kinase Rad53, leading to checkpoint adaptation. *PLoS Biol* **8**, e1000286 (2010).

258. G. Memisoglu, M. C. Lanz, V. V Eapen, J. M. Jordan, K. Lee, M. B. Smolka, J. E. Haber, Mec1(ATR) autophosphorylation and Ddc2(ATRIP) phosphorylation regulates DNA damage checkpoint signaling. *Cell Rep* **28**, 1090-1102.e3 (2019).

259. S. E. Lee, A. Pellicioli, A. Malkova, M. Foiani, J. E. Haber, The *Saccharomyces* recombination protein Tid1p is required for adaptation from G2/M arrest induced by a double-strand break. *Curr Biol* **11**, 1053–1057 (2001).

CHAPTER 2

Rad53 regulates the lifetime of Rdh54 at homologous recombination intermediates

Chapter 2 was published in *Nucleic Acids Research* under the same title.

Jingyi Hu[1], Bryan Ferlez[1], Jennifer Dau[1], and J. Brooks Crickard[1#]

[1.] Department of Molecular Biology and Genetics, Cornell University, Ithaca, NY 14853, USA

#To whom the correspondence should be addressed: jbc287@cornell.edu

Keywords: Homologous recombination, Rad53, Rdh54, DNA repair, single molecule

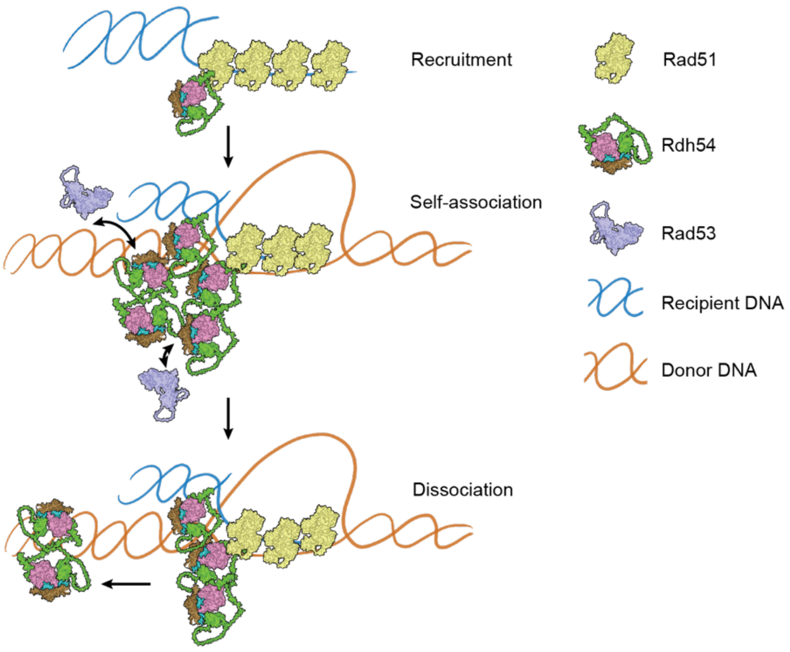

Figure 2.0: Chapter 2 graphic abstract.

Abstract

Rdh54 is a conserved DNA translocase that participates in homologous recombination (HR), DNA checkpoint adaptation, and chromosome segregation. *Saccharomyces cerevisiae* Rdh54 is a known target of the Mec1/Rad53 signaling axis, which globally protects genome integrity during DNA metabolism. While phosphorylation of DNA repair proteins by Mec1/Rad53 is critical for HR progression little is known about how specific post translational modifications alter HR reactions. Phosphorylation of Rdh54 is linked to protection of genomic integrity but the consequences of modification remain poorly understood. Here, we demonstrate that phosphorylation of the Rdh54 C-terminus by the effector kinase Rad53 regulates Rdh54 clustering activity as revealed by single molecule imaging. This stems from phosphorylation dependent and independent interactions between Rdh54 and Rad53. Genetic assays reveal that loss of phosphorylation leads to phenotypic changes resulting in loss-of-heterozygosity (LOH) outcomes. Our data highlight Rad53 as a key regulator of HR intermediates through activation and attenuation of Rdh54 motor function.

2.1 Introduction

DNA double strand breaks (DSBs) are a dangerous type of DNA lesion that if unrepaired result in cell death or loss of genomic integrity (1). DSBs result from normal DNA metabolism, and from exposure to mutagens within the environment (1-3). This makes double strand break repair (DSBR) critical for the maintenance of genomic integrity. DSBR is a multi-tier decision making process in which different pathways can be used to repair the break depending on the phase of the cell cycle. The two primary DSBR pathways are non-homologous end joining (NHEJ) and homologous recombination (HR) (1). HR is a template based DSBR pathway that is primarily active during S/G2 phase of the cell cycle and meiosis (2,4-7). HR outcomes are controlled by the selection of a donor DNA template (8-13), and the alignment of both sides of the DSB. Known asl DNA second end capture (14-18).

In eukaryotes template selection is coordinated by the recombinase Rad51 (7,19,20), which catalyzes the alignment of ssDNA (recipient DNA) from upstream of the DSB to a matching dsDNA (donor DNA) elsewhere in the genome in a process called the homology search. In *Saccharomyces cerevisiae*, Rad51 is aided in alignment of recipient and donor DNA by several accessory factors including Rad52, Rad54, Rdh54, and Rad55/57 (21-31). In mitotic HR, the sister chromatid is the primary template used for repair and results in the highest fidelity outcome (32,33). However, in rare cases the homologous chromosome is used as the template for repair. When the homologous chromosome is used as the template there is potential for gene conversion (34), which can result in a loss-of-heterozygosity (LOH) (35-38) (Figure 2.1A). LOH is a driver in many human cancers making understanding mechanisms that regulate these outcomes important.

LOH outcomes result from exchange of genetic information between homologous chromosomes. These outcomes are dictated by competing pathways that depend on resolution of intermediates that form during HR mediated repair. These pathways include synthesis-dependent strand annealing (SDSA) (34), the classical double Holliday junction pathway (dHJ) (4,39), and break-induced replication (BIR) (17,40-44). Of these pathways the dHJ and BIR have the potential to create large scale rearrangements of chromosomes through reciprocal and non-reciprocal exchange of DNA, respectively (5,44,45). Outcomes during HR are strongly influenced by the timing of each step, which is under the regulation of DNA damage kinases (46). These kinases also play established roles in slowing cell cycle progression. As a result, their activation provides more time for the execution of DNA repair before cell division and reduces the passage of damaged DNA (46). In *S. cerevisiae*, the sensor kinase Mec1 plays a predominant role in activation of damage signaling kinases (47), with a major downstream target being the effector kinase Rad53 (47-50). Rad53 phosphorylates proteins within the HR pathway (46,51), at the replication fork (52-54), and at the kinetochore where it regulates chromosome division (55-58). These kinases are believed to influence DNA repair pathway choice during DSBR.

Rdh54 is a target of the Mec1/Rad53 signaling axis (59), but it is unknown how phosphorylation of Rdh54 regulates function. Rdh54 is a DNA motor protein that uses the power of ATP hydrolysis to physically move along dsDNA and is directly recruited to HR intermediates through interactions with Rad51 (28,30,60,61). Rdh54 has been shown to stabilize Rad51 bound to ssDNA and displacement loops, and to disrupt Rad51 bound to dsDNA (62-65). Rdh54 forms a homo-oligomer through self-association facilitated by a flexible disordered N-terminal region (61,66,67). However, it remains unclear if this behavior has biological function. Rdh54 has been genetically implicated in regulating CO/NCO outcomes (26,68), BIR outcomes (62), interhomolog gene conversion (68,69), and template switching associated with BIR (70,71). Importantly, Rdh54 is not required for completion of these pathways, and instead appears to only influence HR choices indirectly. It has also been suggested that Rdh54 activity is context dependent.

Here we have identified and characterized Rdh54 mutants that affect communications between monomers of Rdh54. Mutations in this region lead to changes in Rdh54 clustering behavior on dsDNA, translocation activity on dsDNA, and interactions with the effector kinase Rad53. We also find this region to be a target of Rad53 whose kinase activity appears to down regulate the translocation activity of Rdh54 on dsDNA. Importantly, mutations in this region have phenotypic consequences on the distribution of LOH outcomes associated with HR. From this data we have classified Rdh54 mutations as translocation fast and slow versions of the enzyme linking these classes of mutants to different phenotypic outcomes. Finally, we have developed a model where Rdh54 activity at DNA repair sites is controlled by a dynamic equilibrium that balances recruitment of Rdh54 by Rad51 and dissociation of Rdh54 through translocation along dsDNA. This dynamic equilibrium helps regulate HR outcomes by a kinetic mechanism which is coordinated by Rad53 activity.

2.2 Results

2.2.1 A Rdh54 phosphorylation mutant displays enhanced sensitivity to DNA damage

Rdh54 is a known target of the Mec1/Rad53 kinases (59). However, the effects of Rdh54 phosphorylation during DNA repair are unknown. To identify potential phosphorylation sites, we used the SuperPhos database (74). Nine phosphorylation sites were identified in Rdh54: S19, S51, S165, S386, S619, S790, S791, T851, and S852 (Figure 2.S1A).

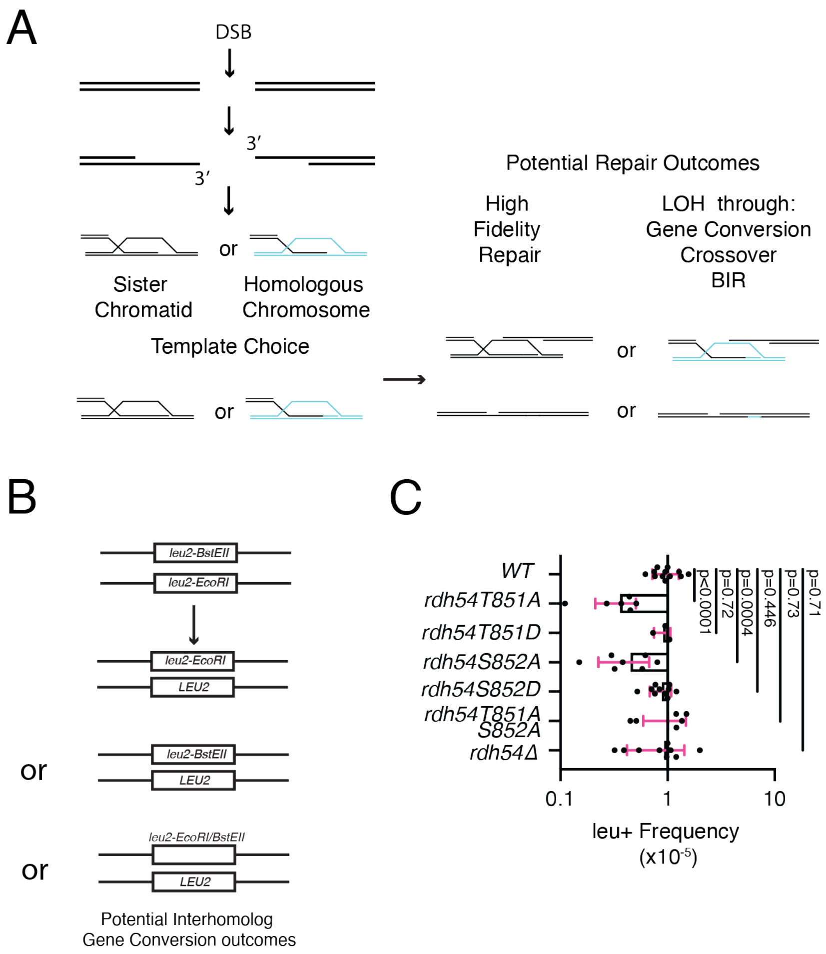

Figure 2.1: Rdh54 mutants' effect on interhomolog recombination.

(A) Schematic diagram illustrating how chromosome template selection can influence the outcome of HR leading to LOH outcomes. (B) Assay designed to identify gene conversion between homologous chromosomes. The assay is dependent on the formation of an *LEU2* from two inactive *leu2* alleles. (C) Comparison of inter-homolog gene conversion frequencies for WT, *rdh54T851A*, *rdh54T851D*, *rdh54S852A*, *rdh54S852D*, *rdh54T851A,S852A*, and *rdh54*Δ. The crossbar represents the mean, and the error bars the standard deviation of at least three independent experiments from multiple crosses. Statistical analysis was performed using a non-parametric Mann-Whitney test.

These numbers are based on Rdh54 from the W303 genetic background. In the reference strain (S288C) there is an additional thirty-four amino acids in the N-terminal region of Rdh54. To map these sites to the reference strain, add thirty-four to the amino acid number used in the W303 strain. For example, S19 in W303 is S53 in the reference strain. Of these nine sites, one was part of a Rad53 consensus sequence (S852) (75), and three were high confidence sites. High confidence sites are defined as >10 peptides identified in the proteomic analysis (S51, S619, and S852) (Figure 2.S1A). We initially converted all suspected phosphorylation sites to alanine and tested them for their ability to complement methyl methanosulfonate (MMS) and camptothecin (CPT) sensitivity phenotypes in *rdh54*Δ haploid yeast strains. In addition to the serine/threonine to alanine mutations, we also tested the *rdh54K318R* allele which harbors a mutation in the Walker A box of Rdh54 preventing hydrolysis of ATP. We used this mutant because it has damage sensitivity phenotypes that are worse than the *rdh54*Δ strain (30). Most of the S to A mutations complemented the weak MMS and CPT phenotypes associated with the *rdh54*Δ (Figure 2.S1B). However, one mutant, *rdh54T851A*, failed to complement sensitivity to CPT and MMS (Figure 2.S1B).

To validate the screen, we integrated *rdh54T851A* into the genome by gene replacement and tested for MMS sensitivity. Because we were testing the potential impact of phosphorylation we also included *rdh54T851D*, *rdh54S852A*, *rdh54S852D*, and *rdh54T851A,S852A*. The S852 residue was included because it was the most highly phosphorylated site on the SuperPhos database and is also a part of a Rad53 consensus sequence. We measured sensitivity by scoring percent survival as compared to WT. Under the conditions used in our experiments WT strains had a survival percentage of 41.6 ± 7 (Figure 2.S2A). In contrast several Rdh54 mutants showed small but reproducible defects in survival. For the *rdh54T851A*, *rdh54T851D*, and *rdh54S852D* strains the survival percentages dropped to 25 ± 6, 25 ± 4, and 24 ± 5.6, respectively

(Figure 2.S2A). These values were comparable to the survival percentage of the *rdh54*Δ strains (26 ± 2). In contrast, the *rdh54S852A* and *rdh54T851A,S852A* alleles were not significantly different from the WT with 40 ± 4 and 48 ± 8 percent survival respectively (Figure 2.S2A). From this data we conclude that mutations in this region of Rdh54 can cause weak MMS sensitivities. We additionally validated that these mutants were expressed at comparable levels in cells by western blot (Figure 2.S2B).

2.2.2 Mutation of phosphorylation sites alters interhomolog recombination

Genetic experiments have implicated *RDH54* in regulating interhomolog (IH) gene conversion, and LOH outcomes (68,69). Therefore, we tested *rdh54T851A*, *rdh54T851D*, *rdh54S852A*, *rdh54S852D*, and *rdh54T851A,S852A* alleles for their ability to promote LOH gene conversion. We used an assay that measures the gene conversion frequency of two inactive *leu2* alleles (*leu2-Eco*RI and *leu2-Bst*EII) located on homologous chromosomes into an active *LEU2* gene (Figure 2.1B). The recombination outcomes that cause conversion to Leu + include the generation of a *LEU2*/*leu2-Eco*RI gene pair, the generation of a *LEU2*/*leu2-Bst*EII gene pair, or the generation of a *LEU2*/*leu2-Eco*RI-*Bst*EII gene pair (Figure 2.1B). This last outcome results from reciprocal exchange of DNA between chromosomes. There are other possible outcomes that can occur due to recombination between heteroalleles. These include non-reciprocal exchange of DNA that does not result in the formation of a *LEU2* allele and instead results in a *leu2-Eco*RI/*leu2-Eco*RI or *leu2-Bst*EII/*leu2-Bst*EII gene pair. Therefore, loss of Leu + frequency can be due to loss of gene conversion, or an increase in outcomes invisible to this assay. The frequency of conversion events is measured by comparing growth on selective and non-selective media. WT strains had a Leu + frequency of 1.03 ± 0.33 × 10^{-5} (Figure 2.1C and Table 2.S3) that was not significantly different from the *rdh54*Δ strains, which had a conversion frequency of 0.92 ± 0.5 × 10^{-5} (Figure 2.1C). In contrast, the *rdh54T851A* and *rdh54S852A* strains had a significant reduction in Leu + frequencies of 0.3 ± 0.19 × 10^{-5} and 0.44 ± 0.21 × 10^{-5}, respectively ($P < 0.0001$ and $P = 0.0004$). The two phosphomimic versions of Rdh54, *rdh54T851D* and *rdh54S852D*, were comparable to WT in conversion frequencies (0.9 ± 0.15 × 10^{-5} and 0.88 ± 0.19 × 10^{-5}, respectively) (Figure 2.1C). Surprisingly, the frequency observed for the *rdh54T851A,S852A* double mutant was 1.03 ± 0.44 × 10^{-5} and comparable to WT (Figure 2.1C). This suggests the *rdh54T851A,S852A* allele may be a compensatory mutation. From these data we conclude that *rdh54T851A* and *rdh54S852A*, alter recombination outcomes between homologous chromosomes.

We next asked which sub-population of HR outcomes were altered in mutant *rdh54* backgrounds. When using the homologous chromosome as a template for repair, LOH events can occur by both reciprocal (CO) and non-reciprocal (BIR) exchange of DNA sequences between chromosomes. *RDH54* reduces BIR outcomes and reduces CO frequency by a mutation to the Walker A box, *rdh54K318R* (26,62). We hypothesized that changes to interhomolog gene conversion induced by the *rdh54T851A* and *rdh54S852A* allele may result from an increase in BIR outcomes, or a decrease in CO outcomes resulting in reciprocal exchange. To test this hypothesis, we used a previously described genetic reporter assay that monitors LOH outcomes (45,76). The reporter is based on an *I-Sce1* site located in an inactive copy of the *ade2* gene on budding yeast

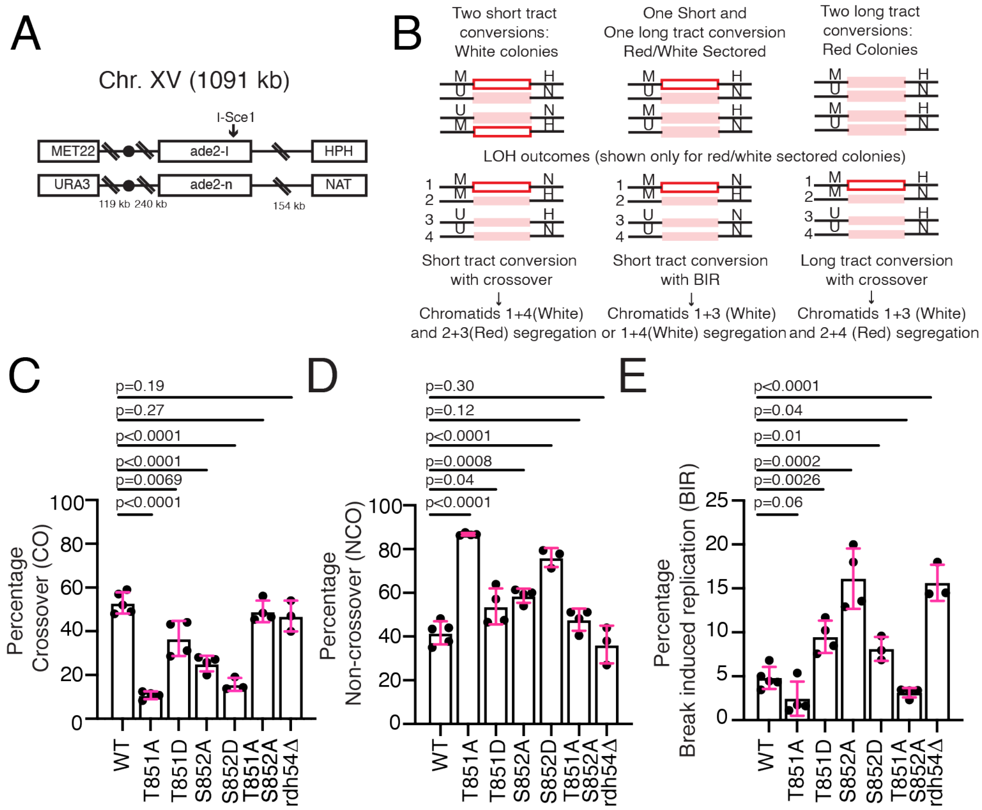

Figure 2.2: Rdh54 mutants have altered CO to NCO outcomes.

(A) Schematic diagram illustrating the configuration of the HR reporter assay used in our study to monitor HR outcomes. (B) Schematic diagram illustrating the potential outcomes from the induced *I-Sce1* double strand break. The assay can inform on LOH outcomes. (C) Percentage of HR outcomes that resulted in CO for WT, *rdh54T851A*, *rdh54T851D*, *rdh54S852A*, *rdh54S852D*, *rdh54T851A,S852A* and *rdh54*Δ. The bars represent the mean, and the error bars represent the standard deviation for three independent experiments and crosses. (D) Percentage of HR outcomes that resulted in NCO for WT, *rdh54T851A*, *rdh54T851D*, *rdh54S852A*, *rdh54S852D*, *rdh54T851A,S852A*, and *rdh54*Δ. The bars represent the mean, and the error bars represent the standard deviation for three independent experiments and crosses. (E) Percentage of HR outcomes that resulted in BIR for WT, *rdh54T851A*, *rdh54T851D*, *rdh54S852A*, *rdh54S852D*, *rdh54T851A,S852A*, and *rdh54*Δ. The bars represent the mean, and the error bars represent the standard deviation for at least three independent experiments and crosses. Statistical tests were performed using a two tailed *t*-test.

chromosome XV. The homologous chromosome has a different, but also inactive, allele of *ade2*. Upon *I-Sce1* induction with galactose both sister chromatids are cut, and repair occurs using the homologous chromosome as a template. Each homolog contains a different antibiotic marker located 154 kbp downstream of the break site (Figure 2.2A). Therefore, this assay can differentiate between long tract gene conversion (LTGC), short tract gene conversion (STGC), CO, NCO, and BIR outcomes associated with gene conversion events (45,76) (Figure 2.2A, B and Figure 2.S3A, B).

The clearest determinant of repair outcomes can be seen when one sister is repaired by STGC, and the other by LTGC, resulting in sectored colonies. These colonies have undergone the first chromosomal division after plating and provide the easiest interpretation of the genetic outcomes following the DSB. In our hands sectored colonies result in a near even distribution of CO to NCO outcomes and a small percentage of BIR outcomes. In contrast solid red or solid white colonies result in a majority NCO outcomes (62). This makes it more difficult to determine if there are significant changes in the population of reciprocal and non-reciprocal exchange outcomes. In this study, our specific question was whether there was a change in the ratio of CO:NCO:BIR in Rdh54 mutants. The sectored colonies represent a genetically sensitive population to answer this question. Therefore, we are reporting only outcomes for red/white sectored colonies.

We observed no difference in the ratio of LTGC versus STGC in any of the Rdh54 mutant alleles (Figure 2.S3B). However, most of the alleles tested did have changes in the distribution of HR outcomes (Figure 2.2C, D, E and Table 2.S4). A general reduction in CO outcomes was observed in *rdh54T851A* (10 ± 1.7%, $P < 0.0001$), *rdh54T851D* (36.7 ± 8%, $P = 0.0069$), *rdh54S852D* (16.9 ± 3.4%, $P < 0.0001$), and *rdh54S852A* (25.2 ± 3.6%, $P < 0.0001$) as compared to WT (53 ± 10%) (Figure 2.2C). Surprisingly, the *rdh54T851A,S852A* allele was again compensatory and there was no significant difference in CO outcomes relative to the WT. There was also an increase in NCO outcomes associated with most of these alleles. In the case of the *rdh54T851A* allele (86.7 ± 0.5%) the magnitude of this change was proportional to the loss of CO outcomes (Figure 2.2D). With *rdh54T851D* (53.7 ± 8%, $P = 0.03$), *rdh54S852A* (58.6 ± 3.2%, $P = 0.0008$), and *rdh54S852D* (76.1 ± 4.2%, $P < 0.0001$) these changes were also accompanied by an increase in BIR outcomes (Figure 2.2E). The magnitude of the increase in BIR was greatest in the *rdh54S852A* strain (16.1 ± 3.4%, $P < 0.0001$), with smaller changes in *rdh54T851D* (9.4 ± 1.8%, $P = 0.0026$) and *rdh54S852D* (9.4 ± 2.8%, $P = 0.01$). The change in the *rdh54S852A* mutant was comparable to the *rdh54*Δ strains (Figure 2.2E). The *rdh54T851A,S852A* was compensatory in all cases and indistinguishable from WT. From these data we conclude that the T851 and S852 residues in Rdh54 constitutes an important site during HR that can regulate exchange of information between chromosomes.

For BIR events to be observed in the red/white assay a distal antibiotic marker needs to be copied (Figure 2.2A). Therefore, BIR of >150 kbp is required to produce a BIR positive colony. DNA template switching is a DNA repair outcome that is associated with BIR in which the DNA being replicated moves to a site of new homology between chromosomes (70). This is believed to be widespread in meiotic recombination (77) and can occur frequently between homologous chromosomes. Importantly, *RDH54* has been implicated in template switching (70,71). We previously proposed that an increase in BIR observed in a *rdh54*Δ strain could result from a loss in DNA template switching during the BIR reaction. This could be caused by more processive BIR which fails to switch templates more frequently copying the necessary distal antibiotic marker. We reasoned that if this were true then there would also be a loss of template switching associated with the *rdh54S852A* allele.

To test this, we used a previously characterized yeast strain (70) that was designed to test template switching outcomes during BIR by reconstitution of a *URA3* marker located at three distinct sites on chromosome III (70) (Figure 2.S4A). DSBs were induced by overexpression of the HO nuclease leading to cleavage of a unique HO site. The frequency of Ura + cells was measured for WT, *rdh54T851A*, *rdh54T851D*, *rdh54S852A*, *rdh54S852D*, and *rdh54T851A,S852A* strains. A Ura + frequency of $0.45 \pm 0.13 \times 10^{-2}$ was measured for the WT strain. This is consistent with previous reports (70) and served as a reference for comparison with the Rdh54 mutants. The *rdh54*Δ strain had a Ura + frequency of $0.08 \pm 0.02 \times 10^{-2}$, a roughly 5.5-fold reduction from WT. There was also significant reduction in Ura + frequency observed in the *rdh54T851A* strain ($0.18 \pm 0.02 \times 10^{-2}$ Ura +, $P < 0.0001$), a 2.5-fold reduction from WT. Surprisingly, there was no significant reduction in template switching observed for *rdh54T851D*, *rdh54S852A*, *rdh54S852D*, or *rdh54T851A,S852A* strains (Figure 2.S4B). This suggests that the observed increase in BIR associated with *rdh54S852A* is not due to a reduction in template switching activity, and that phosphorylation of the S852 residue in our reporter strain likely limits BIR initiation. We cannot rule out the possibility that the increase in BIR observed in the *rdh54*Δ strains stem from more processive BIR due to loss of template switching, and there is a difference between the null and *rdh54S852A* mutant in this instance, as occurs in other assays. In addition, we also conclude that the *rdh54T851A* allele shows a reduction in template switching that is not as severe as with the *rdh54*Δ strain. This could be caused by a general reduction in BIR outcomes in the *rdh54T851A* strain, as BIR was down relative to WT in the red/white assay but was not deemed statistically significant due to the overall low percentage of BIR outcomes in the WT strain (Figure 2.2E).

2.2.3 Biochemical analysis of Rdh54 mutants reveal physical changes in activity on dsDNA

To develop a biochemical hypothesis to understand how mutations in Rdh54 may be affecting the activity of Rdh54, we used the Alphafold2 predicted structure of Rdh54 to produce a molecular model of Rdh54 bound to a short fragment of dsDNA (Figure 2.3A). We aligned the Alphafold2 model of Rdh54 to an existing *Sulfolobus solfataricus* Snf2 DNA translocase structure bound to dsDNA (PDBID:1Z63) (78). Because the *S. solfataricus* crystal structure represents the open form of the enzyme, we also created a closed model of Rdh54 by rotating one of the RecA domains (Figure 2.S5) using the procedure from the original study (78). The closed form of the structure represents the active form of the enzyme (Figure 2.3A and Figure 2.S5). We were surprised to find that the T851 and S852 residues were located a large distance from the enzyme active site at the end of an alpha-helix predicted to extend along the dsDNA. The modelled structure of the alpha helix has a region of high confidence (90 > pLDDT > 70, cyan) at the C-terminal end, with less confidence predicted for the interior (70 > pLDDT > 50, yellow). Rdh54 is known to form an oligomer on dsDNA and the location of these two residues led us to the hypothesis that this region of Rdh54 may affect inter-subunit communication. To test this biochemically, we overexpressed and purified 6xHis-Rdh54 and 6xHis-Rdh54T851A, 6xHis-Rdh54T851D, 6xHis-Rdh54S852A, 6xHis-Rdh54S852D, 6xHis-Rdh54T851AS852A, as well as mCherry versions of each protein from *Escherichia coli* to measure ATP hydrolysis and single molecule activity on dsDNA. The 6xHis tag on this protein does not have detrimental effects on protein activity (28). Throughout this study we will use recombinant 6xHis-Rdh54. For simplicity we will omit using the 6xHis nomenclature in the remainder of the text.

2.2.4 Rdh54 is a functional oligomer

We used single molecule imaging to directly observe Rdh54-mCherry bound to dsDNA. Biochemically, Rdh54 forms a homo-oligomer both in solution, and when bound to dsDNA (61). To better understand the nature of Rdh54 homo-oligomers bound to dsDNA we used photobleaching measurements to determine the size and distribution of Rdh54 clusters bound to DNA (Figure 2.3C, D). For smaller groups of Rdh54-mCherry we counted individual photobleaching steps (Figure 2.3E). The most common size of clusters that could be measured directly contained a dimer of Rdh54 (59%, $N = 27$) (Figure 2.3E). The second most common (26%, $N = 27$) group contained four Rdh54 molecules. Groups of one and three units were also observed but occurred less frequently than the other groups (Figure 2.3E). The majority of Rdh54 formed larger clusters on the DNA that could not be directly measured by photobleaching. To estimate the size of these clusters, we measured the intensity drop associated with individual photobleaching event and created a distribution from this data. The distribution was used to generate a mean intensity for an individual fluorophore (Figure 2.3F). We then divided the measured intensities for Rdh54 clusters bound to DNA by the mean intensity to create an estimated number of Rdh54-mCherry molecules per cluster (Figure 2.3G, H). These measurements resulted in a large distribution of cluster sizes with a median value of 7.06 molecules per cluster for WT-Rdh54 ($N = 201$). We also measured cluster sizes for each of the Rdh54 mutants. We found there was no significant difference in cluster sizes between WT, and Rdh54T851A ($P = 0.14$), Rdh54T851D ($P = 0.28$), Rdh54S852D ($P = 0.08$), and Rdh54K318R ($P = 0.38$) (Figure 2.3H). In contrast, Rdh54S852A and Rdh54T851AS852A were significantly different, with median cluster sizes of 4.22 ($P < 0.0001$) and 5.1 ($P < 0.0001$), respectively (Figure 2.3H). From this data we conclude that Rdh54 forms clusters on dsDNA and that Rdh54S852A and Rdh54T851AS852A have reduced clustering activity.

To determine if clustering had functional consequences, we first determined if different populations of Rdh54 could mix within clusters by combining Rdh54-mCherry and Rdh54-GFP and directly visualizing the outcome via single molecule imaging. In these experiments we measured the percentage of co-localization and the translocation velocity along DNA. Rdh54-mCherry colocalized with Rdh54-GFP in 93% of cases (Figure 2.S6A, B, $n = 132/142$) indicating an interaction between the two populations of molecules. The mixed molecules co-translocated with a mean velocity of 68.5 ± 40.4 bp/s, a mean distance of 14.3 ± 8.8 kbp (Figure 2.S6C, D) and were indistinguishable from un-mixed Rdh54-mCherry ($N = 32$ and $N = 32$, $P = 0.13$ and $P = 0.22$, respectively). We next performed classic translocase poisoning experiments where we mixed an equal amount of WT protein with either Rdh54K318R or Rdh54T851A. The hypothesis was that if proteins within a cluster were functionally dependent on each other, then incorporating mutant versions of the protein would poison the WT protein and reduce

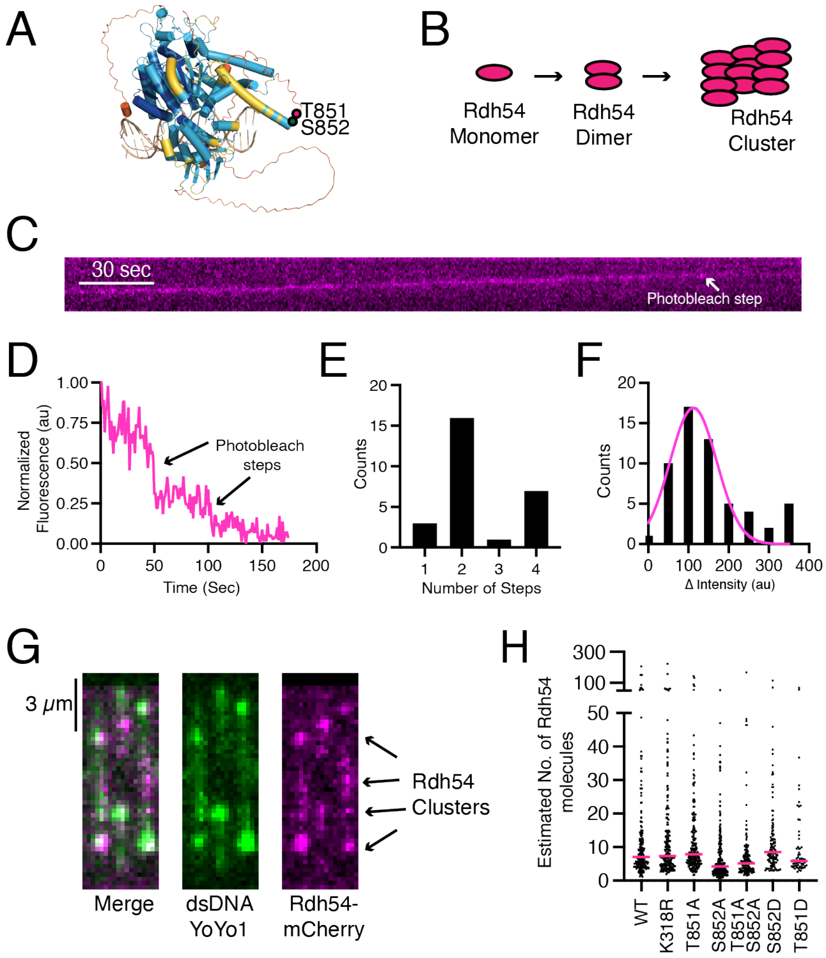

Figure 2.3: Rdh54 sequentially organizes into clusters on dsDNA.

(A) Alphafold2 generated model of Rdh54 bound to dsDNA. The color scheme represents the pLDDT format colored structural model of yRdh54 in a closed conformation. The AlphaFold2 per-residue confidence scores (pLDDT): very high confidence (pLDDT>90), dark blue; high confidence (90>pLDDT>70), cyan; low confidence (70>pLDDT>50), yellow; very low confidence (50>pLDDT), orange. DNA is shown in tan. The location of T851 (magenta) and S852 (green) are indicated by dots. The predicted structure was obtained from uniprot, and the model was generated using PDB:1Z63 and PDB:3PJR. (B) Cartoon diagram of expected assembly of Rdh54 into clusters. (C) Representative kymograph illustrating a translocating Rdh54-mCherry molecule photobleaching. (D) Representative trace showing the intensity loss associated with individual photobleaching steps. (E) Distribution of photobleaching steps observed for individual Rdh54 molecules bound to the DNA ($N = 27$). (F) Distribution of intensity drops associated with photobleaching events. The data are fit by a Gaussian distribution that was used to calculate the mean intensity drop per photobleaching event ($N = 57$). (G) Wide field microscopy images of individual dsDNA (YoYo1) molecules bound by

Rdh54-mCherry clusters. (H) Dot plot representing the distribution of the estimated sizes of Rdh54 clusters for WT (*N* = 201), Rdh54K318R (*N* = 205), Rdh54T851A (*N* = 197), Rdh54S852A (*N* = 214), Rdh54T851AS852A (*N* = 142), Rdh54S852D (*N* = 124), and Rdh54T851D (*N* = 68). The magenta line represents the median of the data. Statistical tests were performed using Mann-Whitney non-parametric tests.

the velocity of the cluster. When we mixed an equal molar amount of Rdh54-mCherry with unlabeled Rdh54K318R, the mean velocity of the total population was reduced to 30.7 ± 20 bp/s ($N = 62$, $P < 0.0001$), representing a significant change from WT (Figure 2.S6C, D). This is consistent with interdependency of Rdh54 subunits with the cluster. We also observed reduced rates of translocation (23 ± 16 bp/s, $N = 31$, $P < 0.0001$) (Figure 2.S6C, D) when unlabeled Rdh54T851A was mixed with equimolar amounts of WT. These data support an oligomeric motor configuration of Rdh54 in which translocation is contingent on the composition of the cluster.

Next, we reasoned that if cluster formation had an impact on HR outcomes, then strains that were heterozygous for *rdh54k318R* and *rdh54T851A* alleles would have altered CO/NCO ratios. We chose to test CO/NCO ratios because this was the most significant difference we observed in our initial experiments and would likely be sensitive enough to detect even a partial change in outcomes. We performed red/white recombination experiments with *RDH54:rdh54K318R* and *RDH54:rdh54T851A* strains. We found that the *RDH54:rdh54K318R* had a reduction in CO (27.3 ± 4.0% versus 53 ± 10%, $P = 0.005$) in favor of NCO (67.9 ± 6% versus 41 ± 10%, $P = 0.004$) outcomes. Likewise, there was a reduction in CO (34 ± 9% versus 53 ± 10%, $P = 0.002$) and an increase in NCO outcomes (64.2 ± 7% versus 41 ± 10%, $P = 0.003$) in the *RDH54:rdh54T851A* strain (Figure 2.S6E). From these data we conclude that Rdh54 forms biologically active

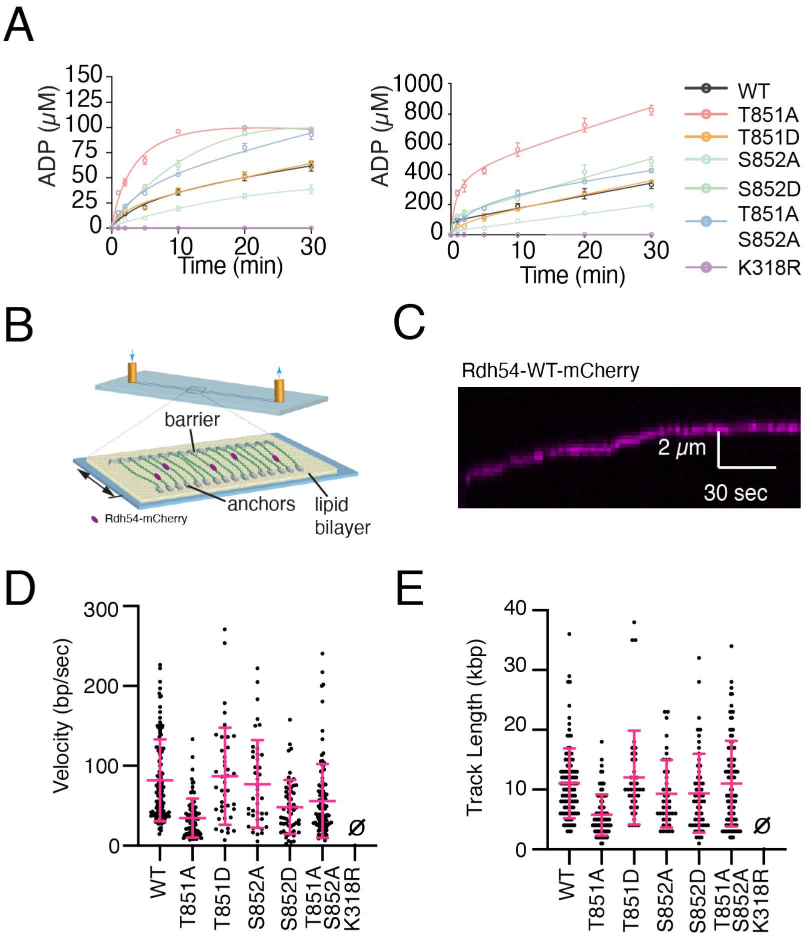

Figure 2.4: Mutations in Rdh54 result decoupling of ATP hydrolysis from translocation.

(A) ATP hydrolysis activity for Rdh54, Rdh54T851A, Rdh54T851D, Rdh54S852A, Rdh54S852D, Rdh54T851AS852A, and Rdh54K318R at a total ATP concentration of 100 µM (Left) and 1000 µM (Right). The points equal the mean, and the error bars the standard deviation of three independent experiments. (B) Schematic diagram illustrating DNA curtains setup, a single molecule approach that allows measurement of Rdh54-mCherry velocity and track length. (C) Representative kymograph illustrating the translocation of Rdh54-mCherry along dsDNA. (D) Translocation velocities (bp/sec) for individual translocation events of Rdh54 (*N* = 110), Rdh54T851A (*N* = 81), Rdh54T851D (*N* = 40), Rdh54S852A (*N* = 42), Rdh54S852D (*N* = 56), Rdh54T851AS852A (*N* = 101), and Rdh54K318R. The crossbar represents the mean of the data, and the error bar represents the standard deviation of the experiment. (E) Track lengths (kbp) for individual translocation events of Rdh54 (*N* = 110), Rdh54T851A (*N* = 81), Rdh54T851D (*N* = 40), Rdh54S852A (*N* = 42), Rdh54S852D (*N* = 56), Rdh54T851AS852A (*N* = 101), and Rdh54K318R. The crossbar represents the mean of the data, and the error bars represent the standard deviation of the data.

clusters during DNA damage response that are likely modulated by inter-subunit communication.

2.2.5 Mutations in Rdh54 result in de-coupling of ATP hydrolysis from translocation

Next, we measured the biochemical activity of the Rdh54 mutants. We initially measured the ATP hydrolysis activity at 100 and 1000 μM ATP concentrations (Figure 2.4A). In both cases we found that WT and Rdh54T851D produced the same amount of ADP at all time points measured. In contrast, the Rdh54S852A mutant produced less ADP indicating a defect in ATP hydrolysis. The opposite effect was observed for the Rdh54T851A which produced higher levels of ADP than WT at all time points (Figure 2.4A). Like the Rdh54T851A mutant, the Rdh54S852D and Rdh54T851AS852A mutants produced a greater amount of ADP over the time course. However, this difference was not as severe as that observed for the Rdh54T851A mutant (Figure 2.4A). From this data we conclude that mutations in this region of Rdh54 alter ATP hydrolysis activity.

We used single molecule imaging (Figure 2.4B), to measure the movement of Rdh54 along dsDNA (Figure 2.4B, C). For WT Rdh54-mCherry, we measured a translocation velocity of 81.7 ± 51 bp/s ($N = 110$), and a track length of 12.1 ± 7.1 kbp ($N = 110$) (Figure 2.4D, E). Both observations are consistent with previous measurements made in different laboratories (60,61). For the Rdh54T851A mutant we observed a reduction in both mean velocity (35.4 ± 26 bp/s, $N = 81$, $P < 0.0001$) and mean track length (5.1 ± 3.0 kbp, $N = 81$, $P < 0.0001$). In contrast, the Rdh54T851D mutant was not different from WT in either mean velocity (86 ± 60 bp/s, *N* = 40, *P* = 0.877) or mean track length (12.0 ± 7.8 kbp, *N* = 40, *P* = 0.9), consistent with the results from the ATP hydrolysis experiments. The reduction in velocity of the Rdh54T851A mutant and the increase in ATP hydrolysis is consistent with a less efficient coupling of ATP hydrolysis to translocation. The Rdh54S852A mutant translocated with a mean velocity of 77 ± 54 bp/s (*N* = 41) and a mean track length of 9.3 ± 5.6 kbp (*N* = 41). These values were not significantly different from the WT and suggest a mutant which is more efficient at coupling ATP hydrolysis to translocation. In contrast, Rdh54S852D had a significant decrease in velocity (48.3 ± 33.3 bp/s, *N* = 60, *P* < 0.0001) and a small decrease in track length (9.3 ± 6.5 kbp, *N* = 60, *P* = 0.03) relative to WT (Figure 2.4D, E). When combined with the ATP hydrolysis results, the S852A and S852D mutants have inverse behaviors relative to WT, and this change is consistent with altered coupling of ATP hydrolysis to translocation. Finally, we tested the activity of the Rdh54T851AS852A mutant. We found this mutant had higher mean velocity (55 ± 46 bp/s) than the Rdh54T851A single mutant but was still significantly less than WT (*P* <0.0001, *N* = 101). We saw an insignificant difference in track length (11.0 ± 7.1 kbp, *P* = 0.34) (Figure 2.4D, E) compared to the WT. This mutant was interesting because it has translocation defects like the Rdh54T851A mutant, but it has reduced clustering capacity like the Rdh54S852A mutant. These data suggest that the compensatory phenotypes observed in cells are an averaging effect caused by defects associated with each individual mutant. Together our data suggests that mutations in this region of Rdh54 lead to altered biochemical activity on dsDNA that may be due to changes in inter-subunit communication.

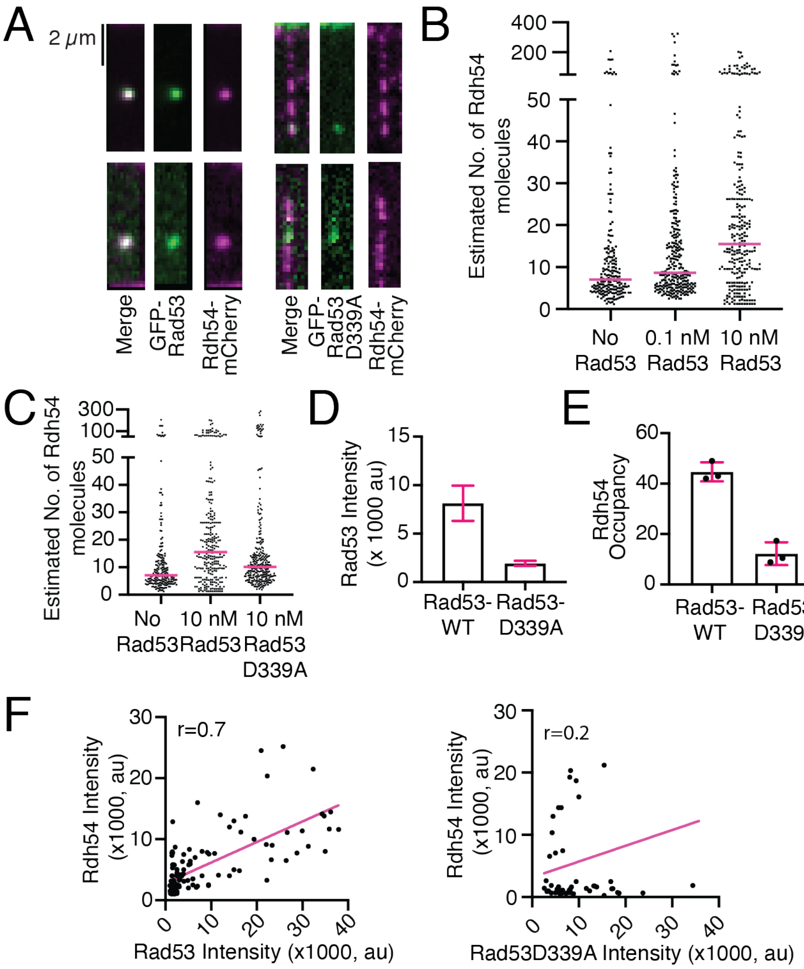

Figure 2.5: Phosphorylated Rad53 preferentially interacts with Rdh54 clusters.

(A) Widefield TIRF microscope images of individual DNA molecules bound by Rdh54-mCherry with GFP-Rad53 (Left) and Rdh54-mCherry with GFP-Rad53D339A (Right). (B) Dot plot representing the distribution of estimated sizes of Rdh54-mCherry clusters bound to DNA with no GFP-Rad53 (*N* = 201), 0.1 nM GFP-Rad53 (*N* = 273), and 10 nM GFP-Rad53 (*N* = 262). The crossbar represents the median of the data. (C) Dot plot representing the distribution of estimated sizes of Rdh54-mCherry clusters bound to DNA in a population. Including No GFP-Rad53 (*N* = 201), 10 nM GFP-Rad53 (*N* = 262) and 10 nM GFP-Rad53D339A (*N* = 282). The magenta line equals the median of the data. (D) Graph representing the signal intensity for GFP-Rad53 and GFP-Rad53D339A bound to Rdh54-mCherry. The bar represents the mean of the data, and the error bars represent the 95% confidence interval of the distribution. (E) A graph representing the percentages of Rdh54-mCherry clusters occupied by GFP-Rad53 and GFP-Rad53D339A. The bar represents the mean, and the error bar represents the standard deviation of at least three independent experiments. (F) Graph representing the correlation of intensity measurements for Rdh54-mCherry with Rad53-WT. The WT in B and C is reproduced from Figure 2.3.

2.2.6 Rad53 forms a physical interaction with Rdh54

The Rdh54S852 residue is part of a consensus Rad53 phosphorylation site, and previous reports genetically link the kinase Rad53 to phosphorylation of Rdh54 (59). However, a direct interaction between these proteins has not been observed. Rad53 is an auto-kinase that can phosphorylate copies of itself in trans (49). Because of this, it can be purified in a hyper-phosphorylated form from *E. coli* (52,79,80). Likewise, a single point mutant in Rad53, Rad53D339A, can eliminate kinase function and results in the purification of an inactive form of Rad53. To directly observe the interaction between Rdh54 and Rad53 we generated GFP-Rad53 and GFP-Rad53D339A constructs and purified them from *E. coli*. The GFP-Rad53 retains auto kinase function and can be purified in a phosphorylated form (Figure 2.S7A). We measured the interactions between GFP-Rad53/Rdh54-mCherry and observed direct and stable binding via single molecule imaging (Figure 2.5A). We next asked if there was an effect on Rdh54 cluster size in the presence of Rad53. We were surprised to find that the median estimated size of Rdh54 clusters was slightly larger at 0.1 nM Rad53 (7.0 versus 8.6, $P = 0.003$), and twice as large at 10 nM Rad53 (7.0 versus 15.5, $P < 0.0001$), suggesting that Rad53 may affect Rdh54 cluster size (Figure 2.5B). To determine if this was dependent on phosphorylation of Rad53 we measured the interaction between Rdh54-mCherry and GFP-Rad53D339A. We also observed a stable binding interaction between this pair (Figure 2.5A). We found that the effect of 10 nM GFP-Rad53D339A on Rdh54 cluster size was reduced (15.5 versus 10, $P < 0.0001$) (Figure 2.5C). This also corresponded with a reduced intensity of GFP-Rad53D339A bound to Rdh54 (Figure 2.5D) and a reduced percentage of Rdh54-mCherry clusters that were occupied by GFP-

Rad53D339A relative to WT (Figure 2.5E). Finally, we observed a strong correlation between the signal intensity of Rdh54-mCherry and GFP-Rad53 in the WT ($r = 0.7$), but only a weak correlation with the GFP-Rad53D339A mutant ($r = 0.2$, Figure 2.5F). This suggests that more molecules of Rdh54 per cluster resulted in more molecules of Rad53 binding. It should be noted that the inclusion of 10 nM GFP-Rad53D339A still resulted in larger clusters than Rdh54 alone. From these data we conclude that Rdh54 and Rad53 form an interaction that is independent of Rad53 phosphorylation. However, phosphorylation of Rad53 enhances the interaction with Rdh54. These data also identify a phosphorylation independent role of Rad53 in the growth of Rdh54 clusters.

We next evaluated whether there was an *in-situ* interaction between Rad53 and Rdh54 using a co-immunoprecipitation experiment. We used a strain of yeast with an HO inducible break that lacked a donor DNA sequence. We used this strain because it had previously been used to demonstrate a genetic interaction between Rad53 and Rdh54 (59). We found that there was an *in-situ* interaction between Rad53 and Rdh54, as predicted by our biochemical experiments (Figure 2.S8 and Figure 2.6A). This interaction was not dependent on DSB formation and formed both with and without galactose. We also tested the interaction between *rdh54T851A* or *rdh54S852A* and Rad53. We found that these mutants were able to interact with Rad53 in a galactose independent manner (Figure 2.6A). From these data we conclude that Rad53 and Rdh54 interact *in-situ*. Our co-immunoprecipitation experiments are non-quantitative, so we next evaluated the interaction between Rad53 and Rdh54T851A or Rdh54S852A *in vitro* using single molecule imaging. Not surprisingly, both proteins interacted with Rad53 (Figure 2.6C). For the Rdh54T851A mutant the resulting change in Rdh54 cluster size was comparable to WT (15.5 versus 12.1, $P = 0.50$). In contrast, the Rdh54S852A mutant had reduced cluster size (5.7 versus 15.5, $P < 0.0001$) (Figure 2.6C). This was comparable to the difference between WT-Rdh54 and the Rdh54S852A mutant in the absence of Rad53. However, we did observe that fewer clusters of the Rdh54S852A mutant were bound by Rad53 (Figure 2.6D). This was contrasted by the RdhT851A mutant which had more clusters with Rad53 bound than WT (Figure 2.6D). From these data we conclude that mutations in Rdh54 lead to an altered interaction with Rad53.

We next measured the ability of Rad53 to phosphorylate Rdh54 using an *in vitro* kinase assay. We found that Rad53 was able to directly phosphorylate Rdh54 *in vitro* (Figure 2.S7B). To further validate that phosphorylation was occurring at the T851/S852 site we performed *in vitro* phosphorylation with mass spectrometry. When we measured the recombinant Rdh54 alone we only observed a single phosphorylation mark both in the absence and presence of ATP (Table 2.S5), and this protein was not phosphorylated at S852. Likewise, only a single phosphorylation mark was observed when Rdh54 was treated with Rad53D339A (Table 2.S5). In contrast, WT-Rad53 phosphorylated Rdh54 at many sites. Many of these sites are likely non-specific because they were not identified by the Superphos database (Figure 2.S7C and Table 2.S5). However, we did identify four residues that were phosphorylated in both the SuperPhos database and in our *in vitro* assay. These sites included T851 and S852 (Figure 2.S7C and Table 2.S5). It should be noted that it is difficult to separate two adjacent potential phosphorylation sites via mass spectrometry, and the phosphorylation mark could be on T851 or S852. Based on these data we conclude that this region is being phosphorylated both *in vivo* and *in vitro*.

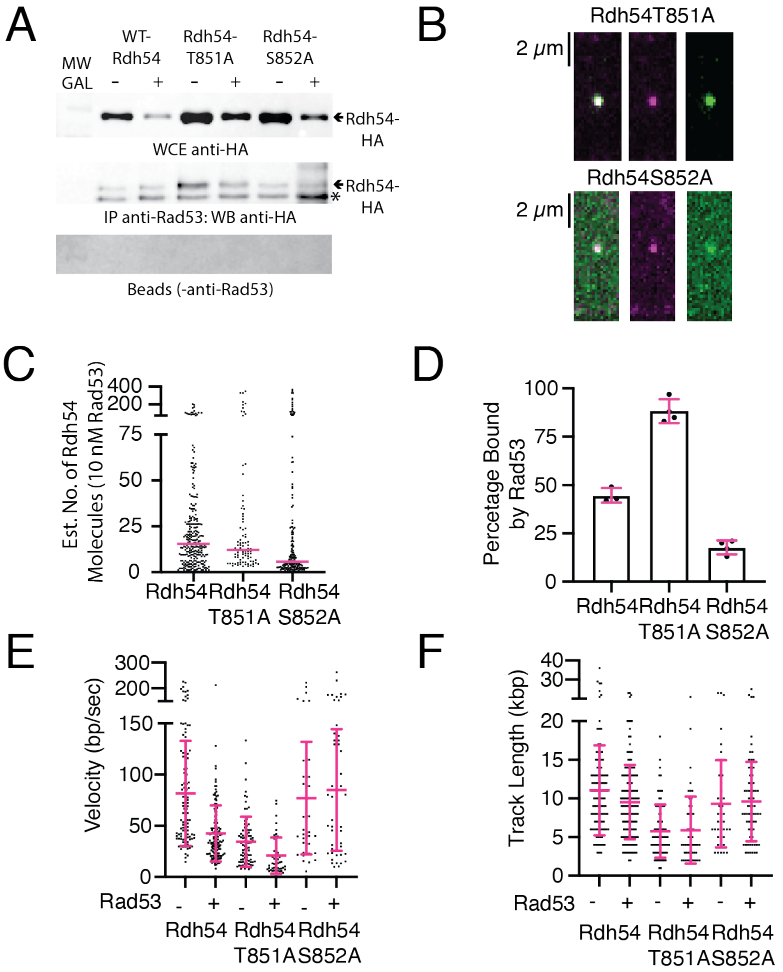

Figure 2.6: Interaction between Rad53 and Rdh54 affects translocation rates.

(A) Co-IP experiments showing an *in-situ* interaction between Rdh54 mutants and Rad53. Shown are WCE (Top), IP samples (Middle), and beads without antibodies (Bottom). * is an unspecific band that also appears in the -No HA tagged (Figure 2.S8). (B) Widefield TIRF microscope images illustrating the interaction between Rdh54T851A-mCherry (magenta) and GFP-Rad53 (green), and the interaction between Rdh54S852A-mCherry (magenta) and GFP-Rad53 (green). (C) Dot plot representing the estimated number of Rdh54 molecules in each cluster for WT (N = 262), Rdh54T851A-mCherry (N = 88), and Rdh54S852A-mCherry (N = 167) in the presence of 10 nM GFP-Rad53. The crossbar represents the median of the data. (D) Graph representing the percentage of Rdh54 clusters occupied by GFP-Rad53 for Rdh54-mCherry (N = 3), Rdh54T851A-mCherry (N = 4), and Rdh54S852A-mCherry (N = 4). The bars represent the mean, and the error bars represent the standard deviation of at least 3 independent experiments. The data for Rdh54-mCherry is reproduced from Figure 2.5. (E) Dot plot representing the velocity measurements for Rdh54-mCherry without (N = 110) and with Rad53 (N = 142), Rdh54T851A-mCherry without (N = 81) and with Rad53 (N = 49), and Rdh54S852A-mCherry without (N = 42) and with (N =

66) Rad53. The crossbar represents the mean of the data, and the error bars represent the standard deviation. (F) Dot plot representing the track length measurements for Rdh54-mCherry without (*N* = 110) and with Rad53 (*N* = 142), Rdh54T851A-mCherry without (*N* = 81) and with Rad53 (*N* = 49), and Rdh54S852A-mCherry without (*N* = 42) and with (*N* = 66) Rad53. The crossbar represents the mean of the data, and the error bars represent the standard deviation. In E and F, the (-) condition is reproduced from Figure 2.3.

Our single molecule data suggested that the phosphomimic mutant of S852, S852D was slow to translocate on DNA. We reasoned that we could directly test whether phosphorylation of the S852 residue caused a similar defect in translocation by incubating Rdh54, Rdh54T851A, or Rdh54S852A with catalytic amounts of Rad53 and monitoring translocation activity. By using phosphorylation site mutants of Rdh54 we could reduce the contribution of non-specific phosphorylation and focus on sites that were identified both *in vitro*, *in vivo*, and had phenotypic consequences. We therefore incubated Rdh54-mCherry, Rdh54T851A-mCherry, or Rdh54S852A-mCherry with catalytic amounts of Rad53 for 60 minutes prior to measuring the translocation velocity via single molecule imaging. Rdh54-mCherry moved with a velocity of 42 ± 21 bp/s (Figure 2.6E, *N* = 140). This was significantly ($P < 0.0001$) different from the translocation velocity of 81.7 ± 51 bp/s observed for untreated Rdh54-mCherry, and comparable to the translocation velocity observed for Rdh54S852D (48 ± 33.7 bp/s). The translocation length for Rad53-treated Rdh54-mCherry (9.5 ± 4.5 kbp) (Figure 2.6F, *N* = 140) was only slightly lower than that observed for WT and was the same as Rdh54S852D. When we measured the velocities of Rdh54T851A-mCherry we found a reduction in velocity to 20 ± 17 bp/s as compared to Rdh54T851A-mCherry untreated (34 ± 24 bp/s, $P < 0.0001$) (Figure 2.6E). There was no difference in the track length

(Figure 2.6F). This is consistent with the T851 site not being the kinase site. However, when we measured the treated Rdh54S852A-mCherry we observed no difference in the translocation velocity along dsDNA (84.9 ± 57 bp/s, $N = 66$ versus 77 ± 54 bp/s, $N = 42$, $P = 0.48$) (Figure 2.6F), or track length on dsDNA as compared to untreated Rdh54S852A-mCherry (Figure 2.6E). Together these data suggest that phosphorylation of Rdh54 by Rad53 at the S852 site slows Rdh54 translocation velocity on dsDNA.

2.3 Discussion

In this study we investigated the regulation of the Rdh54 motor protein during homologous recombination. We identified a previously uncharacterized region of Rdh54 that is critical for function during HR. Mutations to this region caused changes in Rdh54 cluster formation on dsDNA, translocation along dsDNA, and interactions with the effector kinase Rad53. This region is a target of Rad53 whose phosphorylation of Rdh54 results in a reduction in translocation velocity on dsDNA. Importantly, mutants in this region have phenotypic consequences that result in changes in the distribution of LOH outcomes in yeast reporter strains. Based on these findings we present a model where the association and dissociation of Rdh54 clusters from HR repair foci are important for directing HR outcomes.

2.3.1 Mutations in the C-terminal region of Rdh54 alter structure and function

It has been known for several years that Rdh54 is recruited to HR foci by Rad51. This occurs through an interaction between Rad51 and the disordered N-terminal region of Rdh54 (28,30,81). The interaction is highly cooperative, and self-association of Rdh54 molecules likely contributes to its own recruitment (28). In our experiments we defined the size and distribution of self-associating Rdh54 clusters on dsDNA and linked this activity to genetic consequences. While most of the clustering activity is still likely to occur through the N-terminal domain, a single point mutant in the C-terminal region of the protein, S852A, led to a reduction in cluster sizes bound to dsDNA. Enzymatically Rdh54S852A was more efficient at coupling ATP hydrolysis to translocation on dsDNA. In contrast, conversion of this residue to aspartic acid (S852D), led to no changes in cluster size, but instead de-coupled ATP hydrolysis from translocation. We interpret these results to mean that the S852 residue in Rdh54 is regulating the coupling of ATP hydrolysis to translocation. Its connection to cluster size and ATP hydrolysis likely indicates that this interaction occurs in trans between adjacent subunits of Rdh54. By extension, this suggests that phosphorylation of this residue might regulate the crosstalk between adjacent Rdh54 subunits leading to an overall reduction in translocation velocity on DNA. It is unclear if phosphorylation also results from decoupling of ATP hydrolysis or if it alters the interaction between subunits.

When mutated to alanine the T851 residue has the most severe defect both *in vivo* and *in vitro* caused by significant de-coupling of ATP hydrolysis from translocation on dsDNA. There was no difference in Rdh54 cluster size in this mutant. In contrast, the phosphomimic version of this residue, T851D, had no discernable biochemical defect. Without a high-resolution structure it is difficult to determine how these mutations regulate cluster size and ATP hydrolysis rates. However, an attractive model is that Rdh54 may behave like other RecA proteins in forming a short filament along dsDNA. In this case adjacent protomers may form a shared active site like that observed in Rad51. There is evidence that Rad51 can be phosphorylated at the protomer-protomer interface which prevents binding to dsDNA (82). A similar mechanism may reduce translocation by regulating the coupling of ATP hydrolysis to movement.

Phenotypically mutations at T851 and S852 result in different outcomes during interhomolog recombination. We initially tested these mutants in an assay that measures interhomolog recombination between heteroalleles without induction of a break. Alanine substitutions at 851 and 852 sites caused reduced Leu + phenotypes. To determine the cause of these losses, we used a reporter assay that could differentiate between reciprocal and non-reciprocal exchange of information between chromosomes. We found that the T851A mutant had lost reciprocal exchange outcomes due to increases in NCO outcomes at the expense of CO outcomes. In contrast, BIR increased in the S852A mutant at the expense CO outcomes. These outcomes are consistent with a loss of Leu + gene conversion by a reduction in reciprocal exchange or an increase in BIR. We observed that S852D resulted in a reduction in CO outcomes but did not result in a reduction in Leu + conversion frequency. We believe that this is due to differences in the assays with the red/white assay potentially being more sensitive to smaller changes in protein function. For example, S852D still translocates along dsDNA at a higher rate than the T851A mutant, and therefore it is not surprising phenotypes associated with this mutant may be less severe. Likewise, we were unable to see any biochemical differences between Rdh54 and Rdh54T851D, and still saw a slight increase in BIR outcomes and increased MMS sensitivity. One possible reason for this is an alteration in the phosphorylation activity of the adjacent S852 residue. Alternatively, changes in this residue may alter Rdh54 oligomer structure or alter interactions with other proteins during HR based repair. It is also possible that the MMS phenotype is not truly reflective

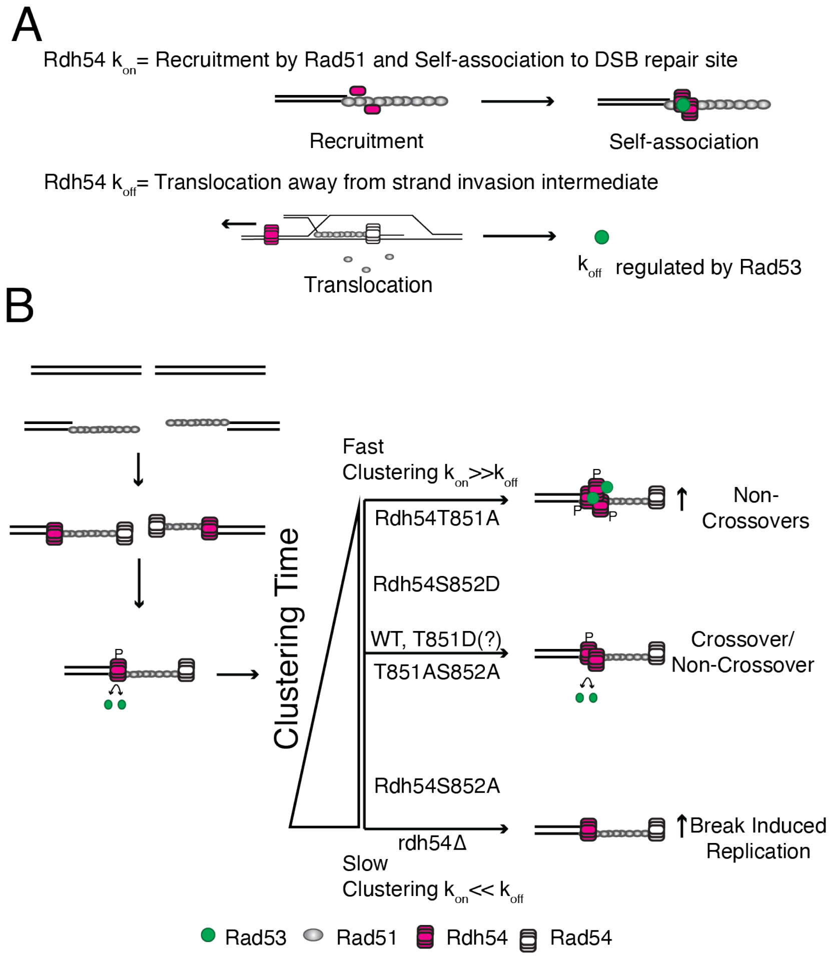

Figure 2.7: Model for the role of Rdh54 clustering in homologous recombination.

(A) A model illustrating components in the lifetime of Rdh54 at HR repair foci. The recruitment is initiated by Rad51, and there are additional contributions from the self-association of Rdh54. This is defined as the k_{on}. The k_{off} is defined as the rate of translocation away from strand invasion intermediates that occur during recombination. This step is regulated by Rad53 phosphorylation. Rad53 can also alter Rdh54 cluster size. (B) Model for biological output of Rdh54 clustering during HR. Our model suggests that fast clustering leads to the development of non-crossover outcomes. In contrast, slow clustering leads to increases in break induced replication. The rate of cluster formation is controlled by the on/off rate of the Rdh54 translocase from HR intermediates.

of HR repair outcomes and may represent a different function of Rdh54. If any of these outcomes are true, it does not alter our overall interpretation of the data.

Based on these data we propose a model in which the kinetic lifetime of Rdh54 at DNA repair foci helps determine recombination outcomes. The lifetime is controlled by the on-rate (k_{on}), which is a combination of recruitment of Rdh54 by Rad51and the self-association of Rdh54 molecules, and the off-rate (k_{off}), which is determined by how quickly Rdh54 translocates away from HR repair intermediates on dsDNA (Figure 2.7A). The off rate is regulated by Rad53 (see below). Based on our data this allows us to group our mutants into categories with the T851A and S852D mutants representing fast clustering mutants. The off rate for these mutants is significantly slower than WT and this results in fast clustering of Rdh54 and an increase in NCO outcomes during interhomolog recombination (Figure 2.7B). Likewise, the S852A mutant represents a mutant that is slow to cluster due to diminished cluster size and increased coupling of ATP hydrolysis to translocation. As discussed below, this mutant cannot be phosphorylated and that will prevent down regulation of translocation along dsDNA. This mutant will have a slow on-rate and fast off-rate leading to an increase in BIR, as is the case in the *rdh54*Δ where no clusters form (Figure 2.7B).

Importantly, we found that the *rdh54T851A,S852A* allele restored WT function in our genetic assays. Biochemically, this mutant exhibited reduced cluster formation, and a reduction in translocation velocity along DNA. However, this mutant was slightly better at cluster formation than the S852A mutant, and it was better at coupling hydrolysis to translocation than the T851A mutant. Finally, it cannot be phosphorylated due to the mutation at the S852 site. This leads to a combination of variables that likely average out to yield the equivalent of a WT protein *in vivo*. Put another way, the mutant protein likely has the same lifetime as the WT protein at HR repair foci (Figure 2.7B).

2.3.2 Rdh54 is directly connected to Rad53

Rdh54 is a target of the Mec1/Rad53 signaling axis (59), and physically interacts with the effector kinase Rad53. Once activated during the DNA damage response Rad53 phosphorylates itself through an interaction with Mrc1 at replication forks or through interactions with the Rad9 scaffold (46,53). Activated Rad53 can diffuse around the nuclear space and phosphorylates targets that slow down active repair processes to ensure genomic integrity. We were surprised to observe that Rdh54 formed a stable, direct interaction with Rad53. This interaction was not dependent on phosphorylation, but phosphorylated Rad53 did bind with higher frequency. Likewise, there was an increase in Rdh54 cluster size in the presence of Rad53. We observed that Rad53 preferentially interacted with larger clusters of Rdh54 and had a reduced interaction with Rdh54S852A. Together these data suggest that Rad53 may interact with Rdh54 through a complex set of interactions instead of at a specific domain interface. Functionally, site specific phosphorylation of Rdh54S852 slows the translocation velocity of Rdh54 along dsDNA, and a protein-protein interaction may physically enhance cluster size leading to two separate ways Rad53 can regulate Rdh54 cluster size or growth: a physical interaction that is phosphorylation independent, and downregulation of translocation activity which alters Rdh54's off-rate that is phosphorylation dependent.

It has previously been shown that Rad53 has the opposite effect on the size of Rad9 clusters in which phosphorylation of the Rad9-BRCT domain leads to reduction in Rad9 cluster size (83). It has been proposed that Rad53 activity may aid in coordinated reduction in Rad9 cluster size. Interestingly, *rad9*Δ strains exhibit a reduction in BIR (84). The opposite is true for Rdh54, and our model would predict that Rad53 may help grow Rdh54 cluster size through both enzymatic and non-enzymatic activities. This counteracts the occurrence of BIR. Larger clusters of Rdh54 may also help to trap Rad53 within a local environment reducing free diffusion, enhancing both Rad53 auto-phosphorylation as well as phosphorylation of Rdh54 and/or other proteins that may occupy similar three-dimensional space. This would create a feed forward mechanism where phosphorylation increases Rdh54 cluster size which could interact with more molecules of Rad53 that then undergo autophosphorylation. It has previously been shown that *rdh54K318R* leads to an accumulation of hyperphosphorylated Rad53 in yeast strains that lack a homologous donor sequence (59), suggesting that Rdh54 clusters may contribute to signal maintenance in this context. It is unclear what would counteract cluster growth and there is likely a missing component to this reaction that leads to diminishing cluster size once DNA repair has occurred. Interestingly, Rad54 has recently been implicated in the development and growth of Rad54 foci in cells, and it is possible that Rdh54 and Rad54 cluster growth is related as they can co-occupy Rad51 filaments during HR mediated repair (85). Ultimately, the interaction between Rad53 and Rdh54 appears to be important for regulation of HR outcomes.

A caveat of our study is that we cannot exclusively determine if the phenotypes observed in T851A and S852A mutants are due to defects in phosphorylation or whether they are simply defective enzymes. These two outcomes are not mutually exclusive, but future work will be needed to determine more conclusively which of these models is correct. Experiments to differentiate these models may include *in vivo* imaging of Rdh54 clusters in the presence or absence of Rad53, or more refined *in vitro* phosphorylation experiments. Ultimately, these mutants provide an interesting new class of Rdh54 mutants that provide new insight into its function during HR.

2.4 Conclusion

Here we present a model where the lifetime of Rdh54 at HR foci helps regulate genetic outcomes. In the *S. cerevisiae* model cluster formation is regulated by specific protein-protein interactions within Rdh54 and through an interaction with Rad53. However, this specific interaction may not be conserved in higher eukaryotes. The homolog of Rdh54 in higher eukaryotes is RAD54B. This homologous motor protein may regulate recombination outcomes through a similar clustering type mechanism that controls the on and off rate of this motor protein at HR repair centers. Interestingly, it has recently been shown that during meiosis in *C. elegans* RAD54-B is active when CHK2, a Rad53 homolog, is also active (86). Thus, even if specific interactions are not conserved, regulation is likely to be conceptually the same or at very least similar. Here we present a new model for the recruitment and regulation of Rdh54 during mitotic recombination between homologous chromosomes.

Data Availability Statement

The data in this manuscript is available upon request.

Acknowledgements

We would like to acknowledge Hannah Klein, Jim Haber, and Lorraine Symington for yeast strains used in this study. We would also like to thank Dirk Remus for the kind gift of the Rad53 overexpression plasmid. We would also like to acknowledge Eric Alani and Marcus Smolka for critical reading of the manuscript. We would also like to thank members of the Cornell R3 group and the Crickard laboratory for helpful input during development of the project.

Author contributions

JH purified proteins, performed experiments, analyzed data, and helped with the writing of the manuscript. BF performed experiments, analyzed data, and helped with writing and editing of the manuscript. JD provided reagents and cloning support. JBC performed experiments, analyzed data, provided reagents, and wrote the manuscript with input from JH and BF. This work was supported by NIGMS R35142457 to JBC and Cornell Startup funds to JBC.

Table 2.S1: Yeast strain list.

Strains	Genotype	Source or reference
LSY-2202-15D (WT)	*MATa ade2-n his3::NatMX4 met22:klURA3*	*(Mazon et al. 2010)*
LSY-2205-11C (WT)	*MATalpha ade2-I lys2:GAL-ISCE1 his3:HphMX4*	*(Mazon et al. 2010)*
JBC0011 (15D)	*RDH54::RDH54-KanMX*	*(Keymakh et al. 2022)*
JBC0013 (11C)	*RDH54::RDH54-KanMX*	*(Keymakh et al. 2022)*
JBC0014 (15D)	*RDH54::rdh54K318R*	*(Keymakh et al. 2022)*
JBC0016 (11C)	*RDH54::rdh54K318R*	*(Keymakh et al. 2022)*
JBC0018 (15D)	*RDH54::rdh54T851A*	*This study*
JBC0020 (11C)	*RDH54::rdh54T851A*	*This study*
JBC0026 (15D)	*RDH54::rdh54S852A*	*This study*
JBC0028 (11C)	*RDH54::rdh54S852A*	*This study*
JBC0054 (15D)	*RDH54::rdh54S852D*	*This study*
JBC0060 (11C)	*RDH54::rdh54S852D*	*This study*
JBC0056 (15D)	*RDH54::rdh54T851D*	*This study*
JBC0062 (11C)	*RDH54::rdh54T851D*	*This study*
JBC0086 (15D)	*RDH54::rdh54T851AS852A*	*This study*
JBC0092 (11C)	*RDH54::rdh54T851AS852A*	*This study*
JBC0080 (15D)	*RDH54::HIS3*	*This study*
JBC0083 (11C)	*RDH54::HIS3*	*This study*
BY4741 (WT)		*Dharmacon*
BY4741	*rdh54Δ*	*Dharmacon*
HK663A-leu2-R1 (A)	*leu2-EcoRI RAD5+ ade2-1 can1-100 his3-11,15 trp1-1 ura3*	*(Klein H 1997)*
HK6793B-leu2BSTEII (alpha)	*leu2-BstEII RAD5+ ade2-1 can1-100 his3-11,15 trp1-1 ura3*	*(Klein H 1997)*
JBC206	*leu2-EcorI RAD5+ ade2-1 can1-100 his3-11,15 trp1-1::TRP1 ura3*	*This study*
JBC207	*leu2-BstEII RAD5+ ade2-1 can1-100 his3-11,15 trp1-1 ura3::URA3*	*This study*
JBC0174	*JBC206 RDH54::RDH54-KanMX*	*This study*
JBC0175	*JBC206 RDH54::rdh54T851A-KanMX*	*This study*
JBC0176	*JBC206 RDH54::rdh54T851D-KanMX*	*This study*
JBC0177	*JBC206 RDH54::rdh54S852A-KanMX*	*This study*
JBC178	*JBC206 RDH54::S852D-KanMX*	*This study*

JBC179	*JBC206 RDH54::rdh54T851AS852A-KanMX*	*This study*
JBC0180	*JBC207 RDH54::RDH54-KanMX*	*This study*
JBC0181	*JBC207 RDH54::rdh54T851A-KanMX*	*This study*
JBC0182	*JBC207 RDH54::rdh54T851D-KanMX*	*This study*
JBC0183	*JBC207 RDH54::rdh54S852A-KanMX*	*This study*
JBC0184	*JBC207 RDH54::S852D-KanMX*	*This study*
JBC0185	*JBC207 RDH54::rdh54T851AS852A-KanMX*	*This study*
JBC228	*JBC206 RDH54::KanMX*	*This study*
JBC229	*JBC207 RDH54::KanMX*	*This study*
yRA53	*MAT*a*::DEL Hocs::hisG uraD851 trp1DEL.63 leu2DEL.::KAN hmlDEL::hisG HMR::ADE3 ade3::GAL::Ho can1DEL::UR::Hocs::NAT, RA::LEU2, A3::TRP1*	*Anand et al 2014*
yRA163	*yRA53 RDH54::HPHMX*	*Anand et al 2014*
JBC0084	*yRA53 leu2::KAN::HPHMX*	*This study*
JBC0099	*JBC0084 RDH54::RDH54KanMX*	*This study*
JBC0100	*JBC0084 RDH54::rdh54T851A*	*This study*
JBC0101	*JBC0084 RDH54::rdh54T851D*	*This study*
JBC0102	*JBC0084 RDH54::rdh54S852A*	*This study*
JBC0103	*JBC0084 RDH54::rdh54S852D*	*This study*
JBC0162	*JBC0084 RDH54::rdh54T851AS852A*	*This study*
JKM179	*hoΔ hml::ADE1 MATα hmr::ADE1 ade1-110 leu2,3-112 lys5 trp1::hisG ura3-52 ade3::GAL:HO*	*Kind gift from J. Haber*
JBC0144	*JKM179 RDH54::RDH54-3xHA-KanMX*	*This study*
JBC0146	*JKM179 RDH54::rdh54T851A-3xHA-KanMX*	*This study*
JBC0148	*JKM179 RDH54::rdh54T851D-3xHA-KanMX*	*This study*
JBC0152	*JKM179 RDH54::rdh54S852A-3xHA-KanMX*	*This study*
JBC0252	*JKM179 RDH54::rdh54S852D-3xHA-KanMX*	*This study*
JBC0164	*JKM179 RDH54::rdh54T851A,S852A-3xHA-KanMX*	*This study*
Diploid (JBC0011XJBC0013)	*RDH54::RDH54-KanMX/ RDH54::RDH54-KanMX*	*This study*
Diploid (JBC0011XJBC0016)	*RDH54::RDH54-KanMX /RDH54::rdh54K318R*	*This study*

Diploid (JBC0011XJBC0020)	*RDH54::RDH54-KanMX/ RDH54::rdh54T851A*	*This study*
Diploid (JBC0018XJBC0020)	*RDH54::rdh54T851A/ RDH54::rdh54T851A*	*This study*
Diploid (JBC0026X0028)	*RDH54::rdh54S852A/ RDH54::rdh54S852A*	*This study*
Diploid (JBC0054XJBC0060)	*RDH54::rdh54S852D/ RDH54::rdh54S852D*	*This study*
Diploid (JBC0056XJBC0062)	*RDH54::rdh54T851D/RDH54::rdh54T851D*	*This study*
Diploid (JBC0086XJBC0092)	*RDH54::rdh54T851AS852A/RDH54::rdh54T851AS852A*	*This study*
Diploid (JBC174XJBC180)	*RDH54::RDH54-KanMX/ RDH54::RDH54-KanMX*	*This study*
Diploid (JBC175XJBC181)	*RDH54::rdh54T851A/ RDH54::rdh54T851A*	*This study*
Diploid (JBC176XJBC182)	*RDH54::rdh54T851D/RDH54::rdh54T851D*	*This study*
Diploid (JBC177XJBC183)	*RDH54::rdh54S852A/ RDH54::rdh54S852A*	*This study*
Diploid (JBC178XJBC184)	*RDH54::rdh54S852D/ RDH54::rdh54S852D*	*This study*
Diploid (JBC179XJBC185)	*RDH54::rdh54T851AS852A/RDH54::rdh54T851AS852A*	*This study*
Diploid (JBC0080XJBC0083)	*RDH54::HIS3/RDH54::HIS3*	*This study*
Diploid (JBC228XJBC229)	*RDH54::KanMX/RDH54::KanMX*	*This study*

Table 2.S2: Plasmid list.

Plasmid backbone	**Construct**	Source
pET15	6xHis-Rdh54-WT	This study
pET15	6xHis-Rdh54K318R	This study
pET15	6xHis-Rdh54T851A	This study
pET15	6XHis-Rdh54T851D	This study
pET15	6xHis-Rdh54S852A	This study
pET15	6xHis-Rdh54S852D	This study
pET15	6xHis-Rdh54T851AS852A	This study
pET15	6xHis-Rdh54-mCherry-WT	This study
pET15	6xHis-Rdh54-mCherryK318R	This study
pET15	6xHis-Rdh54-mCherryT851A	This study
pET15	6xHis-Rdh54-mCherryS852A	This study
pET15	6xHis-Rdh54-mCherryT851D	This study
pET15	6xHis-Rdh54-mCherryS852D	This study
pET15	6xHis-Rdh54-mCherryT851AS852A	This study
pRS415	*RDH54-WT*	This study
pRS415	*rdh54S21A*	This study
pRS415	*rdh54S167A*	This study
pRS415	*rdh54S387A*	This study
pRS415	*rdh54S621A*	This study
pRS415	*rdh54S790A*	This study
pRS415	*rdh54S791A*	This study
pRS415	*rdh54T851A*	This study
pRS415	*rdh54S852A*	This study
pRS415	*rdh54K318R*	This study
pRS415	*rdh54K318RT851A*	This study
pRS305	*RDH54-KanMX*	This study
pRS305	*rdh54T851A-KanMX*	This study
pRS305	*rdh54T851D-KanMX*	This study
pRS305	*rdh54S852A-KanMX*	This study
pRS305	*rdh54S852D-KanMX*	This study
pRS305	*rdh54K318R-KanMX*	This study
pRS305	*rdh54T851AS852A-KanMX*	This study
pET15	6xHis-Rad53	A kind gift from Dirk Remus
pET15	6xHis-Rad53D339A	A kind gift from Dirk Remus
pET15	6xHis-GFP-Rad53	This study
pET15	6xHis-GFP-Rad53D339A	This study

Table 2.S3: Results of interhomolog gene conversion assay.

Strain	Selective Media	Leu + Frequency (Total Population)
WT	345	1.00×10^{-5}
rdh54T851A:rdh54T851A	42	0.45×10^{-5}
rdh54T851D:rdh54T851D	54	1.25×10^{-5}
rdh54S852A:rdh54S852A	51	0.58×10^{-5}
rdh54S852D:rdh54S852D	243	0.77×10^{-5}
rdh54T851AS852A:rdh54T851AS852A	68	0.77×10^{-5}
rdh54:rdh54	258	1.00×10^{-5}

Table 2.S4: The sum of the homologous recombination types identified in red/white assay.

Strain	CO	NCO	BIR	Total	Chromosome Loss
WT	94	72	8	174	0
rdh54T851A:rdh54T851A	76	611	17	704	0
rdh54T851D:rdh54T851D	122	189	32	343	0
rdh54S852A:rdh54S852A	42	93	25	160	0
rdh54S852D:rdh54S852D	74	343	31	448	1
RDH54:rdh54T851A	64	125	7	196	0
RDH54:rdh54K318R	62	125	9	183	0
rdh54T851AS852A:rdh54T851AS852A	186	181	12	379	0

Table 2.S5: Phosphorylated residues identified by mass spectrometry.

		In vitro			
In vivo SuperPhos	Both	WT-Rad53	Rad53D339A	Rdh54 No Rad53 (-ATP)	Rdh54 No Rad53 (+ATP)
S19 (1)	S19	S19	S673	S158	S158
S51		T23			
S165		T28			
S386		T30			
S619		S48			
S790		T54			
S791		S169			
T851 (3)		S189			
S852 (57)		S194			
S901 (1)		T197			
		S456			
		S587			
		T637			
		T691			
		S692			
		S705			
		S738			
		S775			
		S846			
		T847			
		T849			
	T851	T851			
	S852	S852			
		S872			
	S901	S901			

Residues that were identified as phosphorylated after *in vitro* phosphorylation under several different conditions. Also included are residues that are identified from the SuperPhos database.

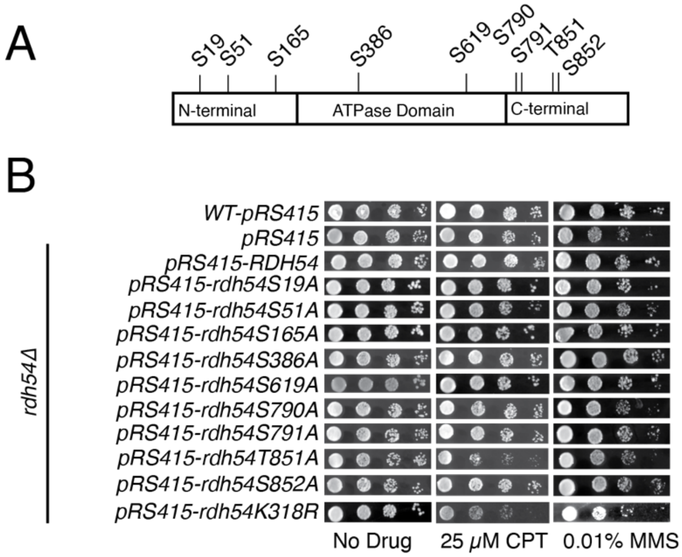

Figure 2.S1: *rdh54T851A* shows enhanced DNA damage phenotype.

(A) Schematic diagram illustrating Rdh54 phosphorylation site as identified by the database SuperPhos. All S/T were converted to A. (B) Yeast growth assays to measure the growth of different *RDH54* alleles in the presence of 25 μM CPT or 0.01% MMS.

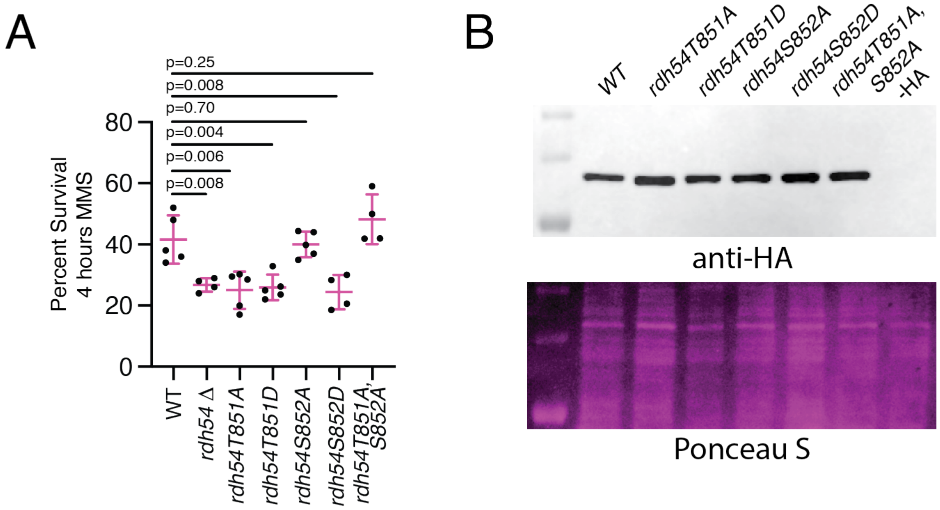

Figure 2.S2: *RDH54* mutants present MMS sensitivity.

(A) Graph representing the percent survival of strains treated with 0.01% MMS for 4 hours. The strains are WT (W303), *rdh54*Δ, *rdh54T851A*, *rdh54T851D*, *rdh54S852A*, *rdh54S852D*, and *rdh54T851A,S852A*. The bars represent the mean of the data, and the error bars represent the standard deviation of at least four independent experiments. P-values were generated using the students *t*-test. (B) Western blot of HA tagged versions of *RDH54*, *rdh54T851A*, *rdh54T851D*, *rdh54S852A*, *rdh54S852D*, and *rdh54T851A,S852A* that illustrates comparable expression.

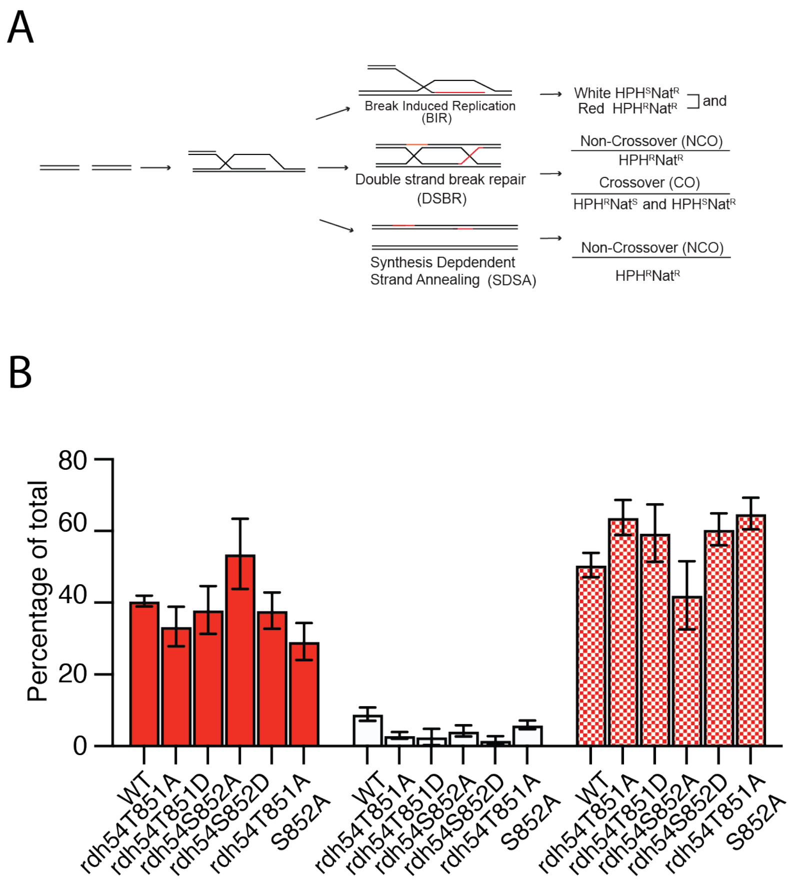

Figure 2.S3: *RDH54* mutants do not affect gene conversion.

(A) Schematic outcome depicting the HR outcomes that can be deduced from the red/white assay. These outcomes result in different levels of genetic exchange between chromosomes and are inferred from color and antibiotic sensitivity of specific sectors. (B) Bar graph illustrating the populations of solid red colonies (LTGC), solid white colonies (STGC), and mixed sectored colonies (One STGC/One LTGC). The bars represent the mean, and the error bars represent the standard deviation of at least three independent experiments.

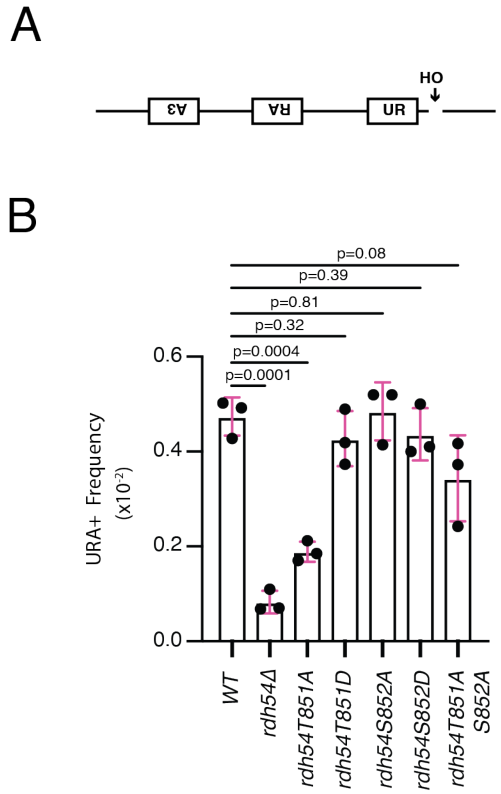

Figure 2.S4: *RDH54* mutants are also defective in DNA template switching.

(A) Template defining assay used to measure intrachromosomal template switching during DSBR. The completion of an intact *URA3* gene requires a template switch to occur during repair. (B) Measured Ura + frequency for *RDH54* WT and different alleles of *RDH54*. The bar represents the mean, and the error bars represent the standard deviation for three independent experiments. The P-values were generated by a two tailed *t*-test.

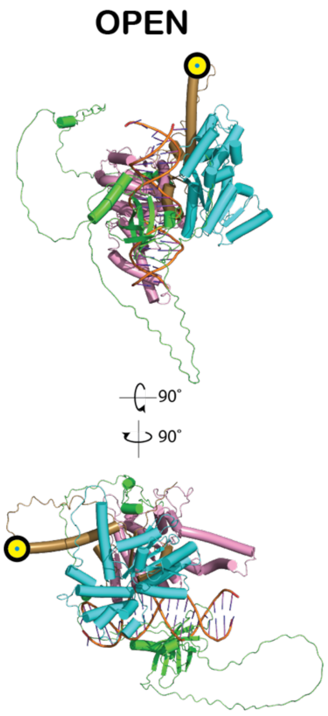

Figure 2.S5: Additional views of the open and closed models of yRdh54.

To generate the open and closed models of yRdh54, the two RecA-like domains in the AlphaFold predicted structure of yRdh54 (https://www.uniprot.org/uniprotkb/B3LN76) were individually superimposed onto the equivalent domains of either the *S. solfataricus* SWI2/SNF2 ATPase in the DNA-bound open state (PDB:1Z63), or AMP-PNP:DNA bound PcrA (PDB:3PJR) in the closed state. Most of the N-terminal domain of yRdh54 (green, residues: 1-261) is predicted to be unstructured (per-residue confidence (pLDDT) score < 50) and its position relative to other parts of the model cannot be interpreted. Lobe 1 (residues: 262-259), pink; lobe 2 (residues: 550-807), cyan; C-terminal domain (residues: 808-924), brown. The position of T851 is indicated with a yellow and cyan bullseye. DNA coordinates (orange) are from the *S. solfataricus* ATPase X-ray crystal structure (PDB:1Z63).

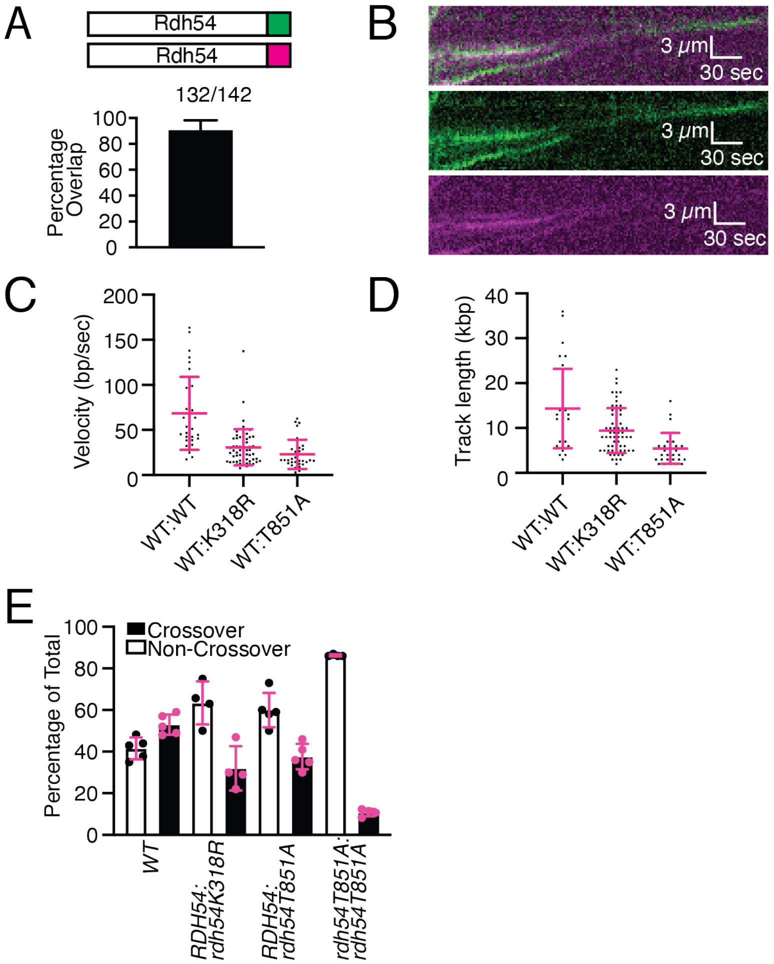

Figure 2.S6: Rdh54 forms a mixed oligomer during translocation.

(A) Schematic illustrating experiments performed with equal molar Rdh54-mCherry and Rdh54-GFP (Top). Graphical representation of the number of Rdh54-mCherry molecules that overlap with Rdh54-GFP molecules. The error bar represents the standard deviation of three independent experiments (Bottom). (B) Representative kymographs illustrating the co-translocation of Rdh54-mCherry and Rdh54-GFP molecules. The channels are merged (Top), magenta (Middle), and green (Bottom). (C) Dot plot representing the velocities (bp/sec) of mixed WT:WT (1:1) (N = 32), WT:Rdh54K318R (1:1) (N = 62), and WT:Rdh54T851A (1:1) (N = 31). The bar and the error bars represent the mean and standard deviation of the data. (D) Dot plot of the track lengths (kbp) of mixed WT:WT (1:1) (N = 32), WT:Rdh54K318R (1:1) (N = 62), and WT-Rdh54T851A (1:1) (N = 31). The bar and the error bars represent the mean and standard deviation of the data. (E) Percentage of CO and NCO outcomes for WT, *RDH54:rdh54K318R*, and *RDH54:rdh54T851A* strains. The bar represents the mean, and the error bars represent the standard deviation of four independent experiments from four different zygotes.

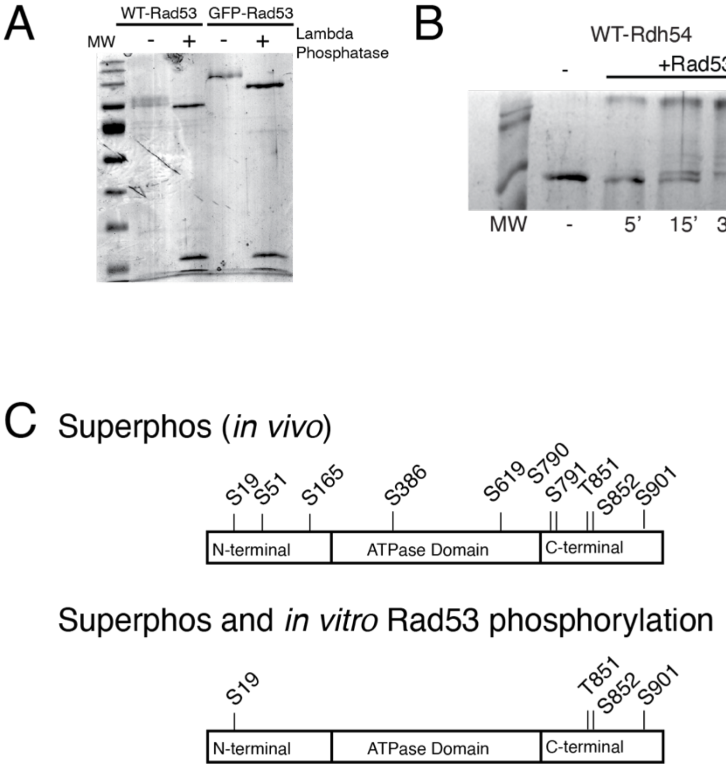

Figure 2.S7: Rdh54 directly interacts with and is a target of Rad53.

(A) Representative SDS-PAGE illustrating purified Rad53 and GFP-Rad53 with and without Lambda phosphatase illustrating that Rad53 and GFP-Rad53 are purified in their phosphorylated form. (B) SDS-PAGE phostag gel with un-phosphorylated Rdh54, and Rdh54 phosphorylated by Rad53 for 5’, 15’, and 30’. (C) Schematic diagram of phosphorylation sites identified in the SuperPhos database (Top, reproduced from Figure 2.S1 and Table 2.S5) and phosphorylation sites identified both from SuperPhos and from an *in vitro* kinase reaction with Rad53 (Bottom, the data can also be found in Table 2.S5).

A

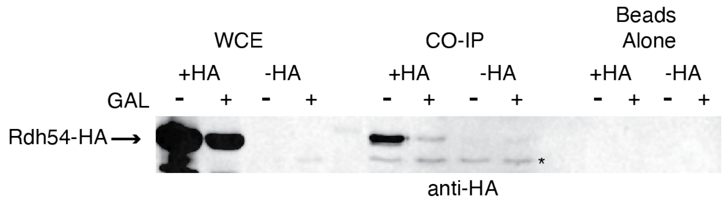

Figure 2.S8: Rdh54 co-immunoprecipitated with Rad53.

(A) Representative western blot illustrating the CO-IP of Rdh54-HA with Rad53. Samples shown are from strains with an HA tagged Rdh54 and NO HA tag on the Rdh54. For WCE, IP'd sample and Beads alone. * is an unspecific band.

References

1. Scully, R., Panday, A., Elango, R. and Willis, N.A. (2019) DNA double-strand break repair-pathway choice in somatic mammalian cells. *Nat. Rev. Mol. Cell. Biol.,* **20**, 698-714.

2. Wyman, C. and Kanaar, R. (2006) DNA double-strand break repair: all's well that ends well. *Annu. Rev. Genet.*, **40**, 363-383.

3. Mehta, A. and Haber, J.E. (2014) Sources of DNA double-strand breaks and models of recombinational DNA repair. *Cold Spring Harb. Perspect. Biol.*, **6**, a016428.

4. Szostak, J.W., Orr-Weaver, T.L., Rothstein, R.J. and Stahl, F.W. (1983) The double-strand-break repair model for recombination. *Cell*, **33**, 25-35.

5. Symington, L.S., Rothstein, R. and Lisby, M. (2014) Mechanisms and regulation of mitotic recombination in *Saccharomyces cerevisiae*. *Genetics*, **198**, 795-835.

6. Hunter, N. (2015) Meiotic recombination: the essence of heredity. *Cold Spring Harb. Perspect. Biol.*, **7**, a016618.

7. Filippo, J.S., Sung, P. and Klein, H. (2008) Mechanism of eukaryotic homologous recombination. *Annu. Rev. Biochem.*, **77**, 229-257.

8. Bell, J.C. and Kowalczykowski, S.C. (2016) RecA: regulation and mechanism of a molecular search engine. *Trends Biochem. Sci*, **41**, 491-507.

9. Kowalczykowski, S.C. (2015) An overview of the molecular mechanisms of recombinational DNA repair. *Cold Spring Harb. Perspect. Biol.*, **7**, a016410.

10. Greene, E.C. (2016) DNA sequence alignment during homologous recombination. *J. Biol. Chem.*, **291**, 11572-11580.

11. Haber, J.E. (2018) DNA repair: the search for homology. *BioEssays*, **40**, 1700229.

12. Renkawitz, J., Lademann, C.A. and Jentsch, S. (2014) Mechanisms and principles of homology search during recombination. *Nat. Rev. Mol. Cell Biol.*, **15**, 369-383.

13. Renkawitz, J., Lademann, C.A., Kalocsay, M. and Jentsch, S. (2013) Monitoring homology search during DNA double-strand break repair *in vivo*. *Mol. Cell*, **50**, 261-272.

14. Mazloum, N. and Holloman, W.K. (2009) Second-end capture in DNA double-strand break repair promoted by Brh2 protein of *Ustilago maydis*. *Mol. Cell*, **33**, 160-170.

15. McIlwraith, M.J. and West, S.C. (2008) DNA repair synthesis facilitates RAD52-mediated second-end capture during DSB repair. *Mol. Cell*, **29**, 510-516.

16. Nimonkar, A.V., Sica, R.A. and Kowalczykowski, S.C. (2009) Rad52 promotes second-end DNA capture in double-stranded break repair to form complement-stabilized joint molecules. *Proc. Nat. Acad. Sci. U.S.A.*, **106**, 3077-3082.

17. Pham, N., Yan, Z., Yu, Y., Faria Afreen, M., Malkova, A., Haber, J.E. and Ira, G. (2021) Mechanisms restraining break-induced replication at two-ended DNA double-strand breaks. *EMBO J.*, **40**, e104847.

18. Mehta, A., Beach, A. and Haber, J.E. (2017) Homology requirements and competition between gene conversion and break-induced replication during double-strand break repair. *Mol. Cell*, **65**, 515-526.

19. Qi, Z., Redding, S., Lee, J.Y., Gibb, B., Kwon, Y., Niu, H., Gaines, W.A., Sung, P. and Greene, E.C. (2015) DNA sequence alignment by microhomology sampling during homologous recombination. *Cell*, **160**, 856-869.

20. Xu, J., Zhao, L., Xu, Y., Zhao, W., Sung, P. and Wang, H.W. (2017) Cryo-EM structures of human RAD51 recombinase filaments during catalysis of DNA-strand exchange. *Nat. Struct. Mol. Biol.*, **24**, 40-46.

21. Lisby, M., Barlow, J.H., Burgess, R.C. and Rothstein, R. (2004) Choreography of the DNA damage response: spatiotemporal relationships among checkpoint and repair proteins. *Cell*, **118**, 699-713.

22. Lisby, M. and Rothstein, R. (2015) Cell biology of mitotic recombination. *Cold Spring Harb. Perspect. Biol.*, **7**, a016535.

23. Roy, U., Kwon, Y., Marie, L., Symington, L., Sung, P., Lisby, M. and Greene, E.C. (2021) The Rad51 paralog complex Rad55-Rad57 acts as a molecular chaperone during homologous recombination. *Mol. Cell*, **81**, 1043-1057.

24. Sugawara, N., Wang, X. and Haber, J.E. (2003) *In vivo* roles of Rad52, Rad54, and Rad55 proteins in Rad51-mediated recombination. *Mol. Cell*, **12**, 209-219.

25. Mazin, A.V., Bornarth, C.J., Solinger, J.A., Heyer, W.D. and Kowalczykowski, S.C. (2000) Rad54 protein is targeted to pairing loci by the Rad51 nucleoprotein filament. *Mol. Cell*, **6**, 583-592.

26. Piazza, A., Shah, S.S., Wright, W.D., Gore, S.K., Koszul, R. and Heyer, W.D. (2019) Dynamic processing of displacement loops during recombinational DNA repair. *Mol. Cell*, **73**, 1255-1266.

27. Tavares, E.M., Wright, W.D., Heyer, W.-D., Le Cam, E. and Dupaigne, P. (2019) *In vitro* role of Rad54 in Rad51-ssDNA filament-dependent homology search and synaptic complexes formation. *Nat. Commun.*, **10**, 4058.

28. Crickard, J.B., Kwon, Y., Sung, P. and Greene, E.C. (2020) Rad54 and Rdh54 occupy spatially and functionally distinct sites within the Rad51-ssDNA presynaptic complex. *EMBO J.*, **39**, e105705.

29. Crickard, J.B., Moevus, C.J., Kwon, Y., Sung, P. and Greene, E.C. (2020) Rad54 drives ATP hydrolysis-dependent DNA sequence alignment during homologous recombination. *Cell*, **181**, 1380-1394.

30. Chi, P., Kwon, Y., Seong, C., Epshtein, A., Lam, I., Sung, P. and Klein, H.L. (2006) Yeast recombination factor Rdh54 functionally interacts with the Rad51 recombinase and catalyzes Rad51 removal from DNA. *J. Biol. Chem.*, **281**, 26268-26279.

31. Petukhova, G., Sung, P. and Klein, H. (2000) Promotion of Rad51-dependent D-loop formation by yeast recombination factor Rdh54/Tid1. *Genes. Dev.*, **14**, 2206-2215.

32. Kadyk, L.C. and Hartwell, L.H. (1992) Sister chromatids are preferred over homologs as substrates for recombinational repair in *Saccharomyces cerevisiae*. *Genetics*, **132**, 387-402.

33. Piazza, A., Bordelet, H., Dumont, A., Thierry, A., Savocco, J., Girard, F. and Koszul, R. (2021) Cohesin regulates homology search during recombinational DNA repair. *Nat. Cell Biol.*, **23**, 1176-1186.

34. Chen, J.-M., Cooper, D.N., Chuzhanova, N., Férec, C. and Patrinos, G.P. (2007) Gene conversion: mechanisms, evolution and human disease. *Nat. Rev. Genet.*, **8**, 762-775.

35. Hügel, A. and Wernert, N. (1999) Loss of heterozygosity (LOH), malignancy grade and clonality in microdissected prostate cancer. *Br. J. Cancer*, **79**, 551-557.

36. Moynahan, M.E. and Jasin, M. (1997) Loss of heterozygosity induced by a chromosomal double-strand break. *Proc. Natl. Acad. Sci. U.S.A.*, **94**, 8988-8993.

37. Nichols, C.A., Gibson, W.J., Brown, M.S., Kosmicki, J.A., Busanovich, J.P., Wei, H., Urbanski, L.M., Curimjee, N., Berger, A.C., Gao, G.F. et al. (2020) Loss of heterozygosity of essential genes represents a widespread class of potential cancer vulnerabilities. *Nat. Commun.*, **11**, 2517.

38. Ryland, G.L., Doyle, M.A., Goode, D., Boyle, S.E., Choong, D.Y.H., Rowley, S.M., Li, J., Australian Ovarian Cancer Study, G., Bowtell, D.D.L., Tothill, R.W. *et al*. (2015) Loss of heterozygosity: what is it good for? *BMC Med. Genomics*, **8**, 45-45.

39. Bzymek, M., Thayer, N.H., Oh, S.D., Kleckner, N. and Hunter, N. (2010) Double Holliday junctions are intermediates of DNA break repair. *Nature*, **464**, 937-941.

40. Kockler, Z.W., Osia, B., Lee, R., Musmaker, K. and Malkova, A. (2021) Repair of DNA breaks by break-induced replication. *Annu. Rev. Biochem.*, **90**, 165-191.

41. Kramara, J., Osia, B. and Malkova, A. (2018) Break-induced replication: the where, the why, and the how. *Trends Genet.*, **34**, 518-531.

42. Malkova, A. and Ira, G. (2013) Break-induced replication: functions and molecular mechanism. *Curr. Opin. Genet. Dev.*, **23**, 271-279.

43. Wu, X. and Malkova, A. (2021) Break-induced replication mechanisms in yeast and mammals. *Curr. Opin. Genet. Dev.*, **71**, 163-170.

44. Jinks-Robertson, S. and Petes, T.D. (2021) Mitotic recombination in yeast: what we know and what we don't know. *Curr. Opin. Genet. Dev.*, **71**, 78-85.

45. Ho, C.K., Mazón, G., Lam, A.F. and Symington, L.S. (2010) Mus81 and Yen1 promote reciprocal exchange during mitotic recombination to maintain genome integrity in budding yeast. *Mol. Cell*, **40**, 988-1000.

46. Waterman, D.P., Haber, J.E. and Smolka, M.B. (2020) Checkpoint responses to DNA double-strand breaks. *Annu. Rev. Biochem.*, **89**, 103-133.

47. Navadgi-Patil, V.M. and Burgers, P.M. (2011) Cell-cycle-specific activators of the Mec1/ATR checkpoint kinase. *Biochem. Soc. Trans.*, **39**, 600-605.

48. Chen, S.-h. and Zhou, H. (2009) Reconstitution of Rad53 Activation by Mec1 through Adaptor Protein Mrc1*. *J. Biol. Chem.*, **284**, 18593-18604.

49. Lee, S.J., Schwartz, M.F., Duong, J.K. and Stern, D.F. (2003) Rad53 phosphorylation site clusters are important for Rad53 regulation and signaling. *Mol. Cell. Biol.*, **23**, 6300-6314.

50. Mordes, D.A., Nam, E.A. and Cortez, D. (2008) Dpb11 activates the Mec1–Ddc2 complex. *Proc. Natl. Acad. Sci. U.S.A.*, **105**, 18730-18734.

51. Sanford, E.J., Comstock, W.J., Faça, V.M., Vega, S.C., Gnügge, R., Symington, L.S. and Smolka, M.B. (2021) Phosphoproteomics reveals a distinctive Mec1/ATR signaling response upon DNA end hyper-resection. *EMBO J.*, **40**, e104566.

52. Devbhandari, S. and Remus, D. (2020) Rad53 limits CMG helicase uncoupling from DNA synthesis at replication forks. *Nat. Struct. Mol. Biol.*, **27**, 461-471.

53. Alcasabas, A.A., Osborn, A.J., Bachant, J., Hu, F., Werler, P.J.H., Bousset, K., Furuya, K., Diffley, J.F.X., Carr, A.M. and Elledge, S.J. (2001) Mrc1 transduces signals of DNA replication stress to activate Rad53. *Nat. Cell Biol.*, **3**, 958-965.

54. Bacal, J., Moriel-Carretero, M., Pardo, B., Barthe, A., Sharma, S., Chabes, A., Lengronne, A. and Pasero, P. (2018) Mrc1 and Rad9 cooperate to regulate initiation and elongation of DNA replication in response to DNA damage. *EMBO J.*, **37**, e99319.

55. Agarwal, R., Tang, Z., Yu, H. and Cohen-Fix, O. (2003) Two Distinct Pathways for Inhibiting Pds1 Ubiquitination in Response to DNA Damage*. *J. Biol. Chem.*, **278**, 45027-45033.

56. Krishnan, V., Nirantar, S., Crasta, K., Cheng, A.Y. and Surana, U. (2004) DNA replication checkpoint prevents precocious chromosome segregation by regulating spindle behavior. *Mol. Cell*, **16**, 687-700.

57. Palou, R., Palou, G. and Quintana, D.G. (2017) A role for the spindle assembly checkpoint in the DNA damage response. *Curr. Genet.*, **63**, 275-280.

58. Schwartz, M.F., Lee, S.J., Duong, J.K., Eminaga, S. and Stern, D.F. (2003) FHA domain-mediated DNA checkpoint regulation of Rad53. *Cell Cycle*, **2**, 384-396.

59. Ferrari, M., Nachimuthu, B.T., Donnianni, R.A., Klein, H. and Pellicioli, A. (2013) Tid1/Rdh54 translocase is phosphorylated through a Mec1- and Rad53-dependent manner in the presence of DSB lesions in budding yeast. *DNA Repair (Amst.)*, **12**, 347-355.

60. Nimonkar, A.V., Amitani, I., Baskin, R.J. and Kowalczykowski, S.C. (2007) Single molecule imaging of Tid1/Rdh54, a Rad54 homolog that translocates on duplex DNA and can disrupt joint molecules. *J. Biol. Chem.*, **282**, 30776-30784.

61. Prasad, T.K., Robertson, R.B., Visnapuu, M.L., Chi, P., Sung, P. and Greene, E.C. (2007) A DNA-translocating Snf2 molecular motor: *Saccharomyces cerevisiae* Rdh54 displays processive translocation and extrudes DNA loops. *J. Mol. Biol.*, **369**, 940-953.

62. Keymakh, M., Dau, J., Hu, J., Ferlez, B., Lisby, M. and Crickard, J.B. (2022) Rdh54 stabilizes Rad51 at displacement loop intermediates to regulate genetic exchange between chromosomes. *PLoS Genet.*, **18**, e1010412.

63. Meir, A., Crickard, J.B., Kwon, Y., Sung, P. and Greene, E.C. (2022) Rad54 and Rdh54 prevent Srs2-mediated disruption of Rad51 presynaptic filaments. *Proc. Natl. Acad. Sci. U.S.A.*, **119**, e2113871119.

64. Shah, P.P., Zheng, X., Epshtein, A., Carey, J.N., Bishop, D.K. and Klein, H.L. (2010) Swi2/Snf2-related translocases prevent accumulation of toxic Rad51 complexes during mitotic growth. *Mol. Cell*, **39**, 862-872.

65. Shah, S.S., Hartono, S., Piazza, A., Som, V., Wright, W., Chédin, F. and Heyer, W.D. (2020) Rdh54/Tid1 inhibits Rad51-Rad54-mediated D-loop formation and limits D-loop length. *elife*, **9**, e59112.

66. Chi, P., Kwon, Y., Seong, C., Epshtein, A., Lam, I., Sung, P. and Klein, H.L. (2006) Yeast recombination factor Rdh54 functionally interacts with the Rad51 recombinase and catalyzes Rad51 removal from DNA*. *J. Biol. Chem.*, **281**, 26268-26279.

67. Santa Maria, S.R., Kwon, Y., Sung, P. and Klein, H.L. (2013) Characterization of the interaction between the *Saccharomyces cerevisiae* Rad51 recombinase and the DNA translocase Rdh54. *J. Biol. Chem.*, **288**, 21999-22005.

68. Shinohara, M., Shita-Yamaguchi, E., Buerstedde, J.M., Shinagawa, H., Ogawa, H. and Shinohara, A. (1997) Characterization of the roles of the *Saccharomyces cerevisiae* RAD54 gene and a homologue of RAD54, RDH54/TID1, in mitosis and meiosis. *Genetics*, **147**, 1545-1556.

69. Klein, H.L. (1997) RDH54, a RAD54 homologue in *Saccharomyces cerevisiae*, is required for mitotic diploid-specific recombination and repair and for meiosis. *Genetics*, **147**, 1533-1543.

70. Anand, R.P., Tsaponina, O., Greenwell, P.W., Lee, C.-S., Du, W., Petes, T.D. and Haber, J.E. (2014) Chromosome rearrangements via template switching between diverged repeated sequences. *Genes Dev.*, **28**, 2394-2406.

71. Tsaponina, O. and Haber, J.E. (2014) Frequent interchromosomal template switches during gene conversion in *S. cerevisiae*. *Mol. Cell*, **55**, 615-625.

72. Collins, B.E., Ye, L.F., Duzdevich, D. and Greene, E.C. (2014) In: Waters, J. C. and Wittman, T. (eds.), *Methods in Cell Biology*. Academic Press, Vol. **123**, pp. 217-234.

73. Crickard, J.B. (2023) Single molecule imaging of DNA-protein interactions using DNA curtains. *Methods Mol. Biol.*, **2599**, 127-139.

74. Lanz, M.C., Yugandhar, K., Gupta, S., Sanford, E.J., Faça, V.M., Vega, S., Joiner, A.M.N., Fromme, J.C., Yu, H. and Smolka, M.B. (2021) In-depth and 3-dimensional exploration of the budding yeast phosphoproteome. *EMBO Rep.*, **22**, e51121.

75. Sidorova, J.M. and Breeden, L.L. (2003) Rad53 checkpoint kinase phosphorylation site preference identified in the Swi6 protein of *Saccharomyces cerevisiae*. *Mol. Cell.* Biol., **23**, 3405-3416.

76. Klein, H.L., Bačinskaja, G., Che, J., Cheblal, A., Elango, R., Epshtein, A., Fitzgerald, D.M., Gómez-González, B., Khan, S.R., Kumar, S. et al. (2019) Guidelines for DNA recombination and repair studies: Cellular assays of DNA repair pathways. *Microb. Cell*, **6**, 1-64.

77. Ahuja, J.S., Harvey, C.S., Wheeler, D.L. and Lichten, M. (2021) Repeated strand invasion and extensive branch migration are hallmarks of meiotic recombination. *Mol. Cell*, **81**, 4258-4270.

78. Dürr, H., Körner, C., Müller, M., Hickmann, V. and Hopfner, K.P. (2005) X-ray structures of the *Sulfolobus solfataricus* SWI2/SNF2 ATPase core and its complex with DNA. *Cell*, **121**, 363-373.

79. McClure, A.W. and Diffley, J.F. (2021) Rad53 checkpoint kinase regulation of DNA replication fork rate via Mrc1 phosphorylation. *eLife*, **10**, e69726.

80. Gilbert, C.S., Green, C.M. and Lowndes, N.F. (2001) Budding Yeast Rad9 Is an ATP-Dependent Rad53 Activating Machine. *Mol. Cell*, **8**, 129-136.

81. Petukhova, G., Van Komen, S., Vergano, S., Klein, H. and Sung, P. (1999) Yeast Rad54 Promotes Rad51-dependent Homologous DNA Pairing via ATP Hydrolysis-driven Change in DNA Double Helix Conformation*. *J. Biol. Chem.*, **274**, 29453-29462.

82. Flott, S., Kwon, Y., Pigli, Y.Z., Rice, P.A., Sung, P. and Jackson, S.P. (2011) Regulation of Rad51 function by phosphorylation. *EMBO Rep.*, **12**, 833-839.

83. Usui, T., Foster, S.S. and Petrini, J.H.J. (2009) Maintenance of the DNA-Damage Checkpoint Requires DNA-Damage-Induced Mediator Protein Oligomerization. *Mol. Cell*, **33**, 147-159.

84. Ferrari, M., Rawal, C.C., Lodovichi, S., Vietri, M.Y. and Pellicioli, A. (2020) Rad9/53BP1 promotes DNA repair via crossover recombination by limiting the Sgs1 and Mph1 helicases. *Nat. Commun.*, **11**, 3181.

85. Ho, B., Sanford, E.J., Loll-Krippleber, R., Torres, N.P., Smolka, M.B. and Brown, G.W. (2023) Mec1-independent activation of the Rad53 checkpoint kinase revealed by quantitative analysis of protein localization dynamics. *eLife*, **12**, e82483.

86.Yamaya, K., Wang, B., Memar, N., Odiba, A.S., Woglar, A., Gartner, A. and V illeneuve, A.M. (2023) Disparate roles for *C. elegans* DNA translocase paralogs RAD-54.L and RAD-54.B in meiotic prophase germ cells. *Nucleic Acids Res.*, **51**, 9183–9202.

CHAPTER 3

Rad54 separation of function mutation highlights unique roles during homologous recombination

Chapter 3 is under review of *PLOS Genetics* with the same title.

Jingyi Hu[1], David Moraga[1], Amanda Xu[1], Lauren Peysakhova[1], and J. Brooks Crickard[1#]

[1.] Department of Molecular Biology and Genetics, Cornell University, Ithaca, NY 14853, USA

#To whom the correspondence should be addressed: jbc287@cornell.edu

Abstract

Homologous recombination (HR) is a DNA repair pathway that utilizes a template-based approach to repair double-strand breaks within the genome. Template utilization requires the exchange of individual DNA strands, which members of the RecA family of recombinases facilitate. Rad51 is a primary strand exchange factor in eukaryotes. During regular mitotic DNA repair, Rad51 is aided by the DNA translocase Rad54, which acts as a motor to remodel the template DNA and stabilize primary-strand exchange intermediates. The regulation of this activity remains incompletely understood. Here, we have identified a conserved site within the C-terminal region of Rad54. The mutation of this site creates a functional separation at early strand-exchange intermediates *in vivo*. Using this mutant protein, we identify a novel intermediate essential for stabilizing displacement loop (D-loop) structures. This precedes the removal of Rad51 and DNA extension. Based on our experiments, we hypothesize that this Rad54 mutant cannot stabilize Rad51-mediated strand-exchange intermediates because it cannot topologically isolate dsDNA regions. Identifying a mutant that disrupts this intermediate before Rad51 removal unifies existing models of Rad54-mediated D-loop formation and extension.

Keywords: Homologous Recombination, Rad51, Rad54, Strand exchange

3.1 Introduction

Homologous recombination (HR) is a DNA double-strand break repair (DSBR) pathway that uses a homologous template to prime DNA synthesis to repair breaks (1-5). In this pathway, ssDNA guides are formed by resection of the two ends of broken DNA (6-9). This DNA is known as the recipient DNA because it will receive information during the recombination reaction. Filaments of the RecA family of recombinases form on the recipient DNA (10-13). The filament guides a search of the genome for a matching DNA sequence (11,14-18). Once a suitable donor homology is identified, the recombinase filament initiates a strand exchange reaction that generates a three-stranded DNA joint known as a displacement loop (D-loop) (12,19,20). DNA polymerase can then initiate synthesis from the 3’ end of the recipient DNA and restore any lost information.

In the classic double-strand break repair pathway, resolution of DNA joints formed during HR can result in non-crossover outcomes (NCO) or crossover outcomes (CO). These outcomes are defined by the extent of genetic exchange between the donor and recipient, with CO outcomes resulting in greater exchange between the two DNA molecules (1,4). Resolution can also occur through synthesis-dependent strand annealing (SDSA). This pathway results in apparent NCO outcomes when the second end of the break is located and used to finish the repair. When the second end of the break is not located, SDSA can transition to Break-induced replication (BIR). This outcome can be extremely mutagenic, leading to complex genomic rearrangements and mosaic repair (21-23).

In eukaryotes, the mitotic RecA homolog is known as Rad51 (24,25), and during the homology search and subsequent transition to DNA synthesis, Rad51 is assisted by the DNA motor protein Rad54 (26-32). The basic biochemical properties of Rad54 are that it hydrolyzes ATP to physically move along double-stranded DNA by tracking the minor groove in the 3’-5’ direction (33). Multiple copies of Rad54 can function as single units, resulting in high processivity levels (27,29,32). The primary role of Rad54 is to act as an accessory cofactor for Rad51, and interactions between these proteins increase the motor output of Rad54 by 3 to 5-fold (29,34,35). The activities of Rad54 include the regulation of Rad51 at stalled or collapsed DNA replication forks (36), the removal of excess Rad51 that is pathogenically bound to dsDNA (37,38), the remodeling of nucleosomes (39-41), driving branch migration (35,42-45), collaboration with Rad51 to catalyze the formation of D-loops (19,29,32,46-48), and to grant accessibility of the 3’ end of the recipient DNA to DNA polymerase (47,49).

In vivo, Rad54 can promote Rad51 recombination activity through multiple mechanisms. One of these involves the removal of Rad51 from dsDNA and its stabilization on ssDNA (28,37,50-53), which aids in the maturation of recombinase filaments. Evidence for this stems from work involving the Rad51 Walker A mutant, Rad51K191R, which is deficient in filament formation *in vivo* (54). The overexpression of Rad54 can suppress the defect in this mutant, but only in the presence of Rad55/57 (55). Rad55/57 are required for efficient Rad51 filament formation and counteracting the effects of the Srs2 helicase (56-60), whose primary function during HR is to remove Rad51 from ssDNA (61-66). During Rad51 filament maturation, Rad54 can act by increasing the available pools of Rad51 and by physically protecting Rad51 filaments from Srs2 activity (53). Srs2 and Rad54 are synthetically lethal (67) and appear to compete during repair. This competition likely occurs before the alignment of donor and recipient DNA and can occur before initial invasion or during reinvasion events during BIR-based repair (22,23).

This model has been extended to support the hypothesis that the removal of Rad51 from newly paired dsDNA at strand-exchange intermediates is how Rad54 stabilizes the three-stranded D-loop structures (47). This hypothesis explains the generation of an accessible 3' end for further DNA extension, promoting repair and intermediate stability. A key feature of this model is that there is no functional separation in Rad54 activity. A contrasting model posits that Rad54's activities are distinct functions, and that its role in forming D-loops does not require the removal of Rad51 from dsDNA (46). The basis for this hypothesis is that Rad54 generates underwound DNA during translocation, and that negatively supercoiled DNA is a more efficient substrate for recombination

(29,46,68). Whether D-loop stabilization and Rad51 removal from dsDNA are distinct or overlapping functions remains unclear *in vivo*.

Here, we investigated potential phosphorylation sites on the Rad54 protein and identified a specific residue in the C-terminal region that modulated activity. While this residue could not be confirmed as phosphorylated, it yielded a separation-of-function mutant. We show that the substitution of Aspartic acid for two Serine residues disrupts a bridging contact between the two RecA lobes of Rad54. Disrupting this contact caused severe defects in D-loop formation *in vivo* but allowed for D-loop extension and the removal of Rad51 from dsDNA. Our data suggest the identification of a novel physiological intermediate during D-loop formation, indicating that this step likely stabilizes the early D-loop and potentially later recombination intermediates. We hypothesize that this is due to Rad54's ability to clamp dsDNA during strand exchange, thereby inducing force-mediated remodeling of the donor DNA. The removal of Rad51 follows this. By using this mutation, our study shows that these steps are mechanistically distinct, reconciling and unifying two existing models of Rad54-mediated D-loop formation.

3.2 Results

We identified potential phosphorylation sites in *Saccharomyces cerevisiae* Rad54 using the SuperPhos database (69). Seven sites were selected, and these residues were mutated to Aspartic acid or Alanine for Serine, and to Glutamic acid or Alanine for Threonine. We performed complementation assays in *rad54* strains using methyl methanesulfonate (MMS) as a DNA-damaging agent (Figure 3.1A). Most of the mutated residues successfully complemented the MMS sensitivity phenotype. The exception was that the substitution of Aspartic acid for Serine at residue 816, which failed to fully complement the MMS sensitivity of the *rad54* strain (Figure 3.1B). We further inspected the S816 site and found that the adjacent residue was also a Serine (Figure 3.1C). We speculated that mutating both residues may result in a more severe phenotype, so we generated *rad54S816A, S817A*, and *rad54S816D, S817D* substitutions and tested them for complementation. We observed an enhanced phenotype in the *rad54S816D, S817D* strain (Figure 3.E1A). There was no observable phenotype when only the S817 was changed to an Aspartic acid residue (Figure 3.E1A). This implies that the S816 site is the most critical amino acid.

Under the MMS conditions used for the initial screen, *rad54S816D, S817D* were as severe as the *rad54* strains. Therefore, we tested whether this mutation could be expressed at similar levels to *RAD54* and whether it could still form foci in response to MMS treatment. We monitored *RAD54-GFP*, *rad54S816A*, *S817A-GFP,* and *rad54S816D, S817D-GFP* for expression with and without MMS (Figure 3.E2A). All three of these proteins were expressed at similar levels with and without MMS and formed Rad54 foci in response to MMS treatment (Figure 3.E2ABC). From this, we concluded that there was no defect in the expression or stability of these Rad54 mutants.

We evaluated the sequence around the S816 site for a potential kinase consensus sequence. The surrounding sequence appeared to be a degenerate polo-like kinase site (Figure 3.E3A) (70). In human RAD54L, the site is a complete polo-like kinase consensus sequence. The yeast polo-like kinase is Cdc5, which is implicated in the resolution of recombination intermediates (71,72). We made several attempts to confirm

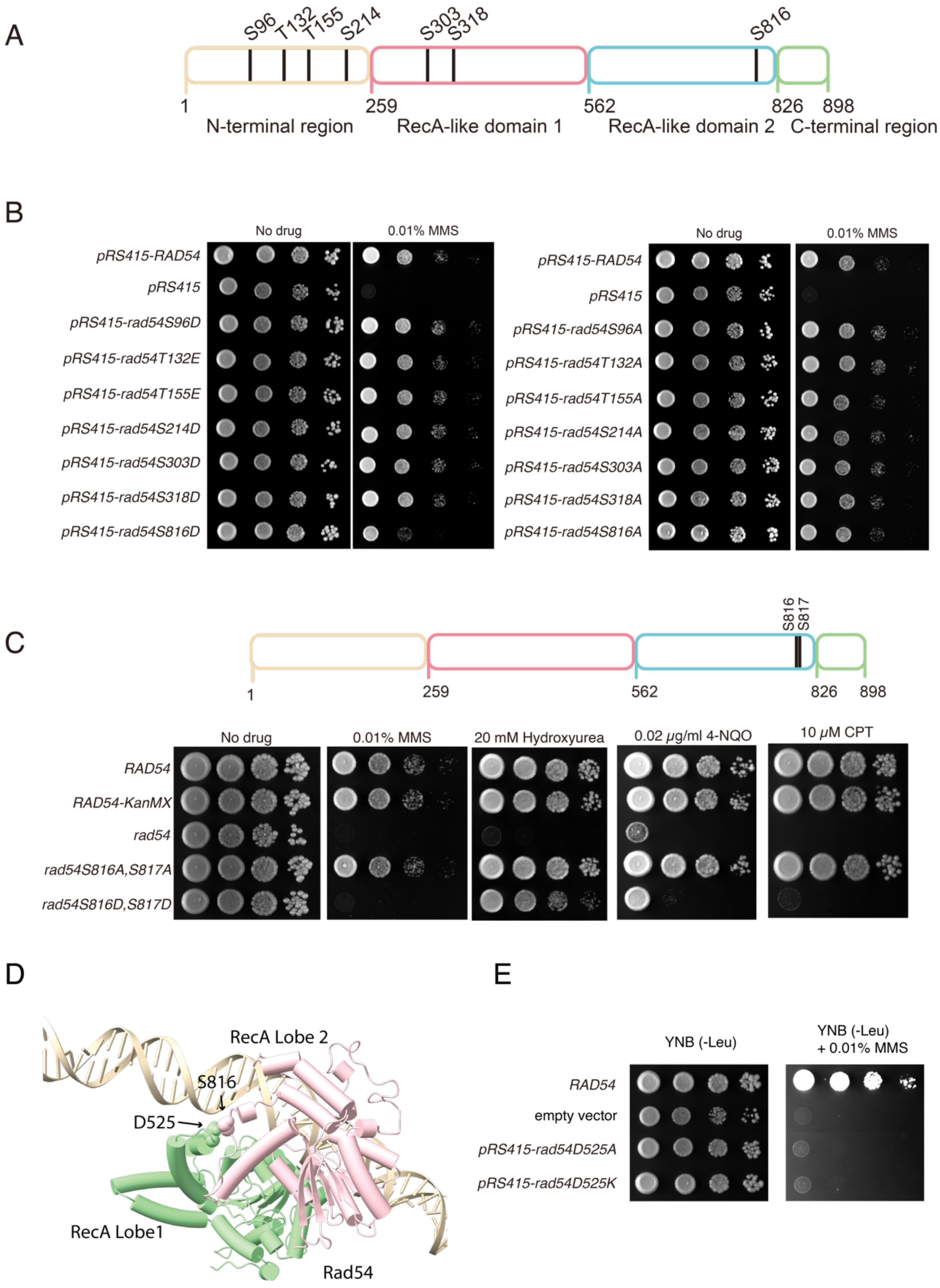

Figure 3.1: Screen of potentially phosphorylated residues in Rad54.

(A) Schematic of residues in Rad54 that were identified as phosphorylated in the SuperPhos database. (B) Yeast complementation spot assay to monitor the effect of phosphomimic mutants (Left) and alanine mutants (Right) of Rad54 at 0.01% MMS. (C) Serial dilution spot assay to monitor the impact of *rad54S816A, S817A*, and *rad54S816D, S817D* on sensitivity to 0.01% MMS, 20 mM Hydroxyurea (HU), 0.02 μg/ml 4-NQO, and 10 μM CPT. (D) AlphaFold generated model of Rad54 bound to dsDNA. The two RecA lobes are color coded, and residues D525 and S816 are shown as spheres. (E) Serial dilution spot assay showing sensitivity of *RAD54*, empty vector, *pRS415-RAD54*, *pRS415-rad54D525K*, and *pRS415-rad54D525A* to 0.01% MMS.

that this site was phosphorylated but were unsuccessful. Therefore, we can only conclude that the previously established phosphoproteomics has indicated this as a phosphorylation site. We next inquired whether this residue was structurally important by performing multiple sequence alignments of 1200 Rad54 sequences from eukaryotes (73) and found that S816 was conserved in 94.7% of sequences. One of the few exceptions was Rad54 from Dictyostelium, in which the Serine was replaced with an Aspartic acid residue (Figure 3.E3B). The natural replacement of Serine by Aspartic acid suggested that *rad54S816D, S817D* may retain partial function.

To determine whether *rad54S816D, S817D* retained partial function, we measured its ability to complement different DNA-damaging agents. MMS is an alkylating agent primarily repaired by the base excision repair pathway (74). However, at sufficiently high concentrations, HR is required to repair DNA breaks caused by stalled replication forks or transcription stress. Because different DNA-damaging agents utilize distinct repair pathways, we evaluated whether *rad54S816D, S817D* was sensitive to other types of damaging reagents. Hydroxyurea (HU) is a drug that depletes nucleotide pools and acts as a damaging agent by inducing replication stress (75). We observed that *rad54* strains are unable to grow in the presence of 20 mM HU (Figure 3.1C). In contrast, we observed only a minor growth defect for *rad54S816D, S817D*, suggesting that this protein retains some function and is relatively unaffected by HU.

Camptothecin (CPT) is a topoisomerase inhibitor that creates protein-DNA adducts (76). These adducts are primarily repaired via cross-link repair pathways. However, at sufficiently high concentration, these adducts cause transcription and replication stress that requires HR for repair. Under CPT treatment conditions, we observed an odd effect. Experiments performed with BY4741 strains obtained from the Dharmacon collection showed that *rad54* strains were completely deficient. In contrast, *rad54S816D, S817D* showed only minor defects (Figure 3.E4). This was not the case using a model strain from the laboratory, which showed severe CPT sensitivity in the *rad54S816D, S817D* mutant (Figure 3.1C). We are uncertain why this difference occurred, but it is likely due to differences in the genetic backgrounds of these strains, which may make the lab model strain more dependent on HR to repair CPT-induced lesions. Finally, we tested sensitivity to 4-Nitroquinoline Oxide (4-NQO). This drug is a UV-mimetic chemical that forms base adducts (77). At sufficiently high concentrations, it can lead to transcription- or replication-induced breaks. Treatment with 4-NQO resulted in sensitivity in the *rad54S816D, S817D* strains. From this, we conclude *that rad54S816D, S817D* retain partial function under some DNA-damaging conditions, depending on the type of damage.

To better understand the defects associated with the substitution of Serine 816 with Aspartic acid, we predicted the structure of *S. cerevisiae* Rad54 (Figure 3.1D and Figure 3.E5A) and *H. sapiens* RAD54 bound to 60 bp of dsDNA (Figure 3.E5B) using AlphaFold3 (78). The S816 residue in *S.c.*Rad54 and S657 in *H.s.*RAD54 formed a bridging interaction by contacting a conserved (92.5%) Aspartic acid residue (D525 in *S.c.*Rad54 and D366 in *H.s.*RAD54) (Figure 3.1D and Figure 3.E5CD). This interaction was not observed in the Danio. rerio crystal structure (79), likely because it lacks double-stranded DNA (dsDNA). We also evaluated the data from the AlphaFold repository, which predicts the pathogenicity of specific amino acid substitutions at a given site for human proteins (Figure 3.E5E) (80). This analysis indicated that substitutions at S657 (equivalent to S816 in *S.c.*Rad54), L658 (equivalent to S817 in *S.c.*Rad54), and D366 (equivalent to D525 in *S.c.*Rad54) could potentially be pathogenic, depending on the specific amino acid substitution.

To further validate these observations, we generated plasmids encoding *rad54D525K* and *rad54D525A* and tested their ability to restore the sensitivity of *rad54* strains to DNA-damaging agents. We found that both *rad54D525K* and *rad54D525A* failed to complement MMS sensitivity (Figure 3.1E). Like the *rad54S816D, S817D* substitution, there was a failure to fully complement CPT and 4-NQO sensitivity, although the phenotype was not as severe as the *rad54S816D, S817D* mutant (Figure 3.E6A). We also observed that this substitution complemented HU phenotypes and therefore retained partial function (Figure 3.E6A). From this analysis, we conclude that the likely defect observed in the *rad54S816D, S817D* mutant is due to a disruption between the two RecA lobes of Rad54.

3.2.1 *rad54S816D, S817D* can perform presynaptic RAD54 functions

The presynaptic phase of HR based repair is characterized by the growth and remodeling of Rad51 filaments on ssDNA. The UvrD helicase Srs2 plays an important role in this

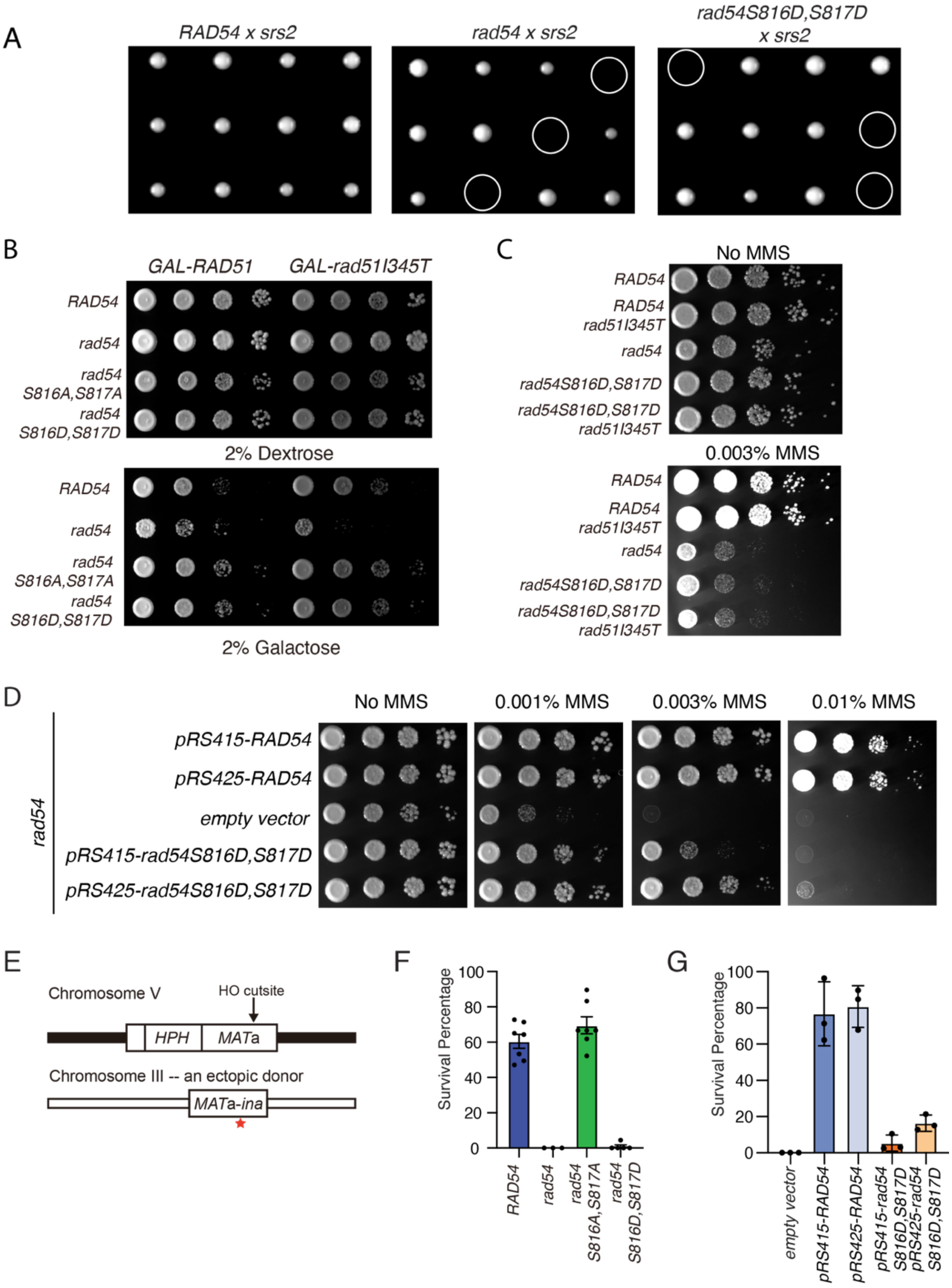

Figure 3.2: Mutations in Rad54 are separation-of-function mutants.

(A) Representative tetrad analysis for *RAD54 x srs2*, *rad54 x srs2*, and *rad54S816D, S817D x srs2*. Each row is separated from one tetrad. White circles highlight synthetic lethal combinations. (B) Serial dilution spot assay to determine the effect of *GAL-RAD51* and *GAL-rad51I345T* over-expression on *RAD54*, *rad54*, *rad54S816A, S817A*, and *rad54S816D, S817D* strains. (C) Serial dilution spot assay to test the MMS sensitivity of *RAD54*, *RAD54 rad54I345T*, *rad54*, *rad54S816D, S817D*, and *rad54 S816D, S817D rad51I345T*. (D) Serial dilution spot assay for rad54 complemented with *pRS415-RAD54*, *pRS425-RAD54*, empty vector, *pRS415-rad54S816D, S817D*, and *pRS425-rad54S816D, S817D*. Strains were tested with no MMS, 0.001%, 0.003%, and 0.01% MMS. (E) Schematic for the experiment used to measure the repair of a double strand break at an ectopic site. (F) Graph representing the colony survival rate for *RAD54*, *rad54*, *rad54S816A, S817A*, *rad54S816D, S817D*. The bars represent the mean, and the error bars represent the standard error measurement of at least three independent experiments. (G) Bar graph representing analysis of *RAD54* overexpression on the complementation of repair of an ectopic double-strand break. All strains are rad54 with the empty vector, *pRS415-RAD54*, *pRS425-RAD54*, *pRS415-rad54S816D, S817D*, and *pRS425-rad54S816D, S817D*. The bar represents the mean, and the error bars represent the standard error measurement of three independent experiments.

step of recombination, modulating the length of Rad51 filaments (62,63,65,66). This role appears to be required for proper Rad51 filament maturation, which is at least needed for ectopic recombination (65). Under these conditions, the activity is pro-recombinogenic. While the pre-synaptic phase occurs widely on ssDNA generated during resection, it can also occur when long stretches of ssDNA are generated during break-induced replication (BIR) (22,81-83). Under these conditions, Srs2 acts as an anti-recombinase, reducing toxic intermediates that arise from potential reinvasion. At stalled replication forks, Srs2 can also act as an anti-recombinase, preventing HR and promoting translesion synthesis (65,84). Rad54 competes with Srs2 by stabilizing Rad51 filaments and preventing promiscuous binding of Rad51 to dsDNA, thereby increasing the active pool of Rad51. Based on this Rad54 activity, if *rad54S816D, S817D* were only defective in the presynaptic phase of HR, we might expect that this mutant would no longer be synthetically lethal with *SRS2*, would be unable to remove Rad51 from dsDNA, and the phenotype would be reversible with overexpression.

RAD54 and *SRS2* are synthetically lethal. Typically, synthetic lethality occurs when genes are required for parallel or compensatory pathways. Divergence of these two pathways may occur during a modified presynaptic phase of HR at stalled replication forks, where HR (Rad54) competes with translesion synthesis (Srs2) (84). In this scenario, Rad54 likely antagonizes Srs2 to promote HR by preventing Rad51 from being removed. We reasoned that if *rad54S816D, S817D* were defective in the presynaptic phase, it would not be synthetically lethal with *SRS2*, as this would allow the use of the *SRS2*-favored pathway. We performed tetrad analysis to measure synthetic lethality. We compared *RAD54 srs2*, *rad54 srs2*, and *rad54 S816D, S817D srs2*. The tetrad dissection pattern showed that the *rad54S816D, S817D* is synthetically lethal with *srs2* (Figure 3.2A). This was not due to defects in meiosis because the spores followed a 1:1:4 (Parental Ditype (DP), Non-Parental Ditype (NPD), Tetra Type (TT)) segregation pattern.

Rad54 can remove Rad51 bound to dsDNA (37,38,51,85). This activity may participate in the recovery of stalled DNA replication forks (36), the stabilization of the nascent D-loop (47), or increase the active pools of Rad51. Overexpression of the recombinase Rad51 can lead to pathological binding of Rad51 to double-stranded DNA (37,38). When Rad51 is overexpressed in a *rad54* strain, there is a minor growth phenotype. We reasoned that if *rad54S816D, S817D* retained this function, then it would suppress this phenotype. We found complementation of this phenotype by both *rad54S816A, S817A*, as well as *rad54S816D, S817D* (Figure 3.2B). This result indicates that these Rad54 mutants can remove Rad51 from dsDNA. To further challenge the mutants, we also performed this experiment with *rad51I345T* overexpression. This mutant form of Rad51 binds to dsDNA more efficiently (57) and should be more difficult to remove. However, overexpression of this Rad51 variant did not significantly impact the *rad54* phenotype or prevent complementation by the Rad54 mutants, compared with overexpression of wild-type Rad51 (Figure 3.2B). From this, we conclude that *rad54S816D, S817D* is competent in removing Rad51 from dsDNA. *rad51I345T* is a *RAD51* variant that also produces longer Rad51 filaments and suppresses the *SRS2* deletion phenotype. If *rad54S816D, S817D* were defective in presynaptic activity, we may expect *rad54I345T* to suppress the MMS sensitivity observed in these strains. However, we observed no suppression when we tested this strain (Figure 3.2C).

The activity of the presynaptic phase is strongly controlled by concentration due to stabilization of Rad51 filaments. As a result, Rad54 overexpression may lead to increased HR. If this were the primary defect in the *rad54S816D, S817D* mutant, then we would expect overexpression of the protein to rescue the DNA damage phenotype. Therefore, we expressed Rad54 from either a centromeric plasmid or a 2 μ plasmid. The 2 μ plasmid is expected to result in 10 to 15-fold overexpression of the protein. When we tested the overexpression strains for complementation of the *rad54* MMS phenotype. We observed a decrease in sensitivity in cells expressing *rad54S816D, S817D* from the 2 μ plasmid (Figure 3.2D). However, this complementation was incomplete and did not fully restore *RAD54* resistance levels (Figure 3.2D). These data suggest that *rad54S816D, S817D* support presynaptic Rad54 activity but are defective later in the HR pathway.

3.2.2 *rad54S816D, S817D* is defective in stable D-loop formation

The ability of the *rad54S816D, S817D* variant to function before displacement loop formation, during the presynaptic phase of HR, suggests that it is a separation-of-function mutant. To fully address the stage at which Rad54 activity is disrupted, we evaluated whether there was a defect in repairing a single double-strand DNA break from an ectopic donor. We used a reporter assay with a *MATa* locus containing an HO endonuclease cleavage site on chromosome V (Figure 3.2E) (86). A homologous non-cleavable *MATa* is located on chromosome III (Figure 3.2E). Upon induction with galactose, the DNA is broken, and repair occurs using the ectopic homologous site. Cells will only survive if they can repair the break. We measured the survival percentage after induction of a break. In wildtype (WT) strains, the survival frequency was 60-65% (Figure 3.2F). This was also the case with the *rad54S816A, S817A* strains (Figure 3.2F). In the *rad54* strain, there is no survival. The *rad54S816D, S817D* strains exhibited only ~1% survival (Figure 3.2F). We further tested whether *rad54D525A* or *rad54D525K* could complement the DSB repair phenotype. With these mutants, the survival rate was approximately 25% (Figure 3.E6C).

Finally, we tested whether overexpression of *rad54S816D, S817D* could complement the repair phenotype. When *rad54S816D, S817D* were expressed from a centromeric plasmid, only 3% of the cells survived, comparable to the gene replacement strains. Expression from the 2 μ plasmid resulted in ~12% survival (Figure 3.2G). While this was significantly better than survival under other conditions, it was not as high as the 75-85% survival observed for *RAD54* overexpression. From these experiments, we conclude that *rad54S816D, S817D* is defective in double-strand break repair.

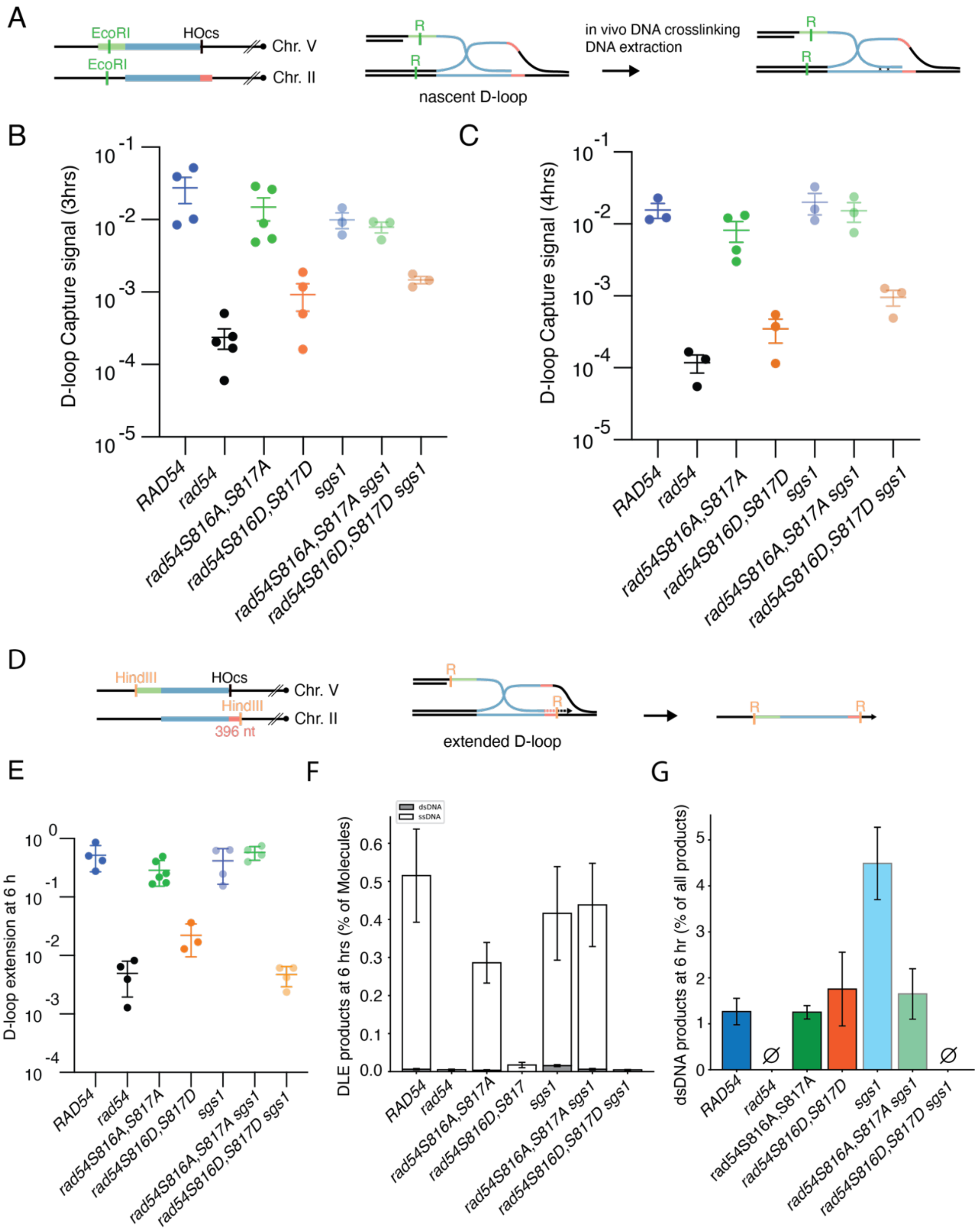

Figure 3.3: Mutations in RAD54 impact recombination intermediates.

(A) Schematic diagram illustrating the D-loop capture assay to trap the formation of nascent D-loops during recombination. (B) Graph representing D-loop capture efficiency at 3 hours post-break induction for *RAD54*, *rad54*, *rad54S816A, S817A*, *rad54S816D, S817D*, *sgs1*, *rad54 S816A, S817A sgs1*, *rad54S816D, S817D sgs1*. The bar represents the mean, and the error bars represent the standard error measurement for at least three independent experiments. (C) Graph representing D-loop capture efficiency at 4 hours post-break induction for *RAD54*, *rad54*, *rad54 S816A, S817A*, *rad54S816D, S817D*, *sgs1*, *rad54S816A, S817A sgs1*, *rad54S816D, S817D sgs1*. The bar represents the mean, and the error bars represent the standard error measurement for at least three independent experiments. (D) Schematic diagram illustrating the assay to monitor D-loop extension. (E) Graph representing D-loop extension at 6 hours for *RAD54*, *rad54*, *rad54 S816A, S817A*, *rad54S816D, S817D*, *sgs1*, *rad54S816A, S817A sgs1*, *rad54S816D, S817D sgs1*. The bar represents the mean, and the error bars represent the standard error measurement for at least three independent experiments. (F) Extension products at 6 hours: single-stranded (ssDNA; DLE signal when both hybrid oligos were added) and double-stranded (dsDNA; DLE signal when no hybrid oligos were added) for *RAD54*, *rad54*, *rad54 S816A, S817A*, *rad54S816D, S817D*, *sgs1*, *rad54S816A, S817A sgs1*, *rad54S816D, S817D sgs1*. The error bars represent the standard error measurement of at least three independent experiments. (G) The percentage of dsDNA among total extension products for *RAD54*, *rad54*, *rad54 S816A, S817A*, *rad54S816D, S817D*, *sgs1*, *rad54S816A, S817A sgs1*, *rad54S816D, S817D sgs1*. The error bars represent the standard error measurement for at least three independent experiments.

To identify the repair intermediate at which the *rad54S816D, S817D* strain is defective, we used a previously established D-loop capture assay (14,19,87,88). This assay also uses an ectopic repair site within the genome. After induction of a break using the HO endonuclease, the cells are cross-linked with psoralen, which can trap the initial three-strand intermediates, known as nascent D-loops. The efficiency of D-loop capture is then quantified by proximity ligation and qPCR (Figure 3.3A and Figure 3.E7AB). We monitored D-loop capture at 3 and 4 hours, and, as expected, the *rad54* strains showed 100-fold lower signals than the WT. This value was also the same as that obtained from qPCR performed without the oligo to restore restriction enzyme sites, indicating this is the background (Figure 3.E7C). The *rad54S816A, S817A* were slightly lower than WT. However, this difference was not significant (Figure 3.3B). The *rad54S816D, S817D* strains were 34- and 47-fold lower than WT at 3 and 4 hours, respectively (Figure 3.3B and Figure 3.E7CDEG), indicating a severe defect in D-loop capture.

We next asked whether the *rad54S816D, S817D* mutations disrupted D-loop formation or were associated with an elevated level of nascent D-loop reversal. Sgs1 is a helicase implicated in the reversal of D-loops (19,87,89). We reasoned that if *rad54S816D, S817D* were subjected to a high level of D-loop reversal, then deletion of *SGS1* might suppress most of the observed defects in D-loop capture. However, if the increase were small, then it would imply that most of the defect is due to the initial capture. An increase in D-loop capture was observed in the *rad54S816D, S817D sgs1* double mutant strain. However, this was still 20- and 12-fold lower than WT at 3 and 4 hours, respectively (Figure 3.3BC and Figure 3.E7C). The increase observed in the *rad54S816D, S817D sgs1* double mutants translates into 1.4- and 4-fold increases in capture efficiency compared with the *rad54S816D, S817D* single mutant. This suggests that most of the deficiency is due to a decrease in initial capture, rather than in reversal.

The extension of D-loops stabilizes the nascent three-strand intermediates, and it is possible that defects in capture may also be related to defects in D-loop extension. D-loop extension from the newly paired 3' end can be measured using the same strains (Figure 3.3D and Figure 3.E8AB). As with the D-loop capture assay, there was only a modest difference from WT in the ability of *rad54S816A, S817A* to extend D-loops, and there was a significant loss (20-fold) of D-loop extension in the *rad54S816D, S817D* strain at 6 hours (Figure 3.3E and Figure 3.E8CDE). This is compared to a 100-fold loss in the *rad54* strain. Surprisingly, in the *rad54S816D, S817D sgs1* strain, there was now a 100-fold loss in D-loop extension, suggesting that while D-loop capture was slightly improved, there was insufficient extension to reach the second restriction site (Figure 3.3E). Importantly, this means that the *rad54S816D, S817D* strains are competent for

D-loop extension if the D-loop is initially stabilized. The primary defect in this mutant occurs at the D-loop capture stage.

The extended D-loops can also be characterized by their ssDNA and dsDNA content (Figure 3.3F). Because this is a break-induced replication system, the amount of dsDNA produced reflects the amount of lagging-strand synthesis. This value is low in WT but is 3 to 4-fold higher in *sgs1* strains (19). We also observed this increase in dsDNA in a *sgs1* strain (Figure 3.3G). Surprisingly, this increase was lost in the *rad54S816A, S817A sgs1* strain (Figure 3.3G). This result suggests a genetic interaction between *RAD54* and *SGS1* during the repair synthesis phase, and a slight defect in the *rad54S816A, S817A* mutant. It should be noted that the extension values for *rad54* and *rad54S816D, S817D sgs1* were so low that this type of analysis could not yield reliable results.

3.2.3 Recombination between alleles

The *rad54S816D, S817D* mutant had diminished D-loop capture and failed to promote survival during ectopic recombination. This type of recombination is generally less efficient than recombination between sister chromatids or homologous chromosomes and, therefore, may be more sensitive to subtle changes in recombination efficiency (86). Consequently, we investigated the impact of the *rad54S816A, S817A*, and *rad54S816D, S817D* alleles on recombination between homologous chromosomes. We used a reporter assay based on the *ADE2* gene in diploid *S. cerevisiae* (90-93). Each copy of chromosome XV has a different inactive allele of *ade2*; one copy contains an *I-Sce1* nuclease site (*ade2-I*), and the other has an inactivating mutation located within the gene (*ade2-n*) (Figure 3.4A). Upon induction of the nuclease and formation of a double-strand break, both sister chromatids are cut, and repair occurs with the *ade2-n* allele located on the homologous chromosomes. Types of gene conversion events can be determined by reconstitution of the *ADE2* genes. If long tract repair occurs, then the gene conversion event will acquire the deleterious mutation from the homolog, and the yeast colony will appear red. If short tract repair occurs, the mutation will not be acquired, and a functional *ADE2* gene will be reconstituted, resulting in a white colony (Figure 3.4B). Each sister can be repaired via a long tract or short tract gene conversion event, and due to independent assortment, a colony can be red (two long tracts), white (two short tracts), or sectored (one long tract and one short tract).

In our hands, sectored colonies are the most common outcome in WT, occurring approximately 65-70% of the time. This was also observed in the *rad54S816A, S817A* mutant (Figure 3.4C). However, with the *rad54S816D, S817D* allele, sectored colonies accounted for only about 20-25% of the population, with most colonies appearing solid red. Approximately 95% of these colonies were recombinants rather than uncut colonies. This observation is based on re-induction with galactose. Recombinants should be able to survive on galactose plates since the DSB is repaired and the original cut site is lost after repair. We also observed a 3-fold increase in the percentage of solid white colonies, though the significance of this finding is unclear. We quantified the ratio of long-tract to short-tract conversion by counting individual conversion events. For example, a solid red or white colony counts as two events, while a sectored colony counts as one short-tract and one long-tract gene conversion. According to this analysis, the WT results in a long-to-short tract ratio of 1.7 (Figure 3.4D). A similar ratio was calculated for the *rad54S816, S817A* mutants (Figure 3.4D), while the ratio was two times higher (3.4) in

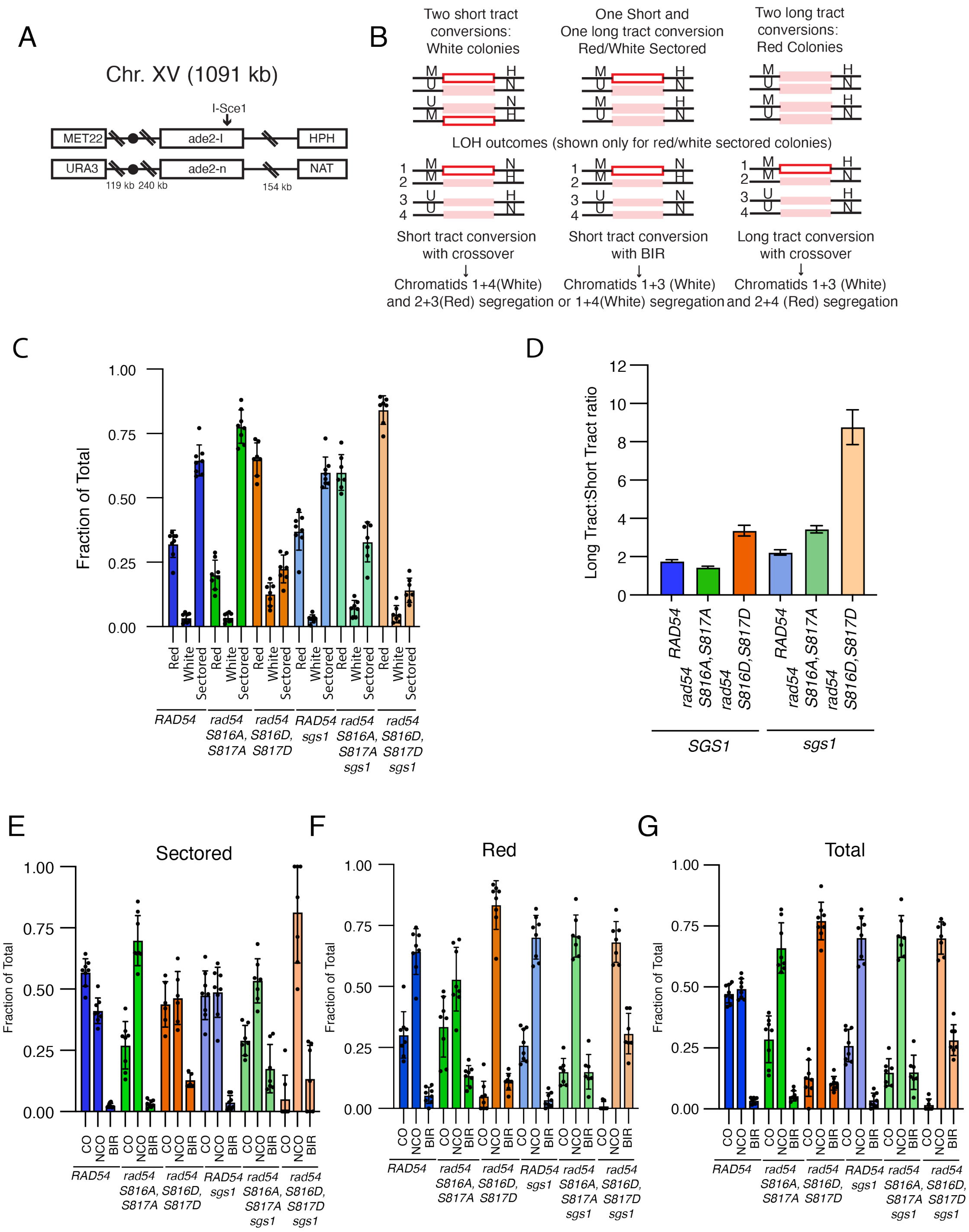

Figure 3.4: Impact of *RAD54* mutations on allelic recombination.

(A) Schematic diagram illustrating the DNA reporter used to analyze the effect of Rad54 mutation on allelic recombination. (B) Schematic diagram illustrating the potential gene conversion outcomes and HR based repair pathways during allelic recombination. (C) A bar graph representing the gene conversion outcomes for *RAD54*, *rad54S816A, S817A*, and *rad54S816D, S817D*. The bars represent the mean of the data, and the error bars represent the standard deviation. The data are the result of at least 6 independent experiments. (D) Graph illustrating the ratio of long tract to short tract gene conversion for *RAD54, rad54S816A, S817A, and rad54S816D, S817D*. The error bars represent the standard error of the measurement. (E) Bar graph representing the recombination outcomes for sectored colonies for *RAD54, rad54S816A, S817A, and rad54S816D, S817D.* The bars represent the mean, and the error bars represent the standard deviation of the data. The data are the results of at least 6 independent experiments. (F) Bar graph representing the recombination outcomes for red colonies for *RAD54, rad54S816A, S817A, and rad54S816D, S817D.* The bars represent the mean, and the error bars represent the standard deviation of the data. The data are the results of at least 6 independent experiments. (G) Bar graph representing the total recombination outcomes for *RAD54, rad54S816A, S817A, and rad54S816D, S817D.* The bars represent the mean, and the error bars represent the standard deviation of the data. The data are the results of at least 6 independent experiments.

the *rad54S816D, S817D* mutant. From these data, we conclude that the mutant form of Rad54 results in more frequent long-tract gene conversion events.

The helicase Sgs1 is known to shorten gene conversion tracts. From our previous experiments, we identified a novel genetic interaction between Rad54 and Sgs1. Therefore, we generated *SGS1* deletion strains with *RAD54*, *rad54S816A, S817A*, and *rad54S816D, S817D*. Deletion of *SGS1* alone resulted in a minor increase in gene conversion tract length (Figure 3.4CD). However, *rad54S816A, S817A sgs1* strains now had a 2-fold increase in the number of long tract conversions, which was comparable to the *rad54S816D, S817D* strain (Figure 3.4CD). In the *rad54S816D, S817D sgs1* strain, there was a further increase in long tract gene conversion to 4 to 5-fold more than WT (Figure 3.4CD). This data further supports a synthetic interaction between Rad54 and Sgs1, and the increase in long tract gene conversion is likely due to reduced stability of the primary strand invasion intermediates.

The reporter strains used in these experiments also carry antibiotic markers downstream of the *ade2* genes. The segregation of these markers can be used to determine whether the recombination results in a Crossover (CO), Non-Crossover (NCO), or Break-induced Replication (BIR) outcome (Figure 3.4AB). Outcomes were analyzed from sectored (Figure 3.4E) and solid red colonies (Figure 3.4F). The same outcomes were also pooled to examine the total recombination outcomes (Figure 3.4G). For the sectored colonies, there was a reduction in CO outcomes for both the *rad54S816A, S817A* and *rad54S816D, S817D* alleles (Figure 3.4E). This occurred due to an increase in NCO outcomes in the *rad54S816A, S817A* strain, and an increase in BIR in the *rad54S816D, S817D* strain. The most dramatic impact was observed in solid red colonies, where the *rad54S816D, S817D* allele primarily repaired through NCO and BIR outcomes (Figure 3.4F). Upon analyzing the total recombination outcomes, we observed a general trend of increased NCO and BIR outcomes (Figure 3.4G). These outcomes are stronger in the *rad54S816D, S817D* strain, but also occur in the *rad54S816A, S817A* strain.

Upon deletion of *SGS1* in the *rad54S816A, S817A* strains, there was an increase in NCO outcomes as well as BIR. This came at the expense of CO outcomes (Figure 3.4EFG). This phenotype is enhanced in the *rad54S816D, S817D* strain, resulting in a near-complete loss of CO outcomes (Figure 3.4EFG). A substantial increase in BIR or BIR-like outcomes balances this loss. The increase in long-tract gene conversion, the increase in BIR, and the loss of CO outcomes likely reflect a reduction in second DNA-end engagement. According to this interpretation, the data suggest that stabilization of the primary strand invasion intermediate by Rad54 and Sgs1 may be a necessary step in properly capturing the second end of DNA for double Holliday junction formation.

3.2.4 Rad54 S816DS817D is defective in binding dsDNA

Through our genetic analysis, we determined that substituting Aspartic acid for S816 and S817 disrupts D-loop stabilization *in vivo* and may also disrupt second-end DNA capture. To further characterize the defects in protein activity, we expressed and purified Rad54 S816AS817A and Rad54 S816DS817D and tested their biochemical properties. Rad54 is a dsDNA-dependent ATPase, and we measured ATP hydrolysis efficiency for WT, Rad54 S816AS817A, and Rad54 S816DS817D. There was no difference between WT and Rad54 S816AS817A (Figure 3.E9A). However, the Rad54 S816DS817D protein poorly hydrolyzed ATP (Figure 3.E9A). This loss of activity could be due to an inactive enzyme or reduced dsDNA binding. Rad51 further stimulates Rad54 ATPase activity by 3-5-fold. To determine if the disruption of ATP hydrolysis was due to a dead enzyme or binding to dsDNA, we added Rad51 to the ATPase reaction. In the WT and Rad54 S816AS817A, there was the expected stimulation of hydrolysis. Unexpectedly, the addition of Rad51 to the Rad54 S816DS817D mutant resulted in a 20-fold stimulation of activity, making hydrolysis levels comparable to the WT (Figure 3.E9A). These data suggest that the Rad54 S816DS817D mutant may have difficulty binding to dsDNA in the absence of Rad51, but this is resolved when Rad51 is present.

Because the Rad54 S816DS817D mutant shows reduced ATPase activity, we next tested its ability to bind dsDNA using an electromobility shift assay. We measured a 2.5-fold reduction in binding to dsDNA for the Rad54 S816DS817D mutant compared to the WT (Kd 27 nM versus 68 nM) (Figure 3.E9BC). A small reduction in the apparent K_d for Rad54 S816AS817A was also observed (K_d 27 nM versus 36 nM) (Figure 3.E9BC). Rad54 is known to form an oligomer (94). A reduction in oligomer formation could cause an apparent defect in binding to dsDNA. The cooperativity of protein binding to DNA would be reflected in this. Therefore, we measured the hill coefficient from our binding plots. We observed no difference in binding cooperativity (*h* constant 3.7 versus 3.6 of WT and Rad54 S816DS817D, respectively), suggesting that the defect is due to direct binding to dsDNA rather than oligomerization.

To more quantitatively evaluate the defect in binding, we used single-molecule DNA curtains (95,96) to monitor the stability of GFP-Rad54, GFP-Rad54 S816AS817A, and GFP-Rad54 S816DS817D (Figure 3.5AB). These experiments measure the dissociation rate of the Rad54 protein, the velocity at which it moves along dsDNA, and the distance it travels (Figure 3.5AB). To accurately determine the rate of Rad54 dissociation, we first validated that the loss of protein signal was due to dissociation rather than photobleaching. We measured the photobleaching rate by monitoring GFP loss when the laser was left on without shuttering. The loss of GFP-Rad54 signal was then measured with shuttering of the laser. If the rate of signal loss exceeds the rate of photobleaching with shuttering, we are measuring dissociation events. Rad54, Rad54 S816AS817A, and Rad54 S816DS817D all dissociated faster than photobleaching (Figure 3.5C). These measurements were converted to dissociation rates, and it was determined that Rad54 S816DS817D dissociated more rapidly than WT or Rad54 S816AS817A (Figure 3.5D). This is consistent with reduced dsDNA binding by the Rad54 S816DS817D mutant.

Rad54 dissociation was measured with the buffer flow on, which applies a force to the proteins and can affect the rate and direction of movement along the dsDNA. Rad54 can translocate in either direction or can switch direction as it moves along dsDNA (29).

The direction depends on the DNA strand used as the tracking strand. In our experiments, when Rad54 translocates toward the barriers, it does so against the flow of buffer or a resisting force. In contrast, if movement is toward the pedestals, then an assisting force is present. We were surprised to observe that there was no difference in the velocity of Rad54 movement with or against the force of flow between the WT, Rad54 S816AS817A, and Rad54 S816DS817D (Figure 3.5E), suggesting no general defect in translocation by the Rad54 S816DS817D mutant.

There were differences in the observed distance translocated both with and against the flow (Figure 3.5F). This difference was small between the WT and Rad54 S816AS817A (4759 ± 2591 bp versus 5671 ± 3391 bp when an assisting force was applied, and 8930 ± 4136 bp versus 6954 ± 3744 bp when a resisting force was applied). However, a much larger difference was observed between the WT and Rad54 S816DS817D (4759 ± 2591 bp versus 7820 ± 4859 bp with an assisting force, 8940 ± 4136 bp versus 5740 ± 3667 bp when with a resisting force). There was also a difference in the direction of movement along the DNA. Surprisingly, 75 to 80% of WT molecules translocated against the buffer flow (Figure 3.5G). This may be due to the DNA in that direction being more tense, which could promote directional movement (97). In contrast, only 15-20% of Rad54 S816DS817D molecules translocated against the flow (Figure 5G). These observations are consistent with weaker binding by Rad54 S816DS817D to the DNA. Lower affinity allows the force of buffer flow to push Rad54 S816DS817D 1-dimensionally along the DNA, resulting in longer tracks only in the direction of flow, but maintaining similar velocities.

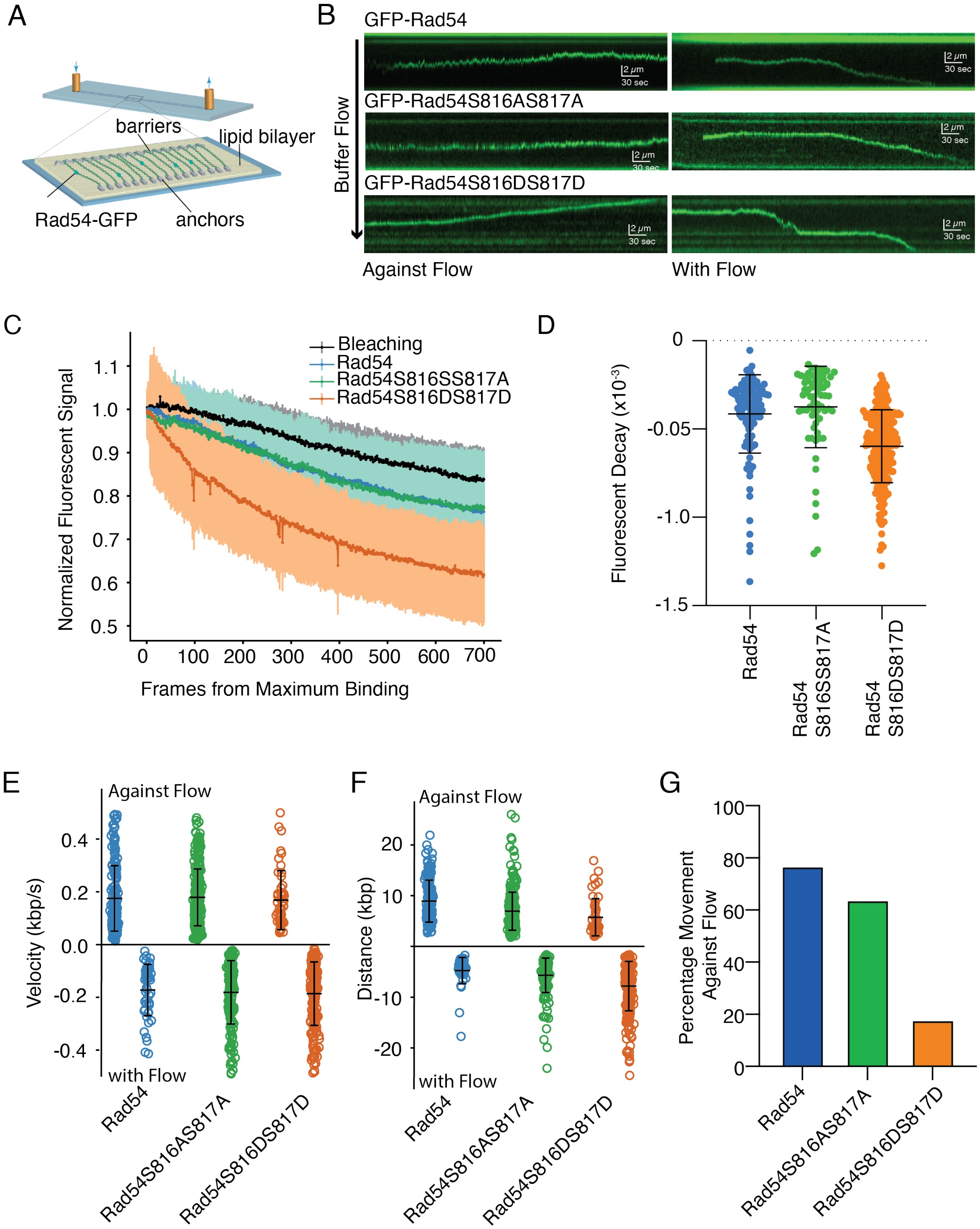

Figure 3.5: Rad54 S816DS816D has reduced affinity for dsDNA.

(A) Schematic diagram illustrating DNA curtains experiments to test the activity of Rad54 on dsDNA. (B) Representative kymographs for GFP-Rad54, GFP-Rad54 S816AS817A, and GFP-Rad54 S816DS817D moving against (Left) and with (Right) buffer flow. (C) Mean fluorescent decay rate for Rad54, Rad54 S816AS817A, and Rad54 S816DS817D. The black line gives the photobleaching rate. The shade represents the standard deviation of the data. (D) Dot plot with the individual fluorescence decay rates for Rad54 (*N* = 117), Rad54 S816AS817A (*N* = 68), and Rad54 S816DS817D (*N* = 232). The bar represents the mean, and the error bars represent the standard deviation of the data. (E) Graph representing the velocity of translocation in kbp/s for Rad54 (*N* = 216), Rad54 S816AS817A (*N* = 446), and Rad54 S816DS817D (*N* = 271). The molecules that moved against the flow are above the X-axis, and the molecules that moved with the flow are below the X-axis. The bar represents the mean, and the error bars represent the standard deviation of the data. (F) Graph representing the distance moved for Rad54 (*N* = 216), Rad54 S816AS817A (*N* = 446), and Rad54 S816DS817D (*N* = 271). The molecules that moved against the flow are above the X-axis, and the molecules that moved with the flow are below the X-axis. The bar represents the mean, and the error bars represent the standard deviation of the data. (G) Bar graph representing the percentage of Rad54 (166/216), Rad54 S816AS817A (285/446), and Rad54 S816DS817D (48/271) that move against the buffer flow.

3.2.5 PSCs with Rad54 S816D817D are less active than WT

The Rad51-ssDNA-Rad54 complex is referred to as the presynaptic filament (PSC) (Figure 3.6A). We previously used PSC reconstitution in combination with DNA curtains to monitor Rad54 activity in the context of the PSC, and this complex is considered active during homology search and strand exchange in HR. The combination of Rad51 and Rad54 in the PSC can exert greater force on the DNA than Rad54 alone (97) and may make it more resistant to buffer flow. Therefore, we tested the activity of PSCs reconstituted with Rad54, Rad54 S816AS817A, and Rad54 S816DS817D (Figure 3.6B).

In WT and the Rad54 mutants, 80-85% of PSCs moved against the flow and exhibited considerably higher velocities and distances during translocation against the buffer flow (Figure 3.6CDE). These observations are all consistent with increased affinity for the DNA relative to Rad54 alone. In contrast to Rad54 alone, there was a difference in the translocation velocity between PSCs with Rad54, Rad54 S816AS817A, and Rad54

S816DS817D. The velocity of Rad54 S816AS817A was 85% of WT, and Rad54 S816DS817D was 60% of WT. These differences were observed only when the PSCs moved against the flow, and no differences were observed when they moved with the flow (Figure 3.6CDE). These differences are consistent with weakened binding by PSCs carrying mutant Rad54. We did not observe differences in the distance of translocation in either direction, suggesting that all PSCs are more stable than Rad54 alone. We used a previously established technique to monitor the number of Rad54 molecules bound in each PSC (29,92). Under conditions where flow is constant, there is no difference in the number of Rad54 molecules bound per PSC. This suggests that the reduction of velocity against flow may occur through different mechanisms. From these experiments, we conclude there is only a minor difference in the movement of the PSC with Rad54 S816DS817D.

We reasoned that defects in PSC movement could result from a loss of force generation by Rad54 on the donor DNA. The application of force to the donor DNA by the PSC results in the DNA's deformation. This distortion can turn the donor into a substrate for the ssDNA binding protein RPA (29,96) (Figure 3.7A). Therefore, a reduction-in-force application should result in differences in RPA binding within the PSC. For these experiments, the PSC was formed and allowed to function with the flow off for 5 minutes before the flow was restored, and the RPA signal was monitored. Approximately 63% (53/83) of WT PSCs recruited RPA. In contrast, only 34% (47/138) of Rad54 S816DS817D PSCs had RPA associated (Figure 3.7B). In the Rad54 S816AS817A mutant, there was a slight reduction in RPA, as well (48%, 58/122). This is consistent with the differences in activity observed for the PSC with Rad54

S816AS817A, which also translated to the physiological setting during allelic recombination and repair synthesis.

These results indicate that mutation of this region of Rad54 reduces DNA remodeling, a consequence of the force applied to the DNA. Rad54 exerts force on the donor DNA by establishing multiple points of contact (97), and this activity is enhanced when DNA tension is reduced. Therefore, we reasoned that turning off the buffer flow would allow PSCs with WT Rad54 to accumulate more Rad54. We measured the estimated number of Rad54 molecules per PSC. This number was 2-fold higher than in our flow experiments with WT and Rad54 S816AS817A. Notably, the number of Rad54 S816DS817D molecules was significantly lower (Figure 3.7C). The change in Rad54 molecules bound in the mutant is likely due to the failure to isolate local donor DNA. It is unlikely to be a self-recruitment issue, given the equivalent cooperativity observed by EMSA. Therefore, we conclude that Rad54 S816DS817D has reduced capacity to remodel local donor DNA structures, likely due to decreased ability to overcome pre-existing force on the DNA.

Previously, we hypothesized that applying force to DNA may promote the stabilization of nascent D-loops. The *rad54S816D, S817D* mutant was defective in D-loop formation both *in vivo* and *in vitro*, particularly under force application to dsDNA. We directly measured whether the Rad54 S816DS817D mutant was defective in forming D-loops *in vitro* using a previously established assay (93,96). The Rad54 S816AS817A mutant was able to promote D-loop formation while the Rad54 S816DS817D protein did not (Figure 3.E9D). This observation is consistent with the lack of D-loop formation obser-

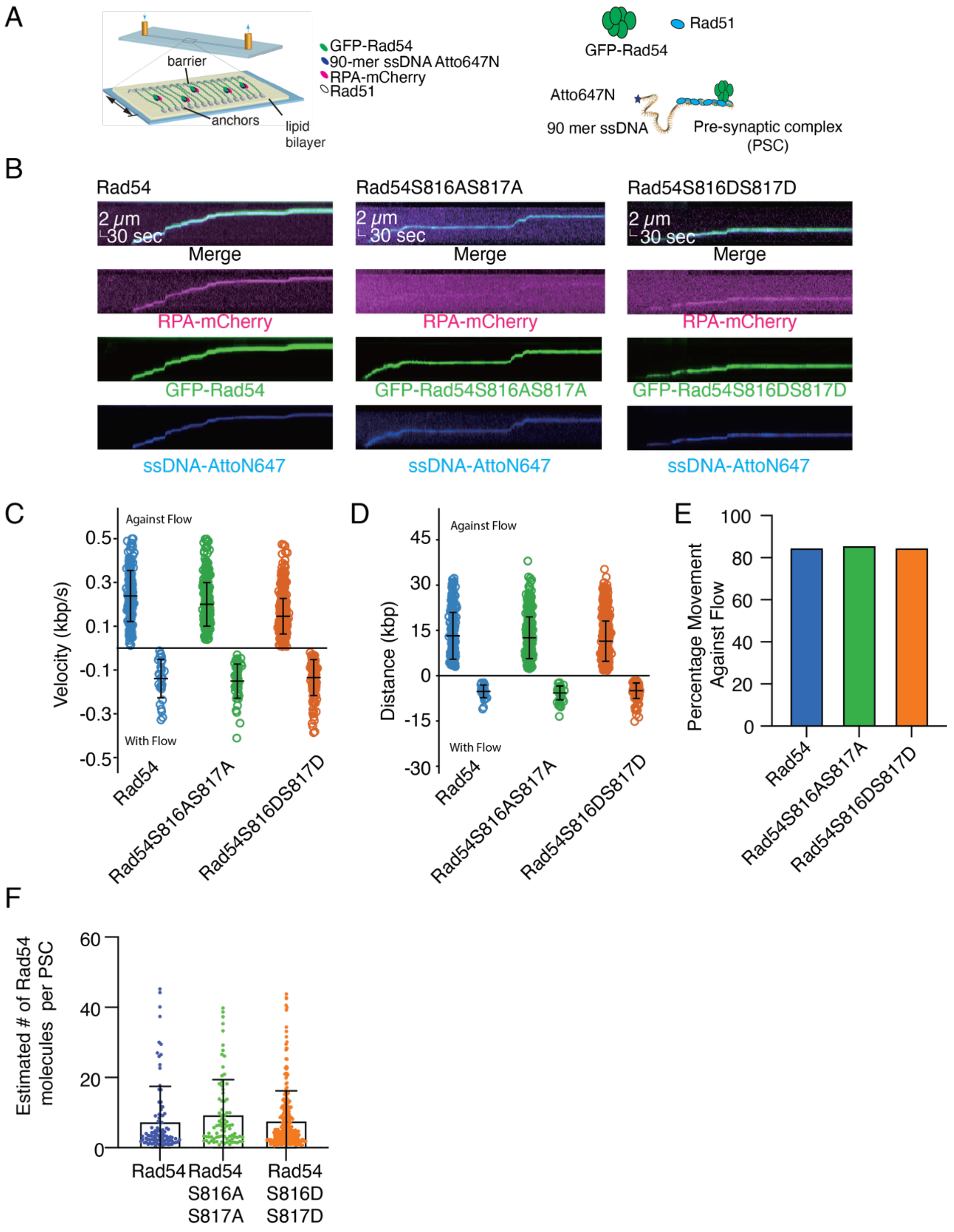

Figure 3.6: Weak general defects in Rad54 S816DS817D in the PSC.

(A) Cartoon diagram illustrating the use of DNA curtains to perform experiments to monitor the activity of the presynaptic complex (PSC) on dsDNA. (B) Representative kymographs for PSCs, PSCs with Rad54 S816AS817A, or PSCs with Rad54

S816DS817D. Shown are merged images of RPA-mCherry, GFP-Rad54, and Atto647-90-mer ssDNA. (C) Measured translocation velocities for the PSC with Rad54 (*N* = 215), PSC with Rad54 S816AS817A (*N* = 378), and PSC with Rad54 S816DS817D (*N* = 835). The PSCs that moved against the flow are above the X-axis, and the PSC values that moved with the flow are below the X-axis. The bars represent the mean, and the error bars represent the standard deviation of the data. (D) Measured translocation distances for the PSC with Rad54 (*N* = 215), PSC with Rad54 S816AS817A (*N* = 378), and PSC with Rad54 S816DS817D (*N* = 835). The PSCs that moved against the flow are above the X-axis, and the PSC values that moved with the flow are below the X-axis. The bars represent the mean, and the error bars represent the standard deviation of the data. (E) Graph representing the percentage of PSC with Rad54 (183/215), PSC with Rad54 S816AS817A (326/378), and PSC with Rad54 S816DS817D (710/835) that moved against the buffer flow. (F) Graph representing the estimated number of Rad54 molecules per PSC with Rad54 (*N* = 96), Rad54S816AS817A (*N* = 82), and Rad54 S816DS817D (*N* = 271). The dot represents the mean, and the error bars represent the standard deviation of the experiment.

ved *in vivo*. It supports a model in which the application of force to DNA is essential for stabilizing nascent D-loops.

3.3 Discussion

In this study, we identified a universally conserved interaction in Rad54, the mutation of which leads to the separation of distinct Rad54 functions. Disruption in contact between the two RecA lobes of Rad54 results in a functional protein that fails to form D-loops both *in vivo* and *in vitro.* However, it remains active in removing Rad51 that is pathologically bound to dsDNA and can complement *rad54* strains in the presence of certain DNA-damaging agents. Our data indicate that the Rad54 mutant is defective in pump activity and has severely diminished capacity to catalyze D-loop formation.

3.3.1 A Pump or a Motor

Brownian ratchets are molecular machines that harness thermal fluctuations in proteins to perform useful directional work (98). This is usually achieved by binding a cofactor,

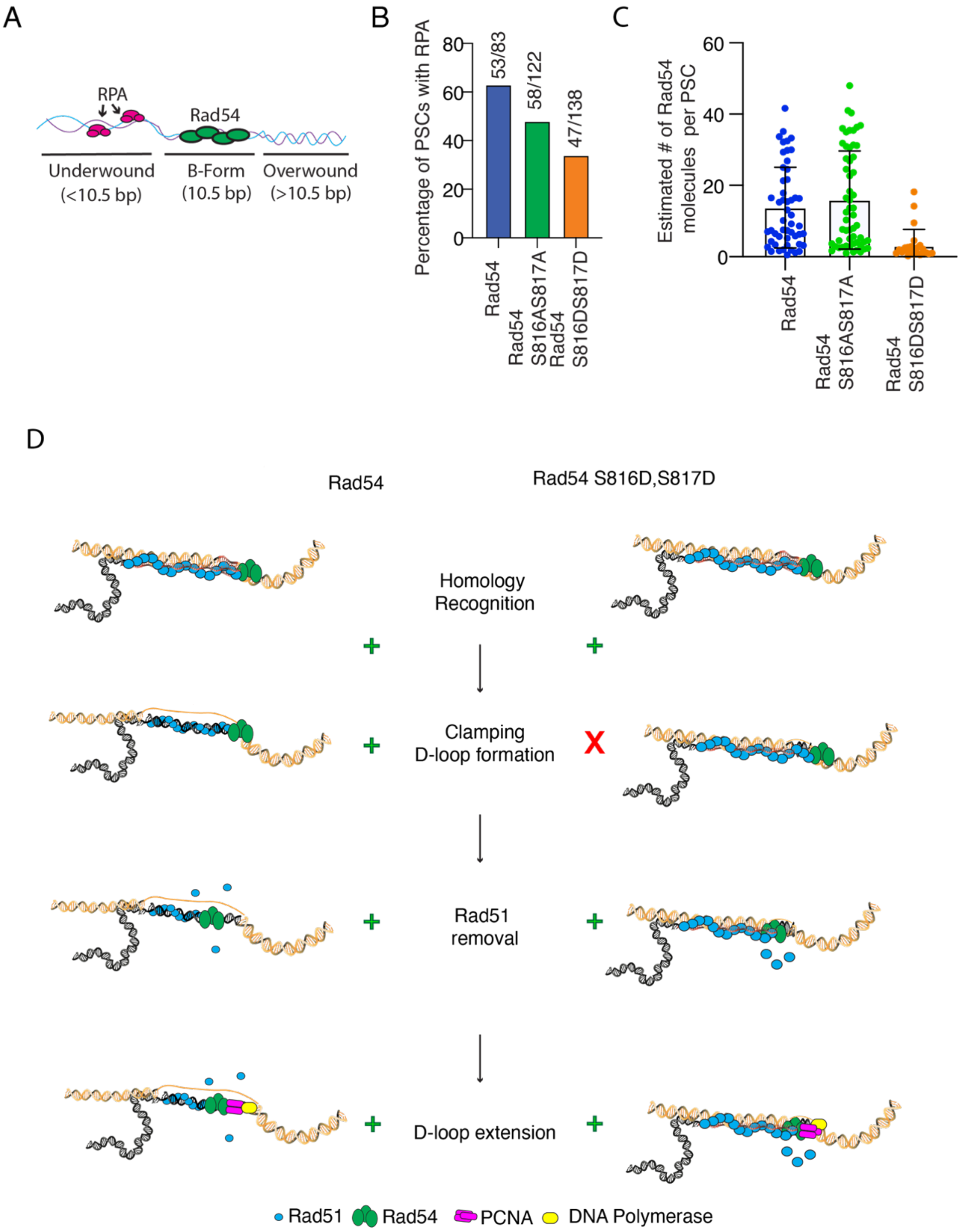

Figure 3.7: Disruption in Rad54 clamping reduced D-loop formation.

(A) Cartoon diagram illustrating the recruitment of RPA to regions of underwound DNA generated by the PSC. (B) Graph representing the percentage of PSCs (53/83), PSCs with Rad54 S816AS817A (58/122), and PSCs with Rad54 S816DS817D (47/138) that have RPA associated with them. (C) Graph representing the estimated number of GFP-

Rad54 molecules bound to the PSC after a 5-minute flow-off incubation for Rad54 (*N* = 51), Rad54 S816AS817A (*N* = 56), and Rad54 S816DS817D (*N* = 24). The bar represents the mean, and the error bar represents the standard deviation of the data. (D) Model illustrating the role of Rad54 during D-loop formation. On the left is the WT case, and on the right is the Rad54 S816DS817D.

such as ATP, which traps specific protein conformations. ATP-dependent ratchets can be categorized as motors or pumps. Motors use ATP hydrolysis to translocate along a linear or rotational track, such as a DNA helix. At the same time, pumps move molecules to create energy gradients. In both cases, motor slippage can reduce movement efficiency or disrupt the concentration gradient. The definition of Rad54 as a motor is obvious, and ATP hydrolysis allows physical movement along the DNA. However, Rad54 can also promote DNA underwinding by isolating short DNA segments (97). These isolated regions store energy in the form of underwound DNA, and by this definition, Rad54 can be considered a pump.

Our data suggest that the Rad54 S816DS817D mutation has little impact on linear translocation along DNA and instead affects Rad54's pump function. This occurs by disrupting the force applied to the DNA. To act as a pump and create a superhelical density gradient in the DNA, Rad54 must form multiple contacts with the substrate (97). If a single point of contact is lost in this organization, then the gradient will dissipate. The instability of the Rad54 S816DS817D mutant could cause it to dissociate from dsDNA more frequently, leading to a loss of topological isolation.

A second possibility is that the mutation generates a slippery ratchet, allowing leakage of isolated turns in the underwound region of DNA. Slippage could occur during Rad51-mediated strand exchange. Previous work has demonstrated that Rad51 invasion results in the addition of negative turns to the DNA (99,100). After enough turns are added to the DNA, the DNA collapses into a plectoneme or melts to relieve torsional stress. The inclusion of Rad54 in the PSC promotes DNA backbone melting as turns are added (97). Slippage of Rad54 would likely reduce the efficiency of this step-in strand exchange (Figure 3.7D). This step precedes the removal of Rad51 from the newly formed joint molecule, thus identifying a novel intermediate. Therefore, several of the activities assigned to Rad54 during HR are likely to depend on balancing its motor, removing Rad51 from dsDNA, and on pump functions that isolate underwound regions of dsDNA.

3.3.2 Specific mechanism of Rad54 separation of function mutant

Based on structural modeling, the substitution of S816 and S817 to Aspartic acid likely disrupts a contact that forms between the two RecA lobes of Rad54. Disruption affects Rad54's affinity for dsDNA. Similar structures and protein sequences are identified in all Rad54/Rdh54 (Rad54B) family members, as well as the closely related replication fork remodeling enzyme ATRX (101). The interaction is not found in other members of the Snf2 family of chromatin remodelers. A second function of Rad54 is to suppress the binding of Rad51 to dsDNA, stemming from the ability of Rad54 to remove Rad51 from dsDNA. This is generally considered a pathogenic state characterized by Rad51 overexpression, a condition that occurs in many types of human cancers (38). In our hands, the *rad54S816D, S817D* alleles suppressed phenotypes associated with pathogenic RAD51 overexpression, indicating that these mutants are separation-of-function. The ability to remove Rad51 from dsDNA has been proposed as the mechanism by which D-loops form. This model explains how Rad51 is removed from DNA, enabling DNA extension and repair (47,49).

The Rad51 removal model is widely accepted but has been challenged by models that propose Rad54 alters topology as a mechanism for D-loop formation. By identifying this separation-of-function mutant, we can clarify these two models. While the *rad54S816D, S817D* mutant has a severe defect in D-loop capture, it still promotes DNA extension at a level consistent with the amount of initial capture. No further defects are observed at extension, because this version of the protein is competent to remove Rad51. This observation is supported by the loss of extension in the *rad54S816D, S817D sgs1* double mutant, suggesting that the small amount of extension that occurs in the *rad54S816D, S817D* is lost. Stabilization is regulated by topology, and extension is regulated by Rad51 removal. Therefore, both activities are required in sequence to explain Rad54's activity at D-loop structures and the transition to DNA synthesis.

Previous phosphoproteomic experiments identified Rad54 S816 as a kinase site. We were unable to identify the specific kinase or context in which this residue might be phosphorylated. However, given that a phosphomimetic mutation at this site results in a separation-of-function mutant, it is possible that phosphorylation is cell-cycle stage-dependent and effectively balances the need to promote strand exchange with the need to remove Rad51 from dsDNA. This mechanism has been proposed for the kinase NEK1 in human cells (102), and a kinase that phosphorylates Rad54 at S816 may collaborate with NEK1 to regulate Rad54 function. Based on our analysis, the most likely kinase would come from the polo-like kinase family. However, further research is needed to validate this hypothesis.

3.3.3 The long and short of it

Mutations in Rad54 resulted in generally higher levels of long-tract gene conversion than WT during allelic recombination. The phenotypes appear distinct from those associated with previous Rad54 hypomorphic alleles, which primarily affect translocation (96). These mutants affected recombination outcomes but did not alter gene conversion tracts. The length of gene conversion tracts is a function of DNA polymerase activity (103). The *ade2-n* mutation is located ~950 bp upstream of the *I-Sce1* site in the *ade2-I* gene. Therefore, a higher proportion of strand exchange outcomes will need to occur on the 5' side of this mutation. Exchange would require longer ssDNA resection products or longer Rad51 filaments to invade upstream of the *ade2* mutation. These events could occur due to reduced D-loop capture efficiency, requiring longer Rad51 filaments, or a higher density of short Rad51 filaments on ssDNA to overcome the limitations imposed by reduced Rad54 function. Alternatively, the increase in long tract repair could be due to high levels of short extension events, followed by disruption and reinvasion (23). This is consistent with the increase in BIR and NCO outcomes observed in our experiments, and with the reduction in DNA extension observed in *rad54S816D, S817D sgs1* strains.

The high incidence of long tract repair, accompanied by increased NCO and BIR outcomes, may also reflect increased replication. In our system, full BIR outcomes require replication to the end of the chromosome. Shorter BIR events may become indistinguishable from NCO outcomes generated by SDSA and would appear as non-crossover outcomes. A current hypothesis is that Srs2 prevents the formation of toxic intermediates that may arise from ssDNA generated during BIR (22). The strand separation activity of Srs2 is not required during HR, and disruption of this activity is not synthetic lethal with *RAD54* (65). However, removal of Rad51 from the ssDNA generated during BIR prevents the accumulation of toxic intermediates. These outcomes have the potential to be more deleterious and involve significant opportunity for non-allelic genomic rearrangements. Therefore, the remodeling of the local DNA environment by Rad54 and Sgs1 may serve a protective function during HR by preventing potentially toxic repair intermediates from forming during the BIR pathway. The loss of CO outcomes and increase in BIR are symptomatic of reduced second-end engagement. Moreover, the near-complete loss of CO outcomes suggests that the double Holliday junction (dHJ) repair pathway may be lost, as this is the most likely repair pathway leading to CO formation. This severe outcome only occurred in the *rad54S816D, S817D sgs1* strain, but a general trend of CO loss and BIR increase is observed in the *sgs1*, *rad54S816A, S817A sgs1*, and *rad54S816D, S817D sgs1* strains. A significant reduction in DNA extension, like that observed in the *rad54S816D, S817D sgs1* strain, will also diminish second-end engagement, potentially impacting second-end capture (104). Both helicases may contribute to the stable formation of this critical intermediate. Biochemically, the reduction of Rad54 binding to dsDNA and the topological isolation of donor DNA regions may contribute to the stable formation of the dHJ. It is less clear how Sgs1 may contribute to this outcome mechanistically. dHJ formation in the absence of Rad54 is observed in many organisms, and during meiosis (105). In these scenarios, alternative proteins may remodel DNA in a manner like Rad54, thereby stabilizing primary-strand exchange intermediates to promote second-end capture and Holliday junction formation. Therefore, the underlying cause of increased second-end engagement is likely regulation of DNA topology.

An alternative possibility is that the inability to regulate topology at strand-exchange intermediates leads to reduced resistance to anti-crossover factors, such as Sgs1-Top3-Rmi1 (STR) (86,106). Rad54 and STR have both been implicated in branch migration during HR. These outcomes are consistent with observations in the *rad54S816A, S817A*, and *rad54S816D, S817D* single mutants. The act of branch migration generates significant topological stress along the DNA, with positive supercoils forming ahead of the branch. Therefore, branch migration to promote dissolution might be inhibited by Rad54's ability to isolate a DNA domain topologically. Alternatively, the lack of Rad54 binding and stabilization could reduce cleavage by the Mus81-Mms4 complex, thereby facilitating the formation of crossovers and half-crossovers (22,91). These possibilities remain speculative, and future work will be needed to understand the impact of Rad54-mediated DNA remodeling on recombination outcomes.

3.4 Conclusions

In this study, we identified a universally conserved mutation in Rad54 that reduces binding to dsDNA. This caused a severe defect in D-loop formation *in vivo* but did not alter the protein's ability to remove Rad51 from double-stranded DNA. From this, we hypothesize that the separation-of-function mutant fails to stabilize initial D-loop formation but remains competent to remove Rad51 from the newly formed D-loop. This apparent separation of function enables us to better understand Rad54's sequential action at initial strand-exchange intermediates, thereby unifying two existing models in the field. Future work should focus on understanding how Rad54's loss of DNA-binding affects outcomes in human cell lines and at DNA replication forks.

Data availability

All data is available upon request.

Acknowledgements

We would like to acknowledge Eric Alani and Eric C. Greene for critical reading of the manuscript. We want to thank Wolf Heyer, Lorraine Symington, and Jim Haber for providing the parent reporter strains used in this study. We would also like to thank the members of the Cornell R3 group and the Crickard laboratory for their helpful input during the project's development.

Author contributions

JH performed the initial screen, performed experiments, analyzed single molecule experiments, and helped write the manuscript. DM performed single molecule experiments, helped analyze the single molecule experiments, and provided input on writing. AX helped with the initial screen and performed imaging of cellular foci. LP performed spot assays for Rad54 mutants. JBC performed allelic recombination experiments, guided the research, provided funding, and wrote the manuscript with input from all authors. This work is supported by NIGMS R35142457 and American Cancer Research Scholar Grant RSG-25-1410641-01-DMC to JBC.

Conflicts of Interest

The authors declare no competing conflicts of interest.

Table 3.E1: Strains used in the study.

Strains	Genotype	Source or reference
BY4741 (WT)		Dharmacon
BY4741-*rad54Δ*	*rad54Δ*	Dharmacon
BY4741	*RAD54::rad54S816A-KANMX*	This study
BY4741	*RAD54::rad54S817A-KANMX*	This study
BY4741	*RAD54::rad54S816A, S817A-KANMX*	This study
BY4741	*RAD54::rad54S816D-KANMX*	This study
BY4741	*RAD54::rad54S817D-KANMX*	This study
BY4741	*RAD54::rad54S816D, S817D-KANMX*	This study
WDHY5511	*ura3::A-HOcs, lys2::A, trp1::GAL-HO-hphMX, his3D200, can1-100, leu2-3, 112, ade2-1, RAD5*	Piazza et al 2020
JBC423 (WDHY5511)	*rad54::KANMX*	This study
JBC281 (WDHY5511)	*RAD54::RAD54-KANMX*	This study
JBC367 (WDHY5511)	*RAD54::rad54S816A, S817A-KANMX*	This study
JBC369 (WDHY5511)	*RAD54::rad54S816D, S817D-KANMX*	This study
JBC380 (WDHY5511)	*sgs1::HISIII*	This study
JBC388 (WDHY5511)	*RAD54::rad54S816A, S817A-KANMX, sgs1::HISIII*	This study
JBC478 (WDHY5511)	*RAD54::rad54S816D, S817D-KANMX, sgs1::HISIII*	This Study
TGI354	*TGI 354 JKM 146 (arg5,6::MATa::HPH)*	Ira et al 2003
JBC425 (TGI354)	*rad54::KANMX*	This study
JBC357 (TGI354)	*RAD54::RAD54-KANMX*	This study
JBC359 (TGI354)	*RAD54::rad54S816A,S817A-KANMX*	This study
JBC361 (TGI354)	*RAD54::rad54S816D,S817D-KANMX*	This study
Protease deficient yeast strain	*MATα leu2 trp1 ura3–52 prb1–1122 his3::pGAL1–GAL*	Crickard et al 2020
11C (LYS2202)	*MATα ade2-I lys2:GAL-ISCEI his3:HphMX4*	Mazon et al. 2010

15D (LYS2205)	*MATa ade2-n his3:NatMX4 met22:klURA3*	Mazon et al. 2010
JBC106	*11C-RAD54::RAD54-KanMX*	Keymakh et al 2022
JBC105	*15D-RAD54::RAD54-KanMX*	Keymakh et al 2022
JBC413	*11C-RAD54::rad54S816A, S817A-KanMX*	This Study
JBC414	*15D-RAD54::rad54S816A, S817A-KanMX*	This Study
JBC479	*11C-RAD54::rad54S816D, S817D-KanMX*	This Study
JBC417	*15D-RAD54::rad54S816D, S817D-KanMX*	This Study
JBC 434	*11C-RAD54::RAD54-KanMX sgs1::HIS3*	This Study
JBC 436	*15D-RAD54::RAD54-KanMX sg1::HIS3*	This Study
JBC 430	*11C-RAD54::rad54S816A, S817A-KanMX sgs1::HIS3*	This Study
JBC 432	*15D-RAD54::rad54S816A, S817A-KanMX sgs1::HIS3*	This Study
JBC522	*11C-RAD54::rad54S816D, S817D-KanMX sgs1::HIS3*	This Study
JBC444	*15D-RAD54::rad54S816D, S817D-KanMX sgs1::HIS3*	This Study
JBC501	*W303 MATa srs2::TRP1*	This Study
JBC506	*W303 MATα RAD54::rad54S816D, S817D-3xHA-KanMX*	This Study
JBC510	*W303 MATα RAD54::RAD54-3xHA-KanMX*	This Study
JBC514	*W303 MATα rad54::KanMX*	This Study
JBC490 (WDHY5511)	*rad51I345T-LEU2*	
JBC517 (WDHY5511)	*rad54 S816D, S817D-KanMx rad51I345T-LEU2*	
Diploids		
JBC106xJBC105		
JBC413xJBC414		This Study
JBC479xJBC417		This Study
JBC434xJBC436		This Study
JBC430xJBC432		This Study
JBC444xJBC522		This Study

Table 3.E2: Plasmid in the study.

Backbone	Construction	Source
pRS305	*RAD54-KANMX*	This study
pRS305	*rad54S816A-KANMX*	This study
pRS305	*rad54S816D-KANMX*	This study
pRS305	*rad54S816A, S817A-KANMX*	This study
pRS305	*rad54S816D, S817D-KANMX*	This study
pRS415	*RAD54*	Crickard et al. 2020
pRS415	*rad54S816A*	This study
pRS415	*rad54S816D*	This study
pRS415	*rad54S816A, S817A*	This study
pRS415	*rad54S816D, S817D*	This study
pRS415	*rad54T85A*	This study
pRS415	*rad54T85E*	This study
pRS415	*rad5T132A*	This study
pRS415	*rad5T132E*	This study
pRS415	*rad5T155A*	This study
pRS415	*rad5T155E*	This study
pRS415	*rad5S214A*	This study
pRS415	*rad5S214D*	This study
pRS415	*rad5T231A*	This study
pRS415	*rad5T231E*	This study
pRS415	*rad5S303A*	This study
pRS415	*rad5S303D*	This study
pRS415	*rad54S318A*	This study
pRS415	*rad54S318D*	This study
pYES	*GST-GFP-RAD54*	Crickard et al, *Cell*, 2020
pYES	*GST-GFP-rad54S816A, S817A*	This study
pYES	*GST-GFP-rad54S816D, S817D*	This study

Table 3.E3: Oligos used in the study.

Name	Sequence	Purpose
90-mer DNA	Atto647N-GATGTTCTGCTGGATATGCACTTTTCCGGGC TGACGTACACCGTGCTCAGCCTGTTTTTCA GCGATCCGGATATGCATCCGCTGGATTTC	Single Molecule imaging
olWDH1760	CAGCGGGCTTGCAGAAGTTG	To amplify genomic DNA at *ARG4*
olWDH1761	GGCCAATTAGTTCACCAAGACG	To amplify genomic DNA at *ARG4*
olWDH1766	GTTTCAGCTTTCCGCAACAG	To quantify DSB induction
olWDH1767	GGCGAGGTATTGGATAGTTCC	To quantify DSB induction
olWDH2009	CACCACTTTGCCATTCAACAC	To amplify at the downstream site of elongation
olWDH2010	TGCTCGGAGATTACCGAATC	To amplify at upstream site of the DSB, used with olWDH2009 to quantify DLE signal
olWDH2011	TGCGAGGTTTTCTTGGTCAG	Used with olWDH2009 to quantify *Hin*dIII recognition site restoration
olWDH2012	CGAGGCATATTTATGGTGAAGG	Used with olWDH2010 to measures *Hin*dIII recognition site restoration
olWDH2052	ATGTGCCTTCCTACCGCTC	To quantify intramolecular ligation efficiency of *Hin*dIII-derived fragments
olWDH2053	TCAAGCGTGGTTACATTCCTTAC	To quantify intramolecular ligation efficiency of *Hin*dIII-derived fragments
olWDH2007	TCTGCTCGGAGATTACCGAATCAAAAAAATTCAAAGAAACCGGAATCAAAAAAAAGAACAAAAAAAAAAAAGATGAATTGAAAAGCTTTATGGACCGAC	To restore *Hin*dIII site
olWDH2046	AATCTTTGTGAAGCTTCGCAAGTATTCATTTTAGACCCATGGTGGAACCCTAGTGTTGAA	To restore *Hin*dIII site

	TGGCAAAGTGGTGATAGAGT TCATAGAATTGGTCAGTAT	
olWDH1762	ACTTCGAATTTCGGCACTTC	To quantify intramolecular ligation efficiency of *Eco*RI-derived fragments
olWDH1763	CGATGAAACGTTAAGTGACC AC	To quantify intramolecular ligation efficiency of *Eco*RI-derived fragments
olWDH1764	AGAGCGGTCAGTAGCAATCC	To amplify at the upstream of DSB
olWDH1765	CACACGCGAAAAACCGCC	To amplify at the upstream of the donor DNA, used with olWDH1764 to quantify DLC signal
olWDH2019	CTTTAACCGGACGCTCGA	To quantify psoralen crosslinking efficiency
olWDH2020	TTGAGTTTATTGCTGCCGTC	To quantify psoralen crosslinking efficiency
olWDH1768	AGGAGCACAGACTTAGATTG G	Used with olWDH1764 to measure *Eco*RI recognition site restoration
olWDH1770	CGAAATCATCTTCGGTTAAA TCCAAAACGGCAGAAGCCT GAATGAAACATATGAACCA ATTGGAGGACGTCAATGAAT TCTGGGGATCCATTGCATTT TT	To restore *Eco*RI site

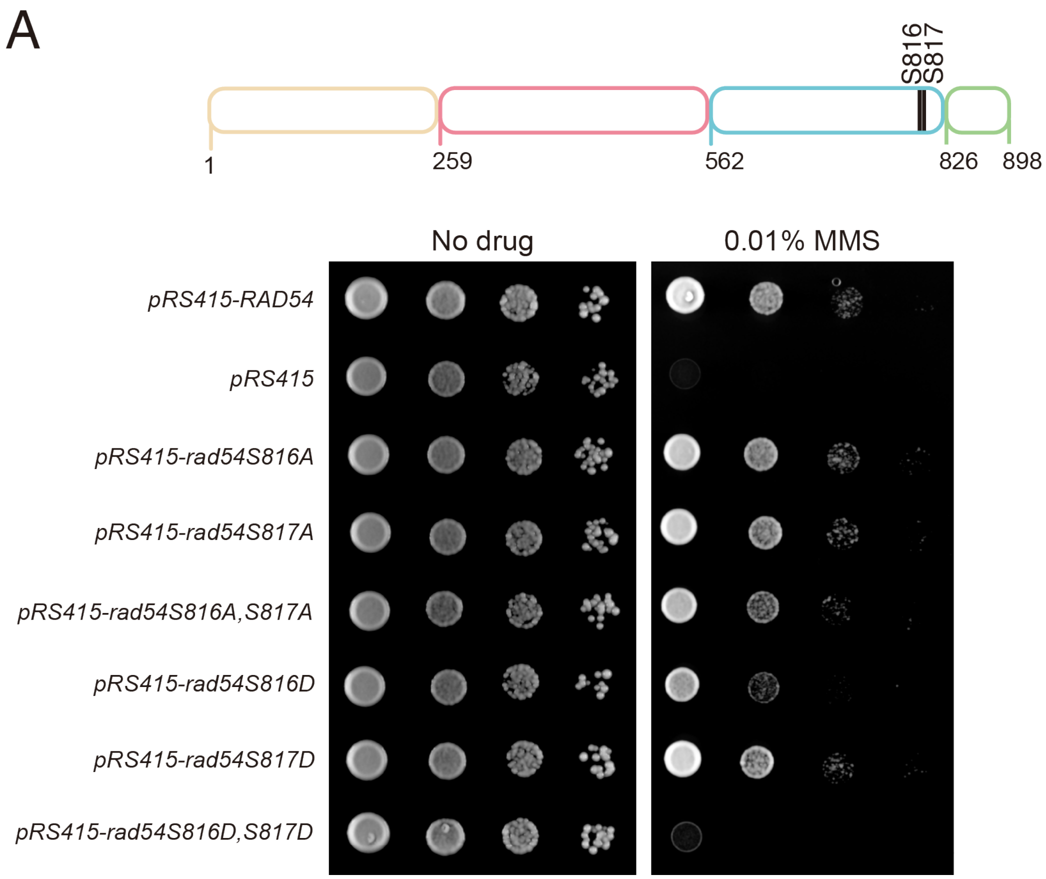

Figure 3.E1: *rad54S816D, S817D* is more deficient than *rad54S816D.*

(A) Serial dilution spot assay to determine the sensitivity of yeast strains with single amino acid substitutions at *RAD54* S816 and S817 or double mutations at the same positions. Serine was mutated to either Alanine or Aspartic acid.

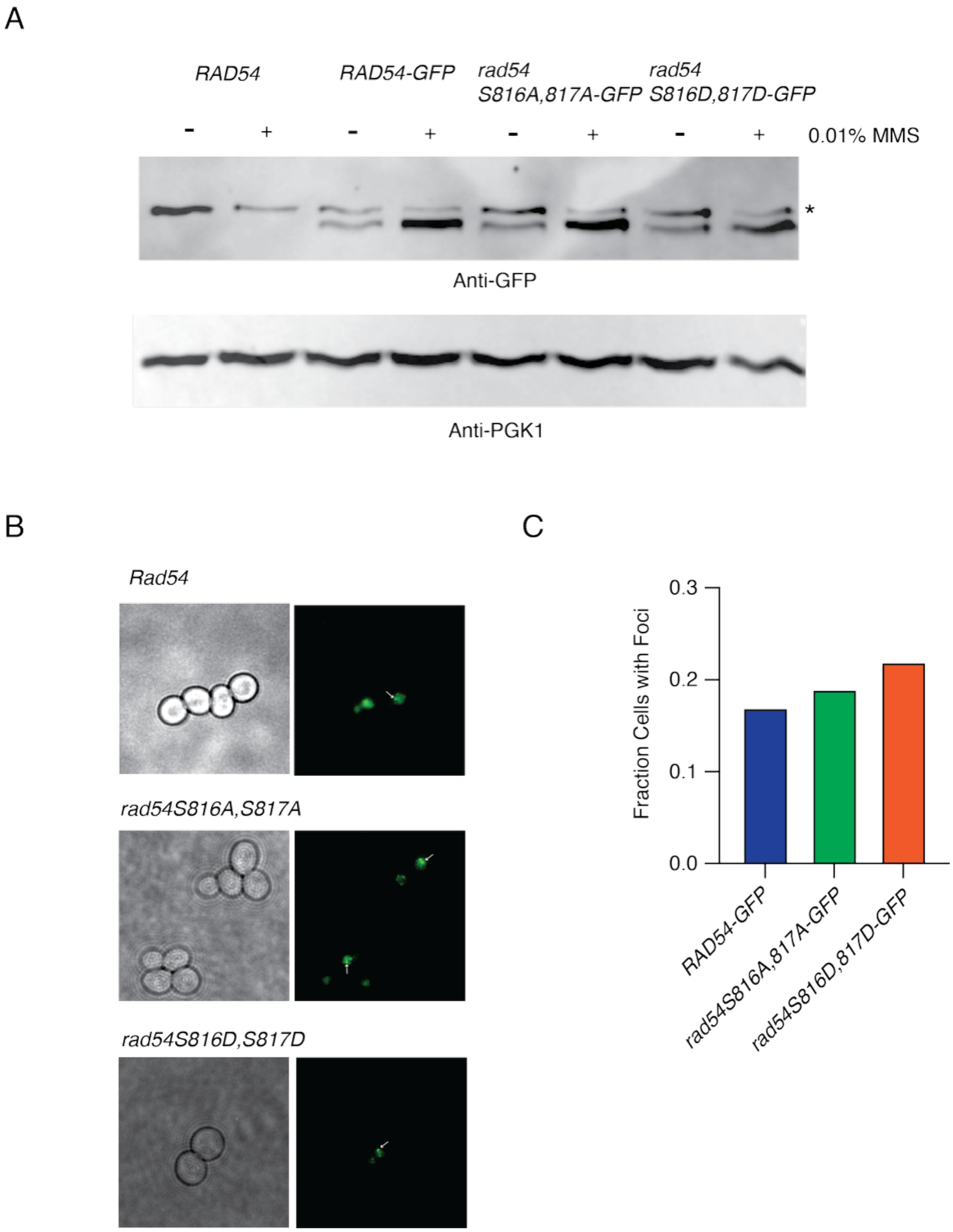

Figure 3.E2: Mutant forms of Rad54 are expressed in cells.

(A) Representative western blot illustrating the expression of *RAD54-GFP*, *rad54S816A, S817A-GFP*, and *rad54S816D, S817D-GFP* with and without 0.01% MMS. PGK1 is used as a loading control. The Asterix represents a non-specific band. (B) Fluorescent microscope images illustrating that *RAD54-GFP*, *rad54S816A, S817A-GFP*, and *rad54S816D, S817D-GFP* form foci in response to MMS treatment. (C) Bar graph quantifying the percentage of cells that form foci in response to MMS treatment.

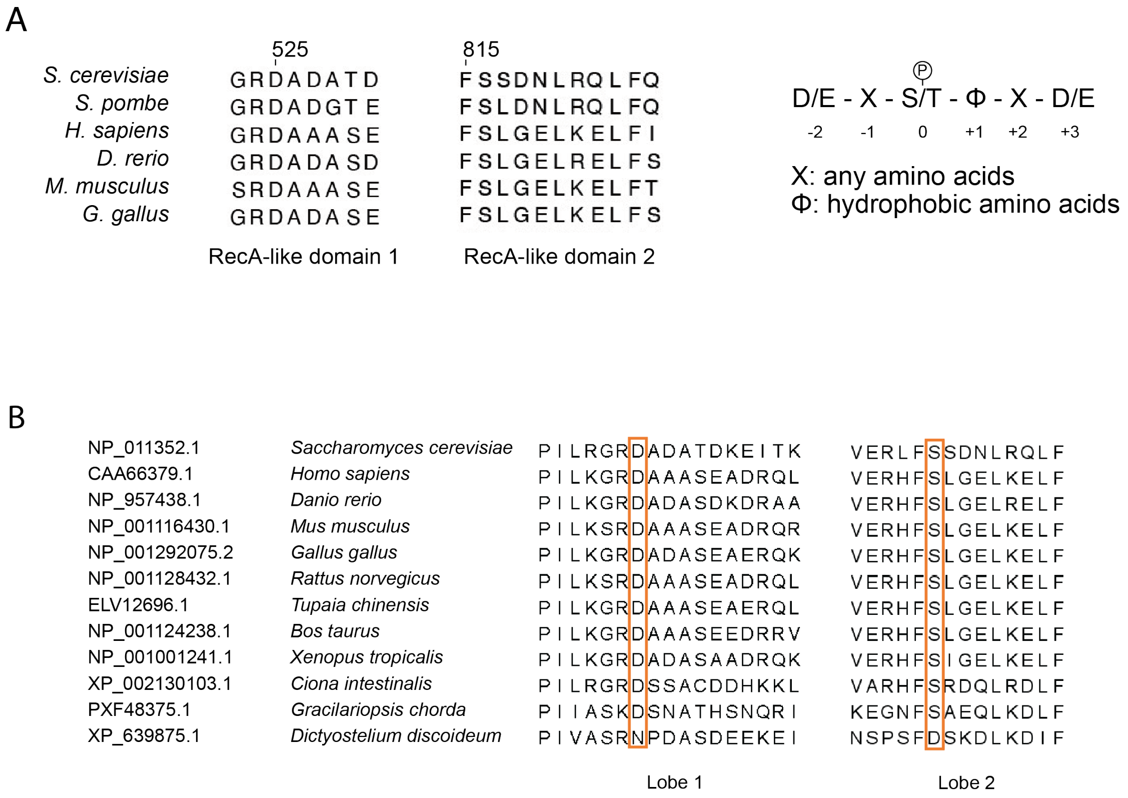

Figure 3.E3: Excerpt from multiple sequence alignment.

(A) Multiple sequence alignment of Rad54 interacting region (Left) and consensus kinase sequence for Polo-like-kinase (Right). The human RAD54 matches the consensus sequence. (B) An excerpt from the Rad54 multiple sequence alignment. Shown are the two interacting regions on lobes 1 and 2, respectively. Included in this alignment in *Dictyostelium discoideum,* which has a naturally occurring Aspartic acid in place of Serine on lobe 2.

A

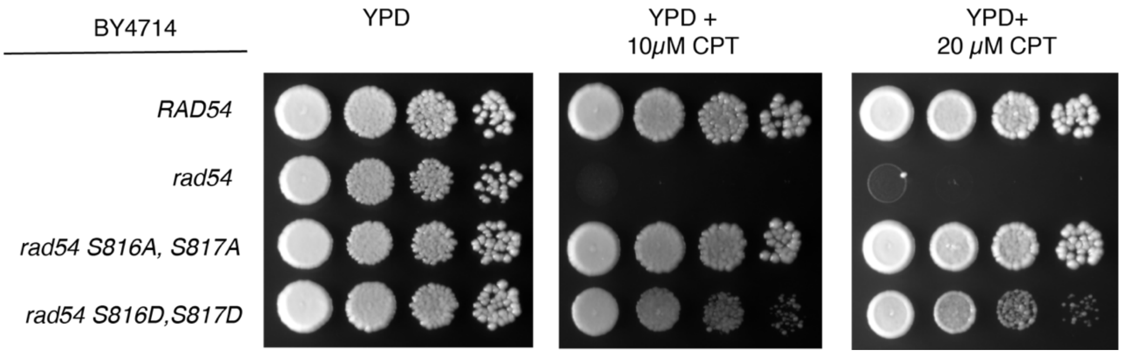

Figure 3.E4: BY4741 are less sensitive to CPT in *rad54S816D, S817D.*

(A) Spot assay illustrating *RAD54*, *rad54*, *rad54S816A, S817A,* and *rad54S816D, S817D* sensitivity to CPT.

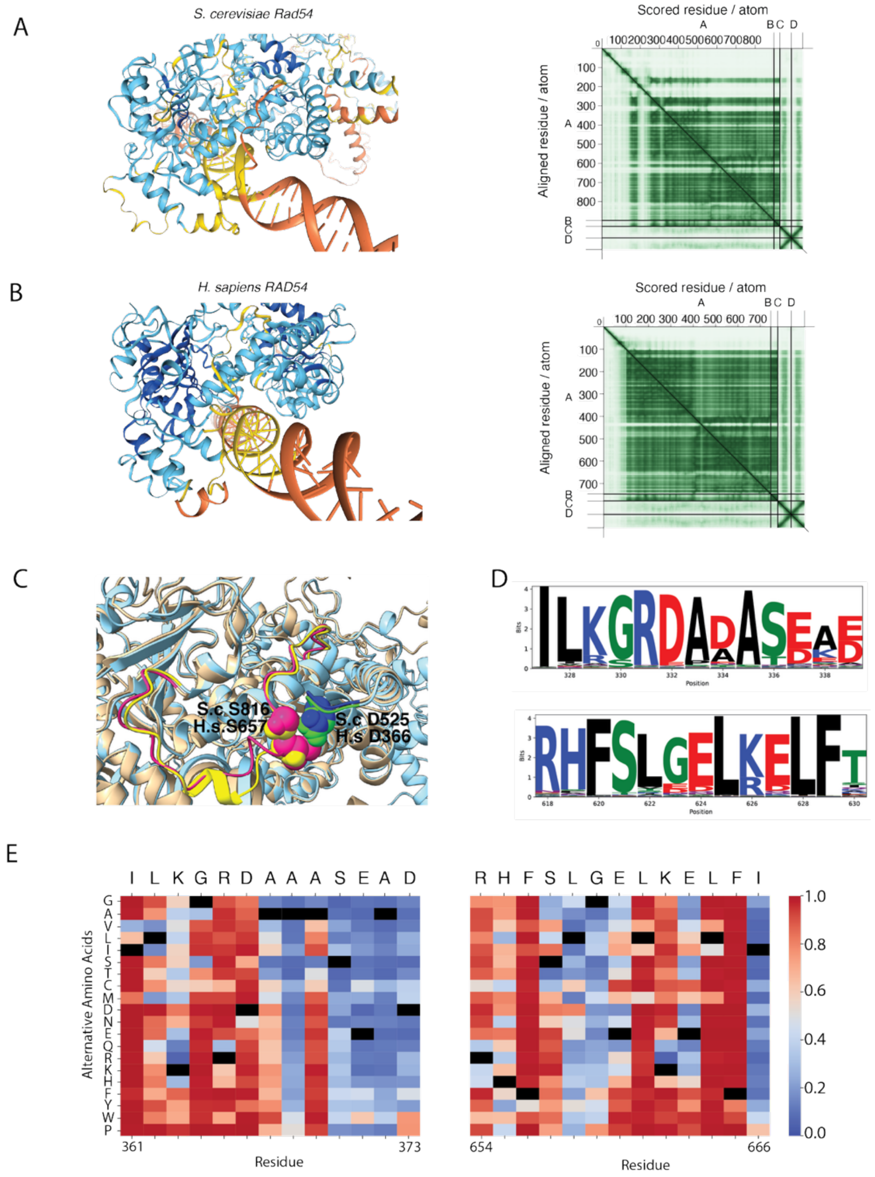

Figure 3.E5: Computational analysis of potential phosphorylation sites on Rad54.

(A) AlphaFold3 model for *S. cerevisiae* Rad54 bound to dsDNA, colored for confidence with the pLDDT formation (Left). PAE plot for *S. cerevisiae* Rad54 AlphaFold structure (Right). (B) AlphaFold3 model for *H. sapiens* RAD54 bound to dsDNA, colored for confidence with the pLDDT formation (Left). PAE plot for *H. sapiens* RAD54 AlphaFold structure (Right). (C) Structural superposition of *S. cerevisiae* Rad54 and *H. Sapiens* RAD54. The predicted interacting residues are shown as space-filling spheres. (D) Protein sequence logos generated from 1224 eukaryotic Rad54 sequences, illustrating the sequence conservation in these two regions using logo maker. (E) Sequence view of interacting region of *H. sapiens* RAD54 using a predicted pathogenicity plot for individual amino acid substitutions generated via AlphaFold.

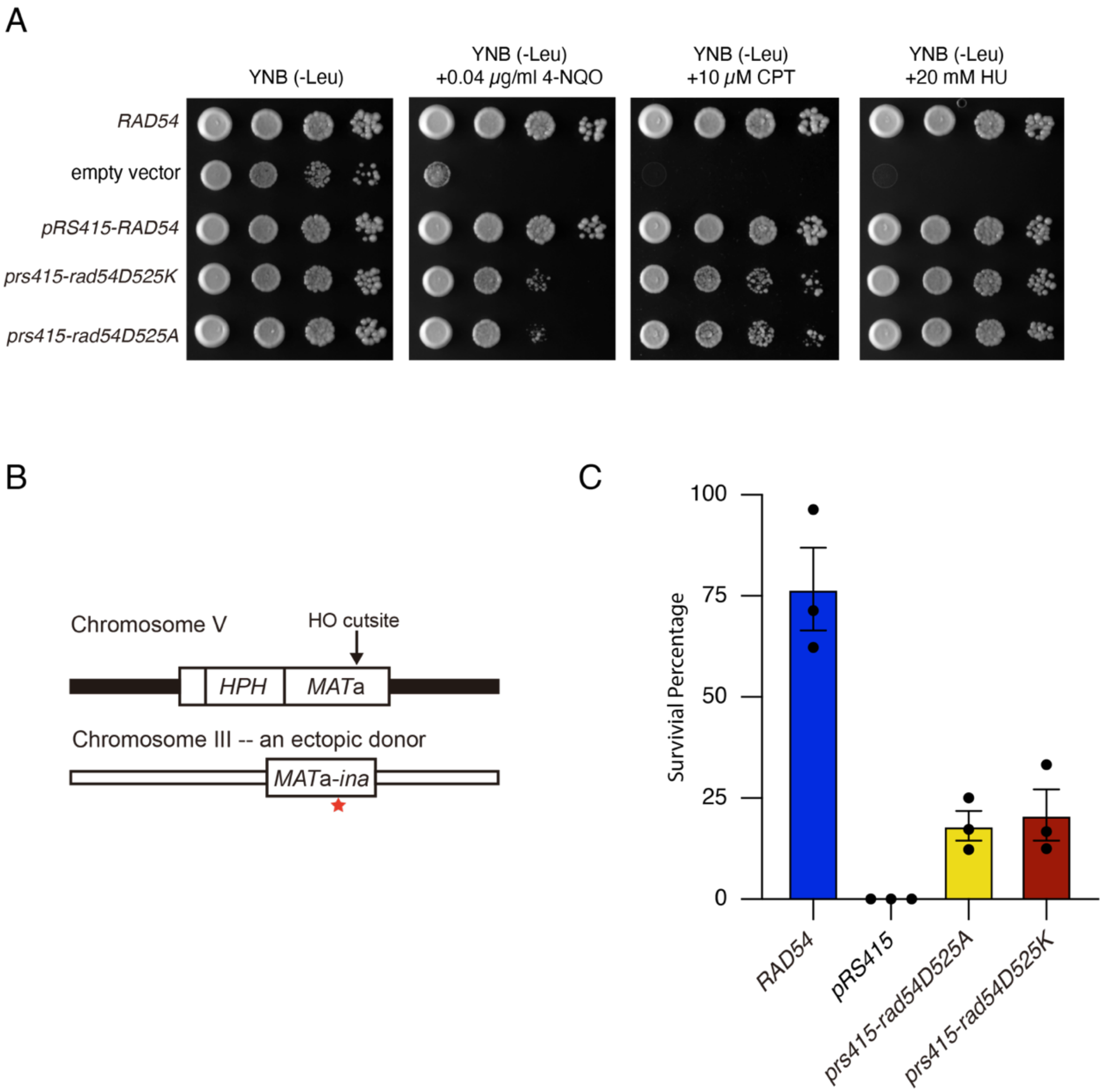

Figure 3.E6: *rad54D525A* and *rad54D525K* phenocopy phosphomimic mutants.

(A) Yeast spot assays testing the ability of *rad54D525A* and *rad54D525K* to complement 4-NQO, CPT, and HU sensitivity. (B) Schematic diagram for ectopic double-strand break repair assay. (C) Bar graph representing the survival percentage of DSB-induced cells in TGI354 *rad54* expressing *pRS415-RAD54*, empty vector, *pRS415-rad54D525A*, and *pRS415-rad54D525K*. The bars represent the mean, and the error bars represent the standard error measurement from three independent experiments.

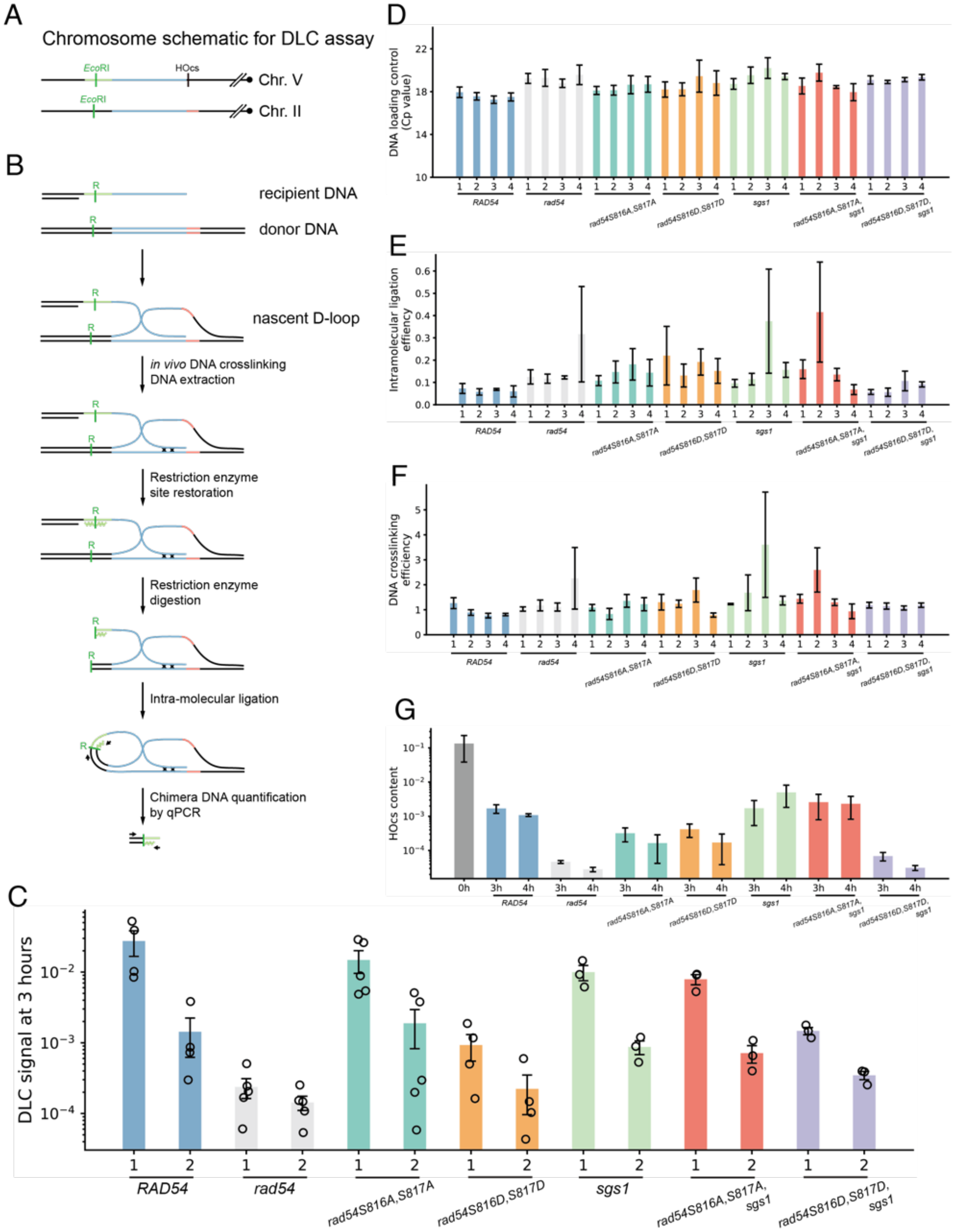

Figure 3.E7: Supplementary information for the DLC assay.

(A) Chromatin schematic for the DLC assay. (B) Rationale for the DLC assay. (C) DLC signal at 3 hours. Column set 1 shows results with a hybrid oligo added; column set 2 shows results without adding a hybrid oligo. (D) DNA loading control (Cp values for amplicons at *ARG4*). Columns: (1) 3 hours with hybrid oligo; (2) 3 hours without hybrid oligo; (3) 4 hours with hybrid oligo; (4) 4 hours without hybrid oligo. (E) Intramolecular ligation efficiency calculated as ([intramolecular ligation amplification efficiency]^[-Cp$_{\text{(ligation)}}$]/[*ARG4* amplification efficiency]^[-Cp$_{(ARG4)}$]). Columns as in (D). (F)

Crosslinking efficiency calculated as ([ssDNA amplification efficiency]^[-$\mathrm{Cp}_{(\mathrm{ssDNA})}$]/[*ARG4* amplification efficiency]^[-$\mathrm{Cp}_{(ARG4)}$]). Columns as in (D). (G) DNA content at HO cut sites, calculated as ([HO cut site ligation amplification efficiency]^[-$\mathrm{Cp}_{(HOcs)}$]/[*ARG4* amplification efficiency]^[-$\mathrm{Cp}_{(ARG4)}$]). The "0h" value represents the mean across all available 0-hour time point groups from different genome types with a hybrid oligo added.

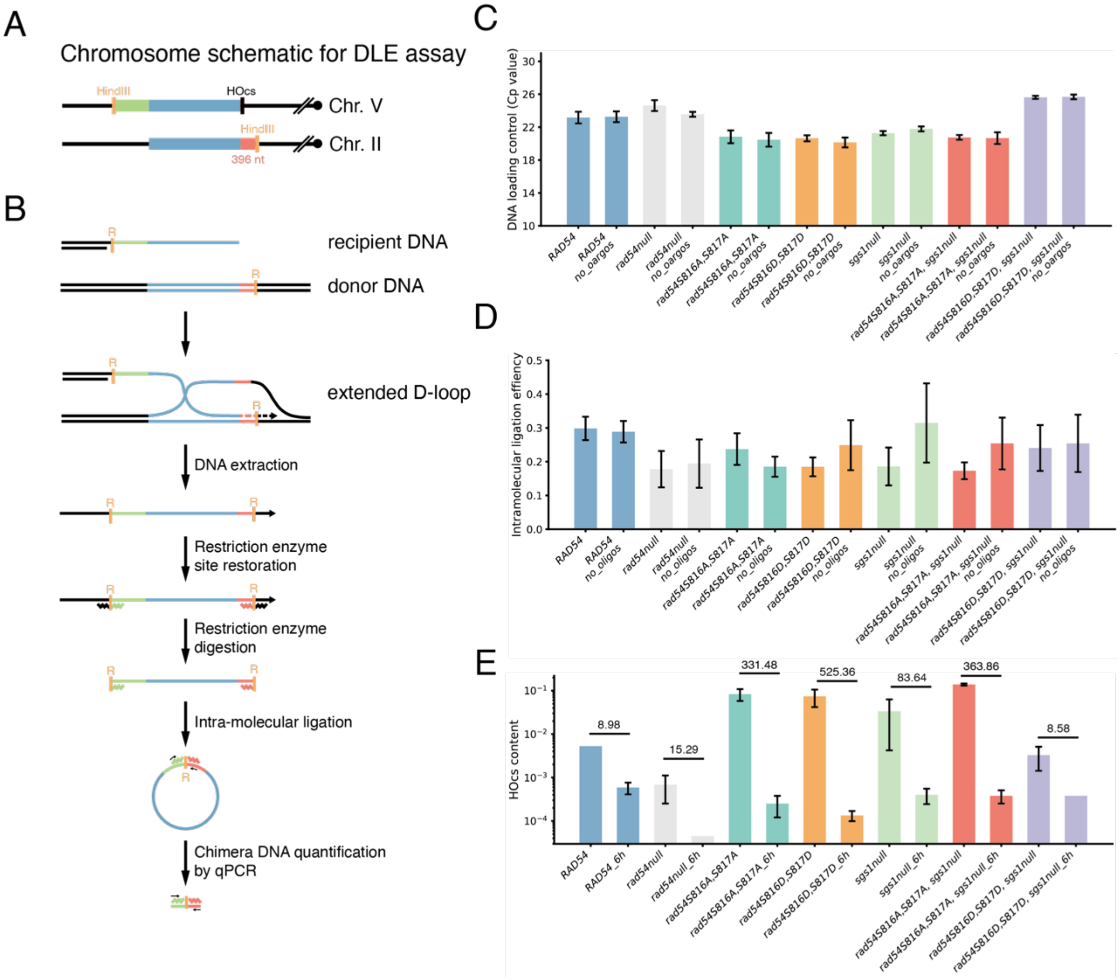

Figure 3.E8: Supplementary information for the DLE assay.

(A) Chromatin schematic for the DLE assay. (B) Rationale for the DLE assay. (C) DNA loading control (Cp values for amplicons at *ARG4*). (D) Intramolecular ligation efficiency calculated as ([intramolecular ligation amplification efficiency]^[-Cp$_{(\text{ligation})}$]/[*ARG4* amplification efficiency]^[-Cp$_{(ARG4)}$]). (E) DNA content at HO cut sites ([HO cut site ligation amplification efficiency]^[-Cp$_{(HOcs)}$]/[*ARG4* amplification efficiency]^[-Cp$_{(ARG4)}$]) at 0-hour and 6-hour time points with hybrid oligos added. Numbers above the bars indicate the reduction of DNA content at the HO cut site after 6 hours.

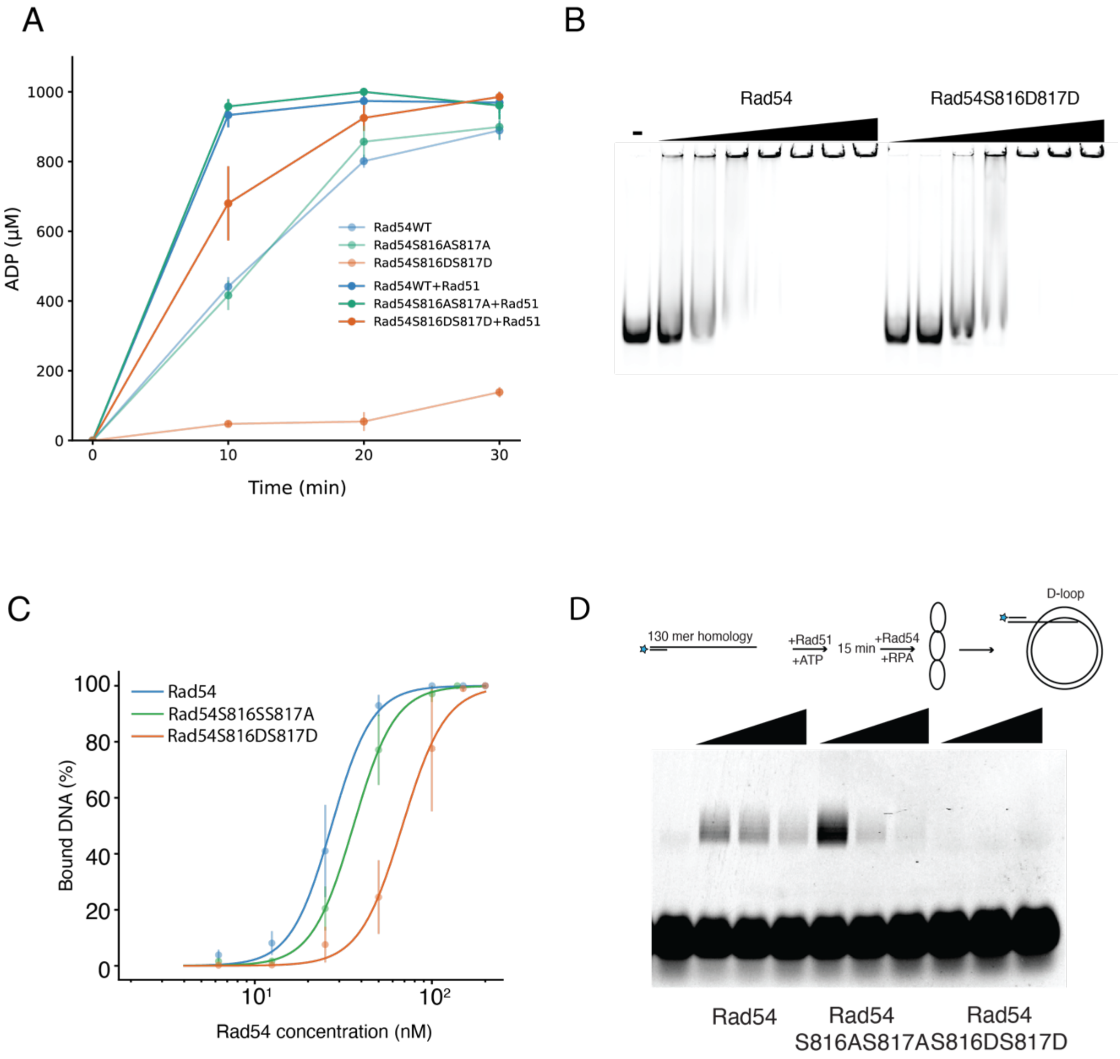

Figure 3.E9: Rad54 S816DS817D has lower ATP hydrolysis activity, lower dsDNA binding affinity and lower *in vitro* D-loop formation efficiency.

(A) Line graph representing ATP hydrolysis experiments for Rad54, Rad54 S816AS817A, and Rad54 S816DS817D with and without Rad51. The error bars represent the standard error measurement of three independent experiments. (B) Representative electromobility shift assay (EMSA) for Rad54 and Rad54 S816DS817D. (C) Quantification of EMSA for Rad54, Rad54 S816AS817A, and Rad54 S816DS817D is performed using a Hill equation. Fitting is done by neutcurve. The dots represent the mean, and the error bars represent the standard error measurement of the data. (D) Representative *in vitro* D-loop formation experiment for Rad54, Rad54 S816AS817A, and Rad54 S816DS817D.

References

1. Symington, L.S., Rothstein, R. and Lisby, M. (2014) Mechanisms and regulation of mitotic recombination in *Saccharomyces cerevisiae*. *Genetics*, **198**, 795-835.

2. Kowalczykowski, S.C. (2015) An Overview of the Molecular Mechanisms of Recombinational DNA Repair. *Cold Spring Harb Perspect Biol*, **7**, a016410.

3. Filippo, J.S., Sung, P. and Klein, H. (2008) Mechanism of Eukaryotic Homologous Recombination. *Annu Rev Biochem*, **77**, 229-257.

4. Raina, V.B., Jessop, A. and Greene, E.C. (2025) Biochemical Mechanisms of Genetic Recombination and DNA Repair. *Annu Rev Biochem*, **94**, 161-193.

5. Szostak, J.W., Orr-Weaver, T.L., Rothstein, R.J. and Stahl, F.W. (1983) The double-strand-break repair model for recombination. *Cell*, **33**, 25-35.

6. Cejka, P. and Symington, L.S. (2021) DNA End Resection: Mechanism and Control. *Annu Rev Genet*, **55**, 285-307.

7. Gnügge, R. and Symington, L.S. (2021) DNA end resection during homologous recombination. *Curr Opin Genet Dev*, **71**, 99-105.

8. Symington, L.S. (2014) End resection at double-strand breaks: mechanism and regulation. *Cold Spring Harb Perspect Biol*, **6**, a016436.

9. Symington, L.S. and Gautier, J. (2011) Double-strand break end resection and repair pathway choice. *Annu Rev Genet*, **45**, 247-271.

10. Bell, J.C., Plank, J.L., Dombrowski, C.C. and Kowalczykowski, S.C. (2012) Direct imaging of RecA nucleation and growth on single molecules of SSB-coated ssDNA. *Nature*, **491**, 274-278.

11. Yang, H. and Pavletich, N.P. (2021) Insights into homology search from cryo-EM structures of RecA-DNA recombination intermediates. *Curr Opin Genet Dev*, **71**, 188-194.

12. Yang, H., Zhou, C., Dhar, A. and Pavletich, N.P. (2020) Mechanism of strand exchange from RecA-DNA synaptic and D-loop structures. *Nature*, **586**, 801-806.

13. Xu, J., Zhao, L., Xu, Y., Zhao, W., Sung, P. and Wang, H.-W. (2017) Cryo-EM structures of human RAD51 recombinase filaments during catalysis of DNA-strand exchange. *Nat Struct Mol Biol*, **24**, 40-46.

14. Dumont, A., Mendiboure, N., Savocco, J., Anani, L., Moreau, P., Thierry, A., Modolo, L., Jost, D. and Piazza, A. (2024) Mechanism of homology search expansion during recombinational DNA break repair. *Mol Cell*, **84**, 3237-3253.

15. Haber, J.E. (2018) DNA repair: the search for homology. *Bioessays*, **40**, e1700229.

16. Qi, Z., Redding, S., Lee, J.Y., Gibb, B., Kwon, Y., Niu, H., Gaines, W.A., Sung, P. and Greene, E.C. (2015) DNA sequence alignment by microhomology sampling during homologous recombination. *Cell*, **160**, 856-869.

17. Renkawitz, J., Lademann, C.A. and Jentsch, S. (2014) Mechanisms and principles of homology search during recombination. *Nat Rev Mol Cell Biol*, **15**, 369-383.

18. Greene, E.C. (2016) DNA sequence alignment during homologous recombination. *J Biol Chem*, **291**, 11572-11580.

19. Piazza, A., Shah, S.S., Wright, W.D., Gore, S.K., Koszul, R. and Heyer, W.D. (2019) Dynamic processing of displacement loops during recombinational DNA repair. Mol *Cell*, **73**, 1255-1266.e1254.

20. Joudeh, L., Appleby, R.E., Maman, J.D. and Pellegrini, L. (2025) Structural mechanism of strand exchange by the RAD51 filament. *eLife*, **14**, RP107114.

21. Anand, R.P., Tsaponina, O., Greenwell, P.W., Lee, C.S., Du, W., Petes, T.D. and Haber, J.E. (2014) Chromosome rearrangements via template switching between diverged repeated sequences. *Genes Dev*, **28**, 2394-2406.

22. Elango, R., Sheng, Z., Jackson, J., DeCata, J., Ibrahim, Y., Pham, N.T., Liang, D.H., Sakofsky, C.J., Vindigni, A., Lobachev, K.S. et al. (2017) Break-induced replication promotes formation of lethal joint molecules dissolved by Srs2. *Nat Commun*, **8**, 1790.

23. Kramara, J., Osia, B. and Malkova, A. (2018) Break-Induced Replication: The Where, The Why, and The How. *Trends Genet*, **34**, 518-531.

24. Shinohara, A., Ogawa, H. and Ogawa, T. (1992) Rad51 protein involved in repair and recombination in *S. cerevisiae* is a RecA-like protein. *Cell*, **69**, 457-470.

25. Sung, P. (1994) Catalysis of ATP-dependent homologous DNA pairing and strand exchange by yeast RAD51 protein. *Science*, **265**, 1241-1243.

26. Agarwal, S., van Cappellen, W.A., Guénolé, A., Eppink, B., Linsen, S.E.V., Meijering, E., Houtsmuller, A., Kanaar, R. and Essers, J. (2011) ATP-dependent and independent functions of Rad54 in genome maintenance. *J Cell Biol*, **192**, 735-750.

27. Amitani, I., Baskin, R.J. and Kowalczykowski, S.C. (2006) Visualization of Rad54, a chromatin remodeling protein, translocating on single DNA molecules. *Mol Cell*, **23**, 143-148.

28. Crickard, J.B. (2021) Discrete roles for Rad54 and Rdh54 during homologous recombination. *Curr Opin Genet Dev*, **71**, 48-54.

29. Crickard, J.B., Moevus, C.J., Kwon, Y., Sung, P. and Greene, E.C. (2020) Rad54 Drives ATP Hydrolysis-Dependent DNA Sequence Alignment during Homologous Recombination. *Cell*, **181**, 1380-1394.e1318.

30. Mazin, A.V., Mazina, O.M., Bugreev, D.V. and Rossi, M.J. (2010) Rad54, the motor of homologous recombination. *DNA Repair*, **9**, 286-302.

31. Solinger, J.A., Lutz, G., Sugiyama, T., Kowalczykowski, S.C. and Heyer, W.D. (2001) Rad54 protein stimulates heteroduplex DNA formation in the synaptic phase of DNA strand exchange via specific interactions with the presynaptic Rad51 nucleoprotein filament. *J Mol Biol*, **307**, 1207-1221.

32. Petukhova, G., Stratton, S. and Sung, P. (1998) Catalysis of homologous DNA pairing by yeast Rad51 and Rad54 proteins. *Nature*, **393**, 91-94.

33. Perera, H.M. and Trakselis, M.A. (2022) Determining translocation orientations of nucleic acid helicases. *Methods*, **204**, 160-171.

34. Mazin, A.V., Bornarth, C.J., Solinger, J.A., Heyer, W.D. and Kowalczykowski, S.C. (2000) Rad54 protein is targeted to pairing loci by the Rad51 nucleoprotein filament. *Mol Cell*, **6**, 583-592.

35. Rossi, M.J. and Mazin, A.V. (2008) Rad51 protein stimulates the branch migration activity of Rad54 protein. *J Biol Chem*, **283**, 24698-24706.

36. Uhrig, M.E., Sharma, N., Maxwell, P., Gomez, J., Selemenakis, P., Mazin, A.V. and Wiese, C. (2024) Disparate requirements for RAD54L in replication fork reversal. *Nucleic Acids Res*, **52**, 12390-12404.

37. Shah, P.P., Zheng, X., Epshtein, A., Carey, J.N., Bishop, D.K. and Klein, H.L. (2010) Swi2/Snf2-related translocases prevent accumulation of toxic Rad51 complexes during mitotic growth. *Mol Cell*, **39**, 862-872.

38. Mason, J.M., Dusad, K., Wright, W.D., Grubb, J., Budke, B., Heyer, W.-D., Connell, P.P., Weichselbaum, R.R. and Bishop, D.K. (2015) RAD54 family translocases counter genotoxic effects of RAD51 in human tumor cells. *Nucleic Acids Res*, **43**, 3180-3196.

39. Alexeev, A., Mazin, A. and Kowalczykowski, S.C. (2003) Rad54 protein possesses chromatin-remodeling activity stimulated by the Rad51-ssDNA nucleoprotein filament. *Nat Struct Biol*, **10**, 182-186.

40. Zhang, Z., Fan, H.Y., Goldman, J.A. and Kingston, R.E. (2007) Homology-driven chromatin remodeling by human RAD54. *Nat Struct Mol Biol*, **14**, 397-405.

41. Wolner, B. and Peterson, C.L. (2005) ATP-dependent and ATP-independent Roles for the Rad54 Chromatin Remodeling Enzyme during Recombinational Repair of a DNA Double Strand Break*. *J Biol Chem*, **280**, 10855-10860.

42. Bugreev, D.V., Mazina, O.M. and Mazin, A.V. (2006) Rad54 protein promotes branch migration of Holliday junctions. *Nature*, **442**, 590-593.

43. Bugreev, D.V., Hanaoka, F. and Mazin, A.V. (2007) Rad54 dissociates homologous recombination intermediates by branch migration. *Nat Struct Mol Biol*, **14**, 746-753.

44. Goyal, N., Rossi, M.J., Mazina, O.M., Chi, Y., Moritz, R.L., Clurman, B.E. and Mazin, A.V. (2018) RAD54 N-terminal domain is a DNA sensor that couples ATP hydrolysis with branch migration of Holliday junctions. *Nat Commun*, **9**, 34.

45. Mazina, O.M. and Mazin, A.V. (2021) Branch migration activity of Rad54 protein. *Methods Mol Biol*, **2153**, 145-167.

46. Van Komen, S., Petukhova, G., Sigurdsson, S., Stratton, S. and Sung, P. (2000) Superhelicity-driven homologous DNA pairing by yeast recombination factors Rad51 and Rad54. *Molecular Cell*, **6**, 563-572.

47. Wright, William D. and Heyer, W.-D. (2014) Rad54 functions as a heteroduplex DNA pump modulated by its DNA substrates and Rad51 during D loop formation. *Mol Cell*, **53**, 420-432.

48. Piazza, A. and Heyer, W.D. (2019) Moving forward one step back at a time: reversibility during homologous recombination. *Curr Genet*, **65**, 1333-1340.

49. Li, X. and Heyer, W.D. (2009) RAD54 controls access to the invading 3'-OH end after RAD51-mediated DNA strand invasion in homologous recombination in *Saccharomyces cerevisiae*. *Nucleic Acids Res*, **37**, 638-646.

50. Mazin, A.V., Alexeev, A.A. and Kowalczykowski, S.C. (2003) A novel function of Rad54 protein. Stabilization of the Rad51 nucleoprotein filament. *J Biol Chem*, **278**, 14029-14036.

51. Li, X., Zhang, X.P., Solinger, J.A., Kiianitsa, K., Yu, X., Egelman, E.H. and Heyer, W.D. (2007) Rad51 and Rad54 ATPase activities are both required to modulate Rad51-dsDNA filament dynamics. *Nucleic Acids Res*, **35**, 4124-4140.

52. Agarwal, S., van Cappellen, W.A., Guénolé, A., Eppink, B., Linsen, S.E., Meijering, E., Houtsmuller, A., Kanaar, R. and Essers, J. (2011) ATP-dependent and independent functions of Rad54 in genome maintenance. *J Cell Biol*, **192**, 735-750.

53. Meir, A., Crickard, J.B., Kwon, Y., Sung, P. and Greene, E.C. (2022) Rad54 and Rdh54 prevent Srs2-mediated disruption of Rad51 presynaptic filaments. *Proc Natl Acad Sci U S A*, **119**, e2113871119.

54. Fung, C.W., Fortin, G.S., Peterson, S.E. and Symington, L.S. (2006) The rad51-K191R ATPase-defective mutant is impaired for presynaptic filament formation. *Mol Cell Biol*, **26**, 9544-9554.

55. Morgan, E.A., Shah, N. and Symington, L.S. (2002) The requirement for ATP hydrolysis by *Saccharomyces cerevisiae* Rad51 is bypassed by mating-type heterozygosity or RAD54 in high copy. *Mol Cell Biol*, **22**, 6336-6343.

56. Roy, U., Kwon, Y., Marie, L., Symington, L., Sung, P., Lisby, M. and Greene, E.C. (2021) The Rad51 paralog complex Rad55-Rad57 acts as a molecular chaperone during homologous recombination. *Mol Cell*, **81**, 1043-1057.e1048.

57. Fortin, G.S. and Symington, L.S. (2002) Mutations in yeast Rad51 that partially bypass the requirement for Rad55 and Rad57 in DNA repair by increasing the stability of Rad51-DNA complexes. *EMBO J*, **21**, 3160-3170.

58. Malik, P.S. and Symington, L.S. (2008) Rad51 gain-of-function mutants that exhibit high affinity DNA binding cause DNA damage sensitivity in the absence of Srs2. *Nucleic Acids Res*, **36**, 6504-6510.

59. Liu, J., Renault, L., Veaute, X., Fabre, F., Stahlberg, H. and Heyer, W.D. (2011) Rad51 paralogues Rad55-Rad57 balance the antirecombinase Srs2 in Rad51 filament formation. *Nature*, **479**, 245-248.

60. Sung, P. (1997) Yeast Rad55 and Rad57 proteins form a heterodimer that functions with replication protein A to promote DNA strand exchange by Rad51 recombinase. *Genes Dev*, **11**, 1111-1121.

61. Dhingra, N., Kuppa, S., Wei, L., Pokhrel, N., Baburyan, S., Meng, X., Antony, E. and Zhao, X. (2021) The Srs2 helicase dampens DNA damage checkpoint by recycling RPA from chromatin. *Proc Natl Acad Sci U S A*, **118**, e2020185118

62. Antony, E., Tomko, E.J., Xiao, Q., Krejci, L., Lohman, T.M. and Ellenberger, T. (2009) Srs2 disassembles Rad51 filaments by a protein-protein interaction triggering ATP turnover and dissociation of Rad51 from DNA. *Mol Cell*, **35**, 105-115.

63. Qiu, Y., Antony, E., Doganay, S., Koh, H.R., Lohman, T.M. and Myong, S. (2013) Srs2 prevents Rad51 filament formation by repetitive motion on DNA. *Nat Commun*, **4**, 2281.

64. Kaniecki, K., De Tullio, L., Gibb, B., Kwon, Y., Sung, P. and Greene, E.C. (2017) Dissociation of Rad51 presynaptic complexes and heteroduplex DNA joints by tandem assemblies of Srs2. *Cell Rep*, **21**, 3166-3177.

65. Meir, A., Raina, V.B., Rivera, C.E., Marie, L., Symington, L.S. and Greene, E.C. (2023) The separation pin distinguishes the pro- and anti-recombinogenic functions of *Saccharomyces cerevisiae* Srs2. *Nat Commun*, **14**, 8144.

66. Krejci, L., Van Komen, S., Li, Y., Villemain, J., Reddy, M.S., Klein, H., Ellenberger, T. and Sung, P. (2003) DNA helicase Srs2 disrupts the Rad51 presynaptic filament. *Nature*, **423**, 305-309.

67. Fabre, F., Chan, A., Heyer, W.-D. and Gangloff, S. (2002) Alternate pathways involving Sgs1/Top3, Mus81/Mms4, and Srs2 prevent formation of toxic recombination intermediates from single-stranded gaps created by DNA replication. *Proc Natl Acad Sci U S A*, **99**, 16887-16892.

68. Ristic, D., Wyman, C., Paulusma, C. and Kanaar, R. (2001) The architecture of the human Rad54–DNA complex provides evidence for protein translocation along DNA. *Proc Natl Acad Sci U S A*, **98**, 8454-8460.

69. Lanz, M.C., Yugandhar, K., Gupta, S., Sanford, E.J., Faça, V.M., Vega, S., Joiner, A.M.N., Fromme, J.C., Yu, H. and Smolka, M.B. (2021) In-depth and 3-dimensional exploration of the budding yeast phosphoproteome. *EMBO Rep*, **22**, e51121.

70. Nakajima, H., Toyoshima-Morimoto, F., Taniguchi, E. and Nishida, E. (2003) Identification of a consensus motif for Plk (Polo-like kinase) phosphorylation reveals Myt1 as a Plk1 substrate*. *J Biol Chem*, **278**, 25277-25280.

71. Lee, B.H. and Amon, A. (2003) Role of Polo-like kinase CDC5 in programming meiosis I chromosome segregation. *Science*, **300**, 482-486.

72. Matos, J., Blanco, M.G., Maslen, S., Skehel, J.M. and West, S.C. (2011) Regulatory control of the resolution of DNA recombination intermediates during meiosis and mitosis. *Cell*, **147**, 158-172.

73. Edgar, R.C. (2004) MUSCLE: multiple sequence alignment with high accuracy and high throughput. *Nucleic Acids Res*, **32**, 1792-1797.

74. Wyatt, M.D. and Pittman, D.L. (2006) Methylating agents and DNA repair responses: Methylated bases and sources of strand breaks. *Chem Res Toxicol*, **19**, 1580-1594.

75. Musiałek, M.W. and Rybaczek, D. (2021) Hydroxyurea-the good, the bad and the ugly. *Genes (Basel)*, **12**, 1096.

76. Staker, B.L., Hjerrild, K., Feese, M.D., Behnke, C.A., Burgin, A.B. and Stewart, L. (2002) The mechanism of topoisomerase I poisoning by a camptothecin analog. *Proc Natl Acad Sci U S A*, **99**, 15387-15392.

77. Downes, D.J., Chonofsky, M., Tan, K., Pfannenstiel, B.T., Reck-Peterson, S.L. and Todd, R.B. (2014) Characterization of the mutagenic spectrum of 4-nitroquinoline 1-oxide (4-NQO) in Aspergillus nidulans by whole genome sequencing. *G3 (Bethesda)*, **4**, 2483-2492.

78. Abramson, J., Adler, J., Dunger, J., Evans, R., Green, T., Pritzel, A., Ronneberger, O., Willmore, L., Ballard, A.J., Bambrick, J. et al. (2024) Accurate structure prediction of biomolecular interactions with AlphaFold 3. *Nature*, **630**, 493-500.

79. Thomä, N.H., Czyzewski, B.K., Alexeev, A.A., Mazin, A.V., Kowalczykowski, S.C. and Pavletich, N.P. (2005) Structure of the SWI2/SNF2 chromatin-remodeling domain of eukaryotic Rad54. *Nat Struct Mol Biol*, **12**, 350-356.

80. Cheng, J., Novati, G., Pan, J., Bycroft, C., Žemgulytė, A., Applebaum, T., Pritzel, A., Wong, L.H., Zielinski, M., Sargeant, T. et al. (2023) Accurate proteome-wide missense variant effect prediction with AlphaMissense. *Science*, **381**, eadg7492.

81. Miura, T., Shibata, T. and Kusano, K. (2013) Putative antirecombinase Srs2 DNA helicase promotes noncrossover homologous recombination avoiding loss of heterozygosity. *Proc Natl Acad Sci U S A*, **110**, 16067-16072.

82. Dupaigne, P., Le Breton, C., Fabre, F., Gangloff, S., Le Cam, E. and Veaute, X. (2008) The Srs2 helicase activity is stimulated by Rad51 filaments on dsDNA: implications for crossover incidence during mitotic recombination. *Mol Cell*, **29**, 243-254.

83. Liu, J., Ede, C., Wright, W.D., Gore, S.K., Jenkins, S.S., Freudenthal, B.D., Todd Washington, M., Veaute, X. and Heyer, W.-D. (2017) Srs2 promotes synthesis-dependent strand annealing by disrupting DNA polymerase δ-extending D-loops. *eLife*, **6**, e22195.

84. Schiestl, R.H., Prakash, S. and Prakash, L. (1990) The SRS2 suppressor of rad6 mutations of *Saccharomyces cerevisiae* acts by channeling DNA lesions into the RAD52 DNA repair pathway. *Genetics*, **124**, 817-831.

85. Reitz, D., Chan, Y.-L. and Bishop, D.K. (2021) How strand exchange protein function benefits from ATP hydrolysis. *Curr Opin Genet Dev*, **71**, 120-128.

86. Ira, G., Malkova, A., Liberi, G., Foiani, M. and Haber, J.E. (2003) Srs2 and Sgs1-Top3 suppress crossovers during double-strand break repair in yeast. *Cell*, **115**, 401-411.

87. Piazza, A., Wright, W.D. and Heyer, W.D. (2017) Multi-invasions are recombination byproducts that induce chromosomal rearrangements. *Cell*, **170**, 760-773.e715.

88. Reitz, D., Savocco, J., Piazza, A. and Heyer, W.D. (2022) Detection of homologous recombination intermediates via proximity ligation and quantitative PCR in *Saccharomyces cerevisiae*. *J Vis Exp*, **187**, e64240.

89. Xie, B., Sanford, E.J., Hung, S.H., Wagner, M., Heyer, W.D. and Smolka, M.B. (2024) Multi-step control of homologous recombination via Mec1/ATR suppresses chromosomal rearrangements. *EMBO J*, **43**, 3027-3043.

90. Klein, H.L., Bačinskaja, G., Che, J., Cheblal, A., Elango, R., Epshtein, A., Fitzgerald, D.M., Gómez-González, B., Khan, S.R., Kumar, S. et al. (2019) Guidelines for DNA recombination and repair studies: cellular assays of DNA repair pathways. *Microb Cell*, **6**, 1-64.

91. Ho, C.K., Mazón, G., Lam, A.F. and Symington, L.S. (2010) Mus81 and Yen1 promote reciprocal exchange during mitotic recombination to maintain genome integrity in budding yeast. *Mol Cell*, **40**, 988-1000.

92. Hu, J., Ferlez, B., Dau, J. and Crickard, J.B. (2023) Rad53 regulates the lifetime of Rdh54 at homologous recombination intermediates. *Nucleic Acids Res*, **51**, 11688-11705.

93. Keymakh, M., Dau, J., Hu, J., Ferlez, B., Lisby, M. and Crickard, J.B. (2022) Rdh54 stabilizes Rad51 at displacement loop intermediates to regulate genetic exchange between chromosomes. *PLoS Genet*, **18**, e1010412.

94. Petukhova, G., Van Komen, S., Vergano, S., Klein, H. and Sung, P. (1999) Yeast Rad54 promotes Rad51-dependent homologous DNA pairing via ATP hydrolysis-driven change in DNA double helix conformation. *J Biol Chem*, **274**, 29453-29462.

95. Crickard, J.B. (2023) Single molecule imaging of DNA-protein interactions using DNA curtains. *Methods Mol Biol*, **2599**, 127-139.

96. Sridalla, K., Woodhouse, M.V., Hu, J., Scheer, J., Ferlez, B. and Crickard, J.B. (2024) The translocation activity of Rad54 reduces crossover outcomes during homologous recombination. *Nucleic Acids Res*, **52**, 7031-7048.

97. Woodhouse, M.V., Hu, J., Wu, M., Qian, J., Inman, J.T., Wang, M.D. and Crickard, J.B. (2025) The eukaryotic homology search complex distorts donor DNA structure to probe for homology. *bioRxiv*, doi: 10.1101/2025.08.28.672940.

98. Hwang, W. and Karplus, M. (2019) Structural basis for power stroke vs. Brownian ratchet mechanisms of motor proteins. *Proc Natl Acad Sci U S A*, **116**, 19777-19785.

99. van der Heijden, T., Modesti, M., Hage, S., Kanaar, R., Wyman, C. and Dekker, C. (2008) Homologous recombination in real time: DNA strand exchange by RecA. *Mol Cell*, **30**, 530-538.

100. De Vlaminck, I., van Loenhout, M.T., Zweifel, L., den Blanken, J., Hooning, K., Hage, S., Kerssemakers, J. and Dekker, C. (2012) Mechanism of homology recognition in DNA recombination from dual-molecule experiments. *Mol Cell*, **46**, 616-624.

101. Aguilera, P. and López-Contreras, A.J. (2023) ATRX, a guardian of chromatin. *Trends Genet*, **39**, 505-519.

102. Spies, J., Waizenegger, A., Barton, O., Sürder, M., Wright, W.D., Heyer, W.D. and Löbrich, M. (2016) Nek1 regulates Rad54 to orchestrate homologous recombination and replication fork stability. *Mol Cell*, **62**, 903-917.

103. Guo, X., Hum, Y.F., Lehner, K. and Jinks-Robertson, S. (2017) Regulation of hetDNA length during mitotic double-strand break repair in yeast. *Mol Cell*, **67**, 539-549.e534.

104. McIlwraith, M.J. and West, S.C. (2008) DNA repair synthesis facilitates RAD52-mediated second-end capture during DSB repair. *Mol Cell*, **29**, 510-516.

105. Tang, S., Hariri, S., Bohn, R., McCarthy, J.E., Koo, J., Pourhosseinzadeh, M., Nguyen, E., Liu, N., Ma, C., Lu, H. et al. (2025) Protecting double Holliday junctions ensures crossing over during meiosis. *Nature*, doi: 10.1038/s41586-025-09555-1.

106. Fasching, Clare L., Cejka, P., Kowalczykowski, Stephen C. and Heyer, W.-D. (2015) Top3-Rmi1 dissolve Rad51-mediated D loops by a topoisomerase-based mechanism. *Mol Cell*, **57**, 595-606.

107. Loes, A.N., Tarabi, R.A.L., Huddleston, J., Touyon, L., Wong, S.S., Cheng, S.M.S., Leung, N.H.L., Hannon, W.W., Bedford, T., Cobey, S. et al. (2024) High-throughput sequencing-based neutralization assay reveals how repeated vaccinations impact titers to recent human H1N1 influenza strains. *J Virol*, **98**, e00689-00624.

CHAPTER 4

Models for how motor proteins regulate HR and future directions

Double-strand break (DSB) repair is orchestrated by a complex interplay among DNA repair machinery, chromosome mobility, checkpoint signaling and cell cycle regulators. This system is governed by kinetic competition and coordination between multiple factors, each defined by its biochemical activity and nuclear occupancy, forming an intricate regulatory network. Interference of any of the key factors might redirect the pathway or sub-pathway decision, thus alternating the repair outcomes, which provides us both mechanistic insights and experimental opportunities to dissect the system.

However, the difficulty remains formidable. Isolating transient DNA repair intermediates and deconvoluting the multifunctional roles of many factors are inherently difficult, making it imprecise and inefficient to infer the intermediate processes solely from end-point observations. This highlights the critical need for both technical advances and separation-of-function mutants to elucidate the molecular choreography of DSB repair.

Indeed, single-molecule imaging has already revolutionized our understanding of recombinase-mediated strand invasion through micro-homology search, as discussed in Chapter 1. Today, the integration of genetics, biochemistry and single-molecule imaging techniques has become essential for addressing unsolved questions and testing mechanistic models. Continued improvements in spatial and temporal resolution are expected to yield even deeper insights into the dynamic regulation of homologous recombination (HR).

In this chapter, I discuss the studies conducted by myself and my colleagues in the Crickard lab over the past five years and offer some personal perspectives on what we gained and how future research might advance from our current understanding.

4.1 The role of Rdh54 in DSB repair.

Rad54 and Rdh54 are paralogs sharing ~30% sequence identity and ~40% sequence similarity. Both possess ATPase-dependent DNA translocation and chromatin-remodeling activities and can promote HR and D-loop formation *in vitro*, with Rad54 generally exhibiting higher activity than Rdh54 (1–7). They also cooperate in forming the presynaptic complex (PSC) by antagonizing Srs2-mediated PSC disruption (8).

Understanding the relationship between Rad54 and Rdh54 *in vivo* is particularly intriguing. Because Rdh54 binding to PSC is resistant to inhibition by Rad54 inhibitor Hed1, which is active during meiosis and serves as a meiosis-specific cofactor for the recombinase Dmc1, Rdh54 is considered more essential for meiotic HR than for mitotic HR (7, 9). Consistent with this, loss of Rdh54 causes only minor defects under DNA damage reagent methyl methyl methanesulfonate (MMS) and camptothecin (CPT) stress, while loss of Rad54 renders cells very susceptible to MMS and CPT. However, in allele recombination assay, loss of *RDH54* leads to higher break-induced replication (BIR) outcome, while a catalysis-inactive form of Rdh54 (*rdh54K318R*), which carries a mutation in the Walker A domain, results in more non-crossover (NCO) outcomes and decreased crossover (CO) and BIR (10), implying a role of Rdh54 in determining HR outcome choice. Furthermore, it is also shown that *rdh54Δ* cells are unable to adapt from an irreparable DSB, suggesting Rdh54 functions in checkpoint adaptation in addition to HR regulation (11).

4.1.1 Antagonism between Rad54 and Rdh54 on 3’ ssDNA extension at D-loops.

Single-molecule imaging reveals that Rad54 and Rdh54 have different preferential binding sites on PSC mediated by their own N-terminal domains, both of which contain highly disordered and less conserved sequences (7). Furthermore, Rdh54 can limit D-loop length, stabilize nascent D-loop by slowing down Rad54-mediated turnover and 3’ DNA synthesis (hereafter referred as D-loop extension) (10, 12). These observations indicate an antagonistic relationship between Rad54 and Rdh54 at nascent D-loops, which regulates HR outcomes *in vivo* (10). We can build a mathematical model to describe this relationship in D-loop extension based on experiment results reported in the work dominated by my colleagues in 2022 and fit that into genetic data. According to their work, Rdh54 kinetically affects D-loop extension with a 65 nucleotide (nt) homology *in vitro*, with Rad54 only holding a reaction half-time ($t_{1/2}$) of 14.5 minutes, Rad54 plus Rdh54 at equal concentration with a $t_{1/2}$ of 25 minutes, and Rad54 plus Rdh54K318R at equal concentration with a $t_{1/2}$ of 50 minutes (Table 4.1) (10). It makes sense because Rdh54K318R totally lost ATP hydrolysis and DNA translocation activity, which can be regarded as a road blockade while wildtype Rdh54 can be considered as an interference item which occupies different sites on PSC with Rad54 and slows down Rad54’s movement and functions.

4.1.1.1 Antagonism model building

Let’s fit D-loop extension reaction into a first-order reaction:

$$D \overset{k}{\rightarrow} D_{ext} \tag{1}$$

where D denotes nascent D-loops, D_{ext} denotes extended D-loops and k is the apparent rate constant. It describes a relationship between reactant concentration and time:

$$\frac{d[D]}{dt} = -k[D] \tag{2}$$

By solving the equation, we get:

$$[D] = D_0 e^{-kt} \tag{3}$$

where D_0 is the initial D-loop concentration. The half-time for this reaction is:

$$t_{1/2} = \frac{ln2}{k} \tag{4}$$

which allows us to calculate the effective rate constant k_{eff} for each reaction (Table 4.1).

Table 4.1: Reaction description of D-loop extension.

Reaction catalyzed by	Half-time $t_{1/2}$ (minutes)*	Rate constant k_{eff} (minute^{-1})
Rad54 (30 nM)	14.5	0.0478
Rad54 (30 nM) + Rdh54 (30 nM)	25	0.0277
Rad54 (30 nM) + Rdh54K318R (30 nM)	50	0.0139

* Data regenerated from Keymakh, M. et al, *PLoS Genet*, **18** (2022) with permission.

This is based on the assumptions including but not limited to (i) the reaction rate depends linearly on one reactant; (ii) each molecule behaves independently; (iii) the rate constant k does not change over time.

Using the three measured effective rate constants, I describe their competition with a simple phenomenological model:

$$k_{eff} = k_0 \frac{1 + \alpha[Rad54]}{1 + \beta[Rdh54] + \gamma[Rdh54K318R]} \tag{5}$$

where k_0 is the baseline extension rate in the absence of modulators. The numerator part expresses the activating role of Rad54 with α describing its driver effect, whereas the denominator part describes the antagonist effect of Rdh54 variants with β and γ parameterizing the antagonism of Rdh54 and Rdh54K318R, respectively.

Using the $t_{1/2}$ and k_{eff} calculated from Table 4.1, we can get the antagonism parameters for Rdh54 and Rdh54K318R (Table 4.2).

Table 4.2: Antagonism for Rdh54 variants.

Rdh54 variants	Antagonism
Rdh54 (β)	0.724
Rdh54K318R (γ)	2.448
Rdh54T851A[#]	4.559

[#]: The data result is derived from the result of genetic experiments rather than from that of biochemical experiments.

Moreover, we can map the D-loop extension rate into the HR outcomes. Based on previous allelic recombination assay (red/white assay) results, there is an increase in NCO in *rdh54Δ*, and a decrease of CO and BIR in *rdh54K318R*. It indicates that the blockage effect of Rdh54 is important in limiting DNA replication and biasing HR into less gene conversion results, which is NCO. Here we will simplify the genetic assay results by grouping three outcomes into two categories, one is gene conversion results (GC, including CO and BIR), the other one is non-gene conversion (NGC, including NCO). The results of wildtype cells (WT), *rdh54Δ* and *rdh54K318R* cells are listed in Table 4.3. To summarize, when Rdh54 is absent, the loss of blockage function leads to higher GC frequency (*GC*). On the contrast, higher antagonism of Rdh54K318R leads to decreased *GC*.

Given that *GC* should saturation at GC_{max} ($GC_{max} < 1$) and mitotic HR still favors NCO results (it's rare to see *GC* exceeding 60%), it's not appropriate to assume that there is a linear relationship between *GC* and D-loop extension rate. Instead, a Hill equation can try to fit that like:

$$GC = GC_{max} \frac{k^n}{k^n + K^n} \tag{6}$$

where *k* stands for D-loop extension rate, which is k_{eff} we calculated above and affected by both Rad54 activation and Rdh54 antagonism; *K* stands for all other disruption factors involved in HR like Mph1 and Sgs1; and *n* stands for the sensitivity of *GC*. Higher *n* means *GC* is more sensitive. The understanding of how Hill equation fits our scenario can be found in APPENDIX C.1.

Table 4.3: Allele recombination results (simplified).

Strains	Similar biochemical condition	*GC* (%)	*NGC* (%)
WT*	Rad54 + Rdh54 (k_{eff} = 0. 0277)	41.06	58.94
*rdh54Δ**	Rad54 only (k_{eff} = 0.0478)	51.83	48.17
*rdh54K318R**	Rad54 + Rdh54K318R (k_{eff} = 0.0139)	18.37	81.63
WT¶	Not applicable	58.62	41.38
rdh54T851A¶	Not applicable	13.21	86.79

* Data regenerated from Keymakh, M. et al, *PLoS Genet*, **18** (2022) with permission.
¶ Data regenerated from Hu, J. et al, *Nucleic Acids Res*, **51** (2023) with permission.

Applying current data from Table 4.3, we can solve: GC_{max} = 57.32%, K = 0.0189 minute^{-1}, n = 2.42 (Figure 4.1A) and the quality of the fitting is good with a low cost ($<10^{10}$), suggesting our model is reasonable.

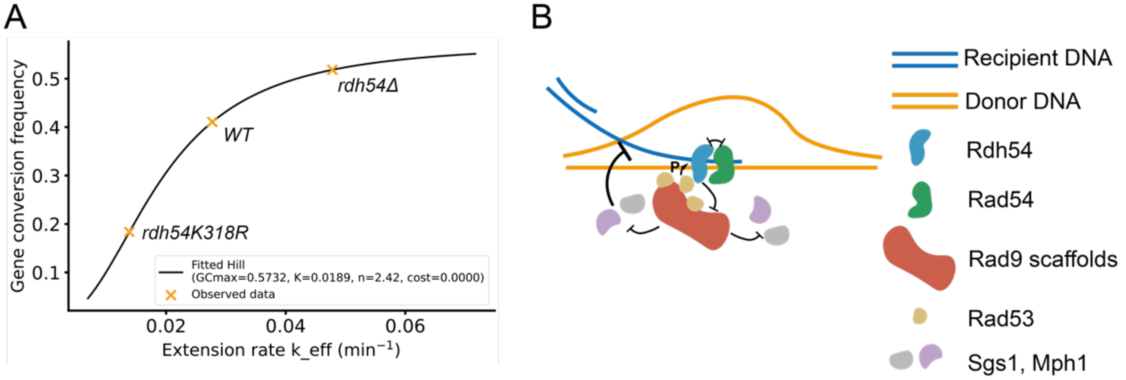

Figure 4.1: Rdh54 in HR regulation.

(A) Fitting the observed *GC* frequency and effective extension rate using a Hill equation. (B) Schematic illustration of Rdh54 functions in HR regulation. Rdh54 antagonizes Rad54 at nascent D-loop to slow down extension and D-loop maturation. During DNA damaged-induced checkpoint, phosphorylation of Rdh54 by Rad53 limits Rad9 hyperactivation, thus releasing Sgs1 and Mph1 from Rad9-mediated suppression.

4.1.1.2 Insights into the model

Moreover, this model reveals several additional insights. Firstly, the resistance strength K, possibly contributed by Sgs1 and Mph1 and other anti-recombination factors, is of a similar magnitude to the activation strength k, which represents the combined activity of Rad54 and Rdh54. This balance suggests that both pro-recombination and anti-recombination activities are essential to maintain homeostasis in HR *in vivo*.

It is also reasonable to classify Rdh54 as part of the anti-recombination group, since its primary effect at nascent D-loops is to limit extension and promote disruption. In this view, varying Rdh54 activity would effectively modulate K rather than k_{eff}, while k_{eff} can be treated as a constant. The model would remain mathematically equivalent, with K changing according to Rdh54 activity. In practice, the available experimental data make the current formulation, where k_{eff} is adjusted and K is fixed, more convenient for quantitative fitting and interpretation.

Second, because the Hill coefficient *n* is larger than 1, the relationship between *GC* and the extension rate *k* is cooperative, implying un ultrasensitive, switch-like behavior in pathway outcomes. In other word, small changes in *k* can lead to large shifts in *GC*. Since in fitting we apply the same coefficient to resistance strength *K* as well, and the good fitting indicates that both extension and dissociation kinetics act as sensitive levers controlling HR outcomes.

Finally, it would be interesting to extend this model to other Rad54 and Rdh54 mutants. In chapter 2, we investigated the interaction between the checkpoint kinase Rad53 and Rdh54 and found that mutating a potential phosphorylation site threonine 851 to alanine (*rdh54T851A*) renders cells more susceptible to DNA damage reagent, similar to *rdh54K318R*. Although subsequent experiments suggested that the adjacent serine 852 is more likely phosphorylation target of Rad53, the phenotype of the *rdh54T851A* mutant remains noteworthy.

Based on the allelic recombination results, *rdh54T851A* exhibits a significant increase in NCO outcomes accompanied by a reduction in CO and BIR events, closely resembling the phenotype of *rdh54K318R* (Table 4.3). Because of the unavoidable technical variability among datasets, direct comparison of absolute values is challenging; however, the relative fold change between WT and *rdh54T851A* strains allow us to estimate the mutant's antagonistic strength. Using the model, antagonism of *rdh54T851A* is approximately 4.56 (Table 4.2), even higher than *rdh54K318R*. This strong antagonism may reflect the decoupling of ATP hydrolysis and translocation in the mutant. Purified Rdh54T851A displays more than 2-fold higher ATP hydrolysis rate but only ~43.3% of the translocation activity of WT protein, making it more effective at competing with Rad54 by rapidly consuming ATP yet releasing DNA slowly. As a result, *rdh54T851A* likely acts as a more potent kinetic inhibitor in the D-loop extension process, consistent with the model predictions. To further test this, *in vitro* D-loop extension assays can be performed using a mixture of Rad54 and Rdh54T851A and it should yield a longer half-time compared with Rad54 alone according to the model.

However, it's clear that the simple antagonism model between Rad54 and Rdh54 cannot fully account for all observations. This framework does not distinguish CO and BIR outcomes, yet previous studies have shown that loss of *RDH54* leads to an increase in BIR accompanied by decreases in both CO and NCO events. In addition, as described in Chapter 2, mutations at T851 and S852 exhibit diverse recombination outcomes that cannot not be fully explained by the antagonism mechanisms, suggesting that Rdh54 also plays broader roles in HR regulation. Another limitation of the current model is that it does not consider the relative concentration balance between Rad54 and Rdh54 into account, which could be critical under physiological conditions.

4.1.2 Rdh54 in checkpoint response

Rdh54 is known to be essential in checkpoint adaptation when cells face an irreparable DSB. Deletion of *RDH54* results in Rad53 hyperphosphorylation and elongated cell cycle arrest, indicating that Rdh54 participates in the adaptation process (11). Although it remains unclear whether Rdh54 also contributes to checkpoint recovery, this possibility cannot be excluded since both recovery and adaptation of checkpoint may share mechanistic features with the spindle assembly checkpoint recovery pathway. In this section, I will therefore focus on checkpoint adaptation, noting that the concepts discussed here may also apply to checkpoint recovery. Further work needs to be done to dissect the mechanisms more precisely.

In Chapter 2, we found a potential Rad53 phosphorylation site on Rdh54, which is serine 852. Although mutating S852 to alanine (*rdh54S852A*) does not make cells susceptible to DNA damage reagent, it biases HR toward NCO and BIR outcomes in allelic recombination assays. Moreover, *in vitro* single-molecule experiments show that Rdh54S852A mutant has a reduced co-localization with Rad53 on DNA curtains. When WT protein is pre-incubated with Rad53, its translocation along DNA slows down, mimicking the behavior of the phosphomimic mutant Rdh54S852D. In contrast, Rad53 incubation has no significant effect on Rdh54S852A, showing its resistance to kinase-mediated regulation. Collectively, these results suggest that Rdh54 acts as a downstream effector of the Mec1-Rad9-Rad53 checkpoint cascade, with S852 serving as the potential phosphorylation site. Biochemical characterization of phosphomimic mutant Rdh54S852D reveals increased ATP hydrolysis activity but approximately 40% lower translocation activity compared with WT protein, potentially reflecting the impact of phosphorylation on Rdh54 function *in vivo*.

Previous studies show that Rad9 promotes long tract gene conversion and increases CO and BIR outcomes by limiting activity of Sgs1 and Mph1 helicases, whereas Rdh54 decreases BIR outcomes, implying an antagonistic relationship between Rad9 and Rdh54 (10, 13). Furthermore, negative feedback exists between Rad53 and Rad9. Rad53 activation triggers its dissociation from Rad9 scaffolds and promotes Rad9 oligomer dissemble (14, 15). These observations illustrate the regulatory balance within the checkpoint network, where downstream factors impose negative feedback on upstream components to prevent hyperactivation. However, the molecular mechanisms underlying these feedback loops remain incompletely understood.

One plausible hypothesis involves dynamic oligomer assembly and nuclear volume partitioning. Rad9 is a scaffold protein, and its oligomerization activity is critical for Rad53 activation. While *in vivo* studies show that Rad53 activation requires both Mec1 and Rad9, *in vitro* assembly of Rad53 oligomers is potent to activate itself even in the absence of Mec1 and Rad9, highlighting the importance of multimerization in checkpoint signal propagation. This phenomenon is reminiscent of biomolecular condensates, in which proteins or nucleic acids with similar functions cluster together to enhance local concentrations and reaction efficiency. In contrast, factors with distinct or opposing functions segregate into immiscible compartments with different biophysical properties (16–18). Formation of such condensates depends on multi-valent inter-molecular interactions often mediated by repeat sequences in DNA/RNA or intrinsically disordered regions in proteins (19, 20). The human Rad9 homolog, 53BP1, is found to form nuclear compartments after DNA damage occurs (21). 53BP1 also generates puncta around DNA lesions under replication stress and transmits them into daughter cells, suggesting a protective and heritable marker role in DNA damage response (22).

Rdh54 contains an intrinsically disordered N-terminal domain, which may confer the capacity of self-assembly and compartment formation. In Chapter 2, we demonstrated that the phosphomimic mutant Rdh54S852D forms cluster with more molecules on DNA curtains than the WT protein, whereas the phosphorylation-deficient mutant Rdh54S852A contains fewer molecules within its foci. Moreover, Rdh54S852D can form larger clusters than WT proteins in solutions, and these assemblies are more resistant to salt concentration change (data not shown). When Rad9 and Rdh54 are mixed, they can co-localize but Rdh54S852D tends to accumulate at the periphery of Rad9 assemblies, suggesting reduced miscibility between Rad9 and phosphorylated Rdh54 (data not shown).

Together, these observations support a model in which checkpoint factors at different regulatory layers occupy distinct nuclear compartments, serving specialized functions and influencing repair pathway choices. Following Rad53-mediated phosphorylation, Rdh54 may undergo condensation-like assembly to form spatially distinct, Rad9-excluding domains to provide a physical basis for checkpoint adaptation and pathway resolution.

4.1.3 How Rdh54 contributes to HR outcome distribution

We have discussed two major functions of Rdh54: its antagonistic effect on Rad54 at nascent D-loops and its role in checkpoint adaptation. Integrating these two functions helps elucidate how Rdh54 influences the kinetics of late HR intermediates and ultimately affects recombination outcomes (Figure 4.1B).

According to the antagonism model, an increase in antagonistic strength results in higher NCO frequency and reduced CO and BIR outcomes, as observed in *rdh54K318R* and *rdh54T851A* mutants. Conversely, loss of antagonism should produce the opposite effect, a decrease in NCO and increases in both CO and BIR (Table 4.4).

Separately, when Rdh54 fails to signal checkpoint adaptation like in *rdh54S852A* mutant, cells tend to resolve DBSs with increased NCO and BIR results and fewer CO events

(Table 4.4 and 4.5). The *rdh54S852A* mutant can be defined as a separation-of-function mutant because its ATP hydrolysis and DNA translocation activities remain comparable to WT proteins, suggesting that it's still capable in competing with Rad54 at nascent D-loops.

We also identified another mutant, *rdh54T851D*, which behaves similarly to *rdh54S852A*. Purified Rdh54T851D exhibits ATP hydrolysis and DNA translocation rate comparable to the WT proteins, but forms smaller clusters on DNA curtains, although the difference is less pronounced than that observed between WT and Rdh54S852A. In allelic recombination assay, *rdh54T851D* also shows decreased CO accompanied by increased NCO and BIR events, though the changes are milder than those of *rdh54S852A*. The similar phenotypes of *rdh54T851D* and *rdh54S852A* suggest that these two residues are involved in the same pathway, and the adjacent threonine may help serine 852 be recognized and modified by Rad53.

To test this hypothesis, *in vitro* binding assays between Rad53 and Rdh54T851D could be performed. It's expected to see less binding of Rad53 to Rdh54T851D, and correspondingly, the translocation activity of Rdh54T851D would be resistant to Rad53 pre-incubation, like Rdh54S852A.

The mechanistic basis for why loss of checkpoint adaptation leads to increased NCO and BIR events remains unclear, but several hypotheses can be proposed. First, prolonged checkpoint might facilitate more accurate donor recognition and heteroduplex rejection, consistent with the reduced interhomolog gene conversion observed in *rdh54S852A*.

Table 4.4: The influence of Rdh54 separation-of-function mutants

Separation-of-function	NCO	CO	BIR
Gain of antagonism (*rdh54T851A*, *rdh54K318R*)	Increase	Decrease	Decrease
Loss of antagonism	Decrease	Increase	Increase
Loss of adaptation (*rdh54S852A*, *rdh54T851D*)	Increase	Decrease	Increase
Gain of adaptation	Decrease	Increase	Increase

Second, failure to adapt in Rdh54 adaptation-deficient mutant may cause persistent Rad9 hyperactivation at DNA damage sites, which suppresses the Sgs1 and Mph1 helicases and thereby promotes BIR. Consistently, inhibition of nascent D-loop by Rdh54 has been reported to in concert with Sgs1-Top3-Rmi1 complex and Mph1 pathway, suggesting a cooperative relationship among Rdh54, Sgs1, and Mph1 in regulating D-loop dynamics and HR outcome distribution (23). Rad9 is also known to restrain Sgs1 and Mph1 to favor CO; however, this effect may not manifest in Rdh54 adaptation-deficient mutants, as Rdh54 phosphorylation and the subsequent negative feedback likely occur at later HR stages. During the early HR stages, the coordination and competition between pro- and anti-recombination reactions, such as those determining NCO versus CO outcomes, remain balanced even in adaptation-deficient cells. At later stages, prolonged cell-cycle arrest increases the likelihood of losing the second broken end. Failure to attenuate Rad9 activity results in extended gene conversion, biasing HR toward BIR and BIR-like events in the mutant.

The summary of Rdh54 separation-of-function mutants is shown in Table 4.4. With these principles in hand, we can next examine how combinations of these mutations further influence HR outcomes.

The first case is the *RDH54* knockout mutant, which lacks both antagonism and adaptation functions. The effects on NCO and CO in two situations cancel each other out, while both mechanisms synergistically promote BIR. So *rdh54Δ* exhibit a substantial increase in BIR events (Table 4.5). Also, the decrease effect on CO and the increase on BIR associated with loss of adaptation offset the changes in *GC*, allowing *rdh54Δ* to still conform to the antagonism model we built in 4.1.1. Another possible reason for this fit is that *GC* of both WT and *rdh54Δ* strains fall within the smooth, transitional region of the Hill equation, where measurement errors have less influence on the overall curve behavior.

The second one is the *rdh54T851A,S852A* double mutant, which combines both gain of antagonism and loss of adaptation properties. Interestingly, biochemical assays show that the double mutant has lower ATP hydrolysis activity and higher translocation activity than Rdh54T851A alone, suggesting that S852A substitution partially suppresses the strong antagonistic phenotype of T851A at a mechanistic level. Similarly, the cluster size of the double mutant is intermediate between RdhS852A mutant and WT proteins. Consequently, this mutation displays only a mild increase in NCO frequency. Although both gain of antagonism and loss of adaptation individually promote NCO events, their combination effects are weakened in this context.

Finally, the phosphomimic mutant *rdh54S852D* has a complex behavior. It is not appropriate to treat *rdh54S852D* simply as the gain of adaptation counterpart of *rdh54S852A*. Checkpoint signaling mediated by Rdh54 likely involves distinct nuclear partitioning rather than direct catalytic regulation. The immiscible properties of Rdh54S852D condensates may impair its recruitment to DSB sites, thereby preventing it from participating in checkpoint regulation. Its observed phenotype is therefore more plausibly explained by its decoupled ATP hydrolysis and DNA translocation activities, which makes it a stronger kinetic antagonist in D-loop extension and results in elevated NCO frequency *in vivo*.

Table 4.5: Allelic recombination results for *RDH54* variants.

Strains	NCO (%)	CO (%)	BIR (%)
*WT**	52.50	41.46	6.42
*rdh54Δ**	48.17	30.68	17.28
*rdh54K318R**	81.63	14.70	3.67
WT¶	41.38	52.02	4.60
rdh54T851A¶	86.79	10.80	2.41
rdh54T851D¶	55.10	35.57	9.33
rdh54S852A¶	58.13	26.25	15.63
rdh54S852D¶	76.56	16.52	6.92
rdh54T851A,S852A¶	47.76	49.08	3.17

* Data regenerated from Keymakh, M. et al, *PLoS Genet*, **18** (2022) with permission.
¶ Data regenerated from Hu, J. et al, *Nucleic Acids Res*, **51** (2023) with permission.

In summary, dissecting the biochemical and checkpoint-associated roles of Rdh54 reveals that this motor protein serves as a multifaceted regulator of HR. Its dual functions jointly shape the distribution of HR outcomes. And applying separation-of-function mutants of Rdh54 provides a powerful framework for dissect the HR regulation network. This highlights the importance of functional separation as a mechanistic tool enabling the identification of distinct regulatory layers that would otherwise be masked by pleiotropic effects in complete loss-of-function mutants.

4.2 Roles of Rad54 in HR

Rad54 is a strong DNA motor that can translocate along DNA, compact DNA and introduce superhelicity into DNA. The versatile functions of Rad54 enable it to facilitate the kinetic dynamics during strand exchange and promote strand invasion both *in vivo* and *in vitro* (2, 4, 24–27). Under physiological conditions, the activity of Rad54 to remodel chromosome is indispensable as DNA is topologically constrained and protected by nucleosomes (1). However, it remains challenging to delineate the specific effects of Rad54 on DNA and to dissect the underlying molecular mechanisms during strand invasion, owing to the rapid kinetics of the reaction and the interdependence among Rad54's multiple functions. In this section, I present a loop extrusion model to integrate these activities to describe how homology search efficiency is enhanced by Rad54.

4.2.1 Loop extrusion model

4.2.1.1 Loop build-up

Like Rdh54, Rad54 also contains an intrinsically disordered N-terminal domain. It forms tetramers in solution and even larger clusters containing ~7.5 molecules on DNA curtains (28 and Chapter 3). A DNA loop might form when multiple motors bind to nearby DNA sites at different translocation velocities. To simplify the system, we can consider only two Rad54 molecules (Figure 4.2A). The leading motor moves faster and acts as a driver, while the slower one serves as an anchor. DNA accumulates between them to form a loop and cause local DNA compaction (Figure 4.2A). The loop extrusion rate (*lxr*) can be expressed simply as the velocity difference between the two motors (v_f is the velocity of the driver, v_s is the velocity of the anchor).

$$lxr = \Delta v = v_f - v_s \tag{7}$$

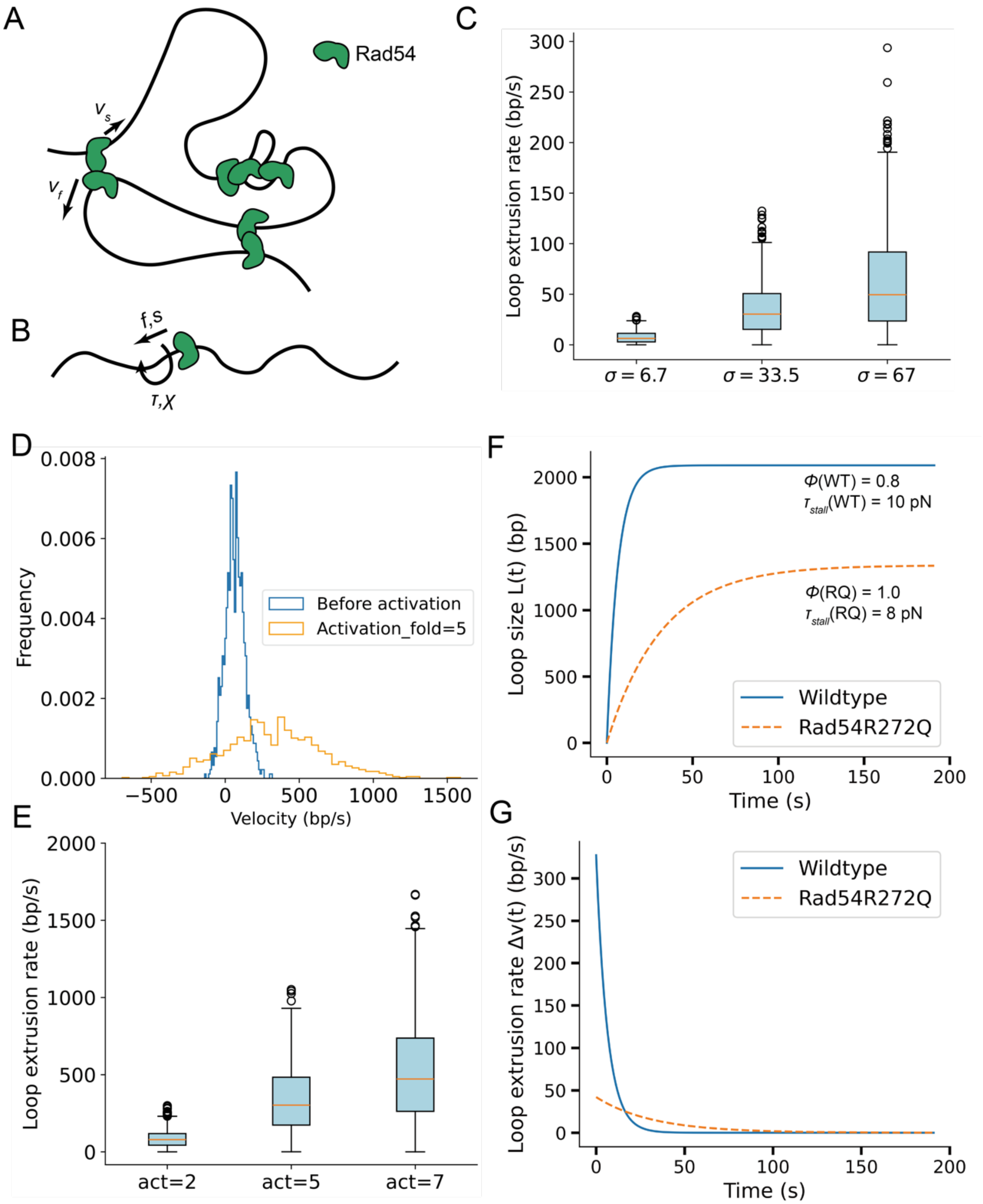

Figure 4.2: Rad54-mediated loop extrusion model.

(A) Multiple Rad54-DNA contacts with distinct motor velocities accumulate DNA between contact points, forming loops and constrained DNA domains. (B) Rad54 translocation along DNA applies both linear and rotational forces: f represents linear driving friction, s the linear step size, τ the rotational friction, and χ the rotation angle. (C) Simulated loop extrusion rate using a mean translocation velocity $\mu = 65$ bp/s and different standard deviations *σ*. (D) Velocity distribution of the inactivated motor (anchor) and activated motor (driver). (E) Loop extrusion rates under different activation folds. Basal anchors have μ = 65 bp/s and σ = 67 bp/s. (F) Time-dependent loop growth showing that the loop reaches a plateau when motors stall due to torque accumulation. (G) Velocity decay of motors caused by increasing torque.

Rad54's translocation activity is intrinsically heterogeneous across individual molecules, as observed in DNA curtain assays. Using data collected by my colleagues, Rad54 velocities along DNA follow a normal distribution $N(\mu, \sigma^2)$, with a mean velocity μ = 65 bp/s and a standard deviation σ = 67 bp/s (28). Randomly selecting two motors from this distribution to represent the driver and anchor allows simulation of loop extrusion rates (Figure 4.2C). Increasing σ leads to higher loop extrusion rate, showing that heterogeneity within the motor population can enhance overall loop growth. Furthermore, the loop extrusion rate can be modulated by changing the motor pool. For example, if the driver is activated by Rad51 to achieve a higher ATP hydrolysis rate and translocation velocity while the anchor remains inactive (Figure 4.2D), the *lxr* increases accordingly (Figure 4.2E). Under physiological conditions, Rad51 enhances Rad54 activity by approximately 4- to 5-fold, yielding a mean loop extrusion rate of ~284 bp/s in a simulation of 1000 cycles with an activation factor of 4.3.

4.2.1.2 Accumulated torque slows loop growing down

However, motor translocation along DNA applies not only a linear force but also a rotational torque to the DNA (Figure 4.2B). In a two-end-tethered DNA, the movement of a translocase such as RNA polymerase generates positive supercoils ahead and negative supercoils behind the enzyme, whereas this effect is absent if the DNA is unconstrained and free to rotate (29). In our case, the DNA segment between the two

Rad54 motors is topologically constrained, so rotations accumulate within the loop and generate torsional stress. The increasing torsion slows motor motion and prevents further loop growth, eventually reaching a maximum loop size when the motors stall.

The angular rotation (χ) added by the motor during translocation is described by:

$$\frac{d\chi}{dt} = a\Phi v \tag{8}$$

where $a = 2\pi / 10.5$ rad/bp, which is approximately 0.589 rad/bp representing the helical twist of B-DNA; v is the motor translocation velocity; Φ is effective protein-DNA rotational coupling coefficient ($0 < \Phi \leq 1$). Φ reflects the fraction of motor rotation that is transferred to DNA rotation and depends on both protein-DNA and DNA-solvent frictions. If no friction exists between protein and DNA, the motor spins without affecting the DNA ($\Phi = 0$); if the interaction is infinitely tight, the motor's rotation is fully transmitted to the DNA ($\Phi = 1$). Between these limits, stronger protein-DNA contacts increase Φ, and external viscous drag on DNA can also modulate Φ. How to measure or calculate Φ under different friction regimes is beyond the scope of this section; here, we focus on how changes in Φ influence loop extrusion.

The accumulated rotation of DNA stores elastic potential energy and builds up torque:

$$\frac{d\tau}{dt} = C\frac{d\chi}{dt} = Ca\Phi v \tag{9}$$

where C is the effective torsional stiffness of DNA, representing its resistance to twisting under applied torque.

The relationship between motor velocity and applied torque can be described phenomenologically as:

$$v = v_0\left(1 - \frac{\tau}{\tau_{stall}}\right) \tag{10}$$

where v_0 is the initial velocity in the absence of torque; τ_{stall} is the highest torque that the motor can tolerant before stalling. Combining Equation 10 and Equation 9, we know that:

$$\frac{d\tau}{dt} = Ca\Phi v_0\left(1 - \frac{\tau}{\tau_{stall}}\right) \tag{11}$$

Defining $\beta = \frac{Ca\Phi v_0}{\tau_{stall}}$ and assuming $\tau(0) = 0$, the solution is:

$$\tau = \tau_{stall}\left(1 - e^{-\beta t}\right) \tag{12}$$

$$v = v_0 e^{-\beta t} \tag{13}$$

In the two-motor loop system, the loop grows at the rate set by the motors' velocity difference. Assuming both motors share the same stall torque, the net velocity changes over time as:

$$\Delta v = \Delta v_0 e^{-\beta t} \tag{14}$$

and the loop growth rate follows:

$$\frac{dL}{dt} = \Delta v = \Delta v_0 e^{-\beta t} \tag{15}$$

$$L = \frac{\Delta v_0}{\beta}\left(1 - e^{-\beta t}\right) = \frac{\tau_{stall}}{Ca\Phi}(1 - e^{-\beta t}) \tag{16}$$

The maximum loop size is thus:

$$L_{max} = \frac{\tau_{stall}}{Ca\Phi} \tag{17}$$

indicating that L_{max} depends on the motor's torque tolerance and rotational coupling efficiency, but not on its initial velocity.

If we apply τ_{stall} = 10 pN·nm, C = 0.01 pN·nm/rad, which is a relatively soft torsional response, and Φ = 0.8, the simulation tells us the growing of L and Δv along time (Figure 4.2FG). And in this simulation, L_{max} is approximately 2000 bp, consistent with the optical-tweezer measurement from my colleague.

4.2.2 How this model fit our current observation

4.2.2.1 Rad54R272Q and Rad54R272A mutant

My colleagues identified two mutations at Rad54 residue arginine 272 (*rad54R272A* and *rad54R272Q*) that confer increased sensitivity to DNA-damaging agents, with the alanine substitution producing a stronger phenotype. AlphaFold predictions place R272 within the ATPase core. It forms contacts with Y562 and D769, thereby linking the two RecA-like lobes of Rad54. Consistently, mutations at these partner sites *rad54D769H*, *rad54D769A* and *rad54Y562A* also increase damage sensitivity, though generally less severe than R272 substitutions. Biochemical assays found that purified Rad54R272A and Rad54R272Q can form tetramers in solution and bind DNA but display reduced ATP hydrolysis activities. With Rad51 activation, they gain higher ATP hydrolysis rates, but still lower than WT protein together with Rad51. The mutants also exhibit reduced energy-transfer efficiency. Notably, in the absence of Rad51, these mutants hydrolyze ATP but fail to translocate along dsDNA; even with Rad51, their translocation velocity reaches only ~10% of WT+Rad51 despite exhibiting ~50% of the ATPase activity. The reduced chemo-mechanical coupling implies greater dissipation, plausibly due to elevated internal friction. Because higher ATPase rates and coupling efficiency typically permit motors to withstand higher opposing loads, we hypothesize that the mutants possess a lower torque tolerance (smaller τ_{stall}) than WT.

In optical-tweezer experiments, the mutants also compact DNA and can form loops in the presence of a presynaptic complex (PSC), but both compaction rate and loop size are reduced relative to WT. Using our loop extrusion model with Rad54R272Q parameters (driver μ = 42 bp/s, σ = 24 bp/s, anchor immobile because the enzyme does not move without activation; data from ref. 28), simulations predict a markedly lower loop extrusion rate (simulation not shown). When a linear force is applied to disrupt compacted DNA, higher force is required to disassemble mutant-generated loops (25), suggesting stronger inter-protein or protein-DNA interactions and greater resistance to distortion, consistent with low energy-transfer efficiency and elevated internal friction. This prediction can be tested directly by measuring the protein-DNA dissociation rate; we expect a lower off-rate for mutants than WT.

Taken together, these observations are captured by treating Rad54R272Q and Rad54R272A as higher Φ and lower τ_{stall} variants. The changes of both two parameters shrinks the maximum loop size. In simulation using τ_{stall} = 8.0 pN·nm and Φ = 1.0 to describe Rad54R272Q mutant, it reaches a smaller plateau of ~1300 bp and a lower generation rate (Figure 4.2FG), consistent with the optical tweezer measurements.

To summarize, the reduced ability of the mutants to catalyze D-loop capture both *in vivo* and *in vitro* may result from several factors:

(i) Slower initiation and growth. The initial Δv is much lower than WT (Figure 4.2G). Although the torque builds more slowly (so suppression to Δv is milder), the overall extrusion rate remains low. And the upper loop limit is smaller, yielding fewer loops within a fixed time window. If loop formation facilitates rapid 1-dimensional sequence search by the PSC under the guidance of Rad54, both a lower search rate and a smaller accessible domain diminish the overall efficiency.

(ii) Lower turnover. Mutant loops require greater force to disrupt; after collapse, residual local torque must dissipate before re-initiation. Reduced capacity to rebind and re-start before torsion clears further depresses loop throughput.

(iii) ATP limitation *in vivo*. When local ATP is limited, reduced chemo-mechanical efficiency exacerbates the shortfall. More ATP is dissipated, less is converted into productive work.

A longer homologous recipient DNA can partially compensate for poor D-loop capture. Longer dsDNA does not stabilize the search intermediates per se since invasion awaits homology, and PSC-mediated compaction is not homology-dependent. Instead, increased length raises the number of Rad51-ssDNA contact opportunities on dsDNA. Prior single-molecule work suggests a minimal search unit of ~8 nt (30–32). Flanking distortion brings the effective unit to ~16 nt (33). Longer filaments can make multiple 16-nt contacts owing to their increased number of binding segments and enhanced spatial flexibility. Once the driver binds Rad54, search converts from 3-dimensional to 1-dimensional along the loop. Multiple loops can form concurrently (Figure 4.2A), boosting local DNA concentration and the probability of PSC recruiting motors.

The mutants' lower search efficiency and turnover also help explain longer gene-conversion tracts *in vivo*. Continued end resection can proceed until homology is found, producing longer recipients that improve search but also increase the chance of large D-loops and CO events. Moreover, slower turnover can trap D-loops locally once formed, further biasing outcomes toward CO (28).

4.2.2.2 Rad54S816DS817D mutant

In Chapter 3, we identified a separation-of-function mutant of Rad54, *rad54S816D,S817D*. The mutant renders cells more sensitive to a range of DNA damage reagents. AlphaFold predicts the two serine residues are located at the interface of two RecA-like domains, where they interact with aspartic acid 525. Mutating D525 to alanine or lysine results similar but milder phenotypes. Biochemical characterization revealed that the mutant protein is deficient in DNA binding, with a ~2.5-fold higher K_d than WT. DNA curtain experiments further identified a ~2.5-fold higher k_{off} rate for the mutant, indicating that its reduced binding affinity arises mainly from easier dissociation rather than impaired association.

The mutant also exhibited a much lower ATP hydrolysis rate compared with WT. On DNA curtains, it shows much higher processivity when moving together with the hydrodynamic flow than when moving against flow, suggesting a passive, slippery-like movement of the mutant rather than active ATP-dependent translocation. The movement is also strongly biased in the direction of flow, with a much lower percentage of trajectories moving against the flow than WT protein, indicating a substantially reduced motor activity. When Rad51 in present, the Rad54S816DS817D mutant gains activation and recovers its ATP hydrolysis rate to WT-like level. Consistently, Rad51 activation enables the mutant to move more efficiently against the flow, although its velocity reaches only about 60% of WT, suggesting a lower chemo-mechanical energy transfer efficiency.

Taken together, we conclude Rad54S816DS817D is a mutant characterized by an easily-fall-off anchor, a lower τ_{stall} driver, and a lower Φ value due to reduced DNA binding activity. Lower τ_{stall} and lower Φ influence the maximum loop size L_{max} in opposite directions, with the former one decreasing it and the latter increasing it. Without more reliable measurements or parameter estimates, we cannot quantitively predict how these two factors jointly affect loop size in our current model. However, the increased k_{off} clearly has a negative impact on loop extrusion, since detachment of the anchor prematurely terminates the growing loop in addition to torque-induced stalling.

The binding deficiency can be partially rescued by increasing protein concentration. According to the Hill equation (Equation 18), elevating protein concentration *[P]* increases the fraction of bound complex θ, thereby compensating for the reduced probability of binding events:

$$\theta = \frac{[P]^n}{[P]^n + K_d^n} \tag{18}$$

However, a reaction typically succeeds only if the protein remains bound for at least a minimal dwell time. For example, during loop formation, it takes approximately 20 seconds for WT to reach it maximum loop size, and about 100 seconds for Rad54R272Q to reach a plateau (Figure 4.2F). For a given time *t*, the fraction of proteins that remain bound in a first-order dissociation process (see APPENDIX B.1) is:

$$P_{retention} = e^{-k_{off}t} \tag{19}$$

where $P_{retention}$ is the retention probability, k_{off} is the dissociation rate. The overall throughput of the protein depends on both bound fractions and the retention probability:

$$R = R_{max}\theta P_{retention} = R_{max}\frac{[P]^n}{[P]^n + K_d^n}e^{-k_{off}t} \tag{20}$$

where R_{max} is the intrinsic maximum throughput of the system. It presents the hypothetical success rate if every binding event lasted indefinitely. Assuming R_{max} does not differ among Rad54 variants, we can see that, for a given observation time t, the asymptotic throughput of the reaction is:

$$\lim_{[P]\to\infty} R = R_{max}e^{-k_{off}t} \tag{21}$$

This relationship shows that the overall throughput depends solely on the dissociation rate of the protein-DNA interaction. Higher dissociation rate inevitably leads to a lower reaction throughput, implying that protein overexpression cannot fully compensate for binding deficiencies, especially when a long dwell time is required for successful completion of the reaction. This is consistent with our experimental observations. When we overexpress Rad54S816DS817D mutant in *rad54S816D,S817D* background using a 2μ plasmid, it partially rescues the phenotype under low MMS concentration, but fails under high MMS stress, where more DNA damage must be processed, and the reaction requires both more protein and longer dwell time for repair.

In contrast, if we design an improved anchor by fusing a stronger DNA binding domain (DBD) to Rad54S816DS817D mutant (Rad54S816DS817D^{DBD}) and overexpress this engineered variant from a 2μ plasmid in *rad54S816D,S817D* background, we would expect enhanced rescue of the phenotype under high MMS stress. Mixing Rad54S816DS817D^{DBD} with Rad54S816DS817D should also promote D-loop formation *in vitro*, whereas Rad54S816DS817D alone barely supports it. This setup allows testing how anchor strength affects D-loop formation efficiency by introducing different DBDs. Nevertheless, adding Rad54S816DS817D^{DBD} cannot completely rescue the phenotype, because Rad54S816DS817D remains deficient in translocation against external force in the presence of Rad51, which fundamentally limits its ability to form large loops under stress.

Similarly, longer recipient DNA can mitigate the phenotype. In ectopic recombination, *rad54S816D,S817D* is less efficient at DNA repair and D-loop capture than WT, whereas in allelic recombination, its survival rate is not significantly reduced. Furthermore, the mutant tends to use longer track gene conversion producing more red colonies. However, this behavior differs from that of *rad54R272A* or *rad54R272Q* mutant because we observed an increase in NCO outcomes in *rad54S816D,S817D*. This finding is interesting because (i) it demonstrates that long track gene conversion does not necessarily lead to CO, implying that the utilization of distal donor sequences is not directly coupled to proximal donor engagement, even when homology is continuous; and (ii) the increased NCO likely reflects the easy disruption of Rad54-mediated multipoint DNA domains, which results in D-loop collapse and potential reinvasion. Consistent with this, we also observed an increase in BIR events in the mutant. Long track gene conversion and BIR events further increase in *rad54S816D,S817D, sgs1Δ* double mutant, where the loss of D-loop disruption factors exacerbates stabilization of collapsed intermediates.

In summary, the model provides a unified framework to explain why both Rad54R272A/Q and Rad54S816DS817D mutants display HR deficiencies. The distinct biochemical properties of these mutans ultimately produce different HR outcomes, underscoring how ATP hydrolysis and protein-DNA binding jointly control DNA translocation and compaction efficiency, which in turn governs HR intermediate development and resolution.

4.2.3 The limitations of the model

Although the current model successfully integrates biochemical measurements and physical parameters to explain Rad54-mediated loop extrusion process and how these molecular behaviors lead to observed genetic outcomes, it remains a simplified framework and should be interpreted qualitatively rather than quantitatively.

First, the model assumes a uniform torque buildup, whereas in reality DNA torsional stress is heterogeneous. The model neglects the torque relaxation through mechanisms such as twisting diffusion, nucleosome breathing and local DNA melting. These dissipative processes could buffer torque and extend the apparent loop growth phase. In fact, local DNA melting may play an important role because it facilitates strand invasion, and the resulting topological changes could impose different mechanical stress on proteins. However, this aspect was not explored here due to its complexity.

Second, the model treats DNA-protein dissociation as a first-order process while in reality multiple conformational states are likely involved. During these transitions, k_{off}, τ_{stall} and Φ may change dynamically in response to ATP concentration fluctuations, local DNA structural rearrangements and other environmental factors, rather than remaining independent constants. In addition, the model does not account for internal and external linear forces, which can also strongly influence the processivity of the motor. Indeed, there is an apparent inconsistency between the experimentally observed k_{off} on DNA curtains and the simulated loop extrusion rate. The k_{off} of WT is 1.73 × 10^{-4} s^{-1}, corresponding to a half-time of $ln2 / k_{off} = 4005$ s (Equation (4)), which is much longer than the simulated time window for loop formation. The half-time for loop formation observed on magnetic tweezer is also around 20 seconds, consistent with the simulation rather than measured k_{off}. This discrepancy suggests the existence of a torque- and force-dependent regulation of k_{off} that is not incorporated in the current model-possibly increasing DNA torque and tension leads to a corresponding rise in the dissociation rate. Such regulation is not readily seen in DNA curtain experiments to measure k_{off}, likely because Rad54 itself does not generate sufficient torque to significantly twist DNA. Consequently, the degree of torque accumulation in this setup may be too subtle to produce a measurable effect on the motor stability.

Third, the model currently describes a minimal two-motor system, whereas Rad54 likely operates as higher-order oligomers or clusters that compact DNA cooperatively. Such motor-motor and motor-DNA cooperativity could substantially alter loop growth kinetics and torque distribution, which are not captured by the present formulation. Additionally, in a physiological context, smaller loops may form within larger loops or become intertwined with neighboring loops (Figure 4.2A), reminiscent of hierarchical loop architectures proposed in chromatin organization models. How these higher-order structural complexities influence overall DNA compaction, mechanical stability and the efficiency of homology search remains important questions for future investigation.

Further refinements incorporating torque relaxation mechanisms, multi-state kinetics, and cooperative oligomerization will improve the model's predictive power and bring it closer to the physical and biological complexity of the system.

4.3 How future works can advance our understanding

Here we've proposed a Rad54-mediated DNA loop extrusion and compaction model that is driven by multiple protein-DNA contacts. This organization is reminiscent of for protein-DNA compartments that enhances local molecular concentrations and reaction efficiency. Therefore, Rad54-DNA assemblies are likely to exhibit condensate-like properties, suggesting that loop extrusion and DNA compaction may represent an intermediate stage of biomolecular condensates. Factors that disrupt Rad54-driven loop extrusion or DNA compaction are thus expected to impair the compartment formation and stability.

Moreover, it would be particularly exciting if discrete protein-DNA contact points could be visualized. Achieving this goal will rely on advances in imaging resolution, as these interactions occur at spatial scales well below the diffraction limitation of conventional optical microscope. Techniques such as super-resolution fluorescence microscopy or cryo-electron microscope offer promising avenues to overcome this limitation. However, reconstructing dynamic biochemical reaction under these observation conditions while preserving most of their native activity remains technically challenging. Future methodological developments will be essential to bridge this gap and to reveal structural and dynamic principles underlying homology search driven by recombinase, helicases and other factors.

References

1. M. Jaskelioff, S. Van Komen, J. E. Krebs, P. Sung, C. L. Peterson, Rad54p is a chromatin remodeling enzyme required for heteroduplex DNA joint formation with chromatin. *J Biol Chem* **278**, 9212–9218 (2003).

2. I. Amitani, R. J. Baskin, S. C. Kowalczykowski, Visualization of Rad54, a chromatin remodeling protein, translocating on single DNA molecules. *Mol Cell* **23**, 143–148 (2006).

3. N. Sugawara, X. Wang, J. E. Haber, *In vivo* roles of Rad52, Rad54, and Rad55 proteins in Rad51-mediated recombination. *Mol Cell* **12**, 209–219 (2003).

4. J. B. Crickard, C. J. Moevus, Y. Kwon, P. Sung, E. C. Greene, Rad54 drives ATP hydrolysis-dependent DNA sequence alignment during homologous recombination. *Cell* **181**, 1380-1394.e18 (2020).

5. G. Petukhova, P. Sung, H. Klein, Promotion of Rad51-dependent D-loop formation by yeast recombination factor Rdh54/Tid1. *Genes Dev* **14**, 2206–2215 (2000).

6. T. K. Prasad, R. B. Robertson, M. L. Visnapuu, P. Chi, P. Sung, E. C. Greene, A DNA-translocating Snf2 molecular motor: *Saccharomyces cerevisiae* Rdh54 displays processive translocation and extrudes DNA loops. *J Mol Biol* **369**, 940–953 (2007).

7. J. B. Crickard, Y. Kwon, P. Sung, E. C. Greene, Rad54 and Rdh54 occupy spatially and functionally distinct sites within the Rad51-ssDNA presynaptic complex. *EMBO J* **39**, e105705 (2020).

8. A. Meir, J. B. Crickard, Y. Kwon, P. Sung, E. C. Greene, Rad54 and Rdh54 prevent Srs2-mediated disruption of Rad51 presynaptic filaments. *Proc Natl Acad Sci U S A* **119**, e2113871119 (2022).

9. H. L. Klein, RDH54, a RAD54 homologue in *Saccharomyces cerevisiae*, is required for mitotic diploid-specific recombination and repair and for meiosis. *Genetics* **147**, 1533–1543 (1997).

10. M. Keymakh, J. Dau, J. Hu, B. Ferlez, M. Lisby, J. Brooks Crickard, Rdh54 stabilizes Rad51 at displacement loop intermediates to regulate genetic exchange between chromosomes. *PLoS Genet* **18** (2022).

11. S. E. Lee, A. Pellicioli, A. Malkova, M. Foiani, J. E. Haber, The *Saccharomyces recombination* protein Tid1p is required for adaptation from G2/M arrest induced by a double-strand break. *Current Biology* **11**, 1053–1057 (2001).

12. S. S. Shah, S. Hartono, A. Piazza, V. Som, W. Wright, F. Chédin, W.-D. Heyer, Rdh54/Tid1 inhibits rad51-rad54-mediated d-loop formation and limits d-loop length. *Elife* **9**, e59112 (2020).

13. M. Ferrari, C. C. Rawal, S. Lodovichi, M. Y. Vietri, A. Pellicioli, Rad9/53BP1 promotes DNA repair via crossover recombination by limiting the Sgs1 and Mph1 helicases. *Nat Commun* **11**, 3181 (2020).

14. T. Usui, S. S. Foster, J. H. J. Petrini, Maintenance of the DNA-damage checkpoint requires DNA-damage-induced mediator protein oligomerization. *Mol Cell* **33**, 147–159 (2009).

15. N. Jia-Lin Ma, D. F. Stern, Regulation of the Rad53 protein kinase in signal amplification by oligomer assembly and disassembly. *Cell Cycle* **7**, 808–817 (2008).

16. M. Feric, N. Vaidya, T. S. Harmon, D. M. Mitrea, L. Zhu, T. M. Richardson, R. W. Kriwacki, R. V. Pappu, C. P. Brangwynne, Coexisting Liquid Phases Underlie Nucleolar Subcompartments. *Cell* **165**, 1686–1697 (2016).

17. A. G. Larson, D. Elnatan, M. M. Keenen, M. J. Trnka, J. B. Johnston, A. L. Burlingame, D. A. Agard, S. Redding, G. J. Narlikar, Liquid droplet formation by HP1α suggests a role for phase separation in heterochromatin. *Nature* **547**, 236–240 (2017).

18. B. R. Sabari, A. Dall'Agnese, A. Boija, I. A. Klein, E. L. Coffey, K. Shrinivas, B. J. Abraham, N. M. Hannett, A. V. Zamudio, J. C. Manteiga, C. H. Li, Y. E. Guo, D. S. Day, J. Schuijers, E. Vasile, S. Malik, D. Hnisz, T. I. Lee, I. I. Cisse, R. G. Roeder, P. A. Sharp, A. K. Chakraborty, R. A. Young, Coactivator condensation at super-enhancers links phase separation and gene control. *Science* **361**, 379 (2018).

19. P. Li, S. Banjade, H. C. Cheng, S. Kim, B. Chen, L. Guo, M. Llaguno, J. V. Hollingsworth, D. S. King, S. F. Banani, P. S. Russo, Q. X. Jiang, B. T. Nixon, M. K. Rosen, Phase transitions in the assembly of multivalent signalling proteins. *Nature* **483**, 336–340 (2012).

20. S. F. Banani, H. O. Lee, A. A. Hyman, M. K. Rosen, Biomolecular condensates: Organizers of cellular biochemistry. *Nat Rev Mol Cell Biol* **18**, 285–298 (2017).

21. S. Kilic, A. Lezaja, M. Gatti, E. Bianco, J. Michelena, R. Imhof, M. Altmeyer, Phase separation of 53BP1 determines liquid-like behavior of DNA repair compartments. *EMBO J* **38**, e101379 (2019).

22. C. Lukas, V. Savic, S. Bekker-Jensen, C. Doil, B. Neumann, R. S. Pedersen, M. Grøhfte, K. L. Chan, I. D. Hickson, J. Bartek, J. Lukas, 53BP1 nuclear bodies form around DNA lesions generated by mitotic transmission of chromosomes under replication stress. *Nat Cell Biol* **13**, 243–253 (2011).

23. A. Piazza, S. S. Shah, W. D. Wright, S. K. Gore, R. Koszul, W.-D. Heyer, Dynamic processing of displacement loops during recombinational DNA repair. *Mol Cell* **73**, 1255-1266.e4 (2019).

24. S. Van Komen, G. Petukhova, S. Sigurdsson, S. Stratton, P. Sung, Superhelicity-driven homologous DNA pairing by yeast recombination factors Rad51 and Rad54. *Mol Cell* **6**, 563–572 (2000).

25. M. V Woodhouse, J. Hu, M. Wu, J. Qian, J. T. Inman, M. D. Wang, J. B. Crickard, The eukaryotic homology search complex distorts donor DNA structure to probe for homology. *bioRxiv*, 2025.08.28.672940 (2025).

26. E. M. Tavares, W. D. Wright, W.-D. Heyer, E. Le Cam, P. Dupaigne, *In vitro* role of Rad54 in Rad51-ssDNA filament-dependent homology search and synaptic complexes formation. *Nat Commun* **10**, 4058 (2019).

27. W. D. Wright, W.-D. Heyer, Rad54 functions as a heteroduplex DNA pump modulated by its DNA substrates and Rad51 during D loop formation. *Mol Cell* **53**, 420–432 (2014).

28. K. Sridalla, M. V. Woodhouse, J. Hu, J. Scheer, B. Ferlez, J. B. Crickard, The translocation activity of Rad54 reduces crossover outcomes during homologous recombination. *Nucleic Acids Res* **52**, 7031–7048 (2024).

29. L. F. Liu, J. C. Wang, Supercoiling of the DNA template during transcription. *Proceedings of the National Academy of Sciences* **84**, 7024–7027 (1987).

30. Z. Qi, S. Redding, J. Y. Lee, B. Gibb, Y. Kwon, H. Niu, W. A. Gaines, P. Sung, E. C. Greene, DNA sequence alignment by microhomology sampling during homologous recombination. *Cell* **160**, 856–869 (2015).

31. C. Danilowicz, D. Yang, C. Kelley, C. Prévost, M. Prentiss, The poor homology stringency in the heteroduplex allows strand exchange to incorporate desirable mismatches without sacrificing recognition *in vivo*. *Nucleic Acids Res* **43**, 6473–6485 (2015).

32. J. Y. Lee, T. Terakawa, Z. Qi, J. B. Steinfeld, S. Redding, Y. Kwon, W. A. Gaines, W. Zhao, P. Sung, E. C. Greene, Base triplet stepping by the Rad51/RecA family of recombinases. *Science* **349**, 977–981 (2015).

33. I. De Vlaminck, M. T. J. van Loenhout, L. Zweifel, J. den Blanken, K. Hooning, S. Hage, J. Kerssemakers, C. Dekker, Mechanism of homology recognition in DNA recombination from dual-molecule experiments. *Mol Cell* **46**, 616–624 (2012).

APPENDIX A

APPENDIX A.1 Materials and methods for Chapter 2.

This part corresponds to work published in *Nucleic Acids Research*. References and tables are provided in Chapter 2.

Yeast strain construction

Most of the *S. cerevisiae* strains used in this study were W303. All recombination outcome experiments were performed in the W303 background. Strains for spot assay experiments were BY4741 and were generated by transformation of *rdh54*Δ strains with pRS415 plasmids. The genotypes for all strains used in this study can be found in Table 2.S1. Plasmids for generation of strains can be found in Table 2.S2.

Yeast spot growth assay and colony growth

For complementation spot assays, overnight cultures were diluted back to an OD_{600} of 0.2 and then allowed to grow to an OD_{600} of 1.0. Cells were then serially diluted and manually spotted on Yeast Nitrogen Base (YNB) (-Leu) + 2% dextrose plates containing either no drug, 0.01% MMS or 25 μM CPT. Plates were incubated at 30 °C for 2-3 days and imaged at 24, 48, and 72 hours. For colony growth, overnight cultures were diluted 100-fold and then allowed to grow 2 hours. Then 0.01% MMS or an equal volume of sterilized H_2O was added to the cultures and allowed to grow 4 hours. Colony forming units (CFU) were determined by plating 1000-fold diluted cultures on YPD + adenine sulfate plates. The plates were scored the for colony growth and survival percentage was calculated by dividing the colonies from MMS-treated culture by the untreated culture.

Interhomolog gene conversion assay

Yeast strains of JBC206 and JBC207 and derivatives were crossed (Table 2.S1), and the diploids were selected on YNB (-Ura/-Trp) + 2% dextrose and allowed to grow for 2-3 days. Fresh diploid colonies were then grown for 15 hours in YPD. 30 μL of saturated culture was plated on YNB (-Leu) + 2% dextrose and 30 μL of culture diluted 1:10,000 was plated on YNB (Synthetic complete, SC) + 2% dextrose and allowed to grow for three days. The colonies on each plate were then counted. The data was analyzed by dividing the adjusted number of colonies on the -Leu plate by the colonies on the SC plate. This generated a frequency. The mean and standard deviation of the data were determined using multiple different colonies from multiple different crosses. Statistical comparisons were also performed using a non-parametric Mann-Whitney test for significance. This did not yield different results from the standard *t*-test.

Red/white recombination assay

The WT strain used in this assay as well as the procedure for diploid formation are described here (45,62). The genotypes for modifications to these strains can be found in Table 2.S1. The assay was performed by growing the appropriate strain overnight in YP + 2% raffinose. The next day cells were diluted to an OD_{600} of 0.2 and allowed to reach an OD_{600} of 0.4-0.5 followed by the expression of *I-Sce1* through the addition of 2% galactose. Cells were allowed to grow for an additional 1.5 hours, after which they were plated on YPD and allowed to grow for 48 hours. After 48 hours they were placed at 4 °C overnight to allow further development of red color. The number of white, red, and sectored colonies was then counted followed by replica plating onto YPD + hygromycin B (200 μg/ml) and YPD + nourseothricin (67 μg/ml, clonNat) for analysis of recombination outcomes. Strains were also replica plated on YNB (-Ura/-Met) + 2% dextrose to insure proper chromosome segregation (Table 2.S4). The data was analyzed by counting colonies that were sectored, and then counting colony survival on different antibiotic sensitivities. The data for each category was then divided by the total population of sectored colonies. The standard deviation between biological replicates analyzed for at least three independent experiments from different crosses.

Template switching assay

The WT strains used for this study were described in (70). The genotypes for modification of these strains can be found in Table 2.S1. The assay was performed by growing the appropriate strain in YP + 2% raffinose overnight. The next day cells were diluted in YP + 2% raffinose to an OD_{600} of 0.2 and allowed to grow for four hours. The cells were then treated with 2% galactose for 3 hours and plated on YNB (-Ura) + 2% dextrose. CFU were determined by plating a dilution of the culture on non-selective media. After three days the plates were scored for colony growth. The Ura+ frequency was determined by dividing the adjusted CFU from the selective plate by the number of colonies on the non-selective plate. The mean and standard deviation were calculated for three independent experiments.

Co-immunoprecipitation experiments

A starter culture was grown in 5 mL YPD for 10 hours. The culture was then inoculated into 100 mL of YP + 3% glycerol + 2% sodium lactate and allowed to grow overnight until the OD_{600} was ~1.0. Then 2% galactose (final concentration) was added to the culture to induce DSBs. In an uninduced control group, 2% dextrose was added. The cells were allowed to grow for 2 hours and harvested by centrifugation. Cell pellets were washed twice with 1xPBS (137 mM NaCl, 2.7 mM NaCl, 1.8 mM KH_2PO_4, 10 mM Na_2HPO_4) + 0.2 mM PMSF, and frozen at -80 °C for at least 30 minutes. Cells were then thawed and resuspended in lysis buffer (20 mM Tris-Cl pH 7.5, 300 mM NaCl, 0.01% NP-40, 10% glycerol, 0.2 mM PMSF, Protease inhibitor cocktail). Glass disruptor beads were added, and the cells were bead beat with 1 minute on and 1 minute off for a total of 8 cycles. The cellular debris was then spun down at ~1,100 x g for 10 minutes at 4 °C. The supernatant was then centrifuged at 26,712 x g for 10 minutes at 4 °C. The supernatant was collected as whole cell extract and incubated with anti-RAD53 (Abcam, ab104232) pre-coated Dynabeads Protein G (Invitrogen, Cat No. 10003D) overnight at 4 °C. To prepare the coated beads, they were first washed with PBST (PBS + 0.1% Tween-20) 3 times, then resuspended with PBST and antibody and incubated at 4 °C for 2 hours. After incubation, the antibody was removed, and the beads were washed with PBST 3 times. Then the beads were ready to be used. For each 1 mL of cell lysate, 1 μL of anti-RAD53 antibody and 15 μL of Dynabeads were used. The immunocomplexes were washed with wash buffer (20 mM Tris-Cl pH 7.5, 500 mM NaCl, 0.01% NP-40, 10% glycerol) 3 times and transferred to a new tube. The whole cell extract and immunocomplex were dissolved in SDS loading buffer. The samples were loaded on an SDS-PAGE, and the proteins were transferred onto a nitrocellulose membrane. The membrane was stained with Ponceau S staining solution (5% glacial acetic, 0.1% Ponceau S) and blocked with 5% non-fat dry milk in TBST (2.4 g Tris, 8.7 g NaCl, 1 mL Tween-20 in 1 L H_2O, pH 7.5) for 1 hour. The membrane was then incubated with the primary antibody (anti-HA, Roche, 11583816001, 1:1000) in TBST + 5% non-fat dry milk overnight at 4 °C followed by incubation with secondary antibodies (Goat anti-Mouse IgG, Invitrogen, Cat No. A16072, 1:3000) at room temperature for 1 hour. The immunoblots were visualized with enhanced chemiluminescence.

Protein expression and purification

6xHis-Rdh54, 6xHis-Rdh54-mCherry, and Rdh54 mutants were purified as follows. Rosetta 2 BL21 (DE3) cells bearing pET15-6xHis-Rdh54 expression plasmids were grown to an OD_{600} between 0.6 and 0.8 at 37 °C. The temperature was lowered to 16 °C and cells were induced with 0.5 mM IPTG overnight. Cells were harvested by centrifugation and stored at -80 °C. Cells were resuspended in buffer A (25 mM Tris-Cl pH 7.5, 1000 mM NaCl, 10 mM Imidazole, 0.01% NP-40, 10% glycerol, 5 mM 2-Mercaptoethanol, 0.2 mM PMSF, and Protease Inhibitor cocktail) and lysed by freeze thaw. Cell lysate was sonicated on ice for 10 cycles with 65% duty cycle and 15 sec on and 45 sec off. Lysate was centrifuged at 10,000 x g for 45 minutes at 4 °C. Clarified extract was then mixed with pre-equilibrated His-Pur Nickel-NTA resin and incubated in batch for 1 hour at 4 °C. After 1 hour the resin was centrifuged and washed 2x with buffer A, followed by 2x washes with buffer B (25 mM Tris-Cl pH 7.5, 200 mM NaCl, 10 mM Imidazole, 0.01% NP-40, 10% glycerol, 5 mM 2-Mercaptoethanol, 0.2 mM PMSF, and Protease Inhibitor cocktail). The resin was then added to a disposable column, and the protein was eluted in buffer C (25 mM Tris-Cl pH 7.5, 200 mM NaCl, 200 mM Imidazole, 0.01% NP-40, 10% glycerol, 5 mM 2-Mercaptoethanol, 0.2 mM PMSF, and Protease Inhibitor cocktail). Fractions were analyzed by SDS-PAGE and the peak fractions were pooled. The protein was further purified using a strong cation exchange column (HiScreen SP FF). The column was resolved using a 20-100%

gradient of buffer D (25 mM Tris-Cl pH 7.5, 0 mM KCl, 1 mM EDTA, 0.01% NP-40, 5 mM 2-Mercaptoethanol, 10% glycerol) and buffer E (25 mM Tris-Cl pH 7.5, 1000 mM KCl, 1 mM EDTA, 0.01% NP-40, 5 mM 2-Mercaptoethanol, 10% glycerol). Fractions were analyzed by SDS-PAGE. Peak fractions were pooled and concentrated by centrifugation at ~1,100 x g at 4 °C using a 10 kDa MWCO Vivaspin 6 column. Protein was finally purified on a 120 mL S300 column (HiPrep Sephacryl S-300 HR) in SEC buffer (30 mM Na-Hepes pH 7.5, 400 mM NaCl, 1 mM EDTA, 0.01% NP-40, 5 mM 2-Mercaptoethanol, 10% glycerol). Peak fractions were pooled, and the protein was concentrated as described above. Purified protein was stored at -80 °C. 6xHis-Rad53, 6xHis-GFP-Rad53, 6xHis-Rad53D339A, and 6xHis-GFP-Rad53D339A were purified as previously described (52). Plasmids for protein expression can be found in Table 2.S2.

In vitro kinase reactions

In vitro kinase assays were performed in Rad53 kinase buffer (25 mM Na-Hepes pH 7.5, 150 mM NaOAc, 10% glycerol, 10 mM $MgCl_2$, 10 mM ATP, 0.2 mM Na Orthovanadate). 1 μM Rdh54 was incubated with 0.1 μM Rad53 for the defined periods of time. Reactions were quenched with SDS-PAGE loading buffer and resolved on a 10% SDS-PAGE impregnated with phostag reagent and 10 mM $MnCl_2$. The gel was stained with Coomassie Brilliant blue and the shift in Rdh54 was directly observed. Mass spectrometry analysis was performed on Rdh54 samples phosphorylated *in vitro* that were excised from a Coomassie-stained SDS-PAGE.

ATPase assay

To measure ATP hydrolysis rates, a commercially available ADP-GLO kit was used. ATP hydrolysis reaction was performed in HR buffer (20 mM Tris-OAc, 50 mM NaCl, 10 mM Mg(OAc)$_2$, 200 ng/L BSA, 1 mM DTT and 10% glycerol) and contained 1 mg/mL sheared salmon sperm DNA, and 100 nM Rdh54.

Flow cell construction

To generate flow cells, metallic chrome patterns were deposited on quartz microscope slides with pre-drilled holes for microfluidic line attachment by electron beam lithography (72). After metal deposition microscope slides were converted to flow cells by adhering a piece of double-sided tape to the side of the microscope slide with the metal barriers. A channel was created by covering the two-sided tape with a small piece of paper in between the two drill holes. The paper was excised to create the flow chamber and a glass coverslip was fixed to the tape. The chamber was sealed by heating to 165 °C in a vacuum oven at 25 mm Hg for 60 minutes. Flow cells were then completed by using hot glue to fit IDEX nano ports over the drill holes on the opposite side of the microscope slide from the coverslip.

Single molecule experiments

All single molecule experiments were conducted on a custom-built prism-based total internal reflection microscope (Nikon) equipped with a 488-nm laser (Coherent Sapphire, 100 mW), a 561-nm laser (Coherent Sapphire, 100 mW), and two Andor iXon EMCCD cameras. DNA substrates for DNA curtains experiments were made by attaching a biotinylated oligo to one end of the 50 kb Lambda phage genome, and an oligo with a digoxygenin moiety on the other. This allowed double tethering of the DNA between chrome barriers and chrome pedestals, as previously described (72,73). Flow cells were attached to a microfluidic system and sample delivery was controlled using a syringe pump (KD Scientific). Two color imaging was achieved by two XION

512x512 back-thinned Andor EM-CCD cameras and alternative illumination using a 488-nm laser and a 561 nM laser at 25% power output. The lasers were shuttered resulting in a 200 msec delay between each frame. Images were collected with a 200 msec integration time. Rdh54-mCherry translocation velocity and distances were measured in HR Buffer (20 mM Tris-OAc, 50 mM NaCl, 10 mM $Mg(OAc)_2$, 200 ng/µL BSA, 1 mM DTT).

Analysis of dsDNA translocation

The velocity and track length for Rdh54-mCherry molecules were measured by importing raw TIFF images as image stacks into ImageJ. Kymographs were generated by defining a 1-pixel wide region of interest (ROI) along the long axis of individual dsDNA molecules. Data analysis was performed from the kymographs. The start of translocation was defined when the Rdh54-mCherry molecule moved > 2 pixels. Pauses were defined as momentary stalls in translocation that lasted 2-4 frames. Termination was defined by molecules that did not move for >10 frames. Velocities were calculated using the following formula $[(|Y_f-Y_i|)*1{,}000 \text{ bp}/[|X_f-X_i|])*\text{frame rate}]$; where Y_i and Y_f correspond to the initial and final pixel position and X_i and X_f correspond to the start and stop time (in seconds). Graphs of individual velocity and distances travelled were plotted in GraphPad Prism 9. The mean was determined from these graphs and significant differences between mutants was determined by performing a student's *t*-test of this data.

Photobleaching measurements and analysis of Rdh54 cluster size

Photobleaching measurements were made by binding Rdh54-mCherry to the dsDNA and then observing the reaction without shuttering of the 561 nM laser at 25% power output (25 mW). Images were collected with 200 msec integration time. Kymographs were generated from individual DNA molecules and were visually inspected for irreversible changes in signal intensity. This was quantified by measuring the signal intensity over time and identifying defined drops. These drops in intensity were used to create a distribution of photobleaching steps. The intensity of individual drops was used to create a distribution to evaluate the mean intensity drop which correlates with the intensity for an individual fluorophore. Cluster size was then determined by subtracting the global background from the flow cell from each cluster, and then dividing by the mean intensity drop for an individual fluorophore. This created an estimated number of molecules per foci. Populations of bound Rdh54 under different conditions were statistically compared for significance using a non-parametric Mann-Whitney test in Graph Pad Prism 9.

Rad53 binding experiments

For Rdh54 binding experiments, 1 nM of 6xHis-Rdh54-mCherry was mixed with 6xHis-GFP-Rad53 and injected onto pre-formed DNA curtains. Initial binding was monitored with a frame rate of 1 frame/3 sec. Data were then processed as described above. The number of Rdh54 molecule bound by GFP-Rad53 were then scored for binding. For functional assays Rdh54-mCherry, Rdh54T851A-mCherry, or Rdh54S852A-mCherry were treated with catalytic amounts of Rad53 for 60 minutes in HR buffer. Translocation was then monitored by single molecule imaging and analyzed as described above.

APPENDIX B

APPENDIX B.1 Materials and methods for Chapter 3.

This part corresponds to work under reviewing in *JOUNRAL*. References and tables are provided in Chapter 3.

Yeast strains construction

Strains for the initial spot assay were BY4741 and generated by centromeric plasmid expression in the *rad54* strain or by gene replacement, as indicated in the context. Strains for the ectopic recombination assay were TGI354 (86) and were generated by gene replacement or centromeric plasmid expression in the *rad54* strain, as indicated in the context. Strains for the *in vivo* D-loop capture (DLC) and extension (DLE) assay were generated in the WDHY5511 (19,88) background by gene replacement. Strains for tetrad dissection were derived from the W303 background and generated by gene replacement. Strains for red/white allelic recombination were generated by gene replacement from parent strains LSY2205 and LSY2202 (91). Strains for the allelic recombination assay were in W303, TGI354, and WDHY5511 backgrounds, which were also used in the spot assay as indicated.

Protein purification

Rad54, Rad54 S816AS817A, Rad54 S816DS817D, Rad51, and RPA-mCherry were purified as previously described (29). In brief, a protease-deficient yeast strain was transformed with GFP-GST-Rad54, GFP-GST-Rad54 S816AS817A, or GFP-GST-Rad54 S816DS817D on a 2μ plasmid under the control of the Gal1/10 promoter. Cells were grown in YNB (-Ura) plus 3% glycerol and 2% lactic acid. When the cells reached an OD_{600} of 1.5, expression was induced by adding 2% galactose for 6 hours. Cells were harvested by centrifugation and stored at -80 °C.

Cell pellets were resuspended in Rad54 resuspension buffer (30 mM Tris-Cl [pH 7.5], 1 M NaCl, 1 mM EDTA, 10% glycerol, 10 mM BME (β-mercaptoethanol), protease inhibitor cocktail and 2 mM PMSF). Cells were disrupted by manual bead beating, and the lysate was clarified by centrifugation at 26,500 x g for 1 hour. The lysate was fractionated by ammonium sulfate (AS) precipitation. AS was gradually added with mixing to a final concentration of 20% followed by centrifugation at 10,000 x g for 10 minutes. The supernatant was discarded, and the AS concentration was raised to 50% followed by centrifugation at 10,000 x g for 10 min. The protein pellet was resuspended in PBS (phosphate buffered saline) plus 1M NaCl and 10 mM BME. The resulting re-suspended protein was then bound to pre-equilibrated GST resin in batch for 1 hour at 4 °C. The GST resin was washed twice with PBS plus 1000 mM NaCl, and twice with PBS plus 500 mM NaCl. The protein was eluted in 20 mM glutathione in PBS plus 500 mM NaCl. The peak fractions were pooled and then applied to a Sephacryl S-300 High Resolution gel filtration column pre-equilibrated with Rad54 SEC buffer (30 mM Tris-Cl [pH 7.5], 500 mM NaCl, 1 mM EDTA, 10% glycerol, and 10 mM BME). The peak was pooled and dialyzed against Rad54 SEC buffer plus 50% glycerol and stored at -80 °C in single-use aliquots.

6xHis-SUMO-Rad51 was transformed into *Escherichia coli* BL21 (DE3) Rosetta2 cells and grown to an OD_{600} of 0.4 to 0.6 at 37 °C. Expression was induced by addition of 0.5 mM IPTG for 3 hours at 37 °C. Cells were harvested and stored at -80 °C. Cells were lysed by freeze-thaw in Cell Lysis Buffer (CLB: 30 mM Tris-Cl [pH 8.0], 1 M NaCl, 10% glycerol, 10 mM imidazole, 5 mM BME, and protease inhibitor cocktail). Crude lysates were sonicated for 6 pulses of 30 seconds on and 2 minutes off, then clarified by centrifugation at 26,500 x g. The extract was precipitated with 50% AS and centrifuged at 26,500 x g for 10 minutes. The pellet was resuspended in CLB and bound to 1 mL of pre-equilibrated Ni-NTA resin for 1 hour with rotation at 4 °C. The resin was washed three times with CLB and eluted in CLB plus 200 mM imidazole. The protein was mixed with 400 units of the SUMO protease Ulp1 and dialyzed overnight at 4°C into Rad51 buffer (30 mM Tris-Cl [pH 8.0], 150 mM NaCl, 1 mM EDTA, 10% Glycerol, 10 mM imidazole). The 6xHis-SUMO tag and SUMO protease were removed by passing the dialyzed proteins over a second 1 mL Ni-NTA column. The purified Rad51 was then stored at -80 °C in single-use aliquots.

Multiple Sequence Alignment

Rad54-like eukaryotic sequences were retrieved by BLASTP (NCBI, nr database; organism filter: Eukaryota) using *S.c.*Rad54 as the query. Redundant entries and obvious fragments were removed. Sequences were aligned with Clustal Omega, the alignment was trimmed with trimAl, and sequence logos were generated from the trimmed alignment using the Python package Logomaker.

Yeast spot growth assay

RAD54 and its designed mutants were expressed using a centromere vector, pRS415, and transformed into the BY4741 *rad54* strain or other background strains as indicated, followed by selection on YNB (-Leu) + 2% dextrose plates. Transformed cells were grown overnight in YNB (-Leu) + 2% dextrose medium. The following day, the overnight cultures were diluted to an OD_{600} of 0.3 and grown to an OD_{600} of 1.0. Cells were then serially diluted and spotted on YNB (-Leu) + 2% dextrose plates containing either no drug, 0.01% methyl methanesulfonate (MMS), or 0.02% MMS. Other drugs were also used, including 0.02 µg/mL 4-NQO, 0.04 µg/mL 4-NQO, 10 µM camptothecin (CPT), and 20 µM CPT as indicated. Plates were incubated at 30 °C for 3 days and imaged at 72 hours. BY4741 strains with RAD54 mutants were also generated via gene replacement. The procedures for the spot assay for these strains were the same as for the centromeric-expressed strains, except that the overnight culture was grown and diluted in Yeast extract + Peptone (YP) + 2% dextrose medium. The serially diluted cells were spotted on YP + 2% dextrose containing either no drug or the drugs mentioned above. Plates were incubated at 30 °C for 2 days and imaged at 48 hours. For *RAD51* or *rad51I345T* on a pYES plasmid, cells were transformed. Cultures were grown overnight in YNB (-Ura) + 2% dextrose and diluted the next day. After cells reached an OD_{600} of 1.0, they were serially diluted onto YNB (-Ura) +2% dextrose or YNB (-Ura) +2% galactose and incubated at 30 °C for 48 hours. They were then images.

Ectopic recombination assay

The wildtype strain used for this study was described in (86). The genotypes for modifying these strains are listed in Table 3.E1. A single colony was picked and grown in YP + 3% glycerol + 2% lactate medium to log phase. The culture was diluted and plated on YP + 2% dextrose and YP + 2% galactose plates, respectively. Plates were incubated at 30 °C for 2 to 3 days, and the number of colonies was counted. The viability rate was calculated by dividing the colony number on the YP + 2% galactose plate by that on the YP + 2% dextrose plate. The mean and standard deviation were calculated for multiple independent experiments as indicated. For centromeric expression of RAD54 and its mutants in *rad54* strains, a single colony was picked and grown in YNB (-Leu) + 2% dextrose overnight. On the second day, the culture was diluted 10-fold into YNB (-Leu) containing 3% glycerol and 2% lactate and grown at 30 °C for 6 hours. Then the culture was diluted and plated onto YNB (-Leu) + 2% dextrose and YNB (-Leu) + 2% galactose, respectively. After being incubated at 30 °C for 3 to 4 days, the numbers of colonies were determined, and the viability was calculated by dividing the colony number on the galactose plate by that on the dextrose plate.

Allelic Recombination assay

The assay was performed by growing the appropriate strain overnight in YP + 2% raffinose. The next day, cells were diluted to an OD_{600} of 0.2 and allowed to reach an OD_{600} of 0.4-0.5, then *I-Sce1* expression was induced by adding 2% galactose. Cells were allowed to grow for an additional 1.5 hours, then plated onto YP + 2% dextrose (YPD) plates and grown for 48 hours. After 48 hours, they were placed at 4 °C overnight to enable further development of the red color. The number of white, red, and sectored colonies was then counted, followed by replica plating onto YPD + hygromycin B (200 µg/ml) and YPD + nourseothricin (67 µg/ml, clonNat) for analysis of recombination outcomes. Strains were also replica plated on YNB (-Ura/-Met) + 2% dextrose to ensure proper chromosome segregation and YNB (-adenine sulfate) +2% galactose to assay for recombinants versus uncut DNA. The data were analyzed by counting sectored colonies and assessing colony survival across different antibiotic sensitivities. The data for each category was then divided by the total population of sectored colonies. The standard deviation between biological replicates was analyzed for at least six independent experiments from different crosses.

Yeast cell imaging

To immobilize yeast cells, an agarose pad was used. A 1% agarose solution was prepared by adding agarose in S media (YNB plus 0.5% ammonium sulfate, then autoclaved) and microwaving to dissolve. An amino acid mix was added to a final concentration of 1x to ensure yeast cells could grow on the agarose pad. The dissolved agarose was kept warm on a 65 °C metal heater. One clean microscope slide was taped at both ends, and 30 μL of 1% agarose was applied to the center of the slide. Another clean and untapped microscope slide was immediately placed on top, and gentle pressure was applied to ensure the agarose spread evenly. Then the slide sandwich was placed on an ice bag for approximately 30 seconds to allow the agarose to solidify. The top slide was carefully slid out, leaving the agarose pad intact on the bottom slide. The agarose pad was allowed to dry for 3 minutes before 3 μL of properly diluted yeast cells was added. A coverslip was then placed over the cells. A Nikon Eclipse Ti microscope equipped with a 488-nm laser. A Plan APO 60XA/1.20 WI objective and an ANDOR Zyla-5.5-CL3 camera were used to observe and capture yeast cells.

Tetrad dissection

Strains used for tetrad dissection were generated by gene replacement in the W303 background and are listed in Table 3.E1. *MATa* strains and *MATα* strains were first mixed on YPD plates and incubated for 4 hours at 30 °C, then re-streaked on YNB (-Leu) + 2% dextrose + 0.25 g/L G418 plates to select for both *TRP1* and *KanMX* markers. Diploid cells were re-streaked onto sporulation plates (1% KOAc, 0.1% yeast extract, 0.05% dextrose, 2% Agar) and grown for 2 days at 30 °C. One loopful of sporulated cells was digested in zymolyase at 37 °C for 9.5 minutes before tetrad dissection. The 10x zymolyase solution for tetrad dissection was prepared by dissolving 25 mg zymolyase in 500 μL of spheroplasting buffer (recipe for spheroplasting buffer described in the DLC assay section). For a working tetrad dissection solution, 2.5 μL of 10x zymolyase solution was diluted into 25 μL sterile water. The digestion was quenched by adding 250 μL sterile water and placing the cells on ice for at least 5 minutes. For dissection, 10 μL of digested spores were added onto one side of a YPD plate, which was then placed vertically to allow the drop flow across the plate. Plates were stored at 4 °C for 2 days before tetrad dissection. Dissection was performed on a dissecting microscope. One tetrad was separated into four spores, which were then placed individually on the plate with ~5 mm spacing. The spores were grown at 30 °C for 2 days before survival rates were assessed.

ATPase assay

A commercially available ADP-GLO kit (Cat No. V6930, Promega) was used to measure ATP hydrolysis activity. ATP hydrolysis reaction was performed in HR buffer (20 mM Tris-OAc [pH 7.5], 50 mM NaCl, 10 mM $Mg(OAc)_2$, 200 ng/μl BSA, 1 mM DTT, and 10% Glycerol) and contained 1 mg/ml sheared salmon sperm DNA, 20 nM Rad54, and 200 nM Rad51 (if added).

Electrophoresis mobility shift assay (EMSA) for Rad54

An Atto647N-labeled 90-mer oligo was annealed with an unlabeled complementary oligo to form a labeled 90-bp dsDNA substrate. The oligo sequences are available in Table 3.E3. The binding reaction was performed in EMSA buffer (35 mM Tris-Cl [pH

7.5], 3 mM $MgCl_2$, 50 mM KCl, 1 mM DTT, 10% glycerol). The final DNA concentration was 10 nM, and proteins were titrated to be 0, 6.25, 12.5, 25, 50, 100, 150, and 200 nM as final concentrations for Rad54 wildtype and Rad54 S816DS817D. Rad54 S816AS817A was titrated to be 0, 6.25, 12.5, 25, 50, 100, and 139 nM as final concentrations. The DNA and proteins were incubated at 30 °C for 5 min and then resolved by 8% Native-PAGE in 0.5x TBE buffer (44.6 mM Tris, 44.5 mM boric acid, 1 mM EDTA, 8% acrylamide / bis-acrylamide (37.5:1), 0.1% APS, 0.1% TEMED) running in 0.5x TBE buffer (44.6 mM Tris, 44.5 mM boric acid, 1 mM EDTA). The hill curve of Rad54-DNA binding was fitted through neutcurve (107).

In vitro D-loop assay

D-loop formation experiments were performed in HR buffer (30 mM Tris-OAc [pH 7.5], 50 mM NaCl, 10 mM $MgOAc_2$, 1 mM DTT, 0.2 mg/ml BSA) using an Atto647N-labeled DNA duplex (15 nM) with homology to the pUC19 plasmid. Rad51 (300 nM) was incubated with recipient DNA at 30 °C for 15 minutes. The resulting Rad51 filaments were mixed with indicated concentrations of Rad54, RPA (500 nM), and pUC19 plasmid (0.3 nM). Reactions were quenched at the indicated time points and treated with 1 unit of Proteinase K at 37 °C for 20 minutes. The reactions were then resolved by electrophoresis on a 0.9% agarose gel and imaged for fluorescence using a Typhoon imager.

Flow cell construction

Metallic chrome patterns were deposited on quartz microscope slides with predrilled holes for microfluidic line attachment by electron beam lithography to generate flow cells. After metal deposition, a channel was created by placing a small piece of paper between the drill holes and covering the two-sided tape. The paper was excised to make the flow chamber, and a glass coverslip was fixed to the tape. The chamber was sealed by heating to 165 °C in a vacuum oven at 25 mmHg for 60 min. Flow cells were then completed by hot-gluing IDEX nano ports over the drill holes on the opposite side of the microscope slide from the coverslip.

Single molecule experiments

All single molecule experiments were conducted on a custom-built prism-based total internal reflection microscope (Nikon) equipped with a 488-nm laser (Coherent Sapphire, 100 mW), a 561-nm laser (Coherent Sapphire, 100 mW), a 640-nm laser (Coherent Obis, 100 mW) and two Andor iXon EMCCD cameras. DNA substrates for DNA curtains experiments were made by attaching a biotinylated oligo to one end of the 50 kb Lambda phage genome and an oligo with a digoxigenin moiety on the other. This enabled double tethering of the DNA between the chrome barriers and the chrome pedestals, as previously described. As for single tethered DNA, if specified in the context, flow cells were attached to a microfluidic system, and sample delivery was controlled using a syringe pump (KD Scientific). Three-color imaging was achieved by two XION 512×512 back-thinned Andor EM-CCD cameras and alternative illumination using a 488 nm laser, a 561 nm laser, and a 640 nm laser at 25% power output. The lasers were shuttered, resulting in a 200-msec delay between each frame. Images were collected with a 200-msec integration time. Translocation velocity and distances were measured in HR Buffer. Channel bleed-through is prevented by shuttering of the laser lines, emission filters, and the use of complementary fluorophores. In this case GFP is not activated by the 561 or 647 laser lines, and the 488 or 561 laser lines do not activate

Atto647N. The 488-laser line can poorly activate mCherry labelled fluorophores. However, the emitted light is split by a dichroic mirror and filtered through a band-pass and long-pass filter to block wavelengths of light above a certain cutoff. This is sufficient to prevent mCherry signal bleed through into the 488 channel.

Analysis of dsDNA translocation

The velocity and track length for GFP-Rad54 molecules were measured by importing raw TIFF images as image stacks into ImageJ. Kymographs were generated by pointing around a fluorophore signal and defining the whole individual dsDNA molecules where the fluorophore bound to a region of interest (ROI) using a home-made script. Data analysis was performed from the kymographs. The start of translocation was defined when the GFP-Rad54 molecule moved > 2 pixels. Pauses were defined as momentary stalls in translocation that lasted 2-4 frames. Termination was defined by molecules that did not move for > 10 frames. Velocities were calculated using the following formula $[(Y_f - Y_i) \times 1031.96 \text{ bp} / [|X_f - X_i|]) \times \text{frame rate}]$; where Y_i and Y_f correspond to the initial and final pixel position and X_i and X_f correspond to the start and stop time (in seconds). Negative values stand for translocations moving from barrier to pedestals, which was assisted by a flow. Positive values stand for translocations against flow directions.

Dissociation rate measurement

The dissociation rate of DNA-GFP-Rad54 was measured by initiating data collection, followed by the injection of 10nM GFP-Rad54 in HR buffer onto single-tethered DNA curtains to allow proteins to bind to DNA. The flow rate was maintained at 0.2 mL/min to allow for initial binding and prevent further binding events. Images were collected with a 100 msec integration time at 200 msec intervals for a duration of 5 minutes for the bleaching experiment, or at 1 sec intervals for a period of 15 minutes for the dissociation experiment. The fluorescent signal decay in both experiments was fit to an exponential function, $A = A_{max}*exp(-k*t)$. The difference between the k values obtained from bleaching experiment and dissociation experiment was used to calculate the dissociation rate: $k_{off} = k_{dissociation} - k_{bleaching}$.

DLC assay

DLC assay was performed as described before (19,88) . In brief, yeast cells were grown in a 5 mL YP + 2% dextrose + 4% adenine sulfate medium overnight. The second day, the culture was diluted by 10-fold in 5 mL YP + 3% glycerol + 2% lactate + 4% adenine sulfate and grown for around 8 hours. Then the culture was inoculated into 100 mL of YP + 3% glycerol + 2% lactate + 4% adenine sulfate medium with an initial $OD_{600} \approx 0.006$ and grown for 16 hours. A 5x psoralen stock solution (0.5 mg/mL trioxsalen in 200-proof ethanol) was made in a 50-mL aluminum foil-covered falcon tube and dissolved on a shaker at room temperature overnight with gentle rocking. Next day, the culture should have an OD_{600} at 0.3-0.8. 7.5 OD_{600} of cells was collected as time 0 control, centrifuged at 2,246 x g, 4 °C for 5 minutes.

The cell pellets were resuspended in 1x psoralen buffer. The 1x psoralen buffer was prepared by diluting 5x psoralen in 200-proof ethanol before collecting cells. The resuspended cells were plated in a 60 mm x 15 mm petri dish, put 2-3 cm below a UV light source with the lip removed atop a pre-chilled metal block. The cell samples were exposed under the UV light for 10 minutes with gentle shaking to crosslink DNA. The cells were transferred to a 15-mL Falcon tube. The petri dish was rinsed with TE1 solution (50 mM Tris-Cl [pH 8.0], 50 mM EDTA), and the TE1 buffer was poured over the cells. The cells were then centrifuged at 2,246 x g, 4 °C for 5 minutes again. The supernatant was properly disposed of, and the pellets were stored at -20 °C. Galactose was added to the culture to a final concentration of 2% to induce DSBs. Cells were collected at the designed time points as described above. For lysis, the cell pellets were thawed on ice, then resuspended in spheroplasting buffer (0.4 M sorbitol, 0.4 M KCl, 40 mM sodium phosphate buffer [pH 7.2], 0.5 mM $MgCl_2$) and transferred to a 1.7 mL microfuge tube.

The cells were spheroplasted in zymolyase solution (2% glucose, 50 mM Tris-Cl [pH 7.5], 5 mg/mL zymolyase 100T) at 30 °C for 20 minutes. The cells were washed with spheroplasting buffer three times at 2,500 x g and restriction enzyme buffer (RE buffer: 50 mM potassium acetate, 20 mM Tris-acetate, 10 mM magnesium acetate, 1 mg/mL BSA) at 16,000 x g three times. The pellets were resuspended in 1.4x RE buffer, either alone or with a hybridization oligo to restore the *EcoR*I restriction sites, and stored at -80 °C. The DNA was solubilized by incubating the cells with 0.1% SDS at 65 °C for 13 minutes. 1% Triton X-100 quenched the SDS. The DNA was digested by 20 U *EcoR*I at 37 °C for 1 hour. The restriction enzyme was deactivated by incubating the DNA with 1.5% SDS at 55 °C for 10 minutes. The cells were returned to ice, and SDS was quenched by the addition of 6% Triton X-100. Ligation buffer (50 mM Tris-Cl [pH 8.0], 10 mM MgCl2, 10 mM DTT, 2.5 µg/mL BSA, 1 mM ATP, pH 8.0, 8 U T4 DNA ligase) was added to perform the ligation reaction at 16 °C for 1 hour and 30 minutes. 25 µg/mL protease K was added to digest the enzymes at 65 °C for 30 minutes. DNA was extracted by adding phenol:chloroform:isoamyl alcohol and vortexing. The upper water phase was moved and incubated with a tenth volume of sodium acetate and a volume of isopropanol at room temperature for 30 minutes and centrifuged at 21,130 x g, 4 °C for 10 minutes to get DNA precipitation. The DNA pellets were dried at 37 °C and dissolved by incubating with 1x TE buffer (10 mM Tris-Cl [pH 8.0], 1 mM EDTA) at 37 °C for 1 hour. The DNA was used as a qPCR template with the primers listed in Table 3.E3. DLC chimera content was calculated by [DLC amplification efficiency]^[-$\mathrm{Cp}_{(\mathrm{DLC})}$], and the intramolecular ligation product content was calculated by [intramolecular ligation amplification efficiency]^[-$\mathrm{Cp}_{(\mathrm{ligation})}$]. The final DLC signal was calculated as DLC chimera content divided by intramolecular ligation product content.

DLE assay

DLE assay was performed as described before(19,88). The procedures were similar with DLC assay except for (1) 2.5 OD_{600} of cells were collect at each time point; (2) DNA crosslinking was omitted and cell pellets were washed by TE1 buffer twice at 2,246 x g; (3) hybridization oligos were different and listed in Table 3.E3; (4) DNA was solubilized by 1% SDS at 65 °C for 15 minutes; (4) DNA digestion was performed by adding 20 U *Hin*dIII; (5) qPCR was performed using some different oligos listed in Table 3.E3.

APPENDIX B.2 Rational for calculating k_{off}.

This part introduces how to use fluorescence signal decay rate to calculate Rad54-DNA dissociation rate k_{off}, associated to Chapter 3.

The binding reaction between ligand (L) and protein (P) is:

$$P + L \underset{k_{off}}{\overset{k_{on}}{\rightleftharpoons}} PL \tag{1}$$

When flow is consistently on in our case to prevent more binding events, so

$$k_{on} = 0 \tag{2}$$

According to chemical kinetics,

$$\frac{d[PL]}{dt} = k_{off}[PL] \tag{3}$$

After solving this equation, we get that,

$$[PL](t) = Ce^{-k_{off}t} \tag{4}$$

where *C* is a constant (equal to $[PL](0)$). We also assume that fluorescence intensity is proportional to the number of fluorophores (here, is GFP-Rad54). Therefore, the fluorescence decays with the same first-order exponential forms:

$$I(t) = I_0 e^{-k_{off}t} \tag{5}$$

where *I* is fluorescence intensity, and I_0 is a constant equaling to $I(0)$.

Similarly, we assume that because of photobleaching, the fluorescence signal decays with first-order exponential forms, but the variable is the number of frames f instead of time t.

$$I(f) = I_0 e^{-k_{bleaching}f} \tag{6}$$

Add photobleaching and dissociation together, we have:

$$I(t,f) = I_0 e^{-k_{off}t - k_{bleaching}f} \tag{7}$$

We need to address that the photobleaching is a discrete event, while protein-DNA dissociation is a continuous function. But for the easy sake, we can map the time and frame numbers according to our capturing settings, $t = \frac{f}{framerate}$ since the observation only happens when snapshot is taken.

Thus, in "photobleaching" experiment, the acquisition is fast and takes 5 frames per second, $t = \frac{1}{5}f$, where t is in seconds. In "dissociation" experiment, the acquisition is slow and only takes 1 frame per second, $t = f$. That is, in "photobleaching experiment",

$$I(f) = I_0 e^{-(k_{bleaching} + \frac{1}{5}k_{off})f} \overset{\text{def}}{=} I_0 e^{-b_1 f} \tag{8}$$

In "dissociation" experiment,

$$I(f) = I_0 e^{-(k_{bleaching} + k_{off})f} \overset{\text{def}}{=} I_0 e^{-b_2 f} \tag{9}$$

b_1 and b_2 can be directly calculated by extracting intensity change from kymographs and fitting the change to a first-order exponential decay (see APPENDIX B.3.3, B.3.4, B.3.5 below), then $k_{bleaching}$ and k_{off} can be solved according to the linear equation in two variables:

$$\begin{cases} k_{bleaching} + \frac{1}{5}\, k_{off} = b_1 \\ k_{bleaching} + k_{off} = b_2 \end{cases} \tag{10}$$

That is,

$$k_{off} = \frac{5}{4}\,(b_2 - b_1) \tag{11}$$

If we neglected dissociation in "photobleaching" experiment, we could simply calculate k_{off} by:

$$k_{off} = b_2 - b_1 \tag{12}$$

APPENDIX B.3 Codes associated to Chapter 3.

B.3.1 Make heat map from AlphaMissense data

```
# Python
import seaborn as sns
import matplotlib.pyplot as plt
import pandas as pd
import numpy as np
import os

AMINO_ACIDS = "GAVLISTRATIONEDQRKHFYWP"
aa_list = list(AMINO_ACIDS)

def get_data_from_heat_map_csv(file, start, end):
    df = pd.read_csv(file)
    data = {}

    for pos in range(start, end + 1):
        data[pos] = []

        for aa in list_aa:
            variant = f"{pos}{aa}"  # e.g., "45G"

            # Find rows where protein_variant[1:] == variant
            match = df[df["protein_variant"].str[1:] == variant]

            if not match.empty:
                value = match.iloc[0, 1]  # second column
                data[pos].append(value)
            else:
                data[pos].append("na")

    return data

# import dataset
path = "/Users/dudu/Documents/hjy/Brooks-Lab/Rad54/AlphaMissense"
fn = "AF-Q92698-F1-aa-substitutions.csv"
# The dataset is downloaded from
# https://alphafold.ebi.ac.uk/entry/AF-Q92698-F1?activeTab=annotations
file = os.path.join(path,fn)
print(get_data_from_heat_map_csv(file,10,12))

# Input sequence (remove line breaks)
seq = """MRRSLAPSQLAKRKPEGRSCDDEDWQPGLVTPRKRKSSSETQIQECFLSPFRKPLSQLTN
QPPCLDSSQHEAFIRSILSKPFKVPIPNYQGPLGSRALGLKRAGVRRALHDPLEKDALVL
YEPPPLSAHDQLKLDKEKLPVHVVVDPILSKVLRPHQREGVKFLWECVTSRRIPGSHGCI
MADEMGLGKTLQCITLMWTLLRQSPECKPEIDKAVVVSPSSLVKNWYNEVGKWLGGRIQP
LAIDGGSKDEIDQKLEGFMNQRGARVSSPILIISYETFRLHVGVLQKGSVGLVICDEGHR
LKNSENQTYQALDSLNTSRRVLISGTPIQNDLLEYFSLVHFVNSGILGTAHEFKKHFELP
ILKGRDAAASEADRQLGEERLRELTSIVNRCLIRRTSDILSKYLPVKIEQVVCCRLTPLQ
TELYKRFLRQAKPAEELLEGKMSVSSLSSITSLKKLCNHPALIYDKCVEEEDGFVGALDL
```

```
FPPGYSSKALEPQLSGKMLVLDYILAVTRSRSSDKVVLVSNYTQTLDLFEKLCRARRYLY
VRLDGTMSIKKRAKVVERFNSPSSPDFVFMLSSKAGGCGLNLIGANRLVMFDPDWNPAND
EQAMARVWRDGQKKTCYIYRLLSAGTIEEKIFQRQSHKKALSSCVVDEEQDVERHFSLGE
LKELFILDEASLSDTHDRLHCRRCVNSRQIRPPPDGSDCTSDLAGWNHCTDKWGLRDEVL
QAAWDAASTAITFVFHQRSHEEQRGLR""".replace("\n", "")

# Define region of interest
start, end = 52, 96  # inclusive
positions = list(range(start, end + 1))
top_aa = list(seq[start - 1:end])  # zero-based indexing

data = get_data_from_heat_map_csv(file, start, end)
df = pd.DataFrame(data, index=list_aa)

df = df.replace("na", np.nan)
df = df.infer_objects(copy=False)

cmap = plt.cm.coolwarm.copy()   # define a colormap object
cmap.set_bad(color='black')     # customize how NaNs appear (black)

# Plot
fig, ax = plt.subplots(figsize=(12, 5))
# Heatmap
heatmap = sns.heatmap(
    df, cmap=cmap, mask=df.isna(),
    linewidths=0,
    cbar=True, ax=ax,
    vmin=0, vmax=1  # Force full color scale
)
ax.tick_params(axis='y', labelsize=11, rotation=0)

# Set colorbar
colorbar = heatmap.collections[0].colorbar
colorbar.ax.tick_params(labelsize=12)
colorbar.set_ticks([0, 0.2, 0.4, 0.6, 0.8, 1.0])
# Set bottom x-axis (positions)
ax.set_xticks(np.arange(len(positions)) + 0.5)
ax.set_xticklabels(positions,fontsize = 10)
ax.set_xlabel("Residue sequence number",fontsize = 13)
ax.tick_params(axis='x',    labelbottom=True,    bottom=True,    top=False,
labeltop=False)

# Top x-axis: amino acids from sequence
ax_top = ax.secondary_xaxis('top')
# Hide the top horizontal line (spine)
ax_top.spines['top'].set_visible(False)
ax_top.set_ticks(np.arange(len(top_aa)) + 0.5)
ax_top.set_xticklabels(top_aa,fontsize = 11)

ax.set_ylabel("Alternative amino acid",fontsize = 13)
plt.tight_layout()

# Save the figures
```

```
#save_path_pdf = os.path.join(path, "AlphaMissense_361I_373D.pdf")
#save_path_eps = os.path.join(path, "AlphaMissense_361I_373D.eps")
#plt.savefig(save_path_pdf, dpi=600, format="pdf")
#plt.savefig(save_path_eps, dpi=600, format="eps") #need to check

plt.show()
```

B.3.2 Make sequence logo using input multiple sequence alignment file

```
# Python
import numpy as np
import pandas as pd
import matplotlib.pyplot as plt
import logomaker as lm
from Bio import SeqIO
import os

#input alignment file
path = r"C:\Users\huqin\Desktop\TEST\Rad54_in_eukaryotes\more_sequences"
file = os.path.join(path, "deduplicated_sequences_clustalo_msa_trimal.fasta")

# read fasta file
raw_seqs = [str(record.seq) for record in SeqIO.parse(file, "fasta")]

#clean up sequences
seqs = [seq.strip() for seq in raw_seqs if ('#' not in seq) and ('>') not in
seq]
print('There are %d sequences, all of length %d'%(len(seqs), len(seqs[0])))

#load the alignment as a count matrix
counts_mat = lm.alignment_to_matrix(seqs)
counts_mat.head()

# Crop the matrix: positions start-end (Python is 0-based, so -1)
start = 327
end = 339
sub_matrix = counts_mat.loc[start-1:end-1]
sub_matrix.index = sub_matrix.index + 1

# Convert to information matrix
info_mat = lm.transform_matrix(sub_matrix, from_type='counts',
to_type='information')

# Plot and save the logo
plt.figure(figsize=(10, 3))
lm.Logo(info_mat, color_scheme='chemistry')
plt.xlabel("Position")
plt.ylabel("Bits")
#plt.title("Sequence Logo (positions 618–630)")
plt.savefig(os.path.join(path, f"logo_{start}_{end}.pdf"), dpi=600,
bbox_inches='tight')
plt.show()
```

B.3.3 Draw box region of interest on a kymograph to extract fluorescent intensity information

Code originally written by David Moraga; reproduced with permission.

```
% MATLAB
%Code to loop through a folder of kymos saved as tifs, open a kymo in
%ImageJ and select line ROIs for background and fluorophore.
%Takes a mean of background ROI and subtracts this value from each value in
the fluorophore roi
%Plots the fluorophore roi with an image showing where the line was drawn.
%Saves the plotted rois in a cell array.
%Saves the plots as matlab figs and pdfs in a folder created within the
%kymo folder
%%
%Input path here
path                                                                       =
"/Users/dudu/Desktop/curtains_from_David/250107_5nMRad54DD_PSC_Dissociation
/250129_KymoFigures_BHF023_bp4_inj1_C4_xyCorrected_transformed";
%%
ImageJ %Launch ImageJ from within Matlab.
%/Users/David/Documents/GitHub/CrickardCurtains/Matlab Functions
%Make the savedir
date = datestr(datetime, 'yymmdd_HHMM');
savefolder = date + "_Linear ROIs drawn in ImageJ";
[savedir,kymofolder] = fileparts(path);
savedir = fullfile(savedir,kymofolder,savefolder);
mkdir(savedir)

kymos = dir(fullfile(path,'*.tif'));

rois = cell(length(kymos),6); %pre-allocate the array to save ints and bg per
roi
%Add labels to rois cell array
rois{1,1} = "ROI data (Before bg subtract)";
rois{1,2} = "Mean background value";
rois{1,3} = "ROI box parameters";
rois{1,4} = "Kymoname";
rois{1,5} = "Background box parameters";
rois{1,6} = "Kymo image";

for i=1:length(kymos)

    displayed_kymo = sprintf("Kymo %s. # %i of %i",
kymos(i).name(),i,length(kymos))

    filename = fullfile(path,kymos(i).name);
    [filepath, kymoname] = fileparts(filename);

    img = imread(filename);
    imgtp = transpose(img);
    IJM.show('imgtp')
```

```
    rois{i+1,4} = kymoname; %Print the kymoname to the saving cell array
    rois{i+1,6} = img;

    %Ask the user if they want to process this kymo or skip it
    promptMessage = sprintf('Do you want to process this kymo: %s?\nType "y"
to continue, "n" to skip.', kymos(i).name);
    userResponse = input(promptMessage, 's');

    if strcmpi(userResponse, 'n')
        fprintf('Skipping kymo: %s\n', kymos(i).name);
        ij.IJ.getImage().close();  % Close the image if skipping
        continue;  % Skip the current kymo and go to the next iteration
    end

    disp('Please draw a box ROI in the ImageJ window for image background.
Click Continue when done');
    keyboard %Let user define region for background subtraction
    background = ij.IJ.getImage().getRoi();
    background_points = background.getPolygon();
    bx1 = background_points.xpoints(1);
    bx2 = background_points.xpoints(2);
    by1 = background_points.ypoints(1);
    by2 = background_points.ypoints(3);
    if bx2 > size(img,2) %Check if the line drawn exceeds image dimensions.
        bx2 = size(img,2); %If the line is longer than the kymo then truncate
to end of kymo
    end

    bg = img(by1:by2,bx1:bx2);
    bgval = mean(mean(bg));

    rois{i+1,2} = bgval; %Store the background value in the second column of
the saver array
    rois{i+1,5} = {sprintf("bg roi line x1 = %i",bx1),sprintf("bg roi line x2
= %i",bx2),sprintf("bg roi line y1 = %i",by1),sprintf("bg roi line y1
= %i",by2)};

    disp('Please draw a box ROI in the ImageJ window on a fluorophore for
data extraction.');
    keyboard %Let user define region for fluorophore identification
    fline = ij.IJ.getImage().getRoi();
    fline_points = fline.getPolygon();
    x1 = fline_points.xpoints(1);
    x2 = fline_points.xpoints(2);

    if x1 ==0
        x1=1;
    end

    if x2 > size(img,2) %Check if the line drawn exceeds image dimensions.
        x2 = size(img,2); %If the line is longer than the kymo then truncate
to end of kymo
```

```
    end

    y1 = fline_points.ypoints(1);
    y2 = fline_points.ypoints(3);

    if y1 == 0
        y1=1;
    end

    roi = img(y1:y2,x1:x2);

    roi_mean = mean(roi,1);
    ints = roi_mean - bgval;
    frames = x1:x2;

    %Store the data for each roi
    %rois{i} = roi;
    rois{i+1,1} = roi_mean;

    rois{i+1,3} = {sprintf("roi box x1 = %i",x1),sprintf("roi box x2
= %i",x2),sprintf("roi box y1 = %i",y1),sprintf("roi box y2 = %i",y2)};

    %Make a figure of where the roi and background are on the kymo
    roiplot = figure("Name",strcat(kymoname," ROI and intensity"));
    ax1 = subplot(2,1,1);
    imshow(img,[min(img,[],'all'),max(img,[],"all")]);
    axis on
    title(strcat(kymoname, " Selected ROI"))
    xlabel("Frames")
    ylabel("Pixels")
    colorbar("location","northoutside");
    rectangle("position", [bx1 by1 bx2-bx1 by2-by1], "EdgeColor", "green",
"Linestyle", ":");
    rectangle("position", [x1 y1 x2-x1 y2-y1], "EdgeColor", "blue",
"Linestyle", ":");
    legend("Box ROI","Background box","Location","southoutside")
    hold on
    ax2 = subplot(2,1,2);
    plot(frames,ints)
    xlim([1,size(img,2)]);
    linkaxes([ax1,ax2], 'x');
    xlabel("Frames")
    ylabel("Fluorescent intensity")
    title(kymoname+" Fluorescent intensity with background subract")


    saveas(gcf,savedir+"/"+kymoname+".pdf")
    savefig(savedir+"/"+kymoname+".fig")
    close
    ij.IJ.getImage().close()
end
save(savedir+"/"+"ROI Data","rois");
ij.IJ.run("Quit","");
```

B.3.4 Make exponential fit on fluorescent intensity extracted from B.3.3

```
% MATLAB
clear()
%%
path                                                                           =
'/Users/dudu/Desktop/curtains_from_David/20241025_5nMWTRad54_Dissociation/2
41028_KymoFigures_BHF030_BP8_5nMWTRad54_Dissociation_inj4_30C001_C1_stackre
gged_rigid_transformed/241119_1444_Linear ROIs drawn in ImageJ';
%%

load(path+"/"+"ROI Data.mat");

results = cell(length(rois), 8);  % Initialize a new cell array with 8 columns

m = length(rois);

starting_point = 150;

% Define the full path for the output folder
output_folder = "fitting_plot_150"
output_folder_path = fullfile(path, output_folder);

% Check if the folder exists, and create it if it doesn't
if ~exist(output_folder_path, 'dir')
    mkdir(output_folder_path);
end

% Initialize the progress bar
h = waitbar(0, 'Processing Data...');

for i = 2:m
    if length(rois{i}) > 0
        % Extract data starting from the 400th index to the end
        y = rois{i}(starting_point:end);
        % Ensure that y is a column vector
        y = y(:);
        % Create x as a column vector (from 1 to the length of y)
        x = (1:length(y))';

        % Fit the data using the 'exp1' model
        [fitresult,  gof]  =  fit(x,  y,  'exp1');   %  Transpose  x  to  match  y
dimensions

        % Extract the coefficients a and b from fitresult
        a = fitresult.a;
        b = fitresult.b;

        % Extract R-squared from gof (goodness of fit)
        r_squared = gof.rsquare;

        % Copy the original rois data to the first 5 columns
        results{i, 1} = rois{i,1};
```

```
        results{i, 2} = rois{i,2};
        results{i, 3} = rois{i,3};
        results{i, 4} = rois{i,4};
        results{i, 5} = rois{i,5};
        % Store 'a' in the 6th column
        results{i, 6} = a;
        % Store 'b' in the 7th column
        results{i, 7} = b;
        % Store R-squared in the 8th column
        results{i, 8} = r_squared;

        % % Create a new figure for the plot
        % figure;
        % hold on;
        %
        % % Plot the original data points
        % plot(x, y, 'o', 'MarkerFaceColor', 'b', 'MarkerEdgeColor', 'b', 'DisplayName', 'Data');
        %
        % % Plot the fitted curve
        % x_fitted = linspace(min(x), max(x), 100); % Generate smooth x values
        % y_fitted = a * exp(b * x_fitted);        % Compute fitted y values
        % plot(x_fitted, y_fitted, '-r', 'LineWidth', 2, 'DisplayName', 'Fitted Curve');
        %
        % % Add title, legend, and labels
        % title(sprintf('%s: a = %.2f, b = %.6f, R^2 = %.2f', rois{i,1}, a, b, r_squared));
        % xlabel('x');
        % ylabel('y');
        % legend('show');
        %
        % % Turn off hold
        % hold off;
        %
        % % Save the plot as an image file
        % filename = fullfile(output_folder_path, sprintf('%s_fit.png', rois{i,4}));
        % disp(['Saving plot to: ', filename]);  % Debugging line
        % print(gcf, filename, '-dpng', '-r300');  % Save as PNG with 300 dpi
        %
        % close; % Close the figure to avoid memory issues
    end

    % Update the progress bar
    waitbar(i / m, h, sprintf('Processing ROI %d of %d...', i, m));
end

% Close the progress bar once the loop is finished
close(h);

k_value = cell2mat(results(:, 7));
r_squared_values = cell2mat(results(:, 8));
```

```
% Create a new figure
figure;

% Left panel: Histogram of column 7
subplot(1, 2, 1); % 1 row, 2 columns, position 1
histogram(k_value);
xlabel('k_values');
ylabel('Frequency');
title('Histogram of k_values');

% Right panel: Histogram of column 8
subplot(1, 2, 2); % 1 row, 2 columns, position 2
histogram(r_squared_values);
xlabel('r_squared_values');
ylabel('Frequency');
title('Histogram of r_squared_values');

% save normalized signal according to r2
r2_threshold = 0.7;

figure;

% Initialize an empty array to store values of results{i, 7}
values_for_mean_sem = [];

% Initialize an empty matrix to store all normalized signals
normalized_signals = [];

for i = 1:length(results)
    % Check if R-squared value is greater than r2_threshold and b is
    % smaller than 0
    if results{i, 8} > r2_threshold & results{i,7} < 0
        % Get the original signal (assuming it's in the first column of
results)
        signal = results{i, 1};

        % Normalize the signal by dividing by 'a' (in the 6th column)
        normalized_signal = double(signal) / signal(starting_point);

        % Create the x-axis (length of the signal)
        x = 1:length(normalized_signal);

        % Plot the normalized signal and exclude it from the legend
        h = plot(x, normalized_signal);

        % Turn off legend for this line

set(get(get(h,'Annotation'),'LegendInformation'),'IconDisplayStyle','off');

        % Hold the plot to overlay subsequent signals
        hold on;
```

```
        % Add the value from results{i, 7} to the array for mean and SEM
        values_for_mean_sem = [values_for_mean_sem; results{i, 7}];

        % Add the normalized signal to the matrix (make sure dimensions match)
        normalized_signals = [normalized_signals; normalized_signal]; % Each
row is a normalized signal
    end
end

% Calculate the mean of each column (mean across all signals for each point)
mean_normalized_signal = mean(normalized_signals, 1); % Mean for each column

% Calculate the mean and SEM for results{i, 7} where results{i, 8} >
% r2_threshold
mean_value = mean(values_for_mean_sem);
sem_value = std(values_for_mean_sem) / sqrt(length(values_for_mean_sem));

% Plot the mean with a thick black line and store the handle
legend_entry = sprintf('Mean Value = %.6f, SEM Value = %.6f', mean_value,
sem_value)
h_mean = plot(x, mean_normalized_signal, 'k', 'LineWidth',
2,'DisplayName',legend_entry);  % 'k' for black, 'LineWidth' for thickness

% Add labels and title for clarity
xlabel('#Frame');
ylabel('Normalized Signal');
title(sprintf('The fitting starts at %.0f and R-squared is larger than %.2f',
starting_point, r2_threshold));
%title(['Plot of Normalized Signals with R^2 > ', num2str(r2_threshold)]);

% Add the legend with final mean and SEM values
legend('show')

hold off;  % Release the plot hold after all signals are plotted

% save(path+"/"+"Fitting_100","results"); % Save the .mat file
figurename = path+"/"+"dissociation_signal_150_07.png";
% Alternatively, use the print function for more control (e.g., specifying
resolution)
print(figurename, '-dpng', '-r600'); % saves as PNG with 600 dpi resolution

% Save the filtered signal to a new spreadsheet
writematrix(normalized_signals, path+"/"+"normalized_150_07.xlsx")
```

B.3.5 Plot normalized fluorescent signal decay using input from B.3.4

```
# Python
import os
import numpy as np
import pandas as pd
from matplotlib import pyplot as plt
import seaborn as sns
import warnings
file_path_signal                                                           =
"/Users/dudu/Desktop/curtains_from_David/dissociation_box_roi_analysis_1025
_1031/normalized_signal"
file_bleaching_signal                                                      =
"1025_BHF030_BP8_Bleaching_30C_02mLpermin_C1_transformed_normalized_from_40
0_filterat07_normalized_signal.csv"
file_wt_signal                                                             =
"1028_BHF030_BP8_5nMWTRad54_Dissociation_inj4_30C001_C1_stackregged_rigid_t
ransformed_normalized_from_150_filterat07_normalized_signal.csv"
file_aa_signal                                                             =
"1212_250211_Rad54S816AS817A_normalized_from_150_filterat_07_normalized_sig
nal.csv"
file_dd_signal                                                             =
"1031_10nM_Rad54_S816D_S817D_singletether_02mLpermin_normalized_from_50_fil
terat_07_normalized_signal.csv"

bleaching_signal = os.path.join(file_path_signal,file_bleaching_signal)
wt_signal = os.path.join(file_path_signal,file_wt_signal)
aa_signal = os.path.join(file_path_signal,file_aa_signal)
dd_signal = os.path.join(file_path_signal,file_dd_signal)

df_bleaching_signal = pd.read_csv(bleaching_signal)
df_wt_signal = pd.read_csv(wt_signal)
df_aa_signal = pd.read_csv(aa_signal)
df_dd_signal = pd.read_csv(dd_signal)

fig,ax = plt.subplots(figsize = (6,5), layout = "constrained")
# Border thickness whole graph
for axis in ['bottom','left']:
    ax.spines[axis].set_linewidth(3)

# Remove the top and right spines
ax.spines['top'].set_visible(False)
ax.spines['right'].set_visible(False)

# Adjust the tick parameters
ax.tick_params(axis="both", width = 2, labelsize=16)

# Add labels and axis
ax.set_ylabel('Normalized fluorescent signal',fontsize = 20)
ax.set_xlabel("#Frame after maximun binding", fontsize = 20)

# Calculate the mean of each column
means_bleaching = df_bleaching_signal.mean()
```

```
std_bleaching = df_bleaching_signal.std()

means_wt = df_wt_signal.mean()
std_wt = df_wt_signal.std()

means_aa = df_aa_signal.mean()
std_aa = df_aa_signal.std()

means_dd = df_dd_signal.mean()
std_dd = df_dd_signal.std()

plotting_length = 700
x = range(1, plotting_length+1)  # x-axis is 1, 2, ..., number of columns

bleaching_line, bleaching_cap, bleaching_bar  = ax.errorbar(
    x,                      means_bleaching.values[400:400+plotting_length],
yerr=std_bleaching.values[400:400+plotting_length],
    fmt='o-',   color='black',   ecolor='grey',   elinewidth=2,   capsize=0,
markersize = 2,
    label='Bleaching'
)

wt_line, wt_cap, wt_bar = ax.errorbar(
    x,                             means_wt.values[150:150+plotting_length],
yerr=std_wt.values[150:150+plotting_length],
    fmt='o-',  color='#377eb8',  ecolor='#9ecae1',  elinewidth=2,  capsize=0,
markersize = 2,
    label='Rad54'
)

aa_line, aa_cap, aa_bar = ax.errorbar(
    x,                             means_aa.values[150:150+plotting_length],
yerr=std_aa.values[150:150+plotting_length],
    fmt='o-',  color='#2ca25f',  ecolor='#99d8c9',  elinewidth=2,  capsize=0,
markersize = 2,
    label='Rad54S816AS817A'
)

dd_line, dd_cap, dd_bar = ax.errorbar(
    x,                               means_dd.values[50:50+plotting_length],
yerr=std_dd.values[50:50+plotting_length],
    fmt='o-',  color='#d95f02',  ecolor='#fdbb84',  elinewidth=2,  capsize=0,
markersize = 2,
    label='Rad54S816DS817D'
)

[bar.set_alpha(0.2) for bar in bleaching_bar]
[bar.set_alpha(0.2) for bar in wt_bar]
[bar.set_alpha(0.2) for bar in aa_bar]
[bar.set_alpha(0.2) for bar in dd_bar]

plt.legend(loc = "lower left", fontsize = 14,frameon=False)
```

```
# Save the figures
save_path_signal_pdf             =             os.path.join(file_path_signal,
"fluorescent_signal_decay_truncated_wt150_r07_aa150_r07_dd50_r07_bigger.pdf
")
save_path_signal_eps             =             os.path.join(file_path_signal,
"fluorescent_signal_decay_truncated_wt150_r07_aa150_r07_dd50_r07_bigger.eps
")
plt.savefig(save_path_signal_pdf, dpi=600, format="pdf")
plt.savefig(save_path_signal_eps, dpi=600, format="eps") #need to check
plt.show()
```

APPENDIX C

APPENDIX C.1 Rational for applying Hill equation in mapping gene conversion frequency and D-loop extension rate.

Hill equation is primarily used to describe cooperative binding between proteins (P) and ligands (L). Let's assume the ligand is DNA here. For a simple one-to-one reversible reaction:

$$P + L \underset{k_{-1}}{\overset{k_1}{\rightleftharpoons}} PL \tag{1}$$

The fraction of reacted L can be described like:

$$\theta = \frac{[P]}{[P] + K_d} \tag{2}$$

where θ represents the fraction of reacted L, *[P]* describes the protein concentration, K_d is the apparent dissociation constant of the reaction having the same unit as *[P]*.

$$K_d = \frac{k_{-1}}{k_1} = \frac{[P][L]}{[PL]} \tag{3}$$

For a cooperative reaction:

$$nP + L \underset{k_{-1}}{\overset{k_1}{\rightleftharpoons}} LP_n \tag{3}$$

The fraction of reacted L can be described like:

$$\theta = \frac{[P]^n}{K_d + [P]^n} \tag{4}$$

Where K_d is the apparent dissociation constant of the reaction and has a unit of $[P]^n$.

$$K_d = \frac{k_{-1}}{k_1} = \frac{[P]^n[L]}{[LP_n]} \tag{5}$$

Equation (2) is the special case where $n = 1$, indicating a non-cooperative reaction. When $n > 1$, it means the reaction is positively cooperative with early reaction steps enhancing the following steps. When $n < 1$, the reaction is negatively cooperative with early steps inhibiting subsequence reaction steps.

To normalize K_d to a single-binding-event constant and give it the same unit as *[P]*, we define an effective dissociation constant K_{eff}.

$$K_{eff} = K_d^{1/n} \tag{6}$$

Then the Hill equation can be rewritten as:

$$\theta = \frac{[P]^n}{K_{eff}^n + [P]^n} \tag{7}$$

This relationship can be regarded as describing a system with two competing states, A (active) and B (inactive), with their ratio to be:

$$\frac{[A]}{[B]} = \left(\frac{[P]}{K_{eff}}\right)^n \tag{8}$$

And the probability of status A is

$$\theta = \frac{[A]}{[A] + [B]} = \frac{[P]^n}{K_{eff}^n + [P]^n} \tag{9}$$

Which is identical with Equation (7).

More generally, Hill equation can describe systems governed by two competing reaction rates - an on rate k_{on} and an off rate k_{off}. The probability of the system to be in the on state is:

$$P_{on} = \frac{k_{on}}{k_{on} + k_{off}} \tag{10}$$

And in our antagonism model discussed in Chapter 4, k_{on} is the rate of D-loop extension k_{eff} while k_{off} is the rate of D-loop disruption K. Accordingly, the final GC can be expressed as:

$$GC = GC_{max} \frac{k_{eff}^{n}}{k_{eff}^{n} + K^{n}} \tag{11}$$

where n describes the cooperativity of the reaction and GC_{max} defines the upper limit of possible gene conversion events without changing the curve shape.

Mapping GC to a Hill equation is conceptually appropriate because D-loop intermediates are subject to kinetic competition between extension (driven by pro-recombination factors such as Rad54) and disruption (mediated by anti-recombination factors such as Rdh54, Sgs1 and Mph1). These competing reactions determine whether a D-loop is stabilized and extended (leading to long track gene conversion results) or disrupted (favoring non-crossover outcomes). When multiple cooperative factors participate in either reaction branch, the system naturally acquires Hill-like behavior, where small changes in activity or concentration can cause sharp, switch-like transitions in GC. Therefore, the Hill formalism provides a compact yet mechanistically interpretable framework for linking biochemical rate competition to HR outcome distributions.

APPENDIX C.2 Codes associated with Chapter 4.

C.2.1 Fit current observed GC frequency to effective D-loop extension rates.

```
# Python
# ---- Rad54/Rdh54: fit Hill mapping GC(k) and plot ----
# Requirements: numpy, pandas, scipy, matplotlib

import numpy as np
import pandas as pd
import matplotlib.pyplot as plt
from scipy.optimize import least_squares
import os

# ----- INPUTS -----
GCmax = 0.65
# Half-times (min) and GC fractions (0..1)
data = pd.DataFrame({
    "condition": ["Rad54", "Rad54+Rdh54", "Rad54+Rdh54K318R"],
    "t_half_min": [14.5, 25.0, 50.0],
    "GC_frac":    [0.5183, 0.4106, 0.1837]
})

# ----- Convert half-times to first-order rates k = ln(2)/t1/2 -----
ln2 = np.log(2.0)
data["k"] = ln2 / data["t_half_min"]

# Convenience
k_Rad54      = data.loc[data.condition=="Rad54","k"].iloc[0]
k_Rad54_Rdh  = data.loc[data.condition=="Rad54+Rdh54","k"].iloc[0]
k_Rad54_KR   = data.loc[data.condition=="Rad54+Rdh54K318R","k"].iloc[0]

# ----- Antagonism parameters from slow-down ratios -----
# k_eff = k_Rad54 / (1 + beta*Rdh54 + gamma*Rdh54KR) at 1× concentrations
beta  = k_Rad54 / k_Rad54_Rdh - 1.0
gamma = k_Rad54 / k_Rad54_KR  - 1.0
print(f"beta = {beta:.6g}, gamma = {gamma:.6g}")

# ----- Define Hill equation -----
def hill_gc(k, GCmax, K, n):
    return GCmax * (k**n) / (K**n + k**n)

# Residue functions
def resid_free(params, k, gc):
    GCmax, K, n = params
    return hill_gc(k, GCmax, K, n) - gc

k_obs  = data["k"].values
gc_obs = data["GC_frac"].values

# --- Fit with all parameters free ---
x0_free = np.array([max(gc_obs)*1.2, np.median(k_obs), 2.0])
```

```
bounds_free = ([0.0, 0.0, 0.0], [1.0, np.inf, np.inf])
fit_free = least_squares(resid_free, x0_free, bounds=bounds_free, args=(k_obs,
gc_obs))
GCmax_free, K_free, n_free = fit_free.x
# ---- Fit summary ----
print("\n=== Hill fit summary ===")
print(f"Best-fit GCmax= {GCmax_free:.4f}")
print(f"Best-fit K = {K_free:.4f} min^-1")
print(f"Best-fit n = {n_free:.4f}")
print(f"Number of iterations: {fit_free.nfev}")
print(f"Final cost (sum of squared residuals): {fit_free.cost:.6e}")
print(f"Residuals (predicted - observed): {fit_free.fun}")
print("========================")

# ----- Plot points + fitted Hill curve -----
k_grid = np.linspace(k_obs.min()*0.5, k_obs.max()*1.5, 400)
gc_fit = hill_gc(k_grid, GCmax_free, K_free, n_free)

fig, ax = plt.subplots(figsize = (6,4), layout = "constrained")
ax.tick_params(axis='both', which='major', width = 2, labelsize=16)
ax.spines['top'].set_visible(False)
ax.spines['right'].set_visible(False)
for axis in ['bottom', 'left']:
    ax.spines[axis].set_linewidth(2)

ax.plot(k_grid, gc_fit, color='black', linewidth=1.6,
         label=f"Fitted    Hill\n(GCmax={GCmax_free:.4f},    K={K_free:.4f},
n={n_free:.2f}, cost={fit_free.cost:.4f})")
ax.scatter(k_obs, gc_obs, color='orange', marker='x', s=70,
            linewidths=2, label="Observed data", zorder=5)

ax.set_xlabel("Extension rate k_eff (min$^{-1}$)", fontsize = 15)
ax.set_ylabel("Gene conversion frequency", fontsize = 15)
plt.legend(loc = "lower right")

# Save the plot
#save_path_pdf  =  os.path.join("/Users/dudu/Documents/hjy/B-exam/antagonism
model", "fitting_plot.pdf")
#save_path_eps  =  os.path.join("/Users/dudu/Documents/hjy/B-exam/antagonism
model", "fitting_plot.eps")
#save_path_png  =  os.path.join("/Users/dudu/Documents/hjy/B-exam/antagonism
model", "fitting_plot.png")
#plt.savefig(save_path_pdf, dpi=600, format="pdf")
#plt.savefig(save_path_eps, dpi=600, format="eps")
#plt.savefig(save_path_png, dpi=600, format="png")
plt.show()
```

C.2.2 Loop extrusion rate simulation with different standard deviations σ

```
# Python
# import the modules that necessary
import numpy as np
import pandas as pd
import matplotlib as mpl
import matplotlib.pyplot as plt
import os
# Let assume that the faster motor is "act"-fold faster than the slower one
def generate_a_loop_int(mu, sigma):
    while True:
        # Generate two values from the normal distribution
        val1, val2 = np.random.normal(mu, sigma, 2)

        # Check if both values are greater than 0
        if val1 > 0 and val2 > 0:
            # Return the difference between the two values
            lpfr = abs(val1-val2)
            return lpfr
#def a function to save all possible results of a certain distribution, target
loop size from rep times
def gen_loops_with_repeats_inc(mu, sigma, rep):
    lpfr_ls = [generate_a_loop_int(mu, sigma) for _ in range(rep)]
    return np.array(lpfr_ls)
#input
mu = 65 #bp/s
sigma_1 = 6.7
sigma_2 = 33.5
sigma_3 = 67

rep = 1000
lpfr_1 = gen_loops_with_repeats_inc(mu,sigma_1,rep)
lpfr_2 = gen_loops_with_repeats_inc(mu,sigma_2,rep)
lpfr_3 = gen_loops_with_repeats_inc(mu,sigma_3,rep)

# Ensure correct shape
lpfr_input = [lpfr_1.flatten(), lpfr_2.flatten(), lpfr_3.flatten()]

#print(lpfr_input)
fig,ax = plt.subplots(figsize = (5,4), layout="constrained")
ax.set_ylabel("Loop extrusion rate (bp/s)", fontsize = 15)
ax.yaxis.set_tick_params(labelsize=15)
ax.xaxis.set_tick_params(labelsize=15)

ax.spines['top'].set_visible(False)
ax.spines['right'].set_visible(False)
ax.spines['top'].set_visible(False)
ax.spines['right'].set_visible(False)

x_label = [r'$\sigma = 6.7$', r'$\sigma = 33.5$', r'$\sigma = 67$']
ax.boxplot(lpfr_input,
              positions=[0, 1, 2],
```

```
              labels=x_label,
              patch_artist=True,  # Enables custom coloring
              boxprops=dict(facecolor="lightblue", color="black"))

save_path = "/Users/dudu/Documents/hjy/Brooks-
Lab/Rad54/Rad54_mediated_loop_formation"
# Save the figures
save_path_pdf = os.path.join(save_path, "Different sigma.pdf")
save_path_eps = os.path.join(save_path, "Different sigma.eps")
plt.savefig(save_path_pdf, dpi=600, format="pdf")
plt.savefig(save_path_eps, dpi=600, format="eps") #need to check whether
doable

plt.show()
```

C.2.3 Loop extrusion rate simulation driven by Rad51-activated motor

```
# Python
# import the modules that necessary for this notebook
import numpy as np
import pandas as pd
import matplotlib as mpl
import matplotlib.pyplot as plt
import os
# Let assume that the faster motor is "act"-fold faster than the slower one
def generate_a_loop(mu, sigma, act):
    while True:
        # Generate two values from the normal distribution
        val1 = np.random.normal(mu, sigma, 1)
        val2 = act*val1 #the second factor is simply act-fold faster than the
first motor

        # Check if both values are greater than 0
        if val1 > 0 and val2 > 0:
            # Return the difference between the two values
            lpfr = abs(val1-val2)
            return lpfr
#def a function to save all possible results of a certain distribution, target
loop size from rep times
def gen_loops_with_repeats(mu, sigma, act, rep):
    lpfr_ls = [generate_a_loop(mu, sigma, act) for _ in range(rep)]
    return np.array(lpfr_ls)
#input
mu = 65 #bp/s
sigma = 67
rep = 1000
lpfr_2 = gen_loops_with_repeats(mu,sigma,2,rep)
lpfr_5 = gen_loops_with_repeats(mu,sigma,5,rep)
lpfr_7 = gen_loops_with_repeats(mu,sigma,7,rep)

# Ensure correct shape
lpfr_input = [lpfr_2.flatten(), lpfr_5.flatten(), lpfr_7.flatten()]

#print(lpfr_input)
fig,ax = plt.subplots(2,1,figsize = (5,8), layout="constrained")
ax[0].set_ylabel("Frequency", fontsize = 15)
ax[0].set_xlabel("Velocity (bp/s)", fontsize = 13)
ax[1].set_ylabel("Loop extrusion rate (bp/s)", fontsize = 15)
#ax[1].set_yscale('log')
#ax[0].set_xlim(0,250)
ax[0].yaxis.set_tick_params(labelsize=15)
ax[1].yaxis.set_tick_params(labelsize=15)
ax[0].xaxis.set_tick_params(labelsize=15)
ax[1].xaxis.set_tick_params(labelsize=15)

ax[0].spines['top'].set_visible(False)
ax[0].spines['right'].set_visible(False)
ax[1].spines['top'].set_visible(False)
```

```
ax[1].spines['right'].set_visible(False)

rate_input = np.random.normal(mu, sigma, 1000)
rate_input_act5=5*rate_input
ax[0].hist(rate_input, bins=50, density = True, histtype =
"step",label="Before activation")
ax[0].hist(rate_input_act5, bins=50, density = True, histtype = "step",color
= "orange", label="Activation_fold=5")
ax[0].legend(
    loc="center left",          # anchor relative to left edge of the box
    bbox_to_anchor=(0.4, 0.5), # (x=1.02 places it just outside right edge,
y=0.5 centers it vertically)
    fontsize=13,
    frameon=True               # optional: remove legend border
)

x_fold = ["act=2","act=5","act=7"]
x_pos = np.arange(len(x_fold))

ax[1].boxplot(lpfr_input,
              positions=[0, 1, 2],
              labels=x_label,
              patch_artist=True,  # Enables custom coloring
              boxprops=dict(facecolor="lightblue", color="black"))

# --- Set x-axis labels and style ---
ax[1].set_xticks(x_pos)
ax[1].set_xticklabels(x_fold, fontsize=15)
ax[1].set_yticks(np.arange(0, 2000 + 1, 500))

save_path = "/Users/dudu/Documents/hjy/Brooks-
Lab/Rad54/Rad54_mediated_loop_formation"
# Save the figures
save_path_pdf = os.path.join(save_path, "Activated_driver.pdf")
save_path_eps = os.path.join(save_path, "Activated_driver.eps")
plt.savefig(save_path_pdf, dpi=600, format="pdf")
plt.savefig(save_path_eps, dpi=600, format="eps") #need to check whether
doable

plt.show()
```

C.2.4 Loop growth simulation

```
# Python
# import the modules that necessary for this notebook
import numpy as np
import pandas as pd
import matplotlib as mpl
import matplotlib.pyplot as plt
import os

# ----- Parameters -----
vf = 394         # bp/s
vs = 67          # bp/s
Delta_v0 = vf - vs
tau_stall_base = 10.0
phi = 0.8

# Mutant
vf_mut = 42
vs_mut = 0
Delta_v0_mut = vf_mut - vs_mut
tau_stall_mut = 8.0
phi_mut = 1.0

alpha = 2*np.pi/10.5    # rad per bp
C = 0.01                # effective torsional stiffness

# ----- Helper functions -----
def beta(phi, Delta_v0, tau_stall):
    return (C * alpha * phi * Delta_v0) / tau_stall

def Lmax(phi, tau_stall):
    return tau_stall / (C * alpha * phi)

def L_of_t(phi, Delta_v0, t, tau_stall):
    b = beta(phi, Delta_v0, tau_stall)
    return (Delta_v0 / b) * (1 - np.exp(-b * t))

def dv_of_t(phi, Delta_v0, t, tau_stall):
    b = beta(phi, Delta_v0, tau_stall)
    return Delta_v0 * np.exp(-b * t)

# ----- Time vector -----
t = np.linspace(0, 6.0 / beta(phi_mut, Delta_v0_mut, tau_stall_mut), 600)

# ----- Compute curves -----
L_base = L_of_t(phi, Delta_v0, t, tau_stall_base)
L_mut = L_of_t(phi_mut, Delta_v0_mut, t, tau_stall_mut)

dv_base = dv_of_t(phi, Delta_v0, t, tau_stall_base)
dv_mut = dv_of_t(phi_mut, Delta_v0_mut, t, tau_stall_mut)

# ----- Plots -----
```

```
plt.figure(figsize=(5,4))
plt.plot(t, L_base, label="Wildtype")
plt.plot(t, L_mut, label="Rad54R272Q", linestyle="--")
plt.xlabel("Time (s)", fontsize=15)
plt.ylabel("Loop size L(t) (bp)",fontsize = 15)
plt.legend(loc = "lower right", fontsize = 15)
# Style: hide top/right spines, thicken ticks, enlarge labels
ax = plt.gca()
ax.spines["top"].set_visible(False)
ax.spines["right"].set_visible(False)
ax.tick_params(width=2, length=6, labelsize=13)

plt.tight_layout()
plt.savefig(os.path.join(save_path, "maximum loop size.png"),dpi = 600)
plt.show()

plt.figure(figsize=(5,4))
plt.plot(t, dv_base, label="Wildtype")
plt.plot(t, dv_mut, label="Rad54R272Q", linestyle="--")
plt.xlabel("Time (s)", fontsize=15)
plt.ylabel("Loop extrusion rate Δv(t) (bp/s)", fontsize = 15)
plt.legend(loc = "upper right", fontsize = 15)
# Style: hide top/right spines, thicken ticks, enlarge labels
ax = plt.gca()
ax.spines["top"].set_visible(False)
ax.spines["right"].set_visible(False)
ax.tick_params(width=2, length=6, labelsize=13)

plt.tight_layout()
plt.savefig(os.path.join(save_path,  "loop_extrusion_rate_drop.png"),dpi  =
600)
plt.show()
```